Le spectre d'absorption du dioxyde de carbone dans le proche infrarouge (1.4-1.7 μm) : Cavity Ring Down Spectroscopy, modélisation globale et bases de données

Boris Perevalov

Université Joseph Fourier - Grenoble 1

T H È S E

Pour obtenir le grade de

DOCTEUR DE L'UNIVERSITE JOSEPH FOURIER

Ecole Doctorale de Physique

Présentée et soutenue publiquement par

Boris Perevalov

le 11 Février 2009

Titre:

Le spectre d'absorption du dioxyde de carbone dans le proche infrarouge (1.4–1.7 μm): Cavity Ring Down Spectroscopy, modélisation globale et bases de données

Directeur de thèse: Alain Campargue

Jury :

Rapporteurs :	Jean Vander Auwera
	Bruno Bézard
Examinateurs :	Claudine Kahane
	Alain Campargue

Thèse réalisée au Laboratoire de Spectrométrie Physique

BP87 - 38402 St. Martin d'Hères, Cedex, France

Remerciement

Cette thèse a été réalisée au Laboratoire de Spectrométrie Physique de l'Université Joseph Fourier de Grenoble en collaboration avec Laboratoire de Spectroscopie Théorique de l'Institut d'Optique Atmosphérique de Tomsk (Académie des Sciences Russe).

Je tiens tout d'abord à remercier Alain Campargue, mon directeur de thèse, pour les conditions de travail exceptionnelle qu'il m'a offertes, pour sa participation, pour sa sympathie et sa patience. Son énergie et son professionnalisme ont été des facteurs clefs de ma réussite.

Je voudrais remercier tout particulièrement Samir Kassi et Daniele Romanini qui ont assuré la base expérimentale de ce travail.

Mes remerciements vont également à An Wen Liu et Bo Gao qui m'ont été d'une aide précieuse pour tout ce qui est relatif à l'enregistrement des spectres.

Je remercie Oleg Lyulin et Shuiming Hu dont les programmes de fit ont été utilisés dans ce travail. Oleg Lyulin m'a appuyée de toutes ses connaissances informatiques, notamment sur la langue de programmation Fortran.

Merci de manière générale à toute l'équipe LAME pour sa bonne humeur permanente, et pour leur chaleureux accueil. C'était un vrai plaisir de travailler au sien de cette équipe.

Un grand merci aux membres du jury; en particulier à Jean Vander Auwera et Bruno Bézard, pour l'intérêt qu'ils ont témoigné pour mon travail en acceptant les rôles de rapporteurs.

Enfin, il va sans dire que je remercie aussi l'ambassade de France en Russie et QUASAAR pour le financement de ma recherche.

Résumé

Les spectres d'échantillons naturel et enrichi en ^{13}C du dioxyde de carbone ont été enregistrés entre 5851 et 7045 cm^{-1} par CW-Cavity Ring Down Spectroscopy à très haute sensibilité. Environ 8000 transitions appartenant à huit isotopologues de CO_2 ($^{12}C^{16}O_2$, $^{13}C^{16}O_2$, $^{16}O^{12}C^{18}O$, $^{16}O^{12}C^{17}O$, $^{16}O^{13}C^{18}O$, $^{16}O^{13}C^{17}O$ and $^{12}C^{18}O_2$) ont été mesurées avec une précision estimée de 1×10^{-3} cm^{-1}. Les paramètres spectroscopiques ont été obtenus pour un total de 238 bandes, la plupart nouvellement observées. Un certain nombre de résonances ont été observées et identifiées. Les données expérimentales disponibles dans la littérature et celles obtenues au cours de cette thèse ont été utilisées pour améliorer les paramètres du modèle effectif qui reproduit les positions avec un accord proche de leurs incertitudes expérimentales.

Les intensités de 2039 et 952 raies ont été mesurées pour $^{13}C^{16}O_2$ et $^{12}C^{16}O_2$. Dans le cas de $^{12}C^{16}O_2$ la plupart des intensités mesurées appartiennent aux bandes perpendiculaires et "interdites". Ces données expérimentales, combinées à des données publiées, ont été utilisées pour améliorer les paramètres du moment dipolaire effectif de ces deux isotopologues. L'ensemble de ces paramètres reproduit les intensités mesurées aux incertitudes expérimentales près. Quatre cas de résonance interpolyade ont été observés pour la première fois dans le cas de CO_2.

Cette thèse apporte une contribution importante aux bases de données spectroscopiques du dioxyde de carbone: CDSD et HITRAN. Les résultats obtenus ont été intégrés dans la base de données HITRAN qui fait référence pour la physique de l'atmosphère.

Mots-clés :

Dioxyde de carbone, CO_2, spectroscopie moléculaire à haute résolution, infrarouge, Cavity Ring Down Spectroscopy, CRDS, positions de raies, intensités de raies, bases de données spectroscopiques.

Abstract

The CW-CRDS spectra of natural and ^{13}C-enriched carbon dioxide in the 5851–7045 cm^{-1} region were analysed including the previously investigated 6130–6750 cm^{-1} region which was re-examined in order to reduce the fraction of unassigned lines. About 8000 line positions belonging to eight CO_2 isotopologues ($^{12}C^{16}O_2$, $^{13}C^{16}O_2$, $^{16}O^{12}C^{18}O$, $^{16}O^{12}C^{17}O$, $^{16}O^{13}C^{18}O$, $^{16}O^{13}C^{17}O$, $^{13}C^{18}O_2$, $^{17}O^{13}C^{18}O$) were newly measured with estimated accuracy of 1×10^{-3} cm^{-1}. Only about 5% of lines, mostly very weak ones, remained unassigned in the 5851–7045 cm^{-1} region. The rovibrational parameters were retrieved for a total of 238 bands belonging to eight CO_2 isotopologues which correspond to a total of 213 vibrational upper states. A number of resonance intersections perturbing upper states were observed and identified. The newly observed line positions were added to the input datasets in order to refine the effective Hamiltonian parameters for six CO_2 isotopologues. The fitted sets of effective Hamiltonian parameters reproduce the line positions from all involved experimental sources close to their experimental uncertainties.

The line strengths of 2039 and 952 transitions were measured for $^{13}C^{16}O_2$ and $^{12}C^{16}O_2$ isotopologues in the 1.6 μm region. In the case of the principal isotopologue ($^{12}C^{16}O_2$) the most part of the measured intensities belong to weak perpendicular and "forbidden" bands. The present results were gathered with the selected intensity data reported in the literature for this region in order to refine the effective dipole moment parameters by least-squares fitting. The fitted sets of effective dipole moment parameters reproduces the line intensities from all involved experimental sources within their uncertainties.

Four occurrences of interpolyad resonance interaction were evidenced in this work for the first time in the case of carbon dioxide.

The present work makes an important contribution in the development of the CDSD and HITRAN databases for carbon dioxide.

Keywords:

Carbon dioxide, CO_2, high resolution molecular spectroscopy, infrared, Cavity Ring Down Spectroscopy, CRDS, line positions, line intensities, specroscopic databases.

Contents

Introduction

Par l'effet de serre qu'il provoque, le dioxyde de carbone (CO_2) est le principal moteur du changement climatique que nous connaissons. Au cours du dernier siècle, la concentration du CO_2 atmosphérique a augmenté rapidement, passant de 280 à 380 ppm. Les modèles climatiques récents ont montré que cette augmentation d'origine anthropique a conduit à augmenter l'effet de serre dans les années 1975–2008. De nombreux travaux sont en cours pour mieux comprendre le lien entre le CO_2 atmosphérique et le changement climatique et pour proposer des scenarios pour les années à venir.

Le dioxyde de carbone est l'un des principaux produits de la combustion des carburants organiques. La connaissance des propriétés radiatives du CO_2 est nécessaire pour modéliser les flux radiatifs dans un certain nombre de systèmes physiques, comme les incendies et les systèmes de combustion.

Les atmosphères de Vénus et Mars sont essentiellement composées de dioxyde de carbone, avec une concentration relative de 96,5 et 95,4%, respectivement. En raison de ces très fortes valeurs, les fenêtres de transparence sont utilisées pour étudier ces atmosphères planétaires. Elles doivent donc être caractérisées avec une grande précision, ce qui suppose des mesures en laboratoire avec des techniques d'absorption de très grande sensibilité vu les longueurs d'absorption en jeu. En outre, les isotopologues minoritaires de CO_2 peuvent contribuer de façon importante à l'absorption dans ces fenêtres de transparence. C'est pourquoi, l'information spectroscopique sur les espèces isotopiques rares de CO_2, en particulier à des températures élevées, est nécessaire pour l'étude des atmosphères de Vénus et Mars.

Pour toutes ces applications, des données spectroscopiques précises et aussi complètes que possible sont indispensables. Il existe plusieurs bases de données spectro-

scopiques fournissant les paramètres des raies du dioxyde de carbone. Ces bases de données présentes différents avantages et inconvénients en termes de complétude et précision.

L'objectif de cette thèse est d'améliorer les connaissances du spectre de CO_2 vers 1.6 micron par la technique Cavity Ring Down Spectroscopy. La grande sensibilité de cette technique donne accès à des raies deux ordres de grandeur moins intenses que ce qui peut être observé avec les techniques traditionnelles (spectroscopie à transformée de Fourier notamment). Il est ainsi possible de détecter des raies très faibles de bandes chaudes et/ou de J très élevé, ce qui permet de modéliser correctement ces bandes qui jouent un rôle dans des conditions de très grands parcours (atmosphères de Mars et Vénus) ou de très haute température (combustion, atmosphère profonde de Vénus).

Atmospheric carbon dioxide (CO_2) is the key gaseous contributors to the greenhouse effect and it has been recognized as principal anthropogenic driver of the climate change. It is well known that atmospheric carbon dioxide increases significantly (see Fig. 1) due to the increase of fossil fuel consumption and deforestation, by which the anthropogenic activities are accompanied. The atmospheric CO_2 has increased rapidly from 280 to 380 ppm during the last century. The recent climate model calculations have shown that increase of carbon dioxide in atmosphere had led to increase of the greenhouse effect in the 1975–2008 years. Numerous surface, suborbital and satellite assets will be deployed during the next decades in the intensive efforts to answer the fundamental science questions surrounding atmospheric CO_2 and its link to climate change. Among these efforts it is planned to lunch two satellites: Orbiting Carbon Observatory (OCO) in USA [1] and Greenhouse gases Observing SATellite (GOSAT) in Japan [2]. Both satellites will be equipped with high resolution Fourier transform interferometers for global monitoring of the greenhouse gases including carbon dioxide. A high quality spectroscopic database of carbon dioxide is required for these purposes.

The atmospheres of Venus and Mars consist mostly of carbon dioxide, with relative concentrations of 96.5% and 95.4%, respectively. These atmospheres are currently being investigated using orbiting observatories (such as Venus Express [3] with SOIR sensor [4] and Mars Express with the Fourier spectrometer [5]) as well as ground-based

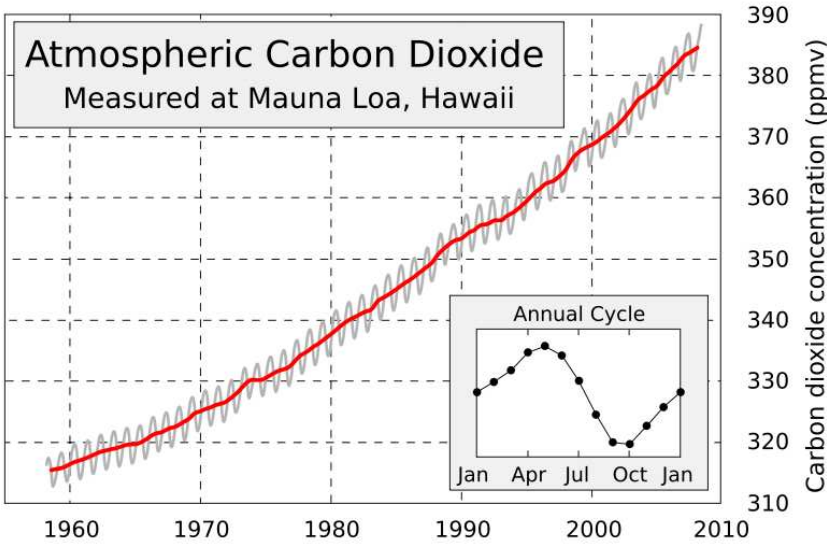

Figure 1. The history of atmospheric carbon dioxide concentrations as directly measured at Mauna Loa, Hawaii (adapted from Wikipedia).

telescopes [6, 7]. Because of very high concentrations of carbon dioxide in the both atmospheres the transparency windows are used and must then be very well characterised. The minor isotopologues may have a dominant contribution in in the light absorption in these transparency windows. This is why the spectroscopic information on rare isotopic species of carbon dioxide, especially at elevated temperatures is very important for studying Venus and Mars atmospheres.

The carbon dioxide is one of the main products of the burning of the organic fuels. The knowledge of radiative properties of combustion gases is required to accurately predict radiative fluxes in a number of physical systems like fires and combustion systems. The radiative properties of carbon dioxide could be deduced from the carbon dioxide spectroscopic databases. The problem of radiative fluxes in the combustion systems needs spectroscopic information at high temperatures.

There exist in the literature several spectroscopic databases in which the spectral line parameters of carbon dioxide are presented. First of all we have to mention HITRAN [8] and GEISA [9] databases which were elaborated for the earth atmosphere applications. The HITEMP database [10], which is the high-temperature ($T_{\mathrm{ref}} = 1000$ K) counterpart of HITRAN, was elaborated for high-temperature applications. Two versions of the

Carbon Dioxide Spectroscopic Databank (CDSD) [11] have been developed by Institute of Atmospheric Optics (Tomsk): a version for atmospheric applications CDSD-296 and a version for high-temperature application CDSD-1000. More recently the new carbon dioxide database [12] has been elaborated in Jet Propulsion Laboratory (JPL) specially to provide the spectroscopic support of OCO satellite mission. All these databases suffer from different disadvantages and do not provide all needs of the above applications. Moreover all these databases need to be validated because all of them contain part of data (or all data) based on the extrapolation calculations (or global modeling). The detailed discussion of these databases will be presented in Chapter 5.

The work presented in this thesis falls within the framework of the development of the CDSD database [11]. It aims to improve the theoretical description of the spectrum of carbon dioxide molecule in the 1.6 μm region by increasing the experimental data set available for the refinement of the effective Hamiltonian and effective dipole moment parameters. The obtained new experimental data set is aimed also to verify the line lists provided by HITRAN [8], GEISA [9], HITEMP [10] and JPL [12] databases.

This work is performed within the framework of the fruitful collaboration between Laboratoire de Spectrométrie Physique, UMR CNRS 5588, Université Joseph Fourier (Grenoble, France) and Laboratory of Theoretical Spectroscopy, Siberian Branch, Russian Academy of Sciences (Tomsk, Russia). These laboratories have complementary competences. In Grenoble the CW-Cavity Ring Down spectrometer with very high sensitivity (typical noise equivalent absorption $\alpha_{\min} = 2 - 5 \times 10^{-10}$ cm^{-1}) combined with the high linearity and dynamics (more than 4 decades) has been elaborated. This spectrometer covers spectral range between 5851 and 7045 cm^{-1} and allows detection of lines with intensities down to 10^{-29} cm/molecule. The global modeling of high resolution spectra of linear molecules with the accuracies close to the experimental uncertainties are performed in Tomsk laboratory using the method of effective operators.

As concerns the 1.6 μm region, before starting this work the observed CO_2 line parameters were obtained mostly by Fourier transform spectroscopy or from Venus measurements [13]. The spectroscopic information only about most abundant isotopic species was known. Fourier transform spectroscopy allowed detecting only lines with the line intensities higher than 10^{-25} cm/molecule. The set of the observed line intensities

even for the principal isotopic species ($^{12}C^{16}O_2$) was not enough to determine all important effective dipole moment parameters and that for the second isotopologue, $^{13}C^{16}O_2$, was not numerous. The detailed analysis of the existed spectroscopic information for carbon dioxide molecule in 1.6 μm region will be given in the Chapters 3 and 4.

This thesis follows the studies by Majcherova et al. [14] and Ding et al. [15] which reported the line position analysis of CW-CRDS spectra in the 6130–6750 cm^{-1} region recorded with natural and ^{13}C-enriched carbon dioxide, respectively. No intensity measurements were made in the above two studies and an significant fraction of the observed transitions remained unassigned. The spectral region covered by our CW-CRDS setup could be extended down to 5851 cm^{-1} and up to 7045 cm^{-1}. The aim of the present thesis is then twofold: (i) to perform the assignment of natural and ^{13}C-enriched carbon dioxide spectra in the 5851–7045 cm^{-1} region (including the revision of previously studied region) in order to provide the most complete experimental line lists for global modeling, (ii) to measure line intensities necessary for satisfactory modeling of $^{12}C^{16}O_2$ and $^{13}C^{16}O_2$ spectra in the 1.6 μm region.

The first Chapter is devoted to the description of the theoretical methods used in this thesis for global modeling of vibration-rotational spectrum of carbon dioxide. We present the main steps of the effective Hamiltonian and effective dipole moment constructions for CO_2 molecule as well as the main features of its rovibration spectrum following from the selection rules.

In the second Chapter, the method of high sensitivity CW-Cavity Ring Down Spectroscopy and our experimental setup are briefly described.

In the third Chapter, we present the detailed and exhaustive line position analysis of the absorption spectra of natural and ^{13}C-enriched carbon dioxide obtained by CW-CRDS between 5851 and 7045 cm^{-1}. The line assignment has been performed with the help of the effective Hamiltonian models. The band-by-band analysis which consists of the fitting of band parameters and identification of accidental resonance perturbations were performed for *all* the bands (including the previously reported bands) observed in the 5851–7045 cm^{-1} region. The new experimental data allowed us to check and improve the extrapolation abilities of the effective Hamiltonian models. The first observation of interpolyad resonance interactions in the case of carbon dioxide is discussed

in this Chapter. The new global fits for $^{16}O^{13}C^{18}O$ and $^{16}O^{13}C^{17}O$ isotopologues are included in the Chapter but the effective Hamiltonian parameters for $^{12}C^{16}O_2$, $^{13}C^{16}O_2$, $^{16}O^{12}C^{18}O$ and $^{16}O^{12}C^{17}O$ were also refined on the basis of the present results in order to provide the most consistent line lists for the new version of the CDSD database [11].

The fourth Chapter is devoted to the measurements and global modelings of line intensities in the $\Delta P = 9$ series of transitions of $^{12}C^{16}O_2$ and $^{13}C^{16}O_2$ isotopologues. The line intensities are retrieved from CW-CRDS spectra, in the 1.6 μm region. The CW-CRDS technique is particularly suitable for absolute intensity measurements because of the high linearity and the large dynamics of the CW-CRDS spectra with respect to the line intensities. It allows to measure accurate line intensities down to 10^{-28} cm/molecule which is at least two orders of magnitude lower than the FTS detection limit.

Before our work, the experimental intensity data near 1.6 μm available in the literature for $^{13}C^{16}O_2$ were very poor, we then decided to perform the line intensity measurements in the 5851–6580 cm^{-1} region. In the case of principal isotopololgue, the line intensities for the strongest cold bands and for their respective hot bands as well as for two cold perpendicular bands have been previously measured by several authors using different experimental techniques. However, important experimental information was still missing for the determination of the effective dipole moment parameters which hampered a satisfactory modeling of the CO_2 absorption spectrum near 1.6 μm. We have chosen four specific spectral intervals for new CW-CRDS measurements in order to retrieve the line intensities of several weak perpendicular and "forbidden" bands necessary for determining of some important effective dipole moment parameters. We have gathered our experimental line intensities with those available in the literature for $^{12}C^{16}O_2$ and $^{13}C^{16}O_2$ isotopologues in order to refine their respective effective dipole moment parameters.

In the fifth Chapter, we present the discussion of the most currently used spectroscopic databases of carbon dioxide: HITRAN [8], GEISA [9], HITEMP [10], and the recent JPL [12] and CDSD [11] databases. We will show that, compared to these databases, the results obtained in this thesis for 1.4–1.7 μm region improve importantly the knowledge of absorption spectrum of carbon dioxide. This is the reason why our line lists have just been adopted for the new version of HITRAN database.

Chapter 1

Theoretical background

Ce chapitre commence par une brève introduction générale des diférentes méthodes utilisées pour décrire globalement le spectre de vibration-rotation d'une molécule dans un état électronique donné. Ensuite, partant du Hamiltonien général d'un système constitué de noyaux et d'électrons, un aperçu des développements théoriques conduisant à l'expression du Hamiltonien quantique d'une molécule linéaire semi-rigide est présenté, de sa paramétrisation dans le cadre de la théorie des perturbations et de l'application de la méthode de la transformation de contact pour obtenir le Hamiltonien effectif utilisé dans ce travail pour décrire globalement la structure de vibration-rotation du dioxyde de carbone dans son état électronique fondamental. Après une brève évocation de la limitation principale de ce modèle liée à la présence de résonances "inter-polyades", le problème de l'identification des niveaux de vibration-rotation de CO_2 est abordé, suivi d'une brève discussion des règles de sélection des transitions permises entre ces niveaux et des types de bandes correspondantes. La fin du chapitre est consacrée aux intensités d'absorption des raies de vibration-rotation de CO_2 et à la modélisation du moment de transition correspondant par un moment dipolaire effectif associé au Hamiltonien effectif décrit précédemment.

1.1 Global treatment of CO_2 rovibrational energy states

1.1.1 Introduction

Several methods have been developed for a global treatment of the rovibrational spectra of a molecule in a given electronic state. These methods can be divided into two groups: variational methods and methods based on effective operators. The first group of methods uses a potential energy surface determined either by means of *ab initio* calculations or by nonlinear least-squares fitting to the experimental rovibrational energy levels. Then the surface can be used to calculate other rovibrational levels of the same electronic state. These methods can differ considerably from the point of view of the computation procedures and adopted approximations. The Direct Numerical Diagonalization (DND) technique is one of these methods [16–19]. The eigenvalue problem is solved by a numerical diagonalization of the matrix of the vibration-rotation Hamiltonian written in the basis of products of the eigenfunctions of the harmonic oscillators and rigid symmetric top rotor, both the truncation of the infinite Hamiltonian matrix and finite expansions of the kinetic energy operator and of the potential function are used. Observed line or band-intensity data are used to generate, by employing a linear least-squares fitting process, a dipole-moment surface appropriate to a molecule. From this surface and the eigenstates obtained from the potential surface, transition intensities are obtained for the needed rovibrational lines. Line positions and intensities of carbon dioxide calculated by DND technique were included in the HITRAN database [8] when laboratory data did not exist.

Technique based on the determination of the potential surface of the molecule can be applied to all the isotopic species simultaneously within the Born-Oppenheimer approximation. This is one of the advantages of this approach since it allows one to calculate the energy levels and the wavefunctions of one isotopic variant on the basis of the spectroscopic information obtained for others. But it should be emphasized that the accuracy of the rovibrational energy levels calculation is theoretically limited by the assumption of the invariance of the force field under isotopic substitution, that is, by the adiabatic and nonadiabatic corrections, even though the main part of the latter can be taken into account by the use of atomic instead of nuclear masses [20, 21]. It should

also be emphasized that these methods necessitate powerful computers.

The other group of methods is based on effective operators. The rovibrational data are used not to fit structural and force field constants of the molecule but to fit parameters of an effective Hamiltonian (EH). Effective Hamiltonian can be obtained from the vibration-rotation Hamiltonian by means of contact transformation aimed to remove non-diagonal matrix elements from Hamiltonian matrix in each order of magnitude successively. In the polyad model (see Section 1.1.5) transformed Hamiltonian matrix has a block-diagonal form in the basis of the eigenfunctions of the harmonic oscillators and rigid symmetric top rotor, hence it is easier to find its eigenvalues by diagonalizing each block separately. Up to a given order of perturbation theory, effective Hamiltonian contains all resonance interaction terms in an explicit form. For a given isotopologue, the adiabatic and nonadiabatic corrections are implicitly taken into account as some contributions to its parameters. The methods based on effective operators require much less computer memory and CPU time. Since in this approach all matrices for a given J have a finite dimensions, there is no any problem related to the wave function basis optimization or truncation of the matrices. The accuracy of the reproduction of the energy levels is generally higher in this case than in the case of variational methods.

1.1.2 Vibration-rotation Hamiltonian for linear semirigid molecules

The stationary Shrödinger equation

$$H\Psi = E\Psi \tag{1.1}$$

with Hamiltonian of the atomic nuclei and electrons system

$$H = -\frac{\hbar^2}{2m_e}\sum_{j=1}^{N_e}\left(\frac{\partial^2}{\partial X_j^2}+\frac{\partial^2}{\partial Y_j^2}+\frac{\partial^2}{\partial Z_j^2}\right)-\frac{\hbar^2}{2}\sum_{i=1}^{N} m_i^{-1}\left(\frac{\partial^2}{\partial X_i^2}+\frac{\partial^2}{\partial Y_i^2}+\frac{\partial^2}{\partial Z_i^2}\right)+V \tag{1.2}$$

expressed in terms of space-fixed coordinates (X_s, Y_s, Z_s) does not lend itself to a description of energy states since its numerical integration would be very difficult even for the simplest molecules. In Eq. (1.2) N, m_i and N_e, m_e denote the numbers and mass of atomic nuclei and electrons respectively, V is potential energy operator. It is well known that the binding electrons hold the atomic nuclei in a configuration with

the approximately constant bond lengths and valence angles (except of some valence angle in nonrigid molecules). The equilibrium configuration of a molecule can be obtained in the result of the solution of the "electronic" Schrödinger equation within the Born-Oppenheimer approximation which allows to consider the vibration-rotation and electronic motions separately. So the most convenient approach to this problem is to develop – first in terms of classical mechanics – a model for the motions of a molecule which would allow for a description of such a system in terms of its translation, its overall rotation, the vibration of its nuclei and its electronic motions. This can be achieved by replacing the space-fixed coordinates of the atomic nuclei and electrons by the molecule-fixed coordinate system suitable for description of the individual types of motions mentioned above. In the next step, the quantum mechanical Hamiltonian can be obtained using the expression for kinetic energy in terms of molecule-fixed coordinates.

The resulting Hamiltonian assumes a more complicated form than that corresponding to Eq. (1.2) but a clear physical interpretation can be given to its individual terms occurring. Furthermore, successive approximations to the complete vibration-rotation Hamiltonian can be found. This has the advantage that the Schrödinger equation in the simplest approximation has frequently a simple analytical solution which can be used in solving the problem to higher approximations by a standard perturbation or variational approaches.

Molecule-fixed axis system

The origin of the moving axes (Fig. 1.1) is defined in the center of mass of the molecule. The following relationship holds for the coordinates of the s-th particle with respect to the moving and space-fixed axis system:

$$\mathbf{R}_s = \mathbf{R}_0 + \mathbf{S}^{-1}(\theta, \phi, \chi) \cdot \mathbf{r}_s, \tag{1.3}$$

where $\mathbf{R}_s$ and $\mathbf{r}_s$ are the position vectors of the s-th particle with respect to space-fixed and molecule-fixed axis systems respectively, $\mathbf{S}(\theta, \phi, \chi)$ is the 3×3 orthogonal transformation matrix and θ, ϕ, χ are the Euler angles.

An equilibrium configuration corresponding to the minimum of potential energy of

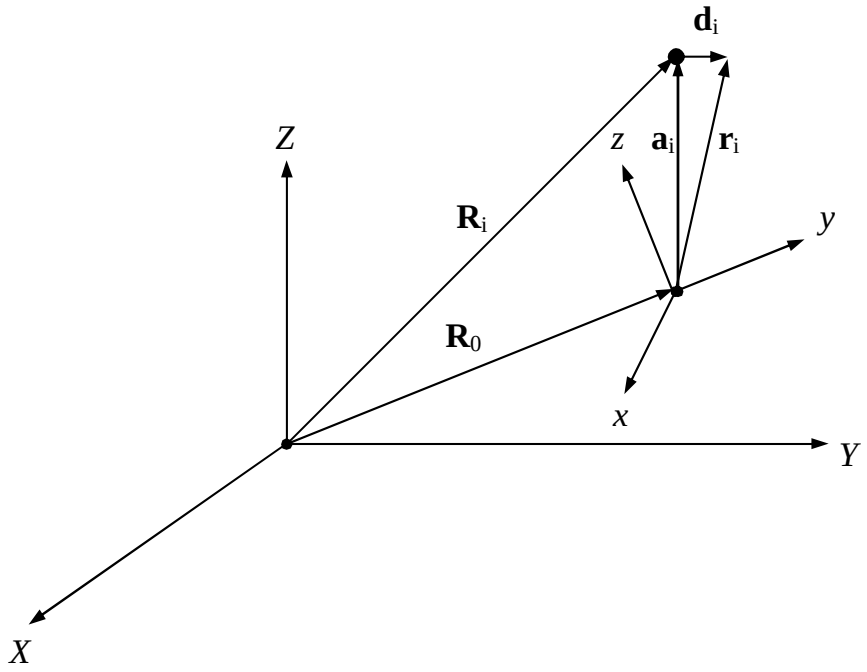

Figure 1.1. The space-fixed axis system (X, Y, Z) and the molecule-fixed axis system (x, y, z).

a molecule is defined by means of N position vectors $\mathbf{a}_i$ $(i = 1, 2, \ldots, N)$ which denote the positions of the atomic nuclei with respect to the molecule-fixed axis system. The position vectors of the atomic nuclei are given by

$$\mathbf{r}_i = \mathbf{a}_i + \mathbf{d}_i \quad (i = 1, 2, \ldots, N), \tag{1.4}$$

where $\mathbf{d}_i$ is the vector of the Cartesian displacement of the i-th atomic nucleus measured with respect to the equilibrium configuration.

Eckart conditions

There are $3N$ variables on the left-hand sides of the equations:

$$\mathbf{R}_i = \mathbf{R}_0 + \mathbf{S}^{-1}(\theta, \phi, \chi) \cdot (\mathbf{a}_i + \mathbf{d}_i) \quad (i = 1, 2, \ldots, N), \tag{1.5}$$

while for nonlinear molecules there are $3N + 6$ variables on the right-hand sides [3 coordinates of the center of mass, 3 Euler angles θ, ϕ, χ and the $3N$ Cartesian displacements

$d_{i\alpha}$ $(i = 1, 2, \ldots, N;\ \alpha = x, y, z)]$. In order to have the same number of independent variables on the both sides of Eqs. (1.5), it is necessary to introduce six constraints[1] for $3N$ variables $d_{i\alpha}$. It is convenient to use the Eckart conditions which can be written in the following form:

$$\sum_{i=1}^{N} m_i \mathbf{d}_i = 0, \tag{1.6}$$

$$\sum_{i=1}^{N} m_i (\mathbf{a}_i \times \mathbf{d}_i) = 0, \tag{1.7}$$

where $\mathbf{a}_i \times \mathbf{d}_i$ denotes a vector product.

Kinetic energy of rotation and vibration

The kinetic energy of a nonlinear semirigid molecule may be expressed as (see Ref. [22])

$$2T = \sum_{\alpha,\beta=x,y,z} I'_{\alpha\beta}\omega_\alpha\omega_\beta + \sum_{k=1}^{3N-6} \left(\dot{Q}_k + \sum_{\alpha,l} \omega_\alpha \zeta^\alpha_{lk} Q_l\right)^2 + \sum_{\alpha,j=1}^{N_e} m_e \left[\dot{r}_{j\alpha} + (\omega_\beta r_{j\gamma} - \omega_\gamma r_{j\beta})\right]^2, \tag{1.8}$$

where

$$I'_{\alpha\alpha} = I_{\alpha\alpha} - \sum_{k,l,m} \zeta^\alpha_{km}\zeta^\alpha_{lm} Q_k Q_l - m_e \sum_{j=1}^{N_e} \left(r^2_{j\beta} + r^2_{j\gamma}\right), \tag{1.9}$$

$$I'_{\alpha\beta} = I_{\alpha\beta} - \sum_{k,l,m} \zeta^\alpha_{km}\zeta^\beta_{lm} Q_k Q_l + m_e \sum_{j=1}^{N_e} r_{j\alpha} r_{j\beta} \tag{1.10}$$

and α, β, γ assumes values $x,\ y,\ z$ with $\alpha \neq \beta \neq \gamma$. In the above equations $\dot{Q}_k = \frac{\mathrm{d}Q_k}{\mathrm{d}t}$, $\dot{r}_{j\alpha} = \frac{\mathrm{d}r_{j\alpha}}{\mathrm{d}t}$, ω_α $(\alpha = x, y, z)$ are the components of angular velocity, Q_k are the normal coordinates and ζ^α_{kl} are the Coriolis interaction constants given by

$$\zeta^\alpha_{kl} = -\zeta^\alpha_{lk} = \sum_i (l_{i\beta,k} l_{i\gamma,l} - l_{i\gamma,k} l_{i\beta,l}), \tag{1.11}$$

where the coefficients $(l_{ix,k},\ l_{iy,k},\ l_{iz,k})$ are the normalized components with respect to the x, y, z axis system of the vibrational diplacement vector of i-th atom nucleus in the

[1] There are only five constraints for a linear molecules because the Euler angle χ is not a dynamical variable in this case but only an arbitrary phase parameter.

k-th vibrational mode:

$$d_{i,\alpha} = \frac{1}{\sqrt{m_i}} \sum_{k=1}^{3N-6} l_{i\alpha,k} Q_k. \tag{1.12}$$

In Eqs. (1.9) and (1.10) the components of the tensor of inertia $I_{\alpha\alpha}$ ($\alpha = x, y, z$) and $I_{\alpha\beta}$ ($\alpha \neq \beta$) are defined as

$$I_{\alpha\alpha} = \sum_{i=1}^{N} m_i \left(r_{i\beta}^2 + r_{i\gamma}^2\right) + m_e \sum_{j=1}^{N_e} \left(r_{j\beta}^2 + r_{j\gamma}^2\right), \tag{1.13}$$

$$I_{\alpha\beta} = -\sum_{i=1}^{N} m_i r_{i\alpha} r_{i\beta} - m_e \sum_{j=1}^{N_e} r_{j\alpha} r_{j\beta}. \tag{1.14}$$

Hamiltonian form of kinetic energy for linear molecule

The classical expression for kinetic energy for a linear molecule is the same as for a nonlinear one Eq. (1.8) except that there are $3N - 5$ normal coordinates because the angle of the rotation around the molecule axis is not a dynamical variable.

According to Eq. (1.8) the expression for the linear vibrational momentum P_k conjugated with the vibrational coordinate Q_k can be written in the form

$$P_k \equiv \frac{\partial T}{\partial \dot{Q}_k} = \dot{Q}_k + \sum_{\alpha,l} \omega_\alpha \zeta_{lk}^{\alpha} Q_l. \tag{1.15}$$

Analogously, for the linear momentum $p_{j\alpha}$ conjugated with coordinate $r_{j\alpha}$ of the j-th electron, it holds that

$$p_{j\alpha} \equiv \frac{\partial T}{\partial \dot{r}_{j\alpha}} = m_e \dot{r}_{j\alpha} + m_e(\omega_\beta r_{j\gamma} - \omega_\gamma r_{j\beta}). \tag{1.16}$$

Let us consider that the quantity J_α ($\alpha = x, y, z$) is defined as $J_\alpha = \frac{\partial T}{\partial \omega_\alpha}$. By taking the derivative of expression (1.8) and substituting for $\dot{Q}_l$ and $\dot{r}_{j\alpha}$ from Eqs. (1.15) and (1.16), the following expression is obtained for J_α:

$$J_\alpha \equiv \frac{\partial T}{\partial \omega_\alpha} = \sum_{\beta=x,y,z} I'_{\alpha\beta}\omega_\alpha + \pi_\alpha + \Pi_\alpha, \tag{1.17}$$

where

$$\pi_\alpha = \sum_{k,l} \zeta_{k,l}^{\alpha} Q_k P_l, \tag{1.18}$$

$$\Pi_\alpha = \sum_{j=1}^{N_e} (r_{j\beta} p_{j\gamma} - r_{j\gamma} p_{j\beta}). \tag{1.19}$$

It can be evidenced [22] that J_α ($\alpha = x, y, z$) are the components of the total angular momentum of the molecule with respect to the molecule-fixed axes. In Eq. (1.17), π_α is called the vibrational angular momentum, Π_α represents the electronic angular momentum.

The matrix $\left[I'_{\alpha\beta}\right]$ takes the following form for a linear molecule:

$$\left[I'_{\alpha\beta}\right] = \begin{bmatrix} I' & 0 & 0 \\ 0 & I' & 0 \\ 0 & 0 & 0 \end{bmatrix}, \tag{1.20}$$

where

$$I' = \frac{1}{I^0}\Big(I^0 + \frac{1}{2}\sum_k a_k Q_k\Big)^2 \tag{1.21}$$

and $I^0 = \sum m_i a_{iz}^2$, $a_k = 2\sum m_i^{\frac{1}{2}} a_{iz} l_{iz,k}$. According to Eqs. (1.17) and (1.20), it holds for the components of the angular momentum of a linear molecule that

$$J_x = I'\omega_x + \pi_x + \Pi_x, \tag{1.22}$$

$$J_y = I'\omega_y + \pi_y + \Pi_y, \tag{1.23}$$

$$J_z = \pi_z + \Pi_z. \tag{1.24}$$

Eq. (1.24) is usually called Sayvetz condition. Using the above equations, the following expression for the kinetic energy of a vibrating and rotating linear molecule is obtained:

$$2T = \mu\Big[(J_x - \pi_x - \Pi_x)^2 + (J_y - \pi_y - \Pi_y)^2\Big] + \sum_{k=1}^{3N-5} P_k^2 + \sum_{\alpha,j=1}^{N_e} p_{j\alpha}^2, \tag{1.25}$$

where $\mu = (I')^{-1}$.

Quantum mechanical Hamiltonian for linear molecule

Transformation of the classical Hamiltonian to the quantum mechanical Hamiltonian is discussed in Ref. [22]. Let us consider only nuclear terms of the Hamiltonian in a linear molecule within a nondegenerate electronic state.

The Eckart conditions (1.6) for a linear molecule is reduced to the following conditions:

$$\sum_i m_i a_{iz} r_{iy} = 0, \tag{1.26}$$

$$\sum_i m_i a_{iz} r_{ix} = 0. \tag{1.27}$$

These conditions are sufficient for the determination of direction of the z axis alone, i.e. they specify the Euler angles $\theta,\ \phi$ but not the orientation of the x and y axes. The angle χ is not a dynamic variable but only an arbitrary phase parameter which defines the orientation of the $x,\ y$ axes with respect to the space-fixed axes.

According to the rigorous treatment by Watson [23], the Euler angle χ can be considered in general as an arbitrary chosen function of Euler angles θ and ϕ. The correct quantum mechanical operator for a linear molecule then has the following form:

$$2H = \mu\Bigg[\Big(J_x - \pi_x + \frac{1}{2}i\hbar\xi_y\Big)\Big(J_x - \pi_x - \frac{1}{2}i\hbar\xi_y\Big) + \Big(J_y - \pi_y + \frac{1}{2}i\hbar\xi_x\Big)\Big(J_y - \pi_y - \frac{1}{2}i\hbar\xi_x\Big)\Bigg] + \sum_{k=1}^{3N-5} P_k^2 + V(Q), \tag{1.28}$$

where

$$\xi_x = \mathrm{cot}\theta\mathrm{cos}\chi + \mathrm{csc}\theta\mathrm{cos}\chi\left(\frac{\partial\chi}{\partial\varphi}\right) + \mathrm{sin}\chi\left(\frac{\partial\chi}{\partial\theta}\right), \tag{1.29}$$

$$\xi_y = -\mathrm{cot}\theta\mathrm{cos}\chi - \mathrm{csc}\theta\mathrm{sin}\chi\left(\frac{\partial\chi}{\partial\varphi}\right) - \mathrm{cos}\chi\left(\frac{\partial\chi}{\partial\theta}\right) \tag{1.30}$$

and $V(Q)$ is the potential energy function.

Watson has shown [23] that operator (1.28) is unitary equivalent with an isomorphic Hamiltonian $H^{iso} = UHU^{-1}$,

$$2H^{iso} = \mu\Big[(J'_x - \pi_x)^2 + (J'_y - \pi_y)^2\Big] + \sum_{k=1}^{3N-5} P_k^2 + V(Q), \tag{1.31}$$

where operators J'_x and J'_y satisfy the commutation relations for the angular momentum operators:

$$[J_i, J_j] = -i\hbar\sum_k \varepsilon_{ijk} J_k, \tag{1.32}$$

ε_{ijk} – the unit antisymmetric tensor.

The isomorphic Hamiltonian H^{iso} has the same eigenvalues as H but an additional degree of freedom, i.e. the Euler angle χ in Eq. (1.31) is considered as independent variable. However, there is no observable quantity which would correspond to this variable in a linear molecule. Since the J_z component of the angular momentum can be only due to vibrational and electronic motions, in order to extract the eigenvalues of vibration-rotation Hamiltonian from the spectrum of eigenvalues of the isomorphic Hamiltonian (1.31) in case of the singlet electronic state the Sayvetz condition (1.24) is used. This equation leads to the following relation between the quantum numbers of triatomic linear molecule:

$$K = \ell_2, \tag{1.33}$$

where K is the quantum number of the angular momentum component, ℓ_2 is the quantum number of the vibrational momentum component. Further we will consider only the isomorphic Hamiltonian.

1.1.3 Parametrization of the vibration-rotation Hamiltonian

The Schrödinger equation (1.1) with the complete rovibrational Hamiltonian (1.31) is difficult to solve in a analytical form. Moreover, the potential energy function $V(Q)$ is not determined. This function can be obtained by means of *ab initio* calculations, but this method does not allow to achieve the experimental accuracy of high resolution spectroscopy. The second method consists of parametrization of vibration-rotation Hamiltonian within the framework of perturbation theory. The rovibrational Hamiltonian parameters are then determined by nonlinear least-squares fitting to the experimental energy levels.

The potential energy function $V(Q)$ and the inverse tensor of inertia μ can be expended in terms of the normal coordinates:

$$V(q) = \frac{1}{2}\sum_k \omega_k q_k^2 + \frac{1}{3!}\sum_{i,j,l} K^{ijl}\omega_k q_i q_j q_l + \ldots, \tag{1.34}$$

$$\mu = \mu^0 + \sum_k \mu^i q_i + \frac{1}{2}\sum_{i,j} \mu^{ij} q_i q_j + \ldots. \tag{1.35}$$

In the above equations the dimensionless vibrational variable are used:

$$\begin{cases} P_k = \sqrt{\omega_k} p_k, \\ Q_k = \dfrac{1}{\sqrt{\omega_k}} q_k, \end{cases} \tag{1.36}$$

where ω_k $(k = 1, 2, \ldots, 3N-5)$ are the normal mode frequencies. The rovibrational Hamiltonian of a linear molecule in terms of dimensionless vibrational coordinates is given by

$$2H = \mu\Big[(J'_x - \pi_x)^2 + (J'_y - \pi_y)^2\Big] + \sum_{k=1}^{3N-5} \omega_k p_k^2 + V(q). \tag{1.37}$$

In order to classify the rotational and vibrational terms of Hamiltonian by order of magnitude Amat-Nielson scheme is used. In this scheme, the scale parameter is chosen as

$$\lambda = \left(\frac{\mu^0}{\omega}\right)^{\frac{1}{2}}, \tag{1.38}$$

and following assumptions are made:

$$\frac{\mu^i}{\mu^0} \sim \frac{\mu^{ij}}{\mu^i} \sim \frac{\mu^{ijl}}{\mu^{ij}} \sim \ldots \sim \lambda, \tag{1.39}$$

$$\frac{K^{ijl}}{\omega} \sim \frac{K^{ijlm}}{K^{ijl}} \sim \ldots \sim \lambda, \tag{1.40}$$

$$p \sim 1,\ q \sim 1,\ J_\alpha \sim \lambda^{-1}. \tag{1.41}$$

According to the above assumptions the vibration-rotation Hamiltonian terms corresponding to different orders of magnitude are given by

$$H^0 = H_0^V + H_0^R = \frac{1}{2}\sum_k \omega_k \left(p_k^2 + q_k^2\right) + \frac{1}{2}\mu^0 \left(J_x'^2 + J_y'^2\right), \tag{1.42}$$

$$H_1 = \frac{1}{3!}\sum_{i,j,l} K^{ijl} q_i q_j q_l + \frac{1}{2}\sum_i \mu^i q_i \left(J_x'^2 + J_y'^2\right) - \mu^0 (J'_x \pi_x + J'_y \pi_y), \tag{1.43}$$

and so on.

The zeroth-order terms of the rovibrational Hamiltonian (1.42) correspond to the harmonic oscillator and rigid symmetric top rotor approaches which have well-known analytical solutions. The wavefunctions of the harmonic oscillator and rigid symmetric top rotor are then used as basis function to calculate higher order correction to the rovibrational energies.

1.1.4 Contact transformations of vibration-rotation Hamiltonian

As a consequence of the space isotropy, the Hamiltonian matrix has block-diagonal form in the harmonic oscillator and rigid rotor wavefunction basis:

$$||H|| = \begin{bmatrix} \ddots & & & & 0 \\ & ||J-1|| & & & \\ & & ||J|| & & \\ & & & ||J+1|| & \\ 0 & & & & \ddots \end{bmatrix}, \tag{1.44}$$

where each block $||J||$, corresponding to a given value of angular momentum quantum number J, has a non-diagonal form in the infinite-dimensional basis of the harmonic oscillator wavefunctions. There are several methods to solve the eigenvalue problem. DND technique consists of a numerical diagonalization of the truncated matrix. This method requires a powerful computer environment because a high dimensional matrices should be diagonalized in order to achieve a satisfactory precision of calculated energy values.

Another technique is based on effective operators. The effective Hamiltonian can be obtained by means of contact unitary transformations. The transformed Hamiltonian matrix $||J||$ has block-diagonal form and each block is diagonalized separately. Since all matrices for a given J value have a finite dimension, there is no problem related to the wavefunction basis optimization or truncation of matrices. The effective Hamiltonian method requires much less computer memory and CPU time.

In order to obtain the effective Hamiltonian a number of contact unitary transformations are applied to rovibrational Hamiltonian:

$$H^{\text{eff}} = \ldots\ e^{i\lambda^n S_n} \ldots\ e^{i\lambda^1 S_1}\ H\ e^{-i\lambda^1 S_1} \ldots\ e^{-i\lambda^n S_n} \ldots, \tag{1.45}$$

where generators of contact transformations S_i are chosen in a such way that non-diagonal matrix elements are removed from Hamiltonian matrix in each order of magnitude successively.

Using the commutator expansion of transformed Hamiltonian proposed by Hausdorff

$$H^{(1)} = e^{i\lambda^1 S_1}\ H\ e^{-i\lambda^1 S_1} = H + \lambda[iS_1, H] + \frac{1}{2}\lambda^2\big[iS_1, [iS_1, H]\big] + \\ + \ldots + \frac{1}{n!}\lambda^n\Big[iS_1, \big[iS_1, \ldots [iS_1, H]\ldots\big]\Big] + \ldots, \quad (1.46)$$

it can be demonstrated that zero-order terms of the transformed Hamiltonian do not change, the first-order terms are not affected by second contact transformation and so on. Finally, the n-order term is given by

$$H_n^{(n)} = H_n^{(n-1)} + [iS_n, H_0]. \quad (1.47)$$

In the above equation the generator S_n can be chosen in a such way that commutator $[iS_n, H_0]$ is equal to minus non-diagonal part of $H_n^{(n-1)}$. In this case operator $H_n^{(n)}$ is equal to diagonal part of $H_n^{(n-1)}$. Here superscript denotes the number of contact transformations.

In the secondary quantization representation, the operators q_k and p_k are replaced by

$$\begin{cases} a_k = \dfrac{1}{\sqrt{2}}(q_k + ip_k), \\ a_k^+ = \dfrac{1}{\sqrt{2}}(q_k - ip_k), \end{cases} \quad (1.48)$$

In this representation every term of the vibration-rotation Hamiltonian can be expressed as

$$h = h^{\alpha\ldots\beta}_{i\ldots j\ l\ldots k} J_\alpha \ldots J_\beta a_i^+ \ldots a_j^+ a_l \ldots a_k. \quad (1.49)$$

It can be shown that the following equation takes place:

$$[h, H_0] = \big\{(\omega_l + \ldots + \omega_k) - (\omega_i + \ldots + \omega_j)\big\} \cdot h. \quad (1.50)$$

According to Eqs. (1.47), (1.49) and (1.50) the generator of n-th contact transformation can be expressed as

$$iS_n = iS^{\alpha\ldots\beta}_{i\ldots j\ l\ldots k} J_\alpha \ldots J_\beta a_i^+ \ldots a_j^+ a_l \ldots a_k, \quad (1.51)$$

where

$$iS^{\alpha\ldots\beta}_{i\ldots j\ l\ldots k} = \frac{h^{\alpha\ldots\beta}_{i\ldots j\ l\ldots k}}{(\omega_i + \ldots + \omega_j) - (\omega_l + \ldots + \omega_k)}. \quad (1.52)$$

If the sums of frequencies in Eq. (1.52) are close to each other, the corresponding matrix element cannot be removed by small contact transformations. The respective resonance term is included in the effective Hamiltonian model in explicit form.

1.1.5 Global effective rovibrational Hamiltonian for CO_2 molecule

Carbon dioxide is a triatomic linear molecule which has four normal vibrational modes (see in Fig. 1.2): symmetric stretching, double degenerate bending mode, and antisymmetric stretching. The harmonic frequencies (ω_i, i = 1–3 in cm^{-1}) and rotational constant (B_e in cm^{-1}) are given for the nine isotopologues of carbon dioxide ordered according to the natural abundance.

Table 1.1. Harmonic frequencies and rotational constant of CO_2 isotopologues.

Isotopologue	Natural abundance	ω_1	ω_2	ω_3	B_e
$^{12}C^{16}O_2$	0.9842040	1354	673	2396	0.391632
$^{13}C^{16}O_2$	0.0110574	1354	654	2328	0.391631
$^{16}O^{12}C^{18}O$	0.00394707	1315	668	2378	0.369495
$^{16}O^{12}C^{17}O$	0.000733989	1333	670	2387	0.379975
$^{16}O^{13}C^{18}O$	0.0000443446	1315	648	2310	0.369475
$^{16}O^{13}C^{17}O$	0.0000082462	1341	654	2321	0.379980
$^{12}C^{18}O_2$	0.0000039573	1276	663	2360	0.348025
$^{13}C^{18}O_2$	0.0000004610	1276	643	2290	0.348671
$^{17}O^{13}C^{18}O$	0.0000000857	1294	646	2299	0.358201

The effective Hamiltonian for a global treatment of carbon dioxide energy levels in the ground electronic state was derived by Chédin [24] up to the fourth order in Amat-Nielsen ordering scheme (1.38–1.41). Teffo et al. [25–27] have extended this Hamiltonian to higher order terms and have taken into account additional Coriolis and anharmonic resonance interaction terms. They considered all the symmetry-allowed terms up to sixth order in Amat-Nielsen ordering scheme arising from the contact transformation treatment due to the approximate relation between harmonic frequencies:

$$\omega_1 \approx 2\omega_2, \quad \omega_3 \approx 3\omega_2. \tag{1.53}$$

After that the effective Hamiltonian was converted into a reduced form by means of unitary transformations.

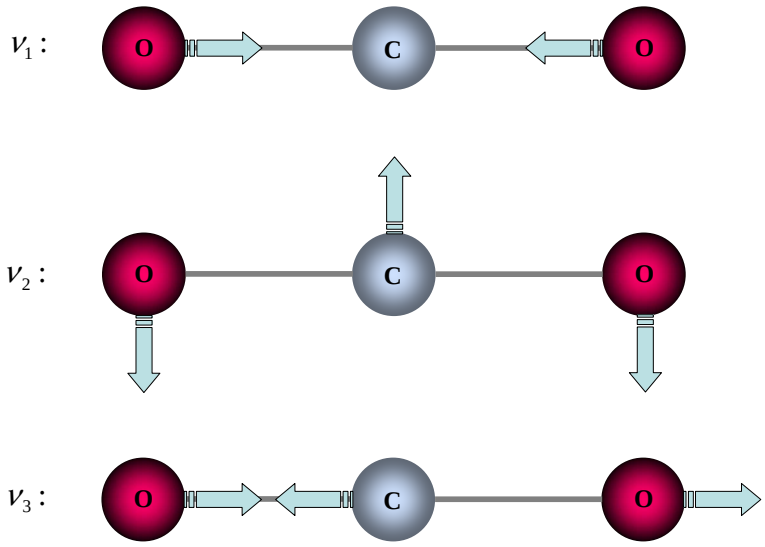

Figure 1.2. Normal modes of carbon dioxide: ν_1 is the symmetric stretch vibration, ν_2 is the double degenerate bending mode, ν_3 is the antisymmetric stretch vibration.

The effective Hamiltonian can be presented by its matrix elements in the basis of harmonic oscillators and rigid symmetric top rotor eigenfunctions

$$\big|v_1 v_2 \ell_2 v_3 J\big\rangle = \big|v_1 v_2 \ell_2 v_3\big\rangle \big|JK = \ell_2\big\rangle. \tag{1.54}$$

The Condon-Shortley phase choice for the rotational wave function $\big|JK\big\rangle$ is used *i.e.* the phase convention for the eigenfunctions of the doubly degenerate harmonic oscillator is chosen in such a way (see, for example Ref. [28] and references therein) that

$$\sigma_{yz}\big|v_2 \ell_2\big\rangle = \big|v_2 - \ell_2\big\rangle. \tag{1.55}$$

Here the z-axis of molecular-fixed frame coincides with the molecular axis, and the degenerate normal dimensionless coordinates q_{2a} and q_{2b} are oriented along the x- and y-axes, respectively.

The different kinds of matrix elements

$$\big\langle v_1\ v_2\ \ell_2\ v_3\ J\big|H^{\text{eff}}\big|v_1 + \Delta v_1\ v_2 + \Delta v_2\ \ell_2 + \Delta\ell_2\ v_3 + \Delta v_3\ J\big\rangle$$

expanded up to the sixth order in the Amat-Nielsen ordering scheme (1.38–1.41) are listed below.

Diagonal matrix element:

$$\begin{aligned}
\left\langle v_1\ v_2\ \ell_2\ v_3\ J\middle|H^{\text{eff}}\middle|v_1\ v_2\ \ell_2\ v_3\ J\right\rangle = \\
&\sum_i \omega_i \left(v_i+\frac{g_i}{2}\right) + \sum_{ij} x_{ij}\left(v_i+\frac{g_i}{2}\right)\left(v_j+\frac{g_j}{2}\right) + x_{\ell\ell}\ell_2^2 \\
&+ \sum_{ijk} y_{ijk}\left(v_i+\frac{g_i}{2}\right)\left(v_j+\frac{g_j}{2}\right)\left(v_k+\frac{g_k}{2}\right) + \sum_i y_{i\ell\ell}\left(v_i+\frac{g_i}{2}\right)\ell_2^2 \\
&+ \sum_{ijkm} z_{ijkm}\left(v_i+\frac{g_i}{2}\right)\left(v_j+\frac{g_j}{2}\right)\left(v_k+\frac{g_k}{2}\right)\left(v_m+\frac{g_m}{2}\right) \\
&+ \sum_{ij} z_{ij\ell\ell}\left(v_i+\frac{g_i}{2}\right)\left(v_j+\frac{g_j}{2}\right)\ell_2^2 + z_{\ell\ell\ell\ell}\ell_2^4 \\
&+ \left\{B_e - \sum_i \alpha_i\left(v_i+\frac{g_i}{2}\right) + \sum_{ij}\gamma_{ij}\left(v_i+\frac{g_i}{2}\right)\left(v_j+\frac{g_j}{2}\right) + \gamma_{\ell\ell}\ell_2^2\right. \\
&\left. + \sum_{ijk}\varepsilon_{ijk}\left(v_i+\frac{g_i}{2}\right)\left(v_i+\frac{g_i}{2}\right)\left(v_k+\frac{g_k}{2}\right) + \sum_i \varepsilon_{i\ell\ell}\left(v_i+\frac{g_i}{2}\right)\ell_2^2\right\}\left[J(J+1)-\ell_2^2\right] \\
&- \left\{D_e + \sum_i \beta_i\left(v_i+\frac{g_i}{2}\right) + \sum_{ij}\eta_{ij}\left(v_i+\frac{g_i}{2}\right)\left(v_j+\frac{g_j}{2}\right) + \eta_{\ell\ell}\ell_2^2\right\}\left[J(J+1)-\ell_2^2\right]^2 \\
&+ \left\{H_e + \sum_i \delta_i\left(v_i+\frac{g_i}{2}\right)\right\}\left[J(J+1)-\ell_2^2\right]^3 + G_e\left[J(J+1)-\ell_2^2\right]^4
\end{aligned} \tag{1.56}$$

ℓ-doubling matrix element:

$$\begin{aligned}
\left\langle v_1\ v_2\ \ell_2\ v_3\ J\middle|H^{\text{eff}}\middle|v_1\ v_2\ \ell_2\pm 2\ v_3\ J\right\rangle = \\
&\sqrt{(v_2\pm\ell_2+2)(v_2\mp\ell_2)[J(J+1)-\ell_2(\ell_2\pm 1)][J(J+1)-(\ell_2\pm 1)(\ell_2\pm 2)]} \\
\times &\left\{L_e + \sum_i L_i\left(v_i+\frac{g_i}{2}\right) + L_J J(J+1) + L_K(\ell_2\pm 1)^2 + \sum_{ij} L_{ij}\left(v_i+\frac{g_i}{2}\right)\left(v_j+\frac{g_j}{2}\right)\right. \\
&+ \sum_i L_{iK}\left(v_i+\frac{g_i}{2}\right)(\ell_2\pm 1)^2 + \sum_i L_{iJ}\left(v_i+\frac{g_i}{2}\right)J(J+1) + L_{JJ}[J(J+1)]^2 \\
&\left. + L_{KK}(\ell_2\pm 1)^4 + L_{JK}J(J+1)(\ell_2\pm 1)^2\right\}
\end{aligned} \tag{1.57}$$

Anharmonic interaction matrix elements:

$$\begin{aligned}\left\langle v_1\ v_2\ \ell_2\ v_3\ J\middle|H^{\text{eff}}\middle|v_1-1\ v_2+2\ \ell_2\ v_3\ J\right\rangle = \\ \sqrt{v_1(v_2+\ell_2+2)(v_2-\ell_2+2)}\Bigg\{F_e+\sum_i F_i\left(v_i+\frac{\Delta v_i+g_i}{2}\right) \\ +F_J\left[J(J+1)-\ell_2^2\right]+F_{\ell\ell}\ell_2^2+\sum_{ij}F_{ij}\left(v_i+\frac{\Delta v_i+g_i}{2}\right)\left(v_j+\frac{\Delta v_j+g_j}{2}\right) \\ +\sum_{iJ}F_{iJ}\left(v_i+\frac{\Delta v_i+g_i}{2}\right)\left[J(J+1)-\ell_2^2\right]+F_{JJ}\left[J(J+1)-\ell_2^2\right]^2\Bigg\}\end{aligned} \tag{1.58}$$

$$\begin{aligned}\left\langle v_1\ v_2\ \ell_2\ v_3\ J\middle|H^{\text{eff}}\middle|v_1-2\ v_2+4\ \ell_2\ v_3\ J\right\rangle = \\ \sqrt{v_1(v_1-1)(v_2+\ell_2+2)(v_2+\ell_2+4)(v_2-\ell_2+2)(v_2-\ell_2+4)} \\ \times\left\{F_e^{IV}+\sum_i F_i^{IV}\left(v_i+\frac{\Delta v_i+g_i}{2}\right)+F_J^{IV}\left[J(J+1)-\ell_2^2\right]\right\}\end{aligned} \tag{1.59}$$

$$\begin{aligned}\left\langle v_1\ v_2\ \ell_2\ v_3\ J\middle|H^{\text{eff}}\middle|v_1-3\ v_2\ \ell_2\ v_3+2\ J\right\rangle = \\ \sqrt{v_1(v_1-1)(v_1-2)(v_3+1)(v_3+2)} \\ \times\left\{F_e^{III}+F_1^{III}(v_1-1)+F_2^{III}(v_2+1)+F_3^{III}\left(v_3+\frac{3}{2}\right)+F_J^{III}\left[J(J+1)-\ell_2^2\right]\right\}\end{aligned} \tag{1.60}$$

$$\begin{aligned}\left\langle v_1\ v_2\ \ell_2\ v_3\ J\middle|H^{\text{eff}}\middle|v_1-2\ v_2-2\ \ell_2\ v_3+2\ J\right\rangle = \\ \sqrt{v_1(v_1-1)(v_2^2-\ell_2^2)(v_3+1)(v_3+2)} \\ \times\left\{F_e^4+F_1^4\left(v_1-\frac{1}{2}\right)+F_2^4v_2+F_3^4\left(v_3-\frac{3}{2}\right)+F_J^4\left[J(J+1)-\ell_2^2\right]\right\}\end{aligned} \tag{1.61}$$

Fermi+ℓ-type interaction matrix element:

$$\begin{aligned}\left\langle v_1\ v_2\ \ell_2\ v_3\ J\middle|H^{\text{eff}}\middle|v_1-1\ v_2+2\ \ell_2\pm2\ v_3\ J\right\rangle = \\ \sqrt{v_1(v_2\pm\ell_2+2)(v_2\pm\ell_2+4)\left[J(J+1)-\ell_2(\ell_2\pm1)\right]\left[J(J+1)-(\ell_2\pm1)(\ell_2\pm2)\right]} \\ \times\Bigg\{F_e^L\pm F_\ell^L(\ell_2\pm1)+\sum_i F_i^L\left(v_i+\frac{\Delta v_i+g_i}{2}\right)+F_J^LJ(J+1)+F_K^L(\ell_2\pm1)^2 \\ \pm\sum_i F_{i\ell}^L\left(v_i+\frac{\Delta v_i+g_i}{2}\right)(\ell_2\pm1)\pm F_{J\ell}^LJ(J+1)(\ell_2\pm1)\pm F_{\ell\ell}^L(\ell_2\pm1)^3\Bigg\}\end{aligned} \tag{1.62}$$

Coriolis interaction matrix elements:

$$\begin{aligned}\big\langle v_1\ v_2\ \ell_2\ v_3\ J\big|H^{\rm eff}\big|v_1-1\ v_2-1\ \ell_2\pm1\ v_3+1\ J\big\rangle =\\ \sqrt{v_1(v_2\mp\ell_2)(v_3+1)\,[J(J+1)-\ell_2(\ell_2\pm1)]}\\ \times\Big\{C_e\pm C_\ell\Big(\ell_2\pm\frac{1}{2}\Big)+\sum_i C_i\Big(v_i+\frac{\Delta v_i+g_i}{2}\Big)+C_JJ(J+1)\\ +C_K\Big[\ell_2(\ell_2\pm1)+\frac{1}{2}\Big]\pm\sum_i C_{i\ell}\Big(v_i+\frac{\Delta v_i+g_i}{2}\Big)\Big(\ell_2\pm\frac{1}{2}\Big)\pm C_{J\ell}J(J+1)\Big(\ell_2\pm\frac{1}{2}\Big)\\ \pm C_{\ell\ell}\Big(\ell_2\pm\frac{1}{2}\Big)^3+\sum_{ij}C_{ij}\Big(v_i+\frac{\Delta v_i+g_i}{2}\Big)\Big(v_j+\frac{\Delta v_j+g_j}{2}\Big)\\ +C_{JJ}[J(J+1)]^2+C_{KK}\Big[\ell_2(\ell_2\pm1)+\frac{1}{2}\Big]^2\Big\}\end{aligned}\tag{1.63}$$

$$\begin{aligned}\big\langle v_1\ v_2\ \ell_2\ v_3\ J\big|H^{\rm eff}\big|v_1\ v_2-3\ \ell_2\pm1\ v_3+1\ J\big\rangle =\\ -\sqrt{(v_3+1)(v_2^2-\ell_2^2)(v_2\mp\ell_2-2)[J(J+1)-\ell_2(\ell_2\pm1)]}\\ \times\Big\{C_e^{(1)}\pm C_\ell^{(1)}\Big(\ell_2\pm\frac{1}{2}\Big)+\sum_i C_i^{(1)}\Big(v_i+\frac{\Delta v_i+g_i}{2}\Big)+C_J^{(1)}J(J+1)\\ +C_K^{(1)}\Big[\ell_2(\ell_2\pm1)+\frac{1}{2}\Big]\pm\sum_i C_{i\ell}^{(1)}\Big(v_i+\frac{\Delta v_i+g_i}{2}\Big)\Big(\ell_2\pm\frac{1}{2}\Big)\\ \pm C_{J\ell}^{(1)}J(J+1)\Big(\ell_2\pm\frac{1}{2}\Big)\pm C_{\ell\ell}^{(1)}\Big(\ell_2\pm\frac{1}{2}\Big)^3\Big\}\end{aligned}\tag{1.64}$$

$$\begin{aligned}\big\langle v_1\ v_2\ \ell_2\ v_3\ J\big|H^{\rm eff}\big|v_1+2\ v_2-1\ \ell_2\pm1\ v_3-1\ J\big\rangle =\\ -\sqrt{v_3(v_1+1)(v_1+2)(v_2\mp\ell_2)[J(J+1)-\ell_2(\ell_2\pm1)]}\\ \times\Big\{C_e^{(2)}\pm C_\ell^{(2)}\Big(\ell_2\pm\frac{1}{2}\Big)+\sum_i C_i^{(2)}\Big(v_i+\frac{\Delta v_i+g_i}{2}\Big)+C_J^{(2)}J(J+1)\\ +C_K^{(2)}\Big[\ell_2(\ell_2\pm1)+\frac{1}{2}\Big]\pm\sum_i C_{i\ell}^{(2)}\Big(v_i+\frac{\Delta v_i+g_i}{2}\Big)\Big(\ell_2\pm\frac{1}{2}\Big)\\ \pm C_{J\ell}^{(2)}J(J+1)\Big(\ell_2\pm\frac{1}{2}\Big)\pm C_{\ell\ell}^{(2)}\Big(\ell_2\pm\frac{1}{2}\Big)^3\Big\}\end{aligned}\tag{1.65}$$

In the above expressions, g_i is the degeneracy index which is 1 for the stretching modes and 2 for the double degenerate bending mode.

The effective Hamiltonian matrix has a polyad structure due to the approximate relations (1.53) between the harmonic frequencies. Each polyad is made up of the

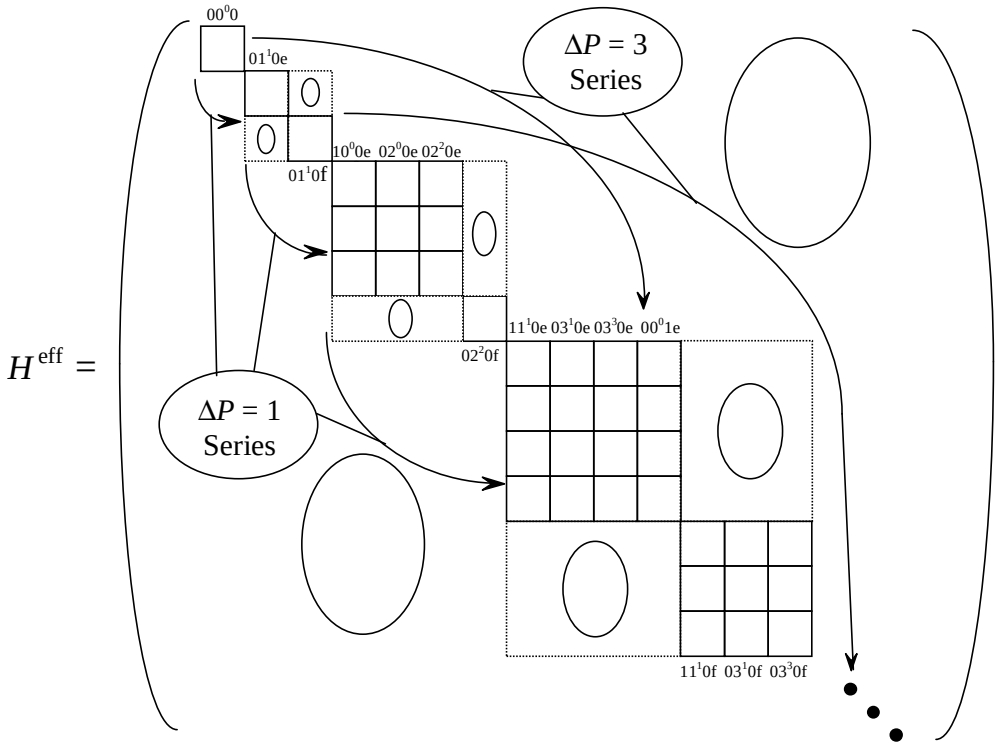

Figure 1.3. Effective Hamiltonian matrix and series of transitions. The e and f sub-blocs correspond to different parity arising from Wang combination of the basis functions (1.71–1.72) (see Section 1.2.1).

vibrational basis states the quantum numbers of which fulfill the equation

$$P = 2v_1 + v_2 + 3v_3. \tag{1.66}$$

Thus, the polyads can be labeled with the integer P value, which may be considered as the polyad quantum number. Figure 1.3 shows the structure of the effective Hamiltonian matrix and the series of bands which are defined by a given value of the differences

$$\Delta P = P' - P'', \tag{1.67}$$

where P' and P'' are the polyad quantum numbers for the upper and lower polyads, respectively.

Parameters of the matrix elements of the effective Hamiltonian (1.56–1.65) are fitted by means of a nonlinear least-squares procedure to the observed line positions. The main advantage of this effective Hamiltonian is that it allows both rotational and vibrational

extrapolation calculations.

1.1.6 Interpolyad resonances

One of the limitations of the presented above model of effective Hamiltonian is the accidental occurrence of interpolyad resonances due to the neighbor polyads energy levels proximity or crossing.

The effective Hamiltonian construction is based on the perturbation theory which is limited by the following condition of convergence of the corrections series:

$$\left| \frac{\langle n|H|k\rangle}{\varepsilon_n - \varepsilon_k} \right| << 1, \tag{1.68}$$

where $\langle n|H|k\rangle$ is the matrix element of interaction between $|n\rangle$ and $|k\rangle$ states, ε_n and ε_k are the unperturbed energies of these states. If some energy levels from different polyads occur close to each other and their interaction matrix element value is not identical zero, the condition (1.68) is not satisfied. In this case the precision of Schrödinger equation solution degrades significantly. This phenomenon, called interpolyad resonance, is not taken into account by the polyad model of effective Hamiltonian discussed above and may lead to accidental perturbations of calculated energy levels (see below).

1.2 Rovibrational spectrum of CO_2 molecule

1.2.1 Energy level labeling

In the case of CO_2 molecule, normal mode labeling fails even for the low vibrational states because of strong Fermi resonance interaction ($\omega_1 \approx 2\omega_2$). We describe below two types of vibration-rotation *quantum numbers*. The HITRAN type is based on Fermi polyad structure of the vibrational energy levels. The second one, used in GIP computer code [29], results of the effective Hamiltonian matrix construction. The Carbon Dioxide Spectroscopic Databank (CDSD) uses both types of energy labeling.

Within the framework of the HITRAN type labeling ($v_1 v_2 \ell_2 v_3 r$) all vibrational states are grouped into Fermi polyads, which are determined by v_1, v_3 and ℓ_2 vibrational quantum numbers of the harmonic oscillator basis states, where v_1 is connected to the

global polyad number P defined in (1.66) by the expression:

$$2v_1 = P - \ell_2 - 3v_3, \tag{1.69}$$

and

$$v_2 = \ell_2. \tag{1.70}$$

The ranking number r runs values $1 \leq r \leq v_1 + 1$ in order of decreasing of the energy value. For example, polyad number 4 ($P = 4$) has four Fermi polyads: (2000), (1220), (0440) and (0111). The first Fermi polyad involves three basis states: $\left|20^00\right\rangle$, $\left|12^00\right\rangle$ and $\left|04^00\right\rangle$, and respective vibrational eigenstates are labeled as 20001, 20002, and 20003. The second Fermi polyad involves two basis states: $\left|12^20\right\rangle$ and $\left|04^20\right\rangle$, and respective vibrational eigenstates are labeled as 12201 and 12202. The third and fourth Fermi polyad involve one vibrational basis state each ($\left|04^40\right\rangle$ and $\left|01^11\right\rangle$) and respective vibrational eigenstates are labeled as 04401 and 01111 respectively. The complete label of a vibration-rotation state includes additionally two good quantum numbers: the parity C (e or f) and the angular momentum quantum number J. The parity C relates to the sign $\varepsilon \pm 1$ of the Wang combinations of the basis functions

$$\left|v_1v_2\ell_2v_3J\varepsilon\right\rangle = \frac{1}{\sqrt{2}}\left(\left|v_1v_2\ell_2v_3\right\rangle\left|JK = \ell_2\right\rangle + \varepsilon\left|v_1v_2(-\ell_2)v_3\right\rangle\left|JK = -\ell_2\right\rangle\right), \tag{1.71}$$

$$\left|v_1v_20v_3J\varepsilon = 1\right\rangle = \left|v_1v_20v_3\right\rangle\left|J0\right\rangle \tag{1.72}$$

in the following way: $e \to \varepsilon = 1,\ f \to \varepsilon = -1$

The HITRAN type labeling is based additionally on the assumption of small mixing of the states with the different values of v_3 and ℓ_2 quantum numbers. But in the case of highly excited states the Coriolis and Fermi+ℓ-type resonance interactions lead to the strong mixing of some states with different ℓ_2 quantum numbers, which belong to the different Fermi polyads. So in such case the HITRAN type labeling fails. For this reason an additionally generalized nomenclature for labeling the energy level (P, J, C, N) is used in GIP computer code [29]. Here N is the index of an eigenvalue of the $J - P - C$ block of the Hamiltonian matrix in the increasing order of the eigenvalues. This nomenclature includes only good quantum numbers and never fails.

1.2.2 Selection rules

The transition probability between two quantum mechanical states can be described by an integral of the form

$$\langle \psi_m | \mu | \psi_n \rangle \equiv \int \psi_m^* \ \mu \ \psi_n \ d\tau, \tag{1.73}$$

where n and m are the two quantum mechanical states and μ is the transition dipole moment operator. In general, computing this integral is difficult, but there are some conditions under which the integral is identically zero, and hence the transition is forbidden. Basing on the symmetry of a molecule group theory provides an efficient method of determining whether a transition is allowed ($\langle \psi_m | \mu | \psi_n \rangle \neq 0$). This method consists of examining the product of the irreducible representations of two quantum mechanical states and dipole moment operator of the possible transition. If this product contains the totally symmetric irreducible representation, then the transition is allowed. This selection rule can be expressed as:

$$\Gamma(\psi_m) \times \Gamma(\mu) \times \Gamma(\psi_n) \supset A, \tag{1.74}$$

where A indicates the totally symmetric representation of any point group.

Carbon dioxide is a linear triatomic molecule which belongs either to the $D_{\infty h}$ (with a center of symmetry) or $C_{\infty V}$ (without a center of symmetry) symmetry point group. So the vibration-rotation energy states of CO_2 molecule can be classified by irreducible representation of $D_{\infty h}$ point group:

$$\underbrace{\Sigma_g^+,\ \Sigma_u^+,\ \Sigma_g^-,\ \Sigma_u^-}_{one-dimensional},\ \underbrace{\Pi_g,\ \Pi_u,\ \Delta_g,\ \Delta_u,\ \Phi_g,\ \Phi_u, \ldots}_{two-dimensional},$$

or $C_{\infty V}$ point group:

$$\Sigma^+,\ \Sigma^-,\ \Pi,\ \Delta\ , \Phi, \ldots$$

The correspondence between symmetry labels and vibration-rotation quantum numbers is given in Table 1.2.

Because of nuclear spin statistics some of the energy levels are forbidden for some of symmetric isotopic species. The nuclear spin statistical weights for symmetric isotopic

Table 1.2. Correspondence between symmetry labels and vibration-rotation quantum numbers.

Relation	Symmetry group
$\varepsilon(-1)^J = \begin{cases} 1 \to \Sigma^+ \\ -1 \to \Sigma^- \end{cases}$	$D_{\infty h},\ C_{\infty V}$
$(-1)^{v_3+\ell_2} = \begin{cases} 1 \to \Sigma_g \\ -1 \to \Sigma_u \end{cases}$	$D_{\infty h}$
$\ell_2 = \begin{cases} 1 \to \Pi \\ 2 \to \Delta \\ \dots \end{cases}$	$D_{\infty h},\ C_{\infty V}$

Table 1.3. Nuclear spin statistical weights for symmetric species of carbon dioxide.

Symmetry type	Nuclear spin statistical weight
Bosons	
$\Sigma_g^+,\ \Sigma_u^-$	$(i+1)(2i+1)$ [a]
$\Sigma_g^-,\ \Sigma_u^+$	$i(2i+1)$
Fermions	
$\Sigma_g^+,\ \Sigma_u^-$	$i(2i+1)$
$\Sigma_g^-,\ \Sigma_u^+$	$(i+1)(2i+1)$

[a] i – oxygen nuclei spin value ($i = 0$ for ^{16}O and ^{18}O, $i = \frac{5}{2}$ for ^{17}O)

species are given in Table 1.3. In the case of asymmetric isotopic species all energy levels have the same nuclear spin statistical weight.

The selection rules for Carbon dioxide vibration-rotation spectra which arise from theorem (1.74) are given in Table 1.4.

1.2.3 Types of band

According to the above selection rules the following types of vibrational bands of CO_2 molecules can be observed.

(1) Transitions for which $\ell_2 = 0$ in both upper and lower vibrational states ($\Sigma \leftrightarrow \Sigma$ transitions) form a parallel band. In such band the transitions only with $\Delta J = \pm 1$ are

Table 1.4. Selection rules for Carbon dioxide vibration-rotation spectra in absorption and emission.

$D_{\infty h}$	$C_{\infty V}$
Vibrational	
$\Delta v_2 - odd \quad \Delta v_3 - even$ $\Delta v_2 - even \quad \Delta v_3 - odd$	All transitions are allowed
Vibration-rotation point group	
$\Sigma_g^+ \leftrightarrow \Sigma_u^-$ $\Sigma_u^+ \leftrightarrow \Sigma_g^-$ [a]	$\Sigma^+ \leftrightarrow \Sigma^-$
$O(3)$ group [b]	
$\Delta J = 0$ [c] $\quad e \leftrightarrow f$	
$\Delta J = \pm 1 \quad e \leftrightarrow e,\ f \leftrightarrow f$	

[a] Because of nuclear spin statistics this kind of transitions does not take place for $C^{16}O_2$ and $C^{18}O_2$ isotopologues.

[b] In the case of $C^{16}O_2$ and $C^{18}O_2$ isotopic species because of nuclear spin statistics one of the transitions $e \leftrightarrow f$ does not take place and Q-branch of parallel bands with $\ell_2 = 0$ is forbidden.

[c] Note that if $\ell_2 = 0$ for both upper and lower state, $\Delta J = 0$ is forbidden.

allowed, that is, it has only the P- and R-branches but no Q-branch. In Fig. 1.4 the rotational levels associated with $\Sigma \leftrightarrow \Sigma$ vibrational transition are illustrated. In such parallel bands, the first observed lines are $R(0)$ and $P(1)$. For symmetric isotopic species ($C^{17}O_2$) belonging to the $D_{\infty h}$ point group, since the symmetric and antisymmetric rotational levels have different nuclear spin statistical weights (see Table 1.3), the lines in each branch show an intensity alternation. In the case of $C^{16}O_2$ and $C^{18}O_2$ isotopologues transitions $\Sigma_u^+ \leftrightarrow \Sigma_g^-$ are forbidden because of zero nuclear spin statistical weights, that is, the interval between two lines is about $4B$. For asymmetric isotopic species there is no such intensity alternation and all J values are allowed.

(2) Transitions with $\Delta\ell_2 = \pm 1$ ($\Pi \leftrightarrow \Sigma$, $\Delta \leftrightarrow \Pi \ldots$) form the perpendicular bands. These bands in addition to P- and R-branches, have the strong Q-branches (see Fig. 1.5). For symmetric species belonging to the $D_{\infty h}$ point group, the intensity alternation ($C^{17}O_2$) and line missing ($C^{16}O_2$, $C^{18}O_2$) for even (or odd) J values still take place in $\Pi \leftrightarrow \Sigma$ bands. In $\Delta \leftrightarrow \Pi$ band of asymmetric species, since each J energy

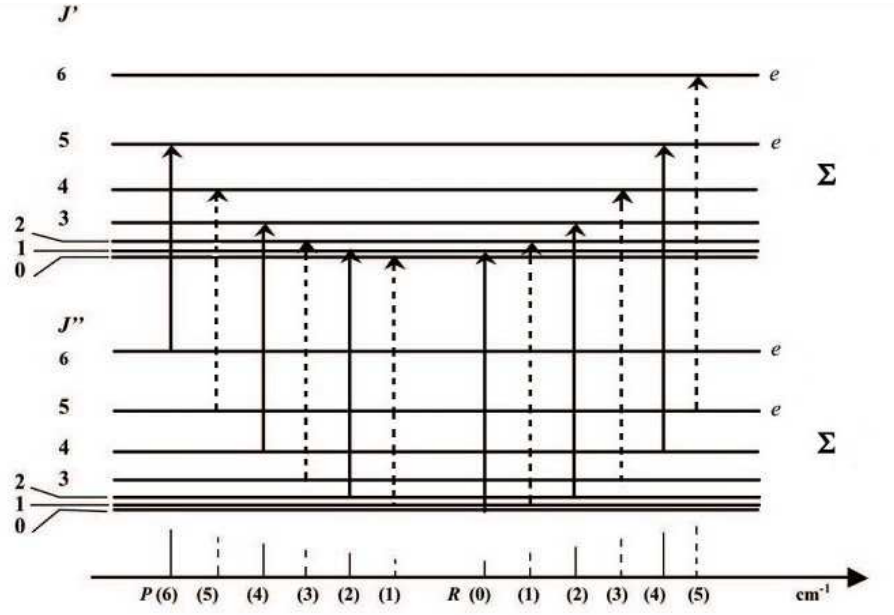

Figure 1.4. Energy level diagram for a $\Sigma \leftrightarrow \Sigma$ vibrational transition in a linear triatomic molecule. In the case of $C^{16}O_2$ and $C^{18}O_2$ isotopologues, the energy levels corresponding to odd J values don't exist and the corresponding transitions (dashed lines) are not observed.

level of both lower and upper states contains two sublevels (e and f), each line is split into two lines. The characteristic of this type of band is nearly the same as type (3) except for the intensity of Q-branch and will be discussed in the following paragraph.

(3) Transitions with $\Delta\ell_2 = 0$ but $\ell_2 \neq 0$. A very weak Q-branch is the distinguishing feature of the respective bands. In Π and Δ vibrational states there exist energy levels for all J values ($J \geqslant 1$ and $J \geqslant 2$ respectively). The energy levels with even J and those with odd J belong to different subsets (e and f). So in $\Pi - \Pi$ and $\Delta - \Delta$ bands the interval between two neighbor lines belonging to the same subset is about $4B$ but interval between neighbor J lines is about $2B$. So it looks like only one set of lines with interval $2B$, especially for low J value, as for $\Sigma \leftrightarrow \Sigma$ cold bands of the asymmetric species. However, since the e and f rotational constants are slightly different, the interval between two lines in each branch is heterogeneous while the interval is homogeneous in $\Sigma \leftrightarrow \Sigma$ cold bands of the asymmetric isotopologues. For species belonging to $C_{\infty V}$ point group, the double lines appear for every J value. Their separation is the difference between the ℓ-doubling (1.57) in the lower and upper state.

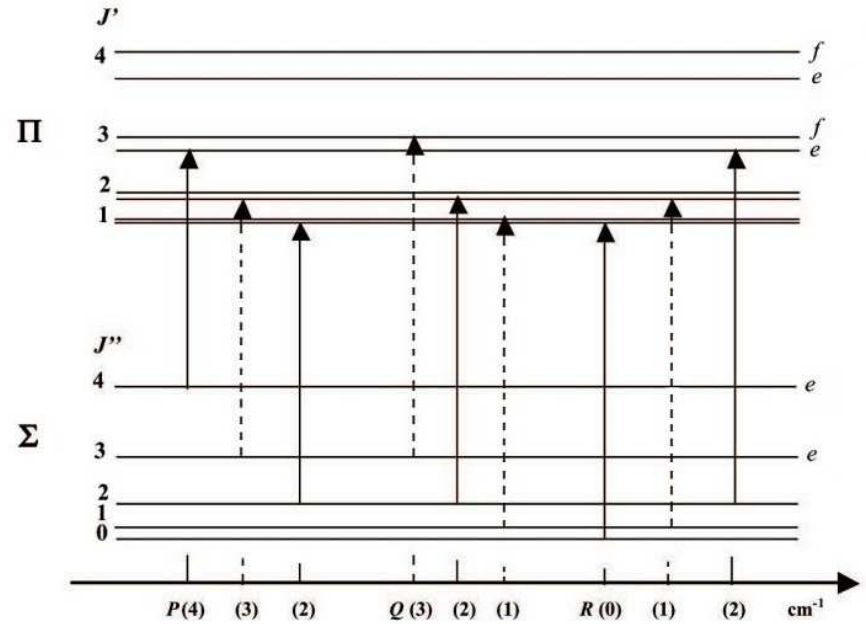

Figure 1.5. Energy level diagram for a $\Pi \leftrightarrow \Sigma$ vibrational transition in a linear triatomic molecule. In the case of $C^{16}O_2$ and $C^{18}O_2$ isotopologues, the energy levels corresponding to odd J values don't exist and the corresponding transitions (dashed lines) are not observed.

(4) Transitions with $|\Delta\ell_2| > 1$ are forbidden in the approximation of harmonic oscillator and symmetric top rotor, where interaction between vibration and rotation is not taken into account. However, these *forbidden* bands appear in higher orders of perturbation theory and can be observed at high sensitivity. They *borrow* most of their intensities from *allowed* bands *via* ℓ-type and anharmonic + ℓ-type interactions which are taken into account by effective Hamiltonian model (1.56–1.65).

1.3 Line intensity

1.3.1 Definition and general equations

According to the Beer-Lambert law, the intensity of transmitted light is proportional to the incident intensity and decreases exponentially with the absorption path length:

$$I(\nu) = I_0 e^{-\alpha(\nu)L}, \tag{1.75}$$

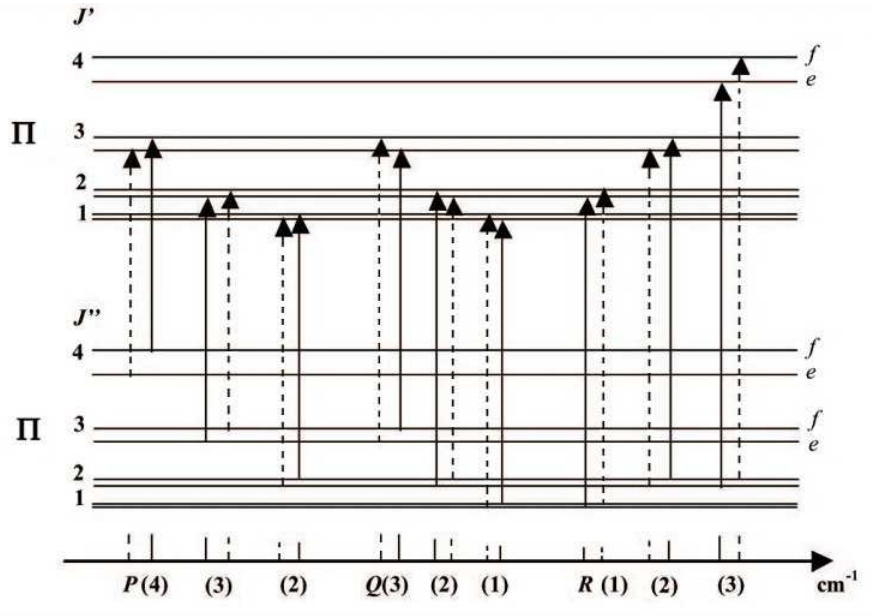

Figure 1.6. Energy level diagram for a $\Pi \leftrightarrow \Pi$ vibrational transition in a linear triatomic molecule. In the case of $C^{16}O_2$ and $C^{18}O_2$ isotopologues, the energy levels with e (f) symmetry corresponding to odd (even) J values don't exist and the corresponding transitions (dashed lines) are not observed.

where ν is wavenumber, L is the absorption path length (in cm), $\alpha(\nu)$ is the absorption coefficient (in cm^{-1}) which is proportional to the density of the absorber N (in molecule/cm^3) and the absorption cross-section $\sigma(\nu)$ (in cm^2/molecule):

$$\alpha(\nu) = N\sigma(\nu). \tag{1.76}$$

If the absorption is caused by a separated line centered at ν_0, then

$$\alpha(\nu) = NS(T)\varphi(\nu - \nu_0), \tag{1.77}$$

where $S(T)$ is integral absorption cross-section (in cm/molecule) at temperature T:

$$S(T) = \int \sigma(\nu)d\nu, \tag{1.78}$$

and $\varphi(\nu - \nu_0)$ is the normalized absorption profile function:

$$\int \varphi(\nu - \nu_0)d\nu = 1. \tag{1.79}$$

Absolute line intensity $\tilde{S}(T)$ (in $\mathrm{cm}^{-2}{\cdot}\mathrm{atm}^{-1}$) is defined as integrated absorption coefficient per pressure unit:

$$\tilde{S}(T) = \frac{1}{P}\int \alpha(\nu)d\nu, \tag{1.80}$$

where P is the sample partial pressure (in atm). The line intensity $S(T_0)$ at standard temperature $T_0 = 296$ K can be deduced from the absolute line intensity $\tilde{S}(T)$ according to the following equation:

$$S(T_0) = \frac{T}{273.15}\frac{1}{N_L}\frac{Q(T)}{Q(T_0)}\exp\left[\frac{hc}{k}E''\left(\frac{1}{T}-\frac{1}{T_0}\right)\right]\frac{1-\exp\left(-\frac{hc\nu}{kT_0}\right)}{1-\exp\left(-\frac{hc\nu}{kT}\right)}\tilde{S}(T), \qquad (1.81)$$

where $N_L = 2.68676 \times 10^{19}$ molecule·cm^{-3}·atm^{-1} is the Loschmidt number, $h = 6.6260755 \times 10^{-27}$ erg·s is Plank constant, $c = 2.99792458 \times 10^{10}$ cm/s is the light speed in vacuum, $k = 1.380658 \times 10^{-16}$ erg/K is Boltzman constant, E'' (in cm^{-1}) is the energy of lower state of the transition and Q is total internal partition function.

The line intensity $S(T)$ of a vibrational-rotational transition $b \leftarrow a$ is given by the following equation

$$S_{b\leftarrow a}(T) = \frac{1}{4\pi\varepsilon_0}\frac{8\pi^3}{3hc}\frac{Cg_a\nu_{b\leftarrow a}}{Q(T)}\exp\left(-\frac{hcE_a}{kT}\right)\left[1-\exp\left(-\frac{hc\nu_{b\leftarrow a}}{kT}\right)\right]W_{b\leftarrow a}, \qquad (1.82)$$

where $\frac{1}{4\pi\varepsilon_0} = 10^{-36}$ erg·cm^3·D^{-2}, C is the isotopic abundance, g_a is nuclear spin statistical weight of the lower state, $\nu_{b\leftarrow a}$ is the wavenumber (in cm^{-1}) of the vibration-rotation transition $b \leftarrow a$, E_a is the energy of the lower state, $W_{b\leftarrow a}$ is the transition moment squared (in D^2) which represent the transition probability and given by

$$W_{b\leftarrow a} = \sum_{\alpha=X,Y,Z}\sum_{MM'}\left|\langle bM'\,|M_\alpha|\,aM\rangle\right|^2. \qquad (1.83)$$

In the above equation the sum is taken over the magnetic quantum numbers M and M' of the lower and upper states and over the dipole moment components in a space-fixed frame.

1.3.2 Transition moment squared, empirical approach

If a vibrational band is considered as isolated, the transition moment squared of the corresponding vibration-rotation transition $b \leftarrow a$ of carbon dioxide can be represented by the standard empirical expression [30]:

$$W_{b\leftarrow a} = |R_{b\leftarrow a}|^2 L_{\Delta J}^{\Delta\ell_2}(J,\ell_2)F(m), \qquad (1.84)$$

where $|R_{b\leftarrow a}|^2$ is the vibrational transition moment squared, $L^{\Delta\ell_2}_{\Delta J}(J,\ell_2)$ is Hönl-London factor, $F(m)$ is Herman-Wallis factor which can be expressed by

$$F(m) = (1 + a_1 m + a_2 m^2 + a_3 m^3)^2, \quad \Delta J = \pm 1 \text{ (P- and R-branches)}; \tag{1.85}$$

$$F(m) = (1 + b_2 m^2)^2, \quad \Delta J = 0 \text{ (Q-branch)} \tag{1.86}$$

and m is equal to $-J$, J and $J+1$ for P-, Q- and R-branches respectively. The Hönl-London factor $L^{\Delta\ell_2}_{\Delta J}(J,\ell_2)$ for parallel bands ($\Delta\ell_2 = 0$) of carbon dioxide, as well as for any triatomic linear molecule, is given by following equations:

$$L^{\Delta\ell_2}_{\Delta J}(J,\ell_2) = \frac{(J+\ell_2)(J-\ell_2)}{J}, \qquad (P\text{-branch}) \tag{1.87}$$

$$L^{\Delta\ell_2}_{\Delta J}(J,\ell_2) = \frac{(2J+1)\ell_2^2}{J(J+1)}, \qquad (Q\text{-branch}) \tag{1.88}$$

$$L^{\Delta\ell_2}_{\Delta J}(J,\ell_2) = \frac{(J+1+\ell_2)(J+1-\ell_2)}{J+1} \qquad (R\text{-branch}) \tag{1.89}$$

and for perpendicular bands ($\Delta\ell = \pm 1$), $L^{\Delta\ell_2}_{\Delta J}(J,\ell_2)$ is

$$L^{\Delta\ell_2}_{\Delta J}(J,\ell_2) = \frac{(J-1-\ell_2\Delta\ell_2)(J-\ell_2\Delta\ell_2)}{2J}, \qquad (P\text{-branch}) \tag{1.90}$$

$$L^{\Delta\ell_2}_{\Delta J}(J,\ell_2) = \frac{(J+1+\ell_2\Delta\ell_2)(J-\ell_2\Delta\ell_2)(2J+1)}{2J(J+1)}, \qquad (Q\text{-branch}) \tag{1.91}$$

$$L^{\Delta\ell_2}_{\Delta J}(J,\ell_2) = \frac{(J+2+\ell_2\Delta\ell_2)(J+1+\ell_2\Delta\ell_2)}{2(J+1)}. \qquad (R\text{-branch}) \tag{1.92}$$

The vibrational transition moment squared $|R_{b\leftarrow a}|^2$ and Herman-Wallis coefficients a_1, a_2, a_3 and b_2 for an observed band are usually determined by least-square fitting to the experimental values of the transition moment squared $W_{b\leftarrow a}$. Satisfactory data reproduction can be achieved only for well-isolated bands because no any resonance interaction is taken into account by this approach. This method does not allow vibrational extrapolation calculation and the extrapolations to high J values are limited by accidental resonance interactions.

1.3.3 Effective dipole moment model

The effective dipole moment model for CO_2 molecule was first developed and applied for band intensity problem in Ref. [31], than it was used for line intensity calculations [31–35]. It allows to describe simultaneously intensities of all transitions belonging

to a ΔP series by a single set of parameters. All intrapolyad resonance interactions, leading to intensity transfers and extra lines appearance, are accounted by this model.

The effective dipole moment method consists in applying the same unitary contact transformations as in the case of effective Hamiltonian development to the dipole moment operator:

$$M_Z^{\text{eff}} = e^{iS}\ M_Z\ e^{-iS} = e^{iS}\ \sum_{\alpha} \lambda_Z^{\alpha} \mu_{\alpha}\ e^{-iS}, \tag{1.93}$$

so that the matrix elements in Eq. (1.83) can be calculated using the eigenfunctions $\Psi_{PNJ\varepsilon}^{\text{eff}}$ of the effective Hamiltonian. In above equation μ_α are the components of the dipole moment operator in the molecule-fixed frame, λ_Z^{α} are the direction cosines. In this approach the transition moment squared of vibrational-rotational transition $P'N'J'\varepsilon' \leftarrow PNJ\varepsilon$ of CO_2 molecule is given by

$$\begin{aligned} W_{P'N'J'\varepsilon'\leftarrow PNJ\varepsilon} = (2J+1)\Bigg| \sum_{v_1 v_2 \ell_2 v_3} \sum_{\substack{2\Delta v_1+\Delta v_2+\Delta v_3=\Delta P \\ \Delta\ell_2=0,\pm1,\pm2,\ldots}} {}^{J}C_{PN\varepsilon}^{v_1 v_2 \ell_2 v_3} \\ \times {}^{J'}C_{P'N'\varepsilon'}^{v_1+\Delta v_1 v_2+\Delta v_2 \ell_2+\Delta\ell_2 v_3+\Delta v_3} M_{\Delta v}^{\Delta\ell_2} \sqrt{f_{\Delta v}^{\Delta\ell_2}(v,\ell_2)(1+\delta_{\ell_2,0}+\delta_{\ell_2',0}-\delta_{\ell_2,0}\delta_{\ell_2',0})} \\ \times \Phi_{\Delta J,\Delta\ell_2}(J,\ell_2)\left(1+\sum_i \kappa_i^{\Delta v} v_i + F_{\Delta v}^{\Delta\ell_2}(J,\ell_2)\right)\Bigg|^2. \end{aligned} \tag{1.94}$$

Here $\delta_{i,j}$ is Kronecker symbol and ${}^{J}C_{PN\varepsilon}^{v_1 v_2 \ell_2 v_3}$ are the expansion coefficients determining the eigenfunction of the lower state

$$\Psi_{PNJ\varepsilon}^{\text{eff}} = \sum_{\substack{2v_1+v_2+3v_3=P \\ \ell_2}} {}^{J}C_{PN\varepsilon}^{v_1 v_2 \ell_2 v_3} \big| v_1 v_2 |\ell_2| v_3 J\varepsilon \big\rangle. \tag{1.95}$$

The summation runs over all states within the polyad involved. In the same way, ${}^{J'}C_{P'N'\varepsilon'}^{v_1' v_2' \ell_2' v_3'}$ stands for the expansion coefficients within the upper-state polyad. The functions $\Phi_{\Delta J,\Delta\ell_2}(J,\ell_2)$ for $\Delta\ell_2 = 0, \pm 1$ coincide with Clebsch-Gordon coefficients

$$\Phi_{\Delta J,\Delta\ell_2}(J,\ell_2) = (1\ \Delta\ell_2\ J\ \ell_2 | J+\Delta J\ \ell_2+\Delta\ell_2), \tag{1.96}$$

which are later related to the Hönl-London factor by the equation:

$$|(1\ \Delta\ell_2\ J\ \ell_2 | J+\Delta J\ \ell_2+\Delta\ell_2)|^2 = \frac{L_{\Delta J}^{\Delta\ell_2}(J,\ell_2)}{2J+1}. \tag{1.97}$$

For $\Delta\ell_2 = \pm 2$ the functions $\Phi_{\Delta J,\Delta\ell_2}(J,\ell_2)$ are given by the following equations:

$$\Phi_{1,\pm 2}(J,\ell_2) = (1\ \ \pm 1\ J\ \ell_2|J+1\ \ell_2 \pm 1)\sqrt{(J \mp \ell_2)(J \pm \ell_2 + 3)}, \tag{1.98}$$

$$\Phi_{0,\pm 2}(J,\ell_2) = (1\ \ \pm 1\ J\ \ell_2|J\ \ell_2 \pm 1)\sqrt{(J \mp \ell_2 - 1)(J \pm \ell_2 + 2)}, \tag{1.99}$$

$$\Phi_{-1,\pm 2}(J,\ell_2) = (1\ \ \pm 1\ J\ \ell_2|J-1\ \ell_2 \pm 1)\sqrt{(J \mp \ell_2 - 2)(J \pm \ell_2 + 1)}. \tag{1.100}$$

The vibrational function $f_{\Delta v}^{\Delta\ell_2}(v,\ell_2)$ consists of the product of the elementary functions for each vibrational mode

$$f_{\Delta v}^{\Delta\ell_2}(v,\ell_2) = f_{\Delta v_1}(v_1) f_{\Delta v_2}^{\Delta\ell_2}(v_2,\ell_2) f_{\Delta v_3}(v_3). \tag{1.101}$$

These elementary vibrational functions are given below:

$$f_{\Delta v_i}(v_i) = \underbrace{(v_i+1)(v_i+2)\ldots(v_i+\Delta v_i)}_{\Delta v_i}, \tag{1.102}$$

$$f_{-\Delta v_i}(v_i) = \underbrace{(v_i+1)\ldots(v_i-\Delta v_i+1)}_{\Delta v_i}, \tag{1.103}$$

where $i = 1, 3$;

$$f_{\Delta v_2}^{\pm\Delta\ell_2}(v_2,\ell_2) = (v_2+\ell_2+2)^{\left\{\frac{1}{2}(\Delta v_2 \pm \Delta\ell_2)\right\}}(v_2-\ell_2+2)^{\left\{\frac{1}{2}(\Delta v_2 \mp \Delta\ell_2)\right\}}, \tag{1.104}$$

$$f_{-\Delta v_2}^{\pm\Delta\ell_2}(v_2,\ell_2) = (v_2+\ell_2)^{\left\{-\frac{1}{2}(\Delta v_2 \mp \Delta\ell_2)\right\}}(v_2-\ell_2)^{\left\{-\frac{1}{2}(\Delta v_2 \pm \Delta\ell_2)\right\}}, \tag{1.105}$$

$$f_{\Delta v_2=0}^{\Delta\ell_2}(v_2,\ell_2) = (v_2+\ell_2+2)^{\left\{\frac{1}{2}\Delta\ell_2\right\}}(v_2-\ell_2)^{\left\{-\frac{1}{2}\Delta\ell_2\right\}}, \tag{1.106}$$

$$f_{\Delta v_2=0}^{-\Delta\ell_2}(v_2,\ell_2) = (v_2-\ell_2+2)^{\left\{\frac{1}{2}\Delta\ell_2\right\}}(v_2+\ell_2)^{\left\{-\frac{1}{2}\Delta\ell_2\right\}}. \tag{1.107}$$

In the above equations the following notations are used:

$$x^{\{n\}} = \underbrace{x(x+2)\ldots[x+2(n-1)]}_{n}, \quad n > 0;$$

$$x^{\{-n\}} = \underbrace{x(x-2)\ldots[x-2(n-1)]}_{n}, \quad n > 0.$$

The Herman-Wallis-type functions appearing in Eq. (1.94) can be written as:

$$F_{\Delta v}^{\Delta\ell_2}(J,\ell_2) = b_J^{\Delta v} m + d_J^{\Delta v}\left[J(J+1) + m - \ell_2^2\right] \tag{1.108}$$

for $\Delta\ell_2 = 0$ matrix elements,

$$F_{\Delta v}^{\Delta\ell_2}(J,\ell_2) = -\frac{1}{2}\left(b_J^{\Delta v} + 2a_K^{\Delta v}\right)(2\ell_2\Delta\ell_2 + 1) + d_{JQ}^{\Delta v}\left[J(J+1) - \ell_2^2 - \Delta\ell_2\left(\ell_2 + \frac{\Delta\ell_2}{2}\right)\right] \tag{1.109}$$

for $\Delta J = 0$, $\Delta\ell_2 = \pm 1$ matrix elements, and

$$F_{\Delta v}^{\Delta\ell_2}(J,\ell_2) = -\frac{1}{4}\left(d_{JQ}^{\Delta v} - d_J^{\Delta v}\right) - \frac{1}{2}\left(b_J^{\Delta v} + d_{JQ}^{\Delta v} + 2a_K^{\Delta v}\right)(2\ell_2\Delta\ell_2 + 1) \\ - d_{JQ}^{\Delta v}\ell_2^2 + b_J^{\Delta v}m + d_J^{\Delta v}m^2 + \left(d_{JQ}^{\Delta v} - d_J^{\Delta v}\right)m\left(\ell_2\Delta\ell_2 + \frac{1}{2}\right) \quad (1.110)$$

for $\Delta J = \pm 1$, $\Delta\ell_2 = \pm 1$ matrix elements. Here m is equal to $-J$, 0 and $J+1$ for P-, Q- and R-branches respectively.

The $M_{\Delta v}^{|\Delta\ell_2|}$, $\kappa_i^{\Delta v}$ $(i = 1, 2, 3)$, $a_K^{\Delta v}$, $b_J^{\Delta v}$, $d_J^{\Delta v}$, $b_{JQ}^{\Delta v}$ parameters of the effective dipole moment matrix elements in Eqs. (1.94) and (1.108–1.110) describe simultaneously intensities of all lines of cold and hot bands belonging to a series of transition characterized by a ΔP value. The equations for these parameters in terms of force field constants and dipole moment derivatives can be obtained by means of contact transformation calculations. Some of these equations are presented in Refs. [25, 31]. The values for these parameters can also be obtained by fitting to the experimental line intensities with the help of known effective Hamiltonian eigenfunctions.

Chapter 2

Experimental technique

Ce chapitre est dédié à la description de la technique expérimentale utilisée pour enregistrer les spectres étudiés au cours de la thèse, à savoir la "Cavity Ring Down Spectroscopy" (CRDS). Les principes généraux de la technique sont d'abord présentés. L'extension de la technique impliquant l'utilisation de lasers à diode à émission continue ("Continuous Wave" ou CW) et de fibres optiques, réalisée dans notre laboratoire, est ensuite décrite. C'est le spectromètre CW-CRDS "fibré" ainsi réalisé qui a été utilisé pour l'enregistrement des spectres. Ce chapitre se termine par une discussion du problème de la calibration en nombres d'onde des spectres enregistrés.

2.1 Cavity ring down spectroscopy

Cavity ring down spectroscopy (CRDS) is a versatile high sensitivity absorption technique which is exploited in an large number of investigations. One of the attractive features of CRDS is its conceptual simplicity. Two high reflection mirrors (typical reflectance $R = 0.99997$) compose a stable optical resonator of length ℓ, which may be vacuumed to confine the sample of interest. Injection and excitation of the ringdown cavity are obtained by the direct transmission of the laser beam (pulsed laser or CW laser with a quick interruption) through one of the mirrors, along the cavity axis. A part of the trapped photons is retransmitted outside the cavity and produces an easily detectable signal. This may well be considered as a multipass technique affording 10 to

1000 times longer pathlength than traditional multiple reflection cells, therefore reliable absorption coefficients can be obtained directly. In addition, the signal is not affected by the source-intensity noise, which is an important advantage over most spectroscopic techniques.

The standard CRDS relies on a pulsed laser to produce instantaneous excitation of the ringdown cavity. The laser pulses often have a duration shorter than the cavity round-trip time, so that the laser spectrum can always overlap some cavity mode in the frequency domain which allow that light is transmitted by the cavity. But this is just a sufficient condition, not a necessary one. One can tune the laser spectrum to make it always overlapping at least one of the cavity mode frequencies, which implies that such mode is excited by the pulse.

The detector records the output signal, which is a series of laser pulses separated by the round-trip time $2\ell/c$, where c is the light velocity. The envelope of this ringdown signal is an exponential decay with a constant time τ (see Fig. 2.1), called the *ringdown time constant*, fixed by the cavity loss rate [36]:

$$\frac{1}{\tau} = (T + L + \alpha(\nu)\ell)\frac{c}{\ell} = \frac{1}{\tau_0} + c\alpha(\nu) \tag{2.1}$$

where T is the transmittance, L is the loses including absorption by the dielectric coating and scattering on the surface of the mirrors and $\alpha(\nu)$ is a simple absorption coefficient.

The diffraction losses due to the mirrors are usually negligible as the light beam remains collimated along the cavity axis. The energy conservation of the injected energy requires

$$R + T + L = 1, \tag{2.2}$$

where R is the reflectance. Since the cavity ringdown time is usually much longer than the round-trip time, the exponential envelope is detected with a detector having a long time constant that smooths the fast structure due to the round trips. By scanning the laser wavelenth, the absorption coefficient $\alpha(\nu)$ is simply obtained by dividing the decay rate $1/\tau$ by the velocity of light. Indeed, the contribution of the mirror losses $1/\tau_0$ to decay rate depends smoothly on the wavelength and gives the baseline of the absorption spectrum. For a rotationally resolved absorption spectrum, the narrow absorption

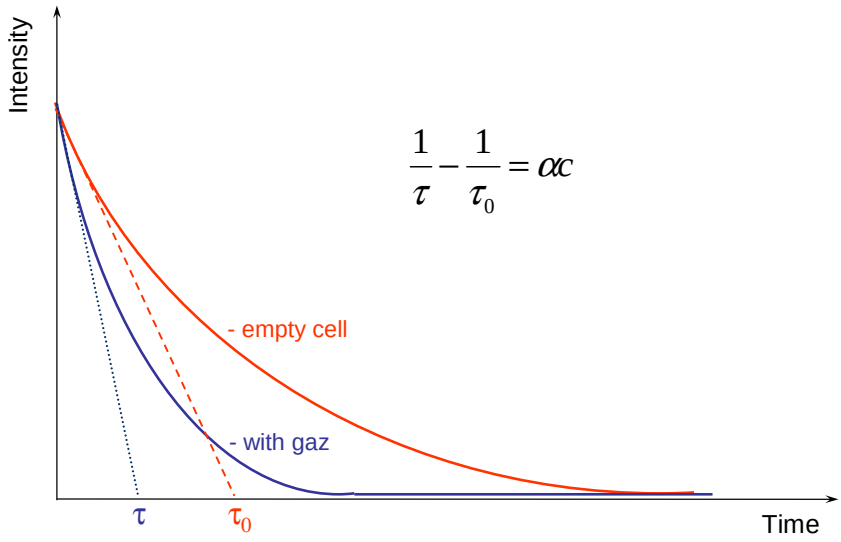

Figure 2.1. Ringdown decay of the output signal.

features are easily distinguished against the baseline profile. In the case of broad unresolved absorption bands, the sample absorption may be obtained from the difference in decay rate measured with and without the sample in the cavity.

2.2 CW-CRDS

A spectral resolution higher then that provided by pulsed lasers can be achieved by applying narrowband CW laser sources. The possibility of implementing low-cost CW diode laser sources for CW-CRDS makes this technique particularly suitable for applications such as high resolution spectroscopy at low pressure, sub-Doppler absorption spectroscopy in a supersonic jet, and trace-gas detection. Meijer et al. [37] and Romanini et al. [38–40] have succeeded in coupling narrowband CW laser sources to ringdown cavities and first developed CW-CRDS applications.

If a CW laser is used to excite the cavity, the ringdown signal may be recorded after a quick interruption of the injected laser beam. It is well known that a large intracavity buildup of the photon field occurs when the frequency of a CW laser coincides with one of the cavity resonances, but the frequency locking of the passive cavity to the

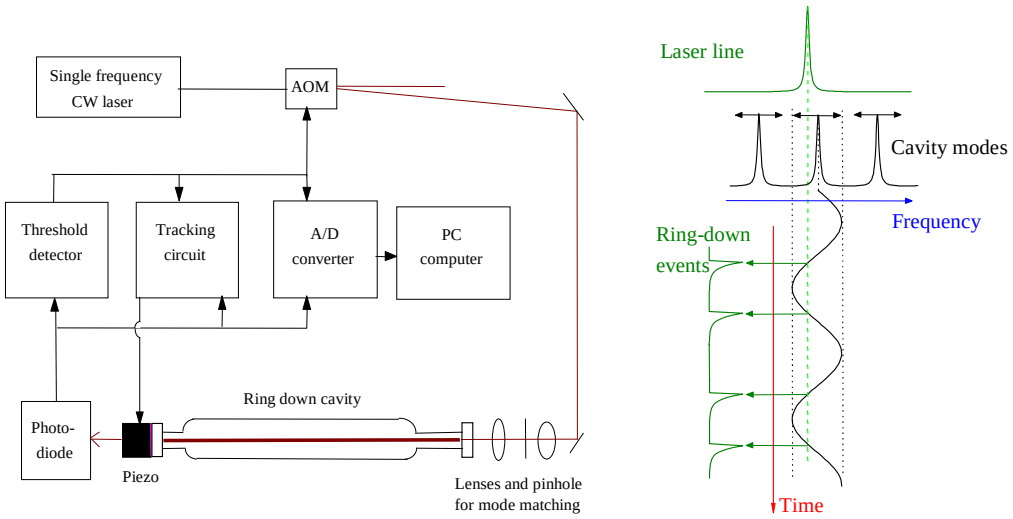

Figure 2.2. Simplified scheme of CW-CRDS setup (adapted from Ref. [38]).

incoming laser is extremely difficult to achieve, in particularly because of frequency jitter of the laser. Romanini et al. [38–40] have proposed a simple and efficient solution to this problem. It is based on the periodic coincidences of the laser frequency with cavity modes, when the length of cavity is modulated. So that a periodic occurrence of buildup events at high and controllable repetition rate can be obtained by dithering the cavity length, each followed by a ringdown decay of the trapped photons.

Fig. 2.2 presents a simplified scheme of the CW-CRDS setup. One of the high reflection mirrors is mounted on a piezoelectric transducer to modulate the cavity length, and therefore, the frequency of one of the cavity modes around the laser line. When sufficient buildup is transmitted by the cavity and measured by photodiode, the threshold circuit interrupts the laser with the help of an acoustooptic modulator. The ringdown signals are digitized, recorded and averaged.

2.2.1 Fibered CW-CRDS setup developed in Grenoble

The fibered CW-CRDS spectrometer, dedicated to the investigation of the near infrared atmospheric window near 1.5 μm, has been developed in Grenoble by Romanini et al [38–40]. These last years, S. Kassi has continuously improved the setup and he recorded almost all the spectra analysed in this thesis. This setup was characterized in Ref. [40] and its application for routine spectroscopic measurements was described in Ref. [15], and therefore we describe here only the main features. In this setup, the fibered components (with low-feedback FC/APC connectors), which can be easily connected together, are used wherever possible (see Fig. 2.3). To cover the spectral region 5851–7045 cm^{-1} (except for an inaccessible 7.7 cm^{-1} gap between 6122.4 and 6130.1 cm^{-1}) 51 fibered distributed feed-back (DFB) diode lasers (with integrated optical isolators) from three industry-leading manufacturers (NEL, Lucent and Alcatel) were used. This spectral region corresponds to the high reflectivity region of the mirror set used. The typical ringdown time (and consequently the sensitivity) decreases from 60 μs at 6550 cm^{-1} to about 20 μs at 5900 and 6950 cm^{-1}. The DFB typical tuning range is about 1 nm by current tuning and 7 nm (about 30 cm^{-1}) by temperature tuning from -10 °C to 60 °C (0.1 nm/°C). In order to avoid perturbation of the laser source, an additional fibered optical isolator is connected to the laser. The fibered acousto-optic switch (AOS) with fast beam shut-off (100 ns) and reasonably short response delay ($\sim$ 2 μs) is used to interrupt the laser beam when the threshold circuit detect a sufficient buildup. All open-path optics are fixed on a linear rail 2 m long, with a single-mode fiber delivering laser radiation to one end of the vacuum-tight ringdown cell, which is 140 cm long. A single lens images the diverging fiber output into the TEM_{00} cavity mode. The cavity output is focused on a sensitive InGaAs Avalanche Photo-Diode (APD) (model Epitaxx ETX240). The cavity mirrors (R = 1 m) are mounted on tilt stages, one of which includes a piezoelectric tube for modulating the cavity length by slightly more than $\lambda/2$. This makes the cavity modes oscillate by more than one FSR thus producing a passage through resonance with the laser line twice per modulation cycle (see Fig. 2.2). The maximum modulation rate permitted by our high-voltage oscillator is about 500 Hz, which gives a ringdown repetition rate of 1 kHz.

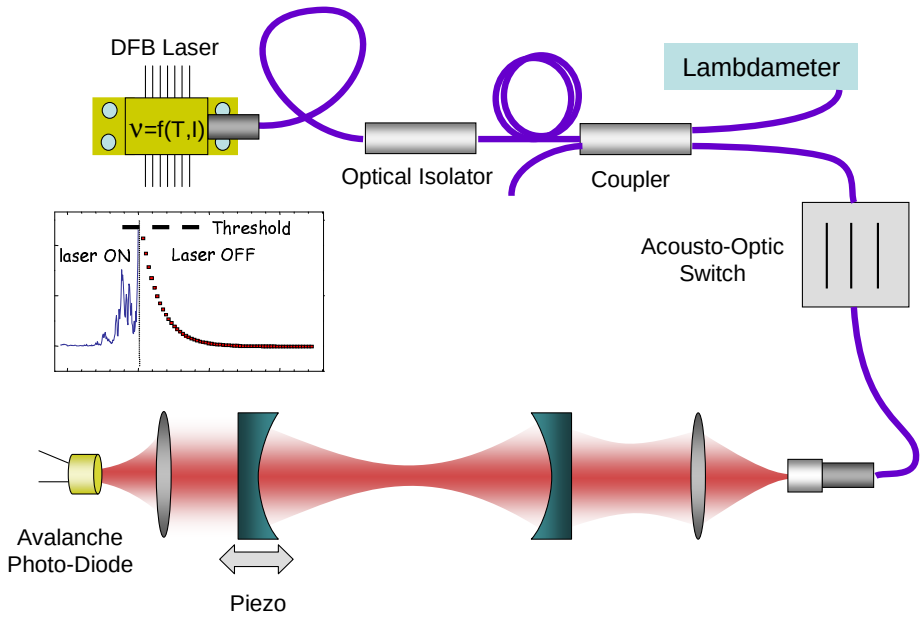

Figure 2.3. Fibered CW-CRDS setup.

The effective repetition rate is somewhat lower since a fraction of passages through resonance may fail to go above the threshold which triggers the AOS shut-down period. About 100 ringdown events are averaged for each spectral data point, and about 70 minutes are needed in order to complete a temperature scan (from -10 °C to 60 °C) for each DFB laser.

2.2.2 Wavenumber calibration

As mentioned above, each DFB laser allows the recording of about 30 cm^{-1} wide spectral region whose wavenumber calibration is performed independently on the basis of the wavelength values provided by a Michelson-type lambdameter (Burleigh WA1640, 60 MHz resolution and 200 MHz accuracy). The way we used this device in the new measurements [35, 41–44] allows significantly improving upon the method using an étalon signal, adopted in Refs. [14, 15], and upgrades the method presented in Ref. [45] where no lambdameter readings correction was performed.

The lambdameter records the frequency of the laser source while the latter is slowly tuned. During one lambdameter scan different laser frequencies, $f(t)$, are thus averaged. As the scan speed, $\mathrm{d}f/\mathrm{d}t$, can be considered constant over the integration time, I_t (1 s), the value provided by the lambdameter, is the laser frequency averaged over I_t. It is then basically $f(t_0 - I_t/2)$, i.e. the laser frequency at half a second before the reading time, t_0. The true frequency is in fact given by $f(t_0) = f(t_0 - I_t/2) + (\mathrm{d}f/\mathrm{d}t)I_t/2$. Even if hardware modifications have been performed in order to improve the linearity of the DFB laser frequency scan, its speed varies by about a factor 3 over the 7 nm tuning range, so that $\mathrm{d}f/\mathrm{d}t$ is not a constant over the whole scan (70 min) leading to a frequency dependent correction between $f(t_0)$ and $f(t_0 - I_t/2)$. However, as the frequency is hardware scanned step by step at constant time interval (0.22 s), one can calculate for each spectral point, the actual $\mathrm{d}f/\mathrm{d}t$, and correct for this shift.

After this speed correction, the entire spectrum becomes linear in terms of frequency. This linearity is transferred from the lambdameter single frequency laser reference which is very stable during the complete scan. However, this frequency is known with a limited precision (200 MHz). A better accuracy can be achieved by stretching the whole spectrum (with an origin at 0 like for FTIR spectra) in order to match accurate positions of reference lines observed in the spectrum.

Chapter 3

Line position analysis

Ce chapitre décrit la première partie du travail de la thèse. Elle consiste en l'analyse en positions de spectres d'absorption d'échantillons naturel et enrichi en ^{13}C du dioxyde de carbone, enregistrés entre 5851 et 7045 cm^{-1} par spectroscopie CW-CRDS. Le travail réalisé a concerné huit isotopologues du dioxyde de carbone: $^{12}C^{16}O_2$, $^{13}C^{16}O_2$, $^{16}O^{12}C^{18}O$, $^{16}O^{12}C^{17}O$, $^{16}O^{13}C^{18}O$, $^{16}O^{13}C^{17}O$ and $^{12}C^{18}O_2$. D'abord, l'attribution de raies observées a été réalisé à l'aide de prédictions du modèle effectif global. Les données expérimentales disponibles dans la littérature et celles obtenues au cours de cette thèse ont ensuite été utilisées pour améliorer les paramètres du modèle effectif de $^{12}C^{16}O_2$, $^{13}C^{16}O_2$, $^{16}O^{12}C^{18}O$, $^{16}O^{13}C^{17}O$ et $^{16}O^{13}C^{18}O$ (seuls les ajustements au modèle effectif global réalisés pour les 2 derniers isotopologues sont décrits dans la thèse). Enfin, chaque bande vibrationnelle a été analysé séparément à l'aide d'un modèle polynomial simple. Les résultats de ce travail, qui concerne 238 bandes de 8 isotopologues du dioxyde de carbone, sont fournis en appendice.

3.1 Introduction

In this Chapter, we present the detailed and exhaustive line position analysis of the absorption spectra of natural and ^{13}C enriched carbon dioxide obtained by high sensitivity CW-Cavity Ring Down spectroscopy (CW-CRDS) between 5851 and 7045 cm^{-1}.

The fibered CW-CRDS spectrometer using DFB diode lasers developed in our lab-

oratory (see Section 2.2.1) is dedicated to the characterization of the important 1.6 μm atmospheric window of transparency used for telecommunications, by high sensitivity absorption spectroscopy. The achieved typical sensitivity of 2–5 $\times$ 10^{-10} cm^{-1} and the 4 to 5 decades dynamics (see for instance, Figs. 3.1, 3.8 of the present Chapter and Fig. 4.2 of Chapter 4) on the intensity scale allow to significantly improve the knowledge of the absorption spectra of carbon dioxide. Indeed, the achieved CW-CRDS detection limit (down to 10^{-29} cm/molecule) is more than three orders of magnitude lower then that accessible by FTS (about 10^{-26} cm/molecule). The most part of CO_2 transitions belonging to $\Delta P = 9$ series (see Section 1.1.5) lies in the spectral region covered by our spectrometer (5851–7045 cm^{-1}).

The first line position analysis of $^{12}CO_2$ and $^{13}CO_2$ CW-CRDS spectra in the 6130–6750 cm^{-1} region were carried out by Majcherova et al. [14] and Ding et al. [15], respectively. Several thousands of new transitions were reported in these two contributions. However, an important fraction of the observed transitions remained unassigned (about 20% for ^{13}C enriched sample). So we decided to re-examine these CW-CRDS spectra in order to decrease the number of unassigned transitions. A new series of DFB diode lasers has become available allowing extending this spectral region both at high and low wavenumbers leading to a continuous coverage over a 1200 cm^{-1} wide spectral range. The present investigation is then a continuation of the above mentioned studies.

The high sensitivity allows to detect a great amount of weak transitions of dominant isotopologues ($^{12}C^{16}O_2$ and $^{13}C^{16}O_2$) with intensities down to 10^{-29} cm/molecule as well as transitions of minor isotopologues with relative concentration as low as 4×10^{-6}. These measurements have great impact on the global modeling of high resolution spectra of carbon dioxide within the framework of the method of effective operators and allow to check the extrapolation abilities of the developed models of effective Hamiltonians and effective dipole moment operators.

The aim of the present work is fivefold: (i) to extend the spectral region investigated by CW-CRDS down to 5851 and up to 7045 cm^{-1}, (ii) to test the data reproduction and predictive abilities of the EH model, (iii) to refine the EH parameters by including in the fit newly assigned transitions (the impact of CW-CRDS data is particularly important for minor isotopologues) in order to provide the improved predictions for

the updated version of CDSD database [11], (iv) to significantly decrease the fraction of unassigned transitions in the previously investigated region (6130–6750 cm^{-1}) on the basis of new EH predictions which allow to apply an automatic search program developed to find the coincidences between the observed and predicted line positions, (v) to gather this information and build the most extensive and consistent experimental datasets for $^{12}CO_2$ [43] and $^{13}CO_2$ [42] isotopologues for the whole 5851–7045 cm^{-1} region.

3.2 Experiment

The 5851–7045 cm^{-1} spectral region could be continuously explored (except for an inaccessible 7.7 cm^{-1} gap between 6122.4 and 6130.1 cm^{-1}) by our fibered CW-CRDS spectrometer using a set of 51 DFB diode lasers. This spectral region corresponds to the high reflectivity region of the mirror set used.

A first series of recordings was carried with natural carbon dioxide (Fluka, stated purity >99.998%) while in a second series, we used a sample with 99% enrichment in ^{13}C. The ^{13}C-enriched sample was purchased from Aldrich Chemical Company. Its stated isotopic composition was 99% ^{13}C, with less than 6% of ^{18}O atoms. For the line intensity measurements (see Section 4.2.1) we have calculated the concentrations of eight CO_2 isotopologues observed in the ^{13}C-enriched sample from the ratio of the measured integrated absorption coefficient and the corresponding line intensity. The obtained composition of the sample is presented in Table 3.1 which leads to the following isotopic abundance of the sample: 98.7% ^{13}C, 1.1% ^{18}O and 0.2% ^{17}O, in agreement with the stated sample composition.

As illustrated in Fig. 3.1, the typical value of the noise level on the spectrum baseline was $\alpha_{min} \sim 5 \times 10^{-10}$ cm^{-1}. The pressure, measured by a capacitance gauge (Baratron), as well as the ringdown cell temperature, was monitored during the spectrum recording. The sample pressure used for the recordings was about 25 hPa. In the very weak absorption regions, spectra were recorded with a higher pressure value ranging from 50 to 65 hPa. In our work devoted to the line intensity retrieval (see Chapter 4), additional spectra were recorded at lower pressures (13, 1.3, 0.27 hPa for ^{13}C-enriched sample and

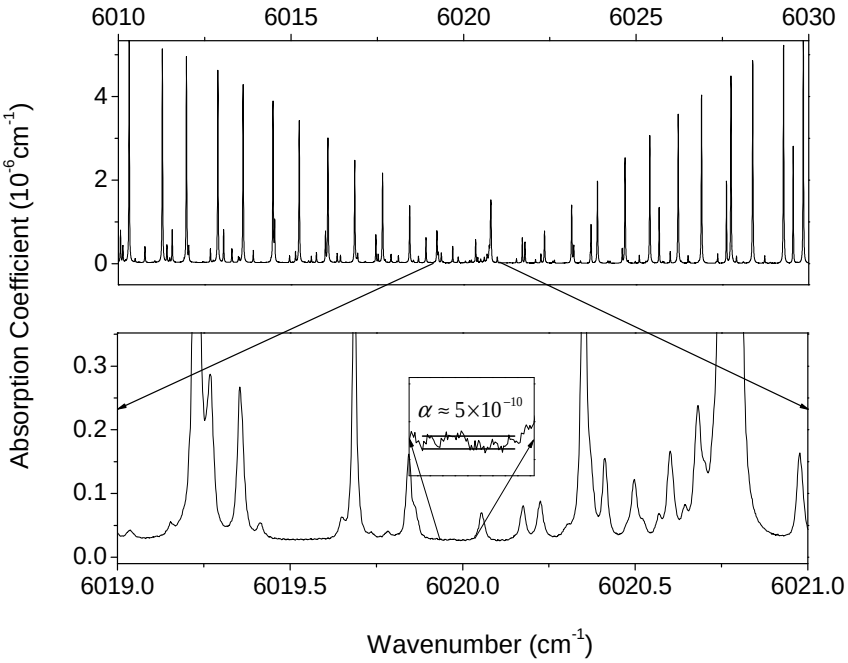

Figure 3.1. CW-CRDS spectrum of natural carbon dioxide between 6010 and 6030 cm^{-1} corresponding to the region of the 31114-01101 band centered at 6020.795 cm^{-1}. The sample pressure was 53 hPa (40 Torr). Two successive enlargements show that the noise level corresponding to the minimum value of the absorption coefficient which can be detected is about 5×10^{-10} cm^{-1}. Note the high dynamics achieved on the intensity scale: absorption coefficients differing by four orders of magnitude can be measured from this single spectrum.

13 hPa for natural CO_2). It allowed assigning additional transitions in particular weak lines in the vicinity of much stronger lines which were overlapped in the first recordings (see Fig. 3.2).

The wavenumber calibration was performed independently for each 30 cm^{-1} wide spectral section using the procedure described in Section 2.2.2. Observed accurate line positions of H_2O, CO_2, CH_4 and C_2H_2 listed in the HITRAN database [8] were used as reference lines to calibrate our spectra. The uncertainty of our wavenumber calibration is estimated to be about 1×10^{-3} cm^{-1}.

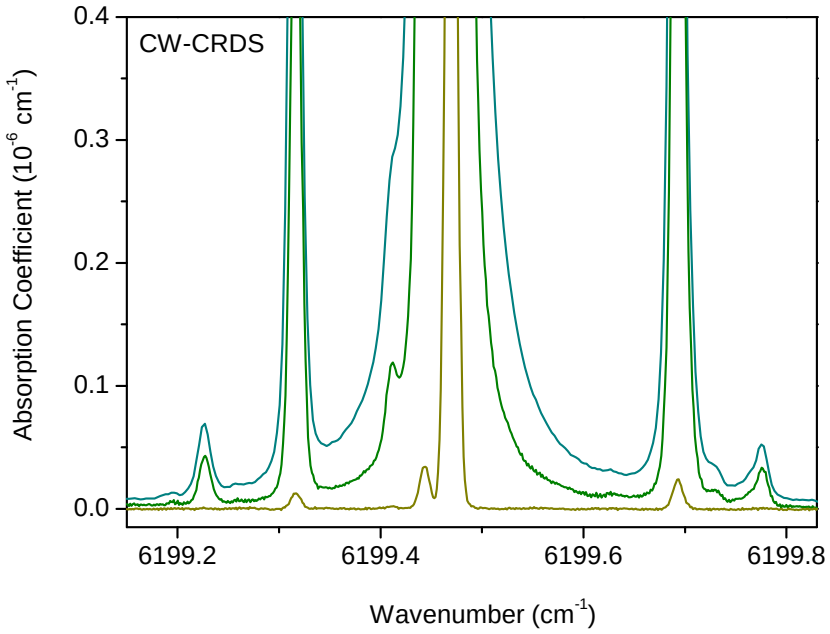

Figure 3.2. Comparison of the CW-CRDS spectra of carbon dioxide with a 99% ^{13}C enrichment recorded at 0.27, 13 and 23 hPa near 6199.5 cm^{-1}.

3.3 Rovibrational analysis

3.3.1 ^{13}C-enriched sample

The high sensitivity combined with the high dynamics led to the observation of a congested spectrum resulting from the contribution of the eight CO_2 isotopologues listed in Table 3.1. The detection of transitions due to $^{17}O^{13}C^{18}O$ and $^{16}O^{12}C^{17}O$ with relative concentration of 6.4×10^{-5} and 3.8×10^{-5}, respectively, illustrates the achieved experimental performances. The observed spectral congestion (average density of CO_2 transitions of about 9 transitions/cm^{-1}) is mainly due to hot bands, some of them having a lower-state energy as high as 2700 cm^{-1} (which corresponds to a relative concentration of 1.4×10^{-6}). The spectrum is further complicated by the presence of lines due to the impurities such as H_2O, HDO and $H_2{}^{18}O$, which were identified by comparison with Refs. [8, 46]. Fig. 3.3 illustrates the difficulty of the line assignment on a 0.6 cm^{-1} wide spectral region near 6660 cm^{-1} where lines belonging to five $^{13}CO_2$ isotopologues are observed.

Table 3.1. Relative isotopic abundance of ^{13}C-enriched sample purchased from Aldrich Chemical Company and used for CW-CRDS experiments.

Isotopologue	Abundance
$^{13}C^{16}O_2$	0.965
$^{16}O^{13}C^{18}O$	0.022(2)
$^{12}C^{16}O_2$	0.0078(4)
$^{16}O^{13}C^{17}O$	0.0041(4)
$^{16}O^{12}C^{18}O$	0.00019(3)
$^{13}C^{18}O_2$	0.00016(2)
$^{17}O^{13}C^{18}O$	0.000064(6)
$^{16}O^{12}C^{17}O$	0.000038(4)

The numbers between parentheses represent the statistical errors in the units of the last digit quoted.

Except for two bands of the $^{16}O^{13}C^{18}O$ isotopologue near 7000 cm^{-1} (see below), all the bands observed in the presently investigated region correspond to a $\Delta P = 9$ variation of the polyad quantum numbers. However, the observation of many hot bands arising from P = 1–4 lower states gives access to the upper levels belonging to the P =10–13 polyads which have a vibrational excitation up to 9347 cm^{-1}.

The assignment process was then a considerable task which could be carried out only because global effective Hamiltonians with good predictive abilities have been developed for the most of the isotopologues considered (see for instance the upper panel of Fig. 3.3 where the predictions of the EH model are displayed): $^{13}C^{16}O_2$ [15]; $^{16}O^{13}C^{18}O$ and $^{16}O^{13}C^{17}O$ (Section 3.5); $^{13}C^{18}O_2$ and $^{17}O^{13}C^{18}O$ [24].

Intensity information was also an important criterion used in the rovibrational assignment process. We used the line intensities predicted by the effective dipole moment model (see Section 1.3.3). Parameters of this model for the $\Delta P = 9$ series of transitions of $^{13}C^{16}O_2$ isotopologues were obtained by the nonlinear fit to the experimental line intensities derived from the present spectra and those available in the literature (see Section 4.2). In absence of absolute intensity measurements for $^{16}O^{13}C^{18}O$, $^{16}O^{13}C^{17}O$, $^{13}C^{18}O_2$ and $^{17}O^{13}C^{18}O$, the same set of parameters was adopted for these four minor isotopologues.

A total of 4015 lines of the $^{13}C^{16}O_2$, $^{16}O^{13}C^{18}O$ and $^{16}O^{13}C^{17}O$ isotopologues have

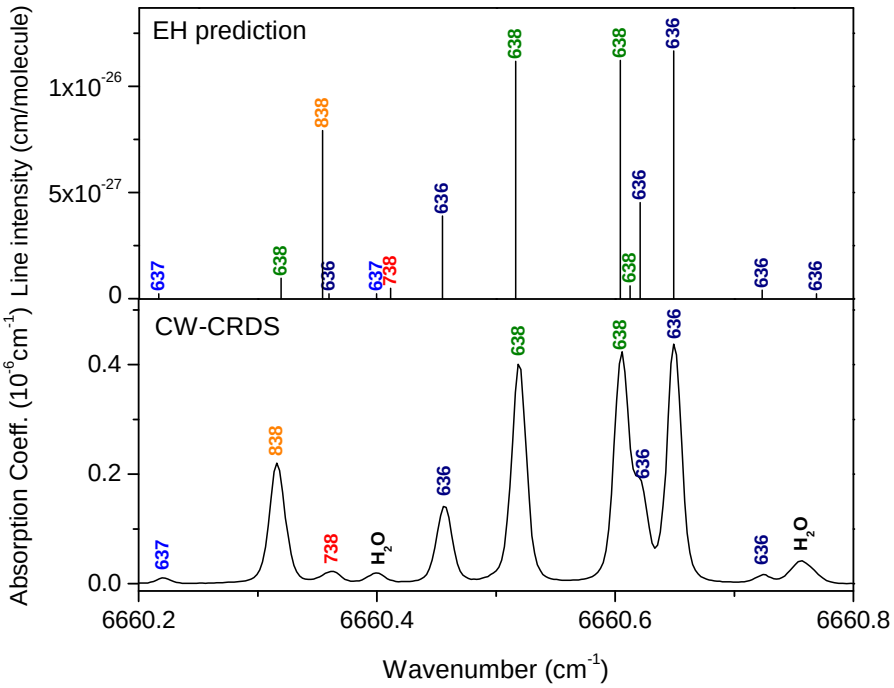

Figure 3.3. Observed and calculated spectra of carbon dioxide with a 99% ^{13}C enrichment, between 6660.2 and 6660.8 cm^{-1}. The lower panel corresponds to the CW-CRDS spectrum recorded with a sample pressure of 23 hPa. Transitions due to five ^{13}C isotopologues are marked: 636 ($^{13}C^{16}O_2$), 638 ($^{16}O^{13}C^{18}O$), 637 ($^{16}O^{13}C^{17}O$), 838 ($^{13}C^{18}O_2$) and 738 ($^{17}O^{13}C^{18}O$). The stick spectrum of the five considered isotopologues as predicted by their respective effective Hamiltonian and dipole moment models is displayed on the upper panel. Note that the line positions of $^{13}C^{18}O_2$ and $^{17}O^{13}C^{18}O$ predicted on the basis of Chédin and Teffo parameters [47] deviate significantly from their observed positions. This example illustrates the difficulty in assigning the CW-CRDS spectrum which exhibits a density of transitions in the order of 9 lines/cm^{-1}.

been assigned by Ding et al. [15] in the 6130–6750 cm^{-1} region (see the top panel of Fig. 3.4). This large amount of new experimental data allowed refining the parameters of the effective Hamiltonian model for $^{13}C^{16}O_2$ [15]. However, in the case of $^{16}O^{13}C^{18}O$ and $^{16}O^{13}C^{17}O$ minor isotopologues these new data were not sufficient for determining some important effective Hamiltonian parameters. In the present study we could significantly enlarge the set of experimental line positions (see Table 3.2) by extending and re-examining the previously investigated spectral region (6130–6750 cm^{-1}) down to 5851 cm^{-1} and up to 7045 cm^{-1} (30 new DFB laser diodes were purchased). Above 6800 cm^{-1}, observations are very scarce: only the 10031-10002 band of $^{13}C^{16}O_2$ and two

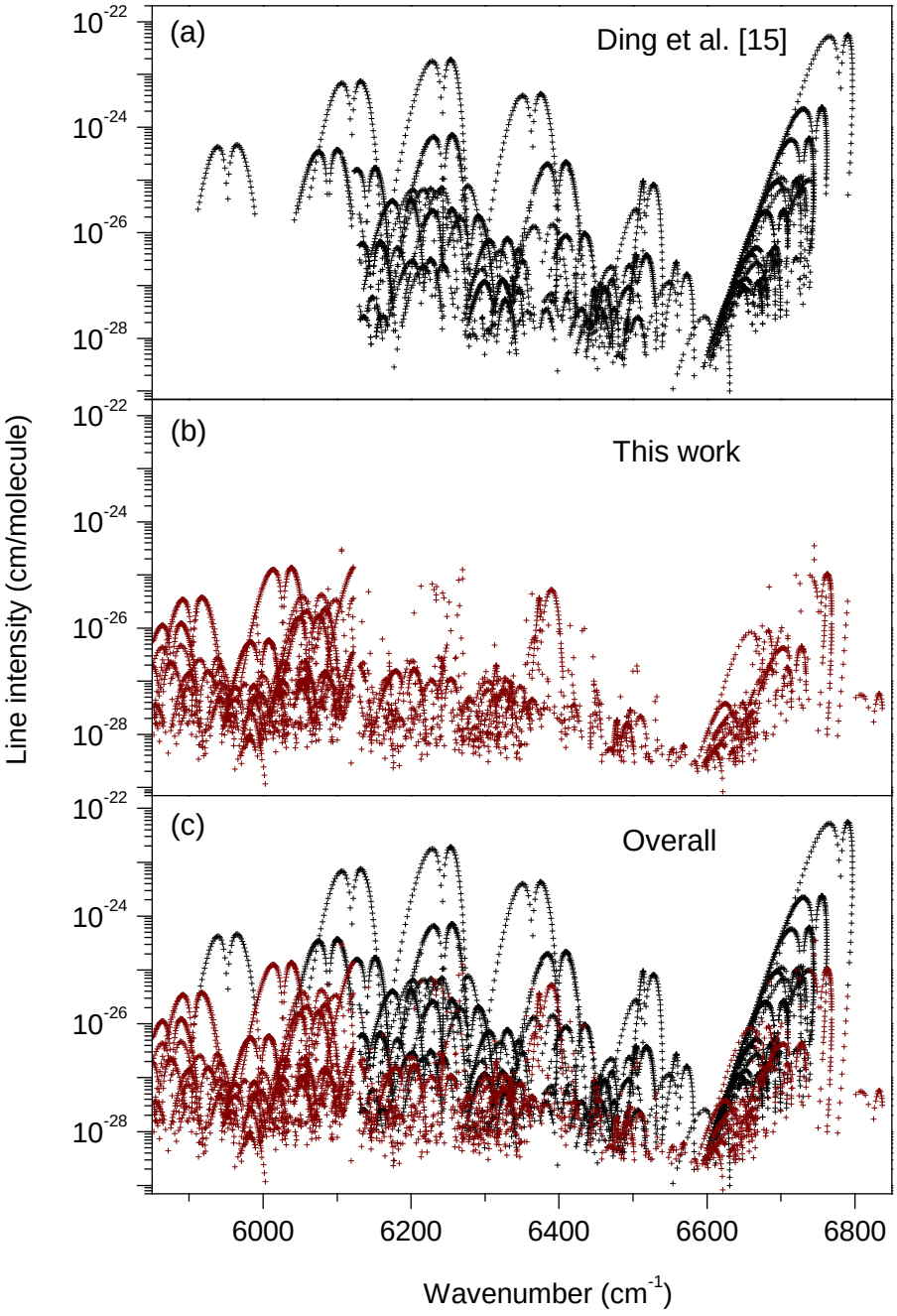

Figure 3.4. Overview of the absorption spectrum of five ^{13}C isotopologues in the 5850–6850 cm^{-1} region: (a) transitions previously assigned by Ding et al. [15] in CW-CRDS (6130–6750 cm^{-1}) and FTS spectra, (b) newly assigned transitions [41,42,48]. (c) overall of the assigned transitions as included in the experimental dataset [42]. Note the logarithmic scale adopted for the line intensities which correspond to the isotopic abundance of our sample (Table 3.1).

Table 3.2. Comparison of the number of $^{13}CO_2$ lines observed by CW-CRDS in the previous study and this work.

Isotopologue	Ding et al. [15]	This work [41, 42, 48]	
	6130–6750 cm^{-1}	6130–6750 cm^{-1}	5851–7045 cm^{-1}
$^{13}C^{16}O_2$	2609 (592)[a]	3506	4881 (866)[a]
$^{16}O^{13}C^{18}O$	1178 (112)	1535	2466 (121)
$^{16}O^{13}C^{17}O$	228 (10)	643	992 (11)
$^{13}C^{18}O_2$	0	96	170
$^{17}O^{13}C^{18}O$	0	45	130
Total	**4015 (714)**	**5825**	**8639 (998)**

[a]The number in parentheses corresponds to the number of line positions measured by FTS in Ref. [15]

$\Delta P = 10$ bands of the $^{16}O^{13}C^{18}O$ isotopologue (20023-00001 and 20022-00001) were observed. The new experimental data allowed us to perform a new global fit of *all* previously published and newly obtained experimental line positions and to refine the EH parameters (see Section 3.5) for $^{16}O^{13}C^{18}O$ and $^{16}O^{13}C^{17}O$. The new predictions based on these parameters and the automatic search program (see below) allowed us to assign an additional number of weak lines. The newly assigned transitions were continuously included as input data of the global fit, in order to further refine the EH parameters and then improve the quality of the predictions. The refined sets of EH parameters of $^{13}C^{16}O_2$, $^{16}O^{13}C^{18}O$ and $^{16}O^{13}C^{17}O$ isotopologues are those adopted in the new version of the CDSD database [11]. Fig. 3.5 illustrates the improvement achieved for $^{13}C^{16}O_2$ by comparing the $(\nu_{obs.} - \nu_{calc.})$ deviations obtained with the EH parameters values of Ref. [15] and with the newly refined ones. The RMS value of the deviations was decreased from 4.2×10^{-3} to 2.7×10^{-3} cm^{-1} in the final fit.

On the basis of this good agreement between the observed and EH predicted line positions, an automatic search program was developed and applied to the assignment of the weak lines of $^{13}C^{16}O_2$, $^{16}O^{13}C^{18}O$ and $^{16}O^{13}C^{17}O$. It consisted simply of finding predicted line positions coinciding within typically 7×10^{-3} cm^{-1} with observed line positions. In order to exclude accidental coincidences, the new assignments were carefully checked on the basis of additional criteria such as line intensities, lower state combina-

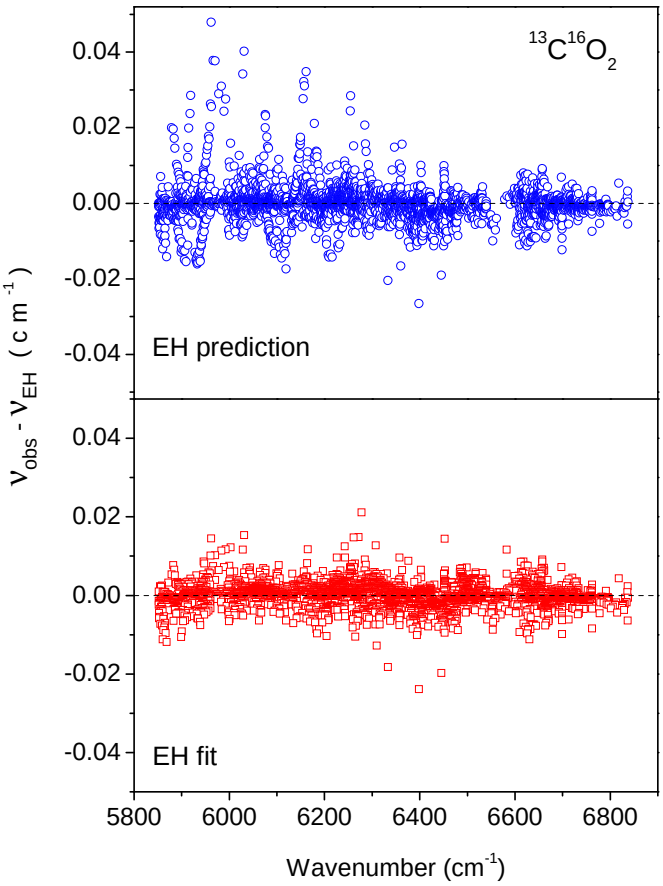

Figure 3.5. Differences between $^{13}C^{16}O_2$ measured line positions and the calculated values provided by the EH model, versus the wavenumber. *Upper panel*: the calculated line positions were obtained by using the published set of EH parameters [15]. *Lower panel*: the calculated line positions were obtained by using a new set of EH parameters obtained from a global fit including the present CW-CRDS observations as input data.

tion differences or detection of additional transitions belonging to the same progression. This automatic procedure was found to be particularly efficient to assign weak series of rotational lines whose progression could be hardly followed when many lines of the series were obscured by stronger transitions. By this way, very weak bands, high J values of previously observed bands and extra lines induced by resonance interaction could be newly assigned all over the spectral region investigated (see the middle panel of Fig. 3.4 and Table 3.2). A few assignment errors were also detected in Ref. [15] and corrected.

At the final stage of the analysis, special efforts were undertaken in order to assign the very few remaining series of unidentified lines. Among them, we successfully identified four bands of the $^{13}C^{18}O_2$ isotopologue and three bands of the $^{17}O^{13}C^{18}O$ isotopologue. Previous reports relative to the $^{17}O^{13}C^{18}O$ isotopologue are limited to the FTS analysis of the ν_2 and ν_3 bands [49]. The knowledge of the absorption spectrum of $^{13}C^{18}O_2$ has been very recently improved from FTS spectra of ^{18}O-enriched and ^{13}C-enriched CO_2 [50]. Eight bands were reported below 5000 cm^{-1}. The available line positions being very limited for both $^{13}C^{18}O_2$ and $^{17}O^{13}C^{18}O$, the spectroscopic parameters of the respective EH model have not been refined for these minor isotopologues. Their predicted spectra were obtained by using the spectroscopic parameters of the EH model as computed by Chédin and Teffo [47] and the effective dipole moment parameters of the $^{13}C^{16}O_2$ isotopologue. As the accuracy of the predicted line positions was not expected to be very good, the automatic search procedure could not be applied and the stronger bands of the $^{13}C^{18}O_2$ and $^{17}O^{13}C^{18}O$ isotopologues were identified after a careful examination of the series of lines left unassigned.

Fig. 3.6 shows the residuals between the predicted and observed line positions for the four minor isotopologues ($^{16}O^{13}C^{18}O$, $^{16}O^{13}C^{17}O$, $^{13}C^{18}O_2$ and $^{17}O^{13}C^{18}O$). A good agreement is noted between the observed and predicted line positions for the $^{16}O^{13}C^{18}O$ and $^{16}O^{13}C^{17}O$ isotopologues (RMS values of 0.007 and 0.002 cm^{-1}, respectively). In the case of the $^{13}C^{18}O_2$ and $^{17}O^{13}C^{18}O$ isotopologues, deviations increase up to 0.112 and 0.064 cm^{-1}, which is however satisfactory considering that extrapolated values of the spectroscopic parameters were used.

Table 3.2 compares to the present results, the total number of lines of the five ^{13}C isotopologues assigned in the previously studied region (6130–6750 cm^{-1}) and in the whole region investigated by CW-CRDS (5851–7045 cm^{-1}). As a result of the automatic search procedure and of the identification of the $^{13}C^{18}O_2$ and $^{17}O^{13}C^{18}O$ bands, the total number of $^{13}CO_2$ assignments was increased from 4015 to 5825 in the previously studied region. In particular, about 900 lines could be added to the 2609 transitions previously assigned for $^{13}C^{16}O_2$ [15]. At the final stage of the analysis, the proportion of unassigned transitions was decreased from about 20% to 5%. We believe that most part of these remaining unidentified transitions is due to impurities. The

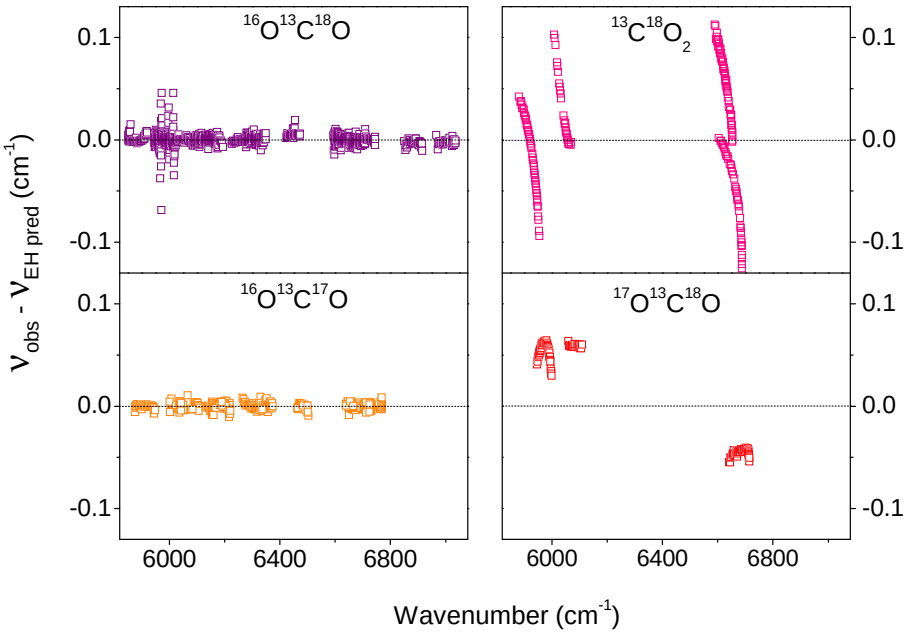

Figure 3.6. Differences between the line positions measured between 5820 and 7080 cm^{-1} and those predicted by the effective Hamiltonian model for four ^{13}C minor isotopologues. $^{13}C^{18}O_2$ and $^{17}O^{13}C^{18}O$ line positions were calculated using the computed values of the EH parameters from Ref. [47], while a new set of EH parameters obtained from a global fit including the present CW-CRDS observations were used for the $^{16}O^{13}C^{18}O$ and $^{16}O^{13}C^{17}O$, isotopologues. Several significant deviations are observed for $^{16}O^{13}C^{18}O$ near 5900 cm^{-1}; they are due to interpolyad resonance anharmonic interactions affecting the 40014-10002 and 31113-01101 bands which are not included in the EH model (see text).

overview spectrum of $^{13}CO_2$ in the full 5851–7045 cm^{-1} region is displayed in Fig. 3.4. The newly assigned transitions are shown separately in the middle panel of Fig. 3.4.

Overall, 8639 lines belonging to 150 bands[1] of $^{13}C^{16}O_2$, $^{16}O^{13}C^{18}O$, $^{16}O^{13}C^{17}O$, $^{13}C^{18}O_2$ and $^{17}O^{13}C^{18}O$ were identified. The number of bands newly detected is the following: $^{13}C^{16}O_2$: 61, $^{16}O^{13}C^{18}O$: 16, $^{16}O^{13}C^{17}O$: 8, $^{13}C^{18}O_2$: 4 and $^{17}O^{13}C^{18}O$: 3. The rotational analysis of previously observed bands was extended to higher J values. Fig. 3.7 shows the overview spectrum corresponding to the CW-CRDS observations of the five ^{13}C isotopologues with the predictions of their respective effective operators model. The intensity values of the weakest lines are in the order of 10^{-29} cm/molecule, which should be compared to an intensity cut off of 3.34×10^{-25} cm/molecule adopted

[1]This counting includes bands which were observed by only a few transitions.

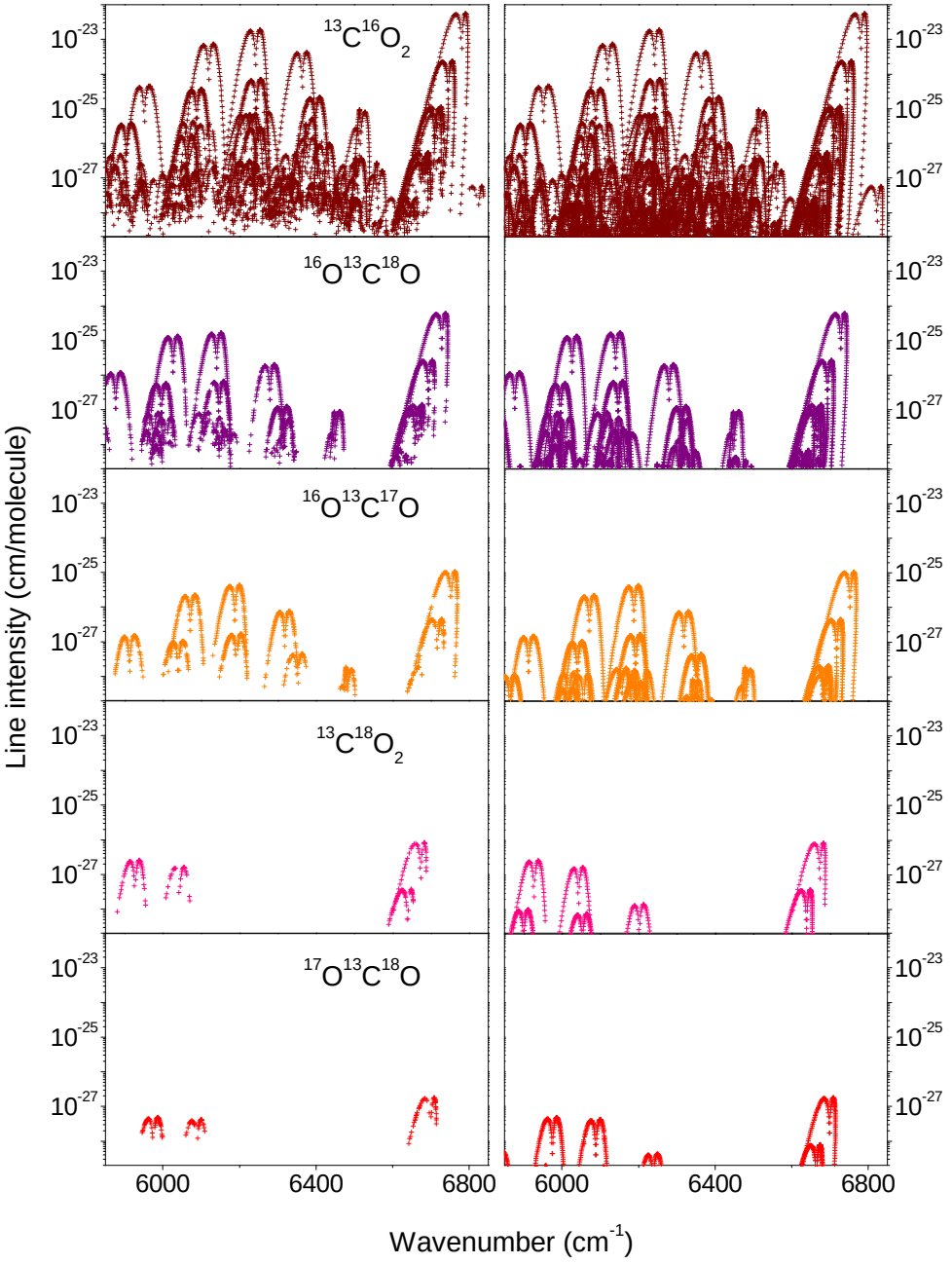

Figure 3.7. Overview comparison of the absorption spectrum of the five ^{13}C isotopologues $^{13}C^{16}O_2$, $^{16}O^{13}C^{18}O$, $^{16}O^{13}C^{17}O$, $^{13}C^{18}O_2$ and $^{17}O^{13}C^{18}O$ between 5850 and 6850 cm^{-1}. Note that the line intensities correspond to the isotopic abundance of our sample (Table 3.1). *Left hand*: observed spectra, *Right hand*: spectra predicted by the effective Hamiltonian and dipole moment models of the different isotopologues.

for pure $^{13}C^{16}O_2$ in the HITRAN database [8].

The corresponding line list has been provided as Supplementary material attached to Ref. [42]. In this line list, the line positions are experimental values (typical uncertainty in the order of 1×10^{-3} cm^{-1}), while line strengths were calculated at 296 K by using the effective operators approach. Note that the values provided for the line intensities correspond to the isotopic abundance of our sample (Table 3.1). As mentioned above, the stronger lines of Ref. [15] were measured from a FTS spectrum recorded at USTC-Hefei (about 1300 $^{13}C^{16}O_2$, $^{16}O^{13}C^{18}O$ and $^{16}O^{13}C^{17}O$ transitions between 5851 and 7045 cm^{-1}), as they were frequently saturated in the CW-CRDS spectra. A label marks the corresponding FTS line positions in the Supplementary material attached to Ref. [15]. About 1000 of these FTS wavenumbers have been transferred from Ref. [15] to the present line list, in particular in the small 6122.4–6130.1 cm^{-1} section which was not recorded by CW-CRDS.

The set of effective dipole moment parameters of the $^{13}C^{16}O_2$ isotopologue obtained in this thesis for the $\Delta P = 9$ series of transitions (see Section 4.2) was adopted for the five isotopologues. An uncertainty better than 5% is estimated for the line strengths of the $^{13}C^{16}O_2$ isotopologue, while larger uncertainties up to 20% are possible for the four other isotopologues. The line strengths of the transitions of the 20023-00001 and 20022-00001 bands of the $^{16}O^{13}C^{18}O$ isotopologue corresponding to the $\Delta P = 10$ series are not provided as the corresponding parameters of effective dipole moment are not yet available.

It is instructive to estimate the impact of the weak unobserved lines in the overall absorbance in the region. For this purpose we have calculated the integrated absorbance for $^{13}C^{16}O_2$ in the whole spectral region of the $\Delta P = 9$ series of transitions (5851–6850 cm^{-1}) as the sum of the line strengths of the observed transitions. A value of 2.547×10^{-21} cm/molecule was obtained for pure $^{13}C^{16}O_2$, while the total absorbance in the same region calculated from the effective operators approach with a line intensity cut off of 1×10^{-29} cm/molecule is 2.556×10^{-21} cm/molecule. In other words, the $^{13}C^{16}O_2$ transitions included in the attached line list represents 99.65% of the total $^{13}C^{16}O_2$ absorbance. An increase of the line intensity cut off up to 1×10^{-28} cm/molecule leaves unchanged the above value, indicating that the 0.35% missing absorbance does

not result from the contribution of very weak still undetected transitions but from lines with intermediate intensities missing in our experimental line list as they are obscured by much stronger transitions.

3.3.2 Natural abundance sample

In the spectra recorded with natural abundance sample we could observe transitions of the seven CO_2 isotopologues: $^{12}C^{16}O_2$, $^{13}C^{16}O_2$, $^{16}O^{12}C^{18}O$, $^{16}O^{12}C^{17}O$, $^{16}O^{13}C^{18}O$, $^{16}O^{13}C^{17}O$ and $^{12}C^{18}O_2$. Our results obtained with ^{13}C-enriched sample (see above) was used to identify the transitions due to the ^{13}C isotopologues and we then limit our analysis to the ^{12}C species contributing to the spectrum, namely, $^{12}C^{16}O_2$, $^{16}O^{12}C^{18}O$ and $^{16}O^{12}C^{17}O$.

The observed spectral congestion (average density of CO_2 transitions of about 9 transitions/cm^{-1}) is mainly due to hot bands, some of them having a lower state energy as high as 3000 cm^{-1} (which corresponds to a relative concentration of 5×10^{-7} at room temperature). The spectrum is further complicated by the presence of lines due to impurities such as H_2O, $H_2{}^{18}O$, HDO and CH_4 which were identified by comparison with Refs. [8, 46]. Fig. 3.8 illustrates the difficulty of the line assignment on a 1.0 cm^{-1} wide spectral region near 6876 cm^{-1} where lines belonging to four $^{12}CO_2$ isotopologues are observed. The assignment process was then a laborious task which could be carried out only with help of global effective Hamiltonian models with very good predictive capabilities (Section 1.1.5).

Except for three $\Delta P = 8$ bands of the $^{16}O^{12}C^{18}O$ isotopologue and two $\Delta P = 8$ bands of the $^{16}O^{12}C^{17}O$ isotopologue near 5900 cm^{-1}, all the bands observed in the presently investigated region correspond to a $\Delta P = 9$ variation of the polyad quantum numbers. However, the observation of many hot bands arising from $P = 1$–4 lower states gives access to upper levels belonging to the $P = 10$–13 polyads at much higher vibrational excitation. For instance the 01141-01111 hot band at 6860.44 cm^{-1} corresponds to an excitation of the 01141 state ($P = 13$) at 9864.45 cm^{-1} from the 01111 state ($P = 4$) at 3004.01 cm^{-1}.

Intensity information was also an important criterion used in the rovibrational as-

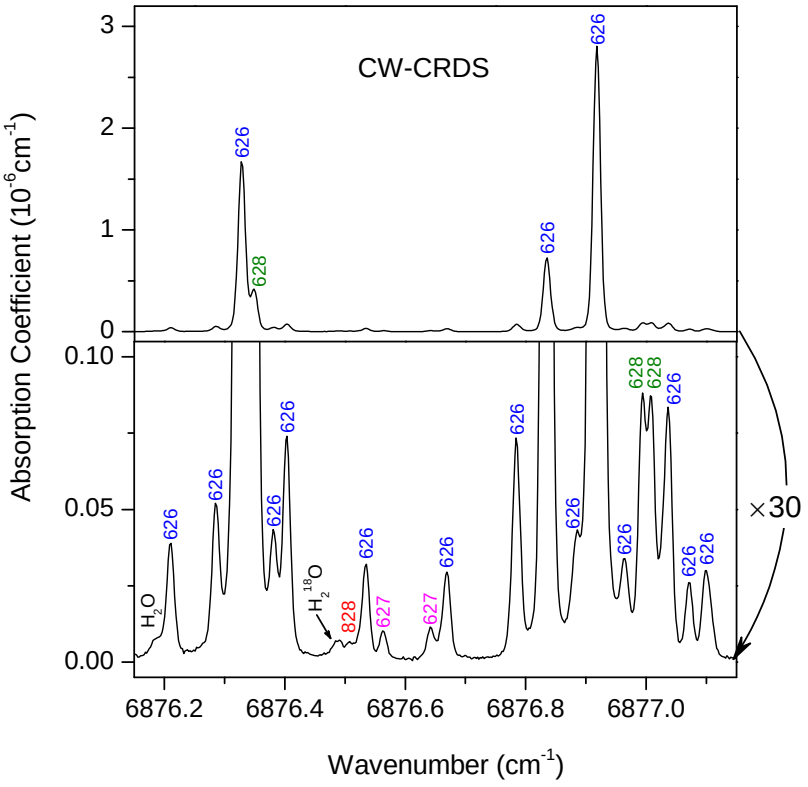

Figure 3.8. The CW-CRDS spectrum ($P = 13.3$ hPa) of natural carbon dioxide between 6876.15 and 6877.15 cm^{-1}. The lower panel corresponds to an amplification factor of 30 for the ordinate scale. The noise equivalent absorption, defined as the standard deviation in a spectral section free of absorption lines, is 2.4×10^{-10} cm^{-1}. Four ^{12}C isotopologues contribute to the observed spectrum: 626 ($^{12}C^{16}O_2$), 628 ($^{16}O^{12}C^{18}O$), 627 ($^{16}O^{12}C^{17}O$) and 828 ($^{12}C^{18}O_2$). Note that only the four most intense lines are provided by the HITRAN database [8] in this spectral region.

signment process. The line intensities were calculated by the effective dipole moment model (see Section 1.3.3).

The 4331 transitions of $^{12}C^{16}O_2$, $^{16}O^{12}C^{18}O$ and $^{16}O^{12}C^{17}O$ isotopologues assigned by Majcherova et al. [14] and the 3962 newly assigned transitions are presented separately on the overview spectrum of Fig. 3.9. The large amount of new experimental data obtained in Ref. [14] allowed refining the parameters of the EH model of $^{12}C^{16}O_2$ [14, 24–26], and significantly improving its predictive abilities. A data reproduction close to the experimental accuracy (typically 2×10^{-3} cm^{-1} in our spectral region) could be achieved for $^{12}C^{16}O_2$. Since the publication of Ref. [14], new measurements have become available in several spectral regions and the EH parameters could

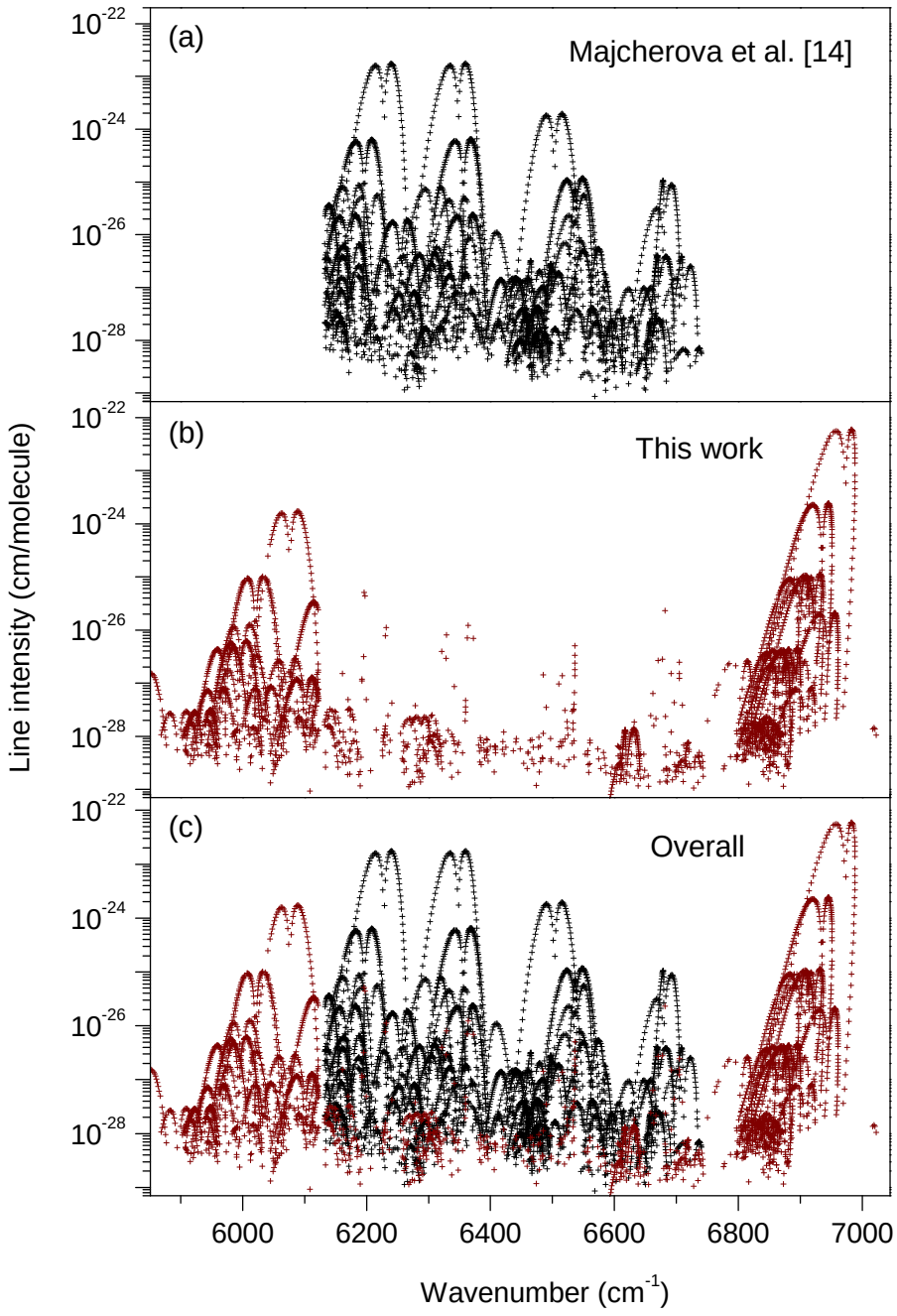

Figure 3.9. Overview of the absorption spectrum of $^{12}C^{16}O_2$, $^{16}O^{12}C^{18}O$ and $^{16}O^{12}C^{17}O$ isotopologues in the 5851–7045 cm^{-1} region: (a) Transitions assigned in the 6132–6747 cm^{-1} region by Majcherova et al. [14]; (b) Newly assigned transitions [41, 43]; (c) Overall of the CW-CRDS observations for $^{12}C^{16}O_2$. Note the logarithmic scale adopted for the line intensities. Three (two) $\Delta P = 8$ bands of the $^{16}O^{12}C^{18}O$ ($^{16}O^{12}C^{17}O$) isotopologues are not displayed near 5900 cm^{-1} because the corresponding $\Delta P = 8$ effective dipole moment parameters are not yet available.

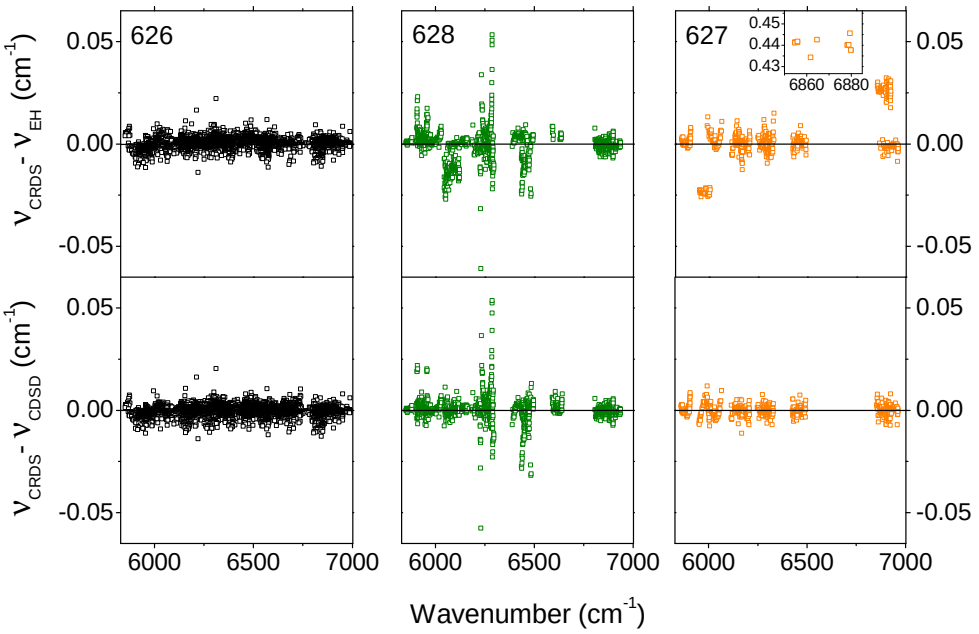

Figure 3.10. Residuals between effective Hamiltonian calculations and CW-CRDS observed values for $^{12}C^{16}O_2$ (626), $^{16}O^{12}C^{18}O$ (628) and $^{16}O^{12}C^{17}O$ (627) isotopologues. *Top panels*: Line positions calculated on the basis of the published set of effective Hamiltonian parameters: Ref. [14] for $^{12}C^{16}O_2$, Ref. [21] for $^{16}O^{12}C^{18}O$ and $^{16}O^{12}C^{17}O$. *Bottom panels*: CDSD line positions (updated version). Note that in the new CDSD database [20], the $^{16}O^{12}C^{17}O$ EH parameters were refined on the basis of the present results but not those of $^{12}C^{16}O_2$ and $^{16}O^{12}C^{18}O$ (see text). The largest deviations in the case of the $^{16}O^{12}C^{18}O$ isotopologue correspond to the 31112-01101 band perturbed by an interpolyad anharmonic resonance.

be further refined. Fig. 3.10 shows a graph of the $(\nu_{obs} - \nu_{EH})$ differences for the whole set of $^{12}C^{16}O_2$ transitions. The comparison is provided both with the line positions calculated with the parameters values of Ref. [14] and with the recently updated CDSD database [11]. The root mean square (RMS) values of the $(\nu_{obs} - \nu_{EH})$ deviations for the whole set of CW-CRDS line positions is unchanged (2.5×10^{-3} cm^{-1}) which indicates that the recent CDSD database does not bring significant improvements in our spectral region. As a better test of the quality of the predictions, we calculated for the newly assigned transitions, the RMS value of the $(\nu_{obs} - \nu_{EH})$ deviations between the experimental line positions and their values calculated with the EH parameters of Ref. [14]. The obtained value of 3.2×10^{-3} cm^{-1} illustrates the very good predictive ability of the EH model of Ref. [14]. In consequence, the future inclusion of the new

$^{12}C^{16}O_2$ observations as input data in the fit of the EH parameters is expected to have a limited impact on the parameter values.

It is interesting to understand whether the data reproduction is limited by the experimental uncertainties or by the quality of the EH model. In order to exclude possible erroneous assignments or large uncertainties due to blended lines or unresolved multiplets, we selected the set of 4258 lines which were included in the fit of the spectroscopic parameters in the band by band analysis (see below). These line positions are reproduced with an overall RMS value of 1.2×10^{-3} cm^{-1} using the standard polynomial expression of the rotational energy term value of an isolated vibrational state. This value of 1.2×10^{-3} cm^{-1} is two times smaller then the corresponding RMS value of the $(\nu_{\rm obs} - \nu_{\rm EH})$ deviations, indicating that small deficiencies in the EH model of $^{12}C^{16}O_2$ are mainly responsible of the $(\nu_{\rm obs} - \nu_{\rm EH})$ residuals.

The EH parameters of the $^{16}O^{12}C^{18}O$ isotopologue were derived in Ref. [51]: more than 6600 line positions of 72 bands could be reproduced within their experimental uncertainty. Since that date, Wang et al. [52] and Toth et al. [53] reported a number of new observations from extensive FTS studies with a long absorption path length (up to 105 m and up to 409.8 m, respectively) using ^{18}O enriched samples. The respective $^{16}O^{12}C^{18}O$ abundance was 28.4% and 46% and, in our spectral region, a total of 12 and 3 bands were reported in Refs. [52] and [53], respectively. A total of 9 $^{16}O^{12}C^{18}O$ bands were assigned by Majcherova et al. [14] in the first CW-CRDS study (6132–6747 cm^{-1}). The observation of 24 $^{16}O^{12}C^{18}O$ bands (including 15 additional bands measured in the present thesis) in the CW-CRDS spectrum of carbon dioxide in natural abundance (3.95×10^{-3}) illustrates the very high sensitivity of our setup. The $(\nu_{\rm obs} - \nu_{\rm EH})$ deviations calculated using the set of EH parameters of Ref. [51] are compared in Fig. 3.10 with the updated version of the CDSD database based on new EH parameters refined on the basis of recent measurements (in particular Refs. [14, 52, 53] and the present results). Important deviations up to 0.06 cm^{-1} are observed for both calculations and no significant improvements are noted for CDSD. We then conclude that contrary to the main isotopologue, the present CW-CRDS observations will be valuable to improve the EH modelling of $^{16}O^{12}C^{18}O$.

As for $^{13}CO_2$ spectra the automatic search program was applied to the assignment

Table 3.3. Comparison of the number of $^{12}CO_2$ lines observed by CW-CRDS in the previous study and this work.

Isotopologue	Majcherova et al. [14]	This work [41, 43]	
	6132–6747 cm^{-1}	6132–6747 cm^{-1}	5851–7045 cm^{-1}
$^{12}C^{16}O_2$	3325	3842 (253)[a]	5604 (409)[a]
$^{16}O^{12}C^{18}O$	612	734	1922
$^{16}O^{12}C^{17}O$	394	394	767
Total	**4331**	**4970**	**8293**

[a]The number between parenthesis corresponds to the number of positions of the strong lines (saturated in our CW-CRDS spectra) which were measured by FTS in Ref. [54] and transferred in our line list.

of the weak lines of $^{12}C^{16}O_2$ and $^{16}O^{12}C^{18}O$ by finding predicted line positions coinciding within typically 7×10^{-3} cm^{-1} with observed line positions. In order to exclude accidental coincidences, the newly assigned lines were carefully checked on the basis of additional criteria: line intensities, lower state combination differences or detection of additional transitions belonging to the same progression. With the help of this program and excellent EH predictions, very weak bands, high J values of previously observed bands and extra lines induced by resonance interaction could be newly assigned all over the investigated spectral region (see middle panel of Fig. 3.9 and Table 3.3).

In the case of the $^{16}O^{12}C^{17}O$ isotopologue, observations are less numerous: only 1800 line positions of 30 bands could be used in the derivation of the EH parameters [51]. Before our study, seven bands were reported from Venus spectra in our region [13]. A total of 11 bands could be detected by CW-CRDS in the 5851–7045 cm^{-1} region: 5 bands were assigned by Majcherova et al. [14] and 6 bands were measured in the present thesis [41,43]. To our knowledge, no FTS observations concerning this isotopologue have recently become available. The five bands reported in Ref. [14] revealed important deviations and led to a first (unpublished) refinement of the EH parameters. However, the situation was not yet satisfactory as our present observations deviate importantly (up to 0.44 cm^{-1}) from the EH predictions (see Fig. 3.10). This is why, in order to correct these important deviations in the updated version of the CDSD database [11], it appears necessary to include the presently reported observations as input data for

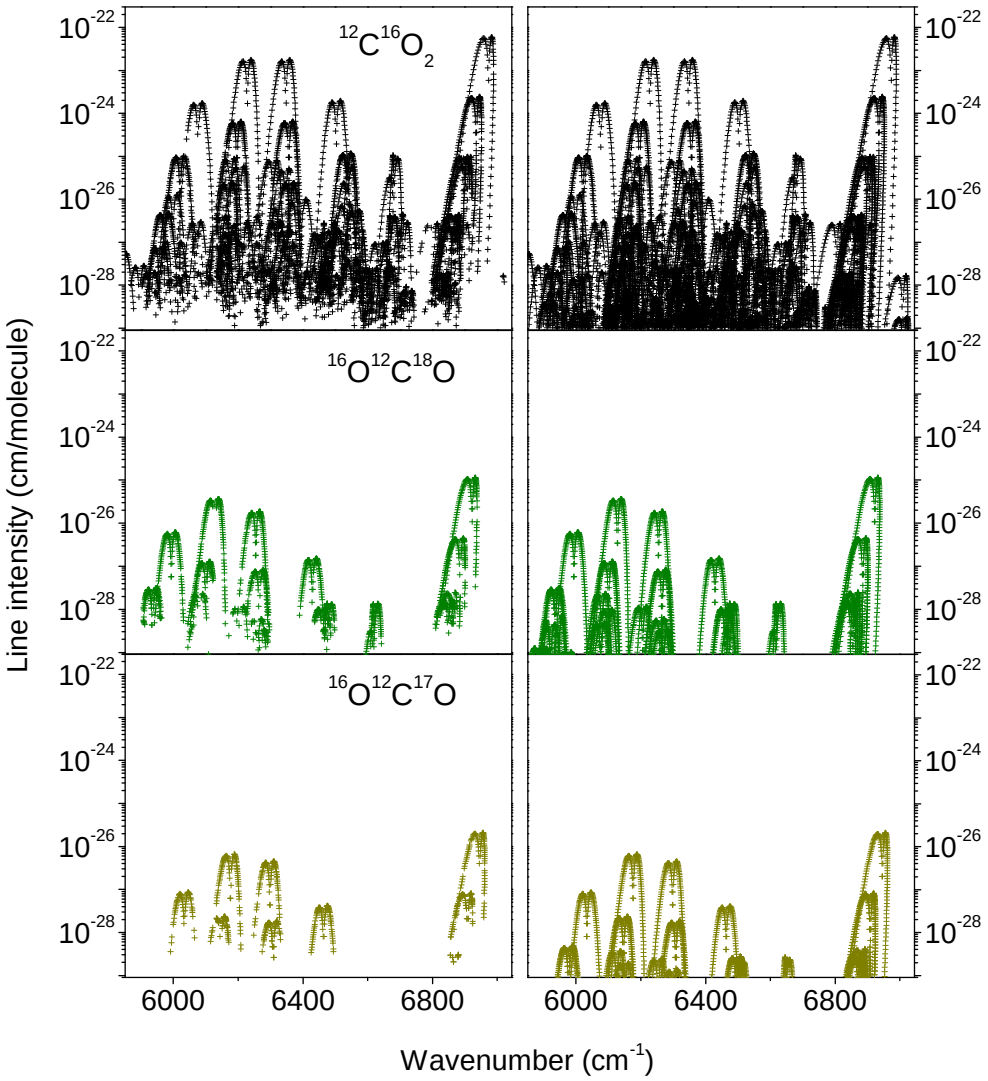

Figure 3.11. Overview comparison of the absorption spectrum of $^{12}C^{16}O_2$, $^{16}O^{12}C^{18}O$ and $^{16}O^{12}C^{17}O$ isotopologues between 5851 and 7045 cm^{-1}. *Left hand*: observed spectra; *Right hand*: spectra predicted by the effective Hamiltonian and dipole moment models. Three (two) $\Delta P = 8$ bands of the $^{16}O^{12}C^{18}O$ ($^{16}O^{12}C^{17}O$) isotopologues are not displayed near 5900 cm^{-1} because the corresponding $\Delta P = 8$ effective dipole momentum parameters are not yet available

a new refinement of the EH parameters. The new fit allowed reducing drastically the $(\nu_{obs} - \nu_{EH})$ residuals, the RMS value of the deviations (2×10^{-3} cm^{-1}) approaching the experimental uncertainty on the line position of these very weak transitions. Nevertheless, the refined set of EH parameters which has been adopted for the new version of the CDSD [11] has to be used with caution as it still suffers of a lack of experimental data in various spectral regions.

In spite of its very weak relative abundance (3.9×10^{-6}), we could detect the $3\nu_3$ (00031-00001) band of the $^{12}C^{18}O_2$ isotopologue (see Fig. 3.8). For this doubly ^{18}O substituted species, the CW-CRDS sensitivity is not sufficient to compensate the very low relative natural abundance and to provide additional information compared to the FTS results obtained with high ^{18}O enrichment [53].

Table 3.3 compares to the present results, the total number of lines of the three ^{12}C isotopologues assigned in the previously studied region (6132–6747 cm^{-1}) [14]. As a result of the extension of the recordings at low and high energies and of the additional assignments in the previously reported regions, the total number of assigned $^{12}CO_2$ transitions were increased from 4331 to 8293. In particular, 2279 lines could be added for the main $^{12}C^{16}O_2$ species, the improvement being also important for $^{16}O^{12}C^{18}O$ (1310 lines added to the 612 previously measured transitions [14]). At the final stage of the analysis, the proportion of unassigned transitions was reduced to a few percent. They are all very weak and we believe that most part of these remaining unidentified transitions is due to impurities.

Overall, 142 bands of $^{12}C^{16}O_2$, $^{16}O^{12}C^{18}O$ and $^{16}O^{12}C^{17}O$ were identified in our CW-CRDS spectra [14, 41, 43]. Compared to the contribution of Majcherova et al. [14] we add the following number of bands: $^{12}C^{16}O_2$: 54, $^{16}O^{12}C^{18}O$: 15, $^{16}O^{12}C^{17}O$: 6. Thirteen of these 75 bands were previously reported from Venus spectra [13] or from FTS laboratory spectra [13,52–54]. Their rotational analysis was extended to higher J values. Fig. 3.11 shows the overview spectrum corresponding to the CW-CRDS observations of the three ^{12}C isotopologues with the predictions of their respective effective operators' model. The intensity values of the weakest lines are on the order of 10^{-29} cm/molecule which should be compared to an intensity cut-off of 3.7×10^{-26} cm/molecule adopted for this region in the HITRAN database [8].

3.4 Band-by-band analysis

The extension of the investigated spectral region together with additional rotational assignments for most of the previously reported bands have made suitable a new fit of the spectroscopic parameters values for all the observed bands.

As far as a vibrational state can be considered as isolated, the standard expression of the vibration-rotational energy levels can be used:

$$F_v(J) = G_v + B_v J(J+1) - D_v J^2(J+1)^2 + H_v J^3(J+1)^3, \tag{3.1}$$

where G_v is the vibrational term value, B_v is the rotational constant, D_v and H_v are centrifugal distortion constants, J is the angular momentum quantum number.

Note that a different expression ($F_v(J) = B_v[J(J+1) - k^2] - D_v[J(J+1) - k^2]^2 + H_v[J(J+1) - k^2]^3$) was adopted in Ref. [15]. The new fits based on the more commonly used polynomial expression (Eq. (3.1)) will then provide a consistent set of parameters for all the bands observed in the region.

The spectroscopic parameters were fitted directly to the observed wavenumbers and, in the case of hot bands involving e and f rotational levels, the ee, ef, fe and ff sub-bands were considered independently. The lower-state rotational constants were constrained to their literature values: $^{12}C^{16}O_2$ [30,55], $^{13}C^{16}O_2$ [30,56], $^{16}O^{12}C^{18}O$ [13, 53], $^{16}O^{12}C^{17}O$ [30], $^{16}O^{13}C^{18}O$ [30], $^{16}O^{13}C^{17}O$ [30], $^{13}C^{18}O_2$ [50] and $^{17}O^{13}C^{18}O$ [49]. In the case of the 03331-03301 hot band of $^{16}O^{13}C^{18}O$, the spectroscopic parameters of the 03301 lower state were not available in the literature. They were derived from the measured wavenumbers by using the method of combination differences in which the upper-state levels were removed from the observed line positions using

$$E(J''+2) - E(J'') = R(J'') - P(J''+2), \tag{3.2}$$

which can be written as [50]

$$R(J'') - P(J''+2) = B''(Y - X) - D''(Y^2 - X^2) + H''(Y^3 - X^3), \tag{3.3}$$

where $Y = (J''+2)(J''+3)$ and $X = (J''+1)$. This method provided the rotational and first centrifugal distortion constants of the 03301 state of $^{16}O^{13}C^{18}O$: $B_v = 0.370105(14)$ and $D_v = 1.22(12) \times 10^{-7}$ cm^{-1}, but the vibrational term value G'' cannot be derived.

The retrieved rovibrational parameter values for the eight isotopologues ordered according to the band centers are listed in the Appendix (Tables 5.3–5.10). A total of 238 bands were fitted. They correspond to a total of 213 vibrational upper states as several upper states are accessed through different bands. For completeness, we have included in these tables all the observed bands even when a fit of the spectroscopic parameters was not possible as a result of too reduced input data set. The typical RMS values of the fits are in the order of 1×10^{-3} cm^{-1} in agreement with our experimental uncertainty.

The results of the band-by-band fit of the spectroscopic parameters are given as Supplementary materials attached to Refs. [42] and [43] for the five ^{13}C and three ^{12}C isotopologues, respectively. This archive files include for each band, spectroscopic parameters of the lower state fixed to the literature values, observed and calculated line positions, fitted spectroscopic parameters of the upper state, errors on the fitted parameters (in % and in cm^{-1}) and RMS value of the fit.

It is necessary to mention that 409 $^{12}C^{16}O_2$ lines were saturated in our CW-CRDS spectra and could not be used for an accurate determination of their position. We adopted for these strong lines, the FTS line positions provided in Ref. [54]. They are specifically marked in the Supplementary material attached to Ref. [43].

It is well known that a number of absorption bands of carbon dioxide are affected by Coriolis or anharmonic interactions which perturb the line positions and may induce the accidental appearance of extra lines. The perturbed line positions were excluded from the fit of the spectroscopic parameters. The interaction mechanism as identified on the basis of the EH model, is given in the last column of Tables 5.3–5.8 (Appendix) which includes the bands for which extra lines could be assigned. Four types of resonance interaction are responsible for the observed perturbations: Coriolis, Coriolis + ℓ-type, anharmonic and anharmonic + ℓ-type interaction. Table 3.4 lists the bands affected by resonance interaction together with the interaction mechanism, J values corresponding to the energy crossing (when it exists) and the maximum value of the deviation from the unperturbed line position (Eq. (3.1)). Depending on the strength of the coupling and of the relative positions of the interacting levels, the perturbation may show up in different ways varying from a smooth and hardly detectable shift of the line positions to strong

local perturbations with shifts as large as a few cm^{-1} associated to the appearance of extra lines (see for instance, Figs. 3 and 4 of Ref. [14]). A smooth perturbation does not prevent a fit of the spectroscopic parameters using Eq. (3.1) but the derived values of the parameters are effective and have bad extrapolation abilities, while in the case of a local perturbation, the perturbed line positions are simply excluded from the input dataset of the fit. It is in particular the case of the Coriolis + ℓ-type resonance interaction which affects only a few rotational levels around the nearby levels crossing. As a rule it leads to the appearance of extra lines as a result of an intensity transfer to "forbidden" transitions with $|\Delta\ell_2| > 1$.

Fig. 3.12 shows the effect of the anharmonic resonance interaction between the 20032 and 50001 states belonging to the $P = 10$ polyad. The perturbation induces a shift of the line positions up to 0.1 cm^{-1} around the energy crossing at $J = 43$. This deviation from the polynomial expression of Eq. (3.1) is fully accounted for by the EH model (see the bottom panel of Fig. 3.12). This is the case for *all* the resonance interactions which have been evidenced up to now in the spectrum of the different CO_2 isotopologues.

Nevertheless, an important result of this thesis is that interpolyad resonance interactions were evidenced in this work for the first time in the case of carbon dioxide (see Table 3.4). Four occurrences of interpolyad resonance interactions were found to affect bands of non-symmetric CO_2 isotopologues are of anharmonic type: $^{16}O^{12}C^{18}O$: 1 occurrence [43], $^{16}O^{13}C^{18}O$: 2 occurrences [42, 48], $^{16}O^{13}C^{17}O$: 1 occurrence [48]. In Section 3.5.3, we present the detailed analysis of the 31113 ($P = 10$) $\leftrightarrow$ 51106 ($P = 11$) interpolyad resonance interaction observed in CW-CRDS spectrum of $^{16}O^{13}C^{18}O$. The interpolyad resonance vibration-rotation interactions are observed in the high energy region when the energy levels of different polyads with the same angular momentum quantum number J begin to overlap. The possibility for interpolyad coupling also exists for low lying polyads in the case of very high J values but the respective lines have very low intensity and are then hardly detectable. These interpolyad perturbations are seldom in the case of the carbon dioxide molecule and induce shifts on the energy levels in the order of a few hundredths of wavenumber. They are not yet accounted for in the frame of the present EH model which is a polyad one. In consequence, a few deviations between the EH predictions and the real values of the line positions and line intensities

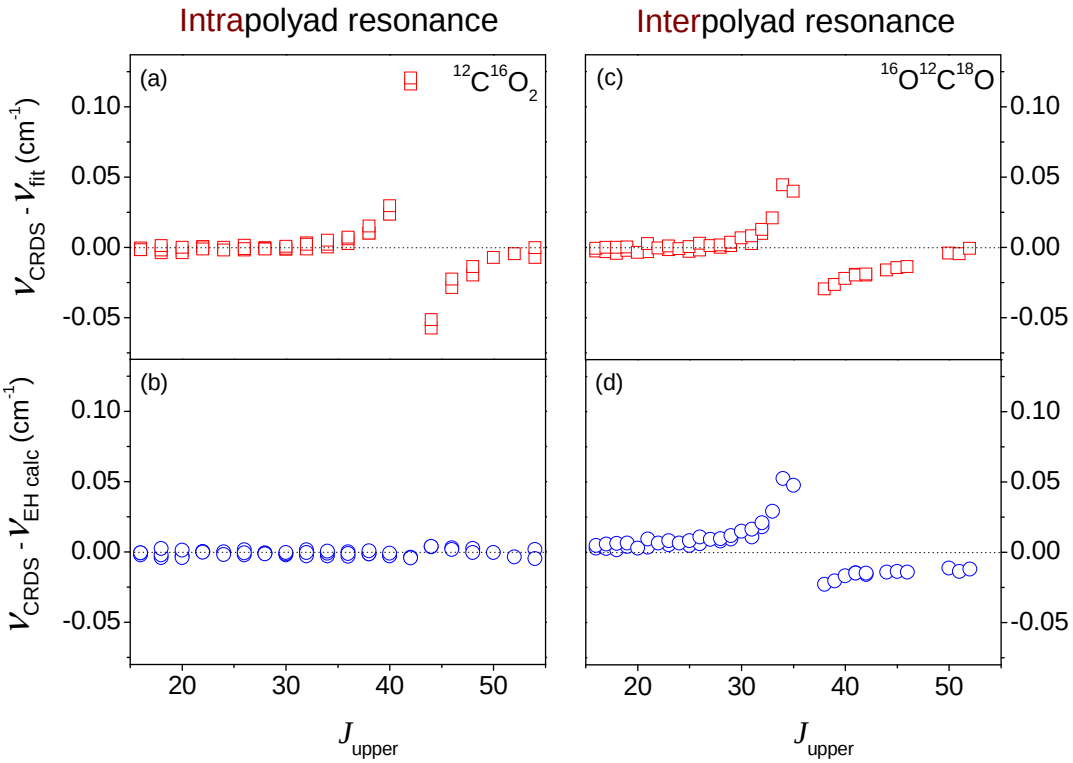

Figure 3.12. *Left hand*: Intrapolyad anharmonic resonance interaction between 20023 ($P = 10$) and 50001 ($P = 10$) vibrational states of $^{12}C^{16}O_2$ isotopologue (energy levels crossing at $J = 43$). (a) Residuals between the unperturbed line positions calculated with the fitted values of the spectroscopic parameters (see Eq. (3.1)) and the values measured by CW-CRDS, versus the J rotational quantum number for the 20023-01101 band affected by a perturbation. Perturbed lines ($36 < J < 54$) were not fitted. Note that 20023e-01101e and 20023e-01101f sub-bands were fitted independently but they are in close coincidence and then indistinguishable on the plot. (b) Differences between the effective Hamiltonian calculations [14] and the CW-CRDS values. The corresponding RMS value is 2.2×10^{-3} cm^{-1} indicating that the perturbation is fully accounted for by the EH model. *Right hand*: Interpolyad anharmonic resonance interaction between the 31112f ($P = 10$) and 51105f ($P = 11$) vibrational states (energy levels crossing at $J = 39$) of the $^{16}O^{12}C^{18}O$ isotopologue. (c) Residuals between the unperturbed line positions calculated with the fitted values of the spectroscopic parameters (see Eq. (3.1)) and the values measured by CW-CRDS, versus the J rotational quantum number. Perturbed lines ($31 < J < 53$) were not fitted. (d) Differences between the effective Hamiltonian calculations [51] and the CW-CRDS values. The deviations are mostly unchanged as interpolyad couplings are not included in the EH model.

reaching highly excited vibrational states cannot be totally ruled out (see Fig. 3.12 right hand). Note that although interpolyad interactions were observed up to now only in nonsymmetric isotopologues, they may also affect the symmetric species.

Table 3.4. Summary of the resonance interactions detected from the band-by-band analysis of the $^{12}C^{16}O_2$, $^{13}C^{16}O_2$, $^{16}O^{12}C^{18}O$, $^{16}O^{13}C^{18}O$ and $^{16}O^{13}C^{17}O$ spectra in the 5851–7045 cm^{-1} spectral region.

Interacting states	Isotopologue	J_{cross} [a]	Bands affected	N_{obs} [b]	$\lvert\nu_{obs} - \nu_{calc}\rvert_{max}$ [c]
Coriolis resonance interaction					
31114e↔50003e	$^{16}O^{12}C^{18}O$	33	31114e 01101e	56	1.446
31114e↔42203e	$^{12}C^{16}O_2$	84	31114e 01101e	62	0.115
40013e↔51102e	$^{13}C^{16}O_2$	–	40013e 10002e	56	1.863
			40013e 10001e	47	1.837
			51102e 10002e	30	–
			51102e 10001e	28	–
	$^{16}O^{13}C^{18}O$	–	40013e 10001e	62	0.003
			40013e 10002e	36	0.005
50014e↔61103e	$^{12}C^{16}O_2$	–	50014e 20002e	22	0.047
30022e↔41111e	$^{13}C^{16}O_2$	20	41111e 11101e	27	–
			30022e 00011e	14	–
			41111e 00011e	9	–
			30022e 11101e	6	–
40012e↔21123e	$^{12}C^{16}O_2$	65	40012e 10001e	54	2.136
			21123e 10001e	28	–
			40012e 10002e	47	0.025
			21123e 10002e	26	0.071
33312e↔22223e	$^{12}C^{16}O_2$	–	33312e 03301e	25	–
33312f↔22223f	$^{12}C^{16}O_2$	–	33312f 03301f	27	0.119
12222e↔23311e	$^{12}C^{16}O_2$	58	12222e 01101e	42	0.478
			12222e 01101f	24	0.293
	$^{13}C^{16}O_2$	20	12222e 01101e	27	–
			12222e 01101f	18	–
			23311e 01101e	8	–
			23311e 01101f	5	–
12222f↔23311f	$^{12}C^{16}O_2$	58	12222f 01101f	42	0.727
			12222f 01101e	22	0.078
	$^{13}C^{16}O_2$	20	12222f 01101f	28	–
			12222f 01101e	14	–
			23311f 01101f	11	–

Table 3.4. (Continued)

Interacting states	Isotopologue	J_{cross}[a]	Bands affected	N_{obs}[b]	$\lvert\nu_{\text{obs}} - \nu_{\text{calc}}\rvert_{\text{max}}$[c]
			23311f 01101e	5	–
30011e↔11122e	$^{13}C^{16}O_2$	71	30011e 00001e	79	1.645
			11122e 00001e	64	1.582
32211e↔21122e	$^{12}C^{16}O_2$	28	32211e 02201e	49	11.927
			32211e 02201f	8	–
			21122e 02201e	32	–
			21122e 10002e	35	–
	$^{13}C^{16}O_2$	41	32211e 02201e	45	4.478
			21122e 02201e	19	–
			21122e 10002e	19	–
			32211e 10002e	5	–
32211f↔21122f	$^{12}C^{16}O_2$	32	32211f 02201e	8	0.108
			32211f 02201f	53	8.949
			21122f 02201f	28	–
			21122f 10002f	20	–
	$^{13}C^{16}O_2$	48	32211f 02201f	46	2.994
			21122f 02201f	17	–
			21122f 10002e	14	–
Coriolis + ℓ-type resonance interaction ($\Delta\ell = \pm 3$)					
41102e↔14412e	$^{12}C^{16}O_2$	56	41102e 00001e	29	0.112
			14412e 00001e	1	–
40013e↔43302e	$^{12}C^{16}O_2$	67	40013e 10001e	56	0.315
			40013e 10002e	57	0.320
30012e↔33301e	$^{13}C^{16}O_2$	79	30012e 00001e	83	0.196
			33301e 00001e	1	–
	$^{16}O^{13}C^{18}O$	58	30012e 00001e	138	0.041
31112e↔34401e	$^{13}C^{16}O_2$	32	31112e 01101e	65	0.012
			34401e 01101e	6	–
			34401e 01101f	1	–
31112f↔34401f	$^{13}C^{16}O_2$	37	31112f 01101f	65	0.006
			34401f 01101f	5	–
22212e↔25501e	$^{12}C^{16}O_2$	65	22212e 00001e	50	0.059
			25501e 00001e	2	–
33311e↔60001e	$^{12}C^{16}O_2$	31	33311e 03301e	29	–
			60001e 03301e	4	–
Anharmonic resonance interaction					

Table 3.4. (Continued)

Interacting states	Isotopologue	J_{cross}[a]	Bands affected	N_{obs}[b]	$\lvert\nu_{\text{obs}} - \nu_{\text{calc}}\rvert_{\text{max}}$[c]
30022e↔60001e	$^{12}C^{16}O_2$	50	30022e 00011e	26	0.374
50001e↔20023e	$^{12}C^{16}O_2$	43	50001e 01101e	34	0.102
			20023e 01101e	46	0.116
			20023e 01101f	26	0.120
Anharmonic + ℓ-type resonance interaction ($\Delta\ell = \pm 2, \pm 4$)					
31112e↔15511e	$^{13}C^{16}O_2$	50	31112e 01101e	65	0.006
			15511e 01101e	1	–
31112f↔15511f	$^{13}C^{16}O_2$	61	31112f 01101f	65	0.013
			15511f 01101f	1	–
42201e↔20023e	$^{13}C^{16}O_2$	54	42201e 01101e	31	0.014
30012e↔14411e	$^{13}C^{16}O_2$	39	30012e 00001e	83	0.001
			14411e 00001e	8	–
Interpolyad anharmonic resonance interaction					
31112e↔51105e	$^{16}O^{12}C^{18}O$	39	31112e 01101e	54	0.092
$(P = 10)\leftrightarrow(P = 11)$					
31112f↔51105f	$^{16}O^{12}C^{18}O$	35	31112f 01101f	63	0.045
$(P = 10)\leftrightarrow(P = 11)$					
40014e↔60007e	$^{16}O^{13}C^{18}O$	38	40014e 10002e	59	0.041
$(P = 11)\leftrightarrow(P = 12)$					
31113e↔51106e	$^{16}O^{13}C^{18}O$	33	31113e 01101e	95	0.039
$(P = 10)\leftrightarrow(P = 11)$					
31113f↔51106f	$^{16}O^{13}C^{18}O$	30	31113f 01101f	54	0.070
$(P = 10)\leftrightarrow(P = 11)$	$^{16}O^{13}C^{17}O$	31	31113f 01101f	39	0.011

[a] Value of the rotational quantum number corresponding to the energy crossing of the two interacting vibrational states (when it exists).

[b] Number of observed line positions.

[c] Maximum amplitude of the perturbation of the line positions calculated as the difference between the observed line positions values and those extrapolated with the fitted spectroscopic parameters (Tables 5.4–5.8 of the Appendix).

3.5 Global fit of $^{16}O^{13}C^{18}O$ and $^{16}O^{13}C^{17}O$ line positions

3.5.1 Introduction

As demonstrated in Figs. 3.10 and 3.5, the effective Hamiltonian for three most abundant istopologues ($^{12}C^{16}O_2$, $^{13}C^{16}O_2$ and $^{16}O^{12}C^{18}O$) leads to calculated line positions in very close agreement with their observed values. But in the case of the $^{16}O^{12}C^{17}O$, $^{16}O^{13}C^{18}O$ and $^{16}O^{13}C^{17}O$ minor isotopologues, several newly observed bands exhibit large residuals between predicted and observed line positions (see Figs. 3.10 and 3.13). In the case of the 02231-02201 band of $^{16}O^{12}C^{17}O$ and 42202-011011 band of $^{16}O^{13}C^{18}O$, the residuals reach the values of 0.44 and 0.35 cm^{-1}, respectively. These large discrepancies resulted of the lack of spectroscopic information which is necessary to determine several important effective Hamiltonian parameters. Indeed, the natural abundance is only 4.4×10^{-5} and 8.2×10^{-6} for $^{16}O^{13}C^{18}O$ and $^{16}O^{13}C^{17}O$, respectively, and the corresponding bands are usually extremely weak and blended with much stronger transitions of the other isotopologues.

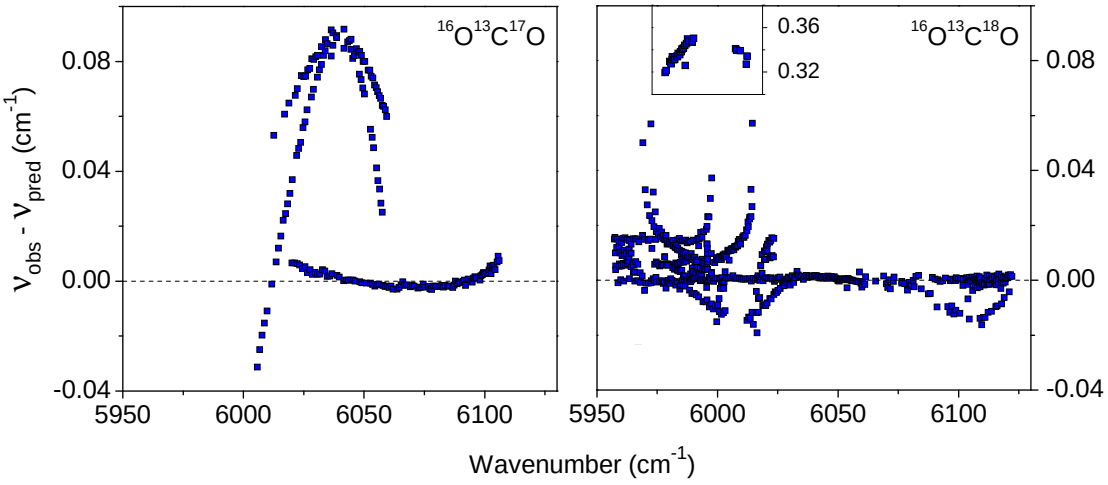

Figure 3.13. Residuals between the CW-CRDS line positions measured in the 5957–6122 cm^{-1} region and those predicted by the effective Hamiltonian models for the $^{16}O^{13}C^{18}O$ and $^{16}O^{13}C^{17}O$ isotopologues.

The experimental datasets for $^{16}O^{12}C^{17}O$, $^{16}O^{13}C^{18}O$ and $^{16}O^{13}C^{17}O$ istopologues were significantly extended in the present thesis (see Tables 3.2 and 3.3). It allowed us to refine the EH parameters for these isotopologues. In this thesis we present the global

fits for $^{16}O^{13}C^{18}O$ and $^{16}O^{13}C^{17}O$ which include *all* the line positions available from the literature and the newly observed transitions.

Note that the EH parameters $^{16}O^{13}C^{17}O$ still suffer of a lack of experimental data and should be used with caution. In the case of $^{12}C^{16}O_2$, $^{13}C^{16}O_2$ and $^{16}O^{12}C^{18}O$ isotoplogues the EH parameters were also slightly refined in order to provide the improved predictions for new version of CDSD database [11].

3.5.2 Least-squares fittings

The least-squares fittings of the effective Hamiltonian parameters to the observed line positions have been performed using the GIP computer code [26, 29] which minimizes the dimensionless weighted standard deviation defined as:

$$\chi = \sqrt{\frac{\sum_{i=1}^{N} \left(\frac{\nu_i^{\text{obs}} - \nu_i^{\text{calc}}}{\delta_i} \right)^2}{N - n}}, \tag{3.4}$$

where, ν_i^{obs} and ν_i^{calc} are the observed and calculated wavenumbers, N is the number of fitted transitions, n is the number of adjusted parameters and δ_i is the experimental uncertainty of the i-th wavenumber. Before fittings, the consistency of all collected data was checked using the Ritz principle (see for example, Ref. [57]). When necessary the calibration factors were used to correct the observed line positions.

To characterize the quality of the fit, we use together with the weighted standard deviation the root mean squares of the residuals defined as

$$\text{RMS} = \sqrt{\frac{\sum_{i=1}^{N} \left(\nu_i^{\text{obs}} - \nu_i^{\text{calc}} \right)^2}{N}}. \tag{3.5}$$

3.5.3 $^{16}O^{13}C^{18}O$

The effective Hamiltonian parameters for $^{16}O^{13}C^{18}O$ were previously refined on the basis of the observations obtained by Fourier Transform Spectroscopy [57]. However, the observed line positions used as input data were not sufficient to determine all important effective Hamiltonian parameters. As illustrated in Fig. 3.7, the input dataset of experimental positions available in the literature [13,56–68,68–70] has been considerably extended by CW-CRDS studies (Ding et al. [15] and the present study [41,42,48]).

Table 3.5. Spectrum-by-spectrum analysis of the experimental data and statistics of the line positions fit for $^{16}O^{13}C^{18}O$.

Reference	Calibration factor	Precision (10^{-3} cm^{-1})	N_{fit} [a]	RMS (10^{-3} cm^{-1})
This work	1.000000000	2.0	564	2.21
Bradley et al. [58]	1.000000000	0.001	74	0.0016
Toth [59]	1.000000000	0.10	46	0.27
Miller et al. [56]	1.000000000	0.10[b]	370	0.25
Jolma et al. [60]	1.000000000	0.30[b]	331	0.24
Malathy Devi et al. [61]	1.000000071	0.50[c]	19	1.37
Rinsland et al. [62]	1.000000068	0.50[c]	14	0.70
Bailly et al. [63]	0.999999935	0.50[b]	752	0.45
Esplin et al. [64]	1.000000000	0.50	885	1.00
Esplin et al. [65–67]	0.999999897	0.50	578	1.16
Esplin et al. [65–67][d]	0.999999897	2.00	155	2.29
Ding et al. [57]	0.999999983	1.00	1130	1.05
Mandin [13]	0.999999381	2.00[c]	125	2.44
Ding et al. [15]	1.000000000	2.00	1183	2.59
Baldacci et al. [68]	0.999999829	3.00	40	1.13
Baldacci et al. [69]	1.000000091	5.00	31	2.20
Ding et al. [70]	1.000000399	5.00	114	4.06

[a] N_{fit} is the number of lines included in the fit.
[b] Our average estimated value.
[c] Experimental precision is set to a guessed value.
[d] 02211-02201 band.

The characteristics of the input data are presented in Table 3.5. Using 6411 observed line positions, 61 parameters of the effective Hamiltonian could be fitted. A weighted standard deviation $\chi = 1.77$ and a global RMS = 0.0017 cm^{-1} have been achieved in the result of the fitting. The RMS for each experimental source is presented in Table 3.5 and the obtained set of effective Hamiltonian parameters is given in Table 3.7.

To reach the above presented results, we had to exclude from the fit the line positions of the 31113-01101 hot band with J_{up} lying between 22 and 48. Before this, we attempted but failed in fitting this band within the framework of the polyad model of effective Hamiltonian: the behaviour of the residuals presented in Fig. 3.14 remained mostly unchanged. After a careful analysis, we found that the 31113 vibrational state belonging to the $P = 10$ polyad is perturbed by the 51106 vibrational state belonging to the $P = 11$ polyad. The interaction mechanism is an anharmonic resonance via the

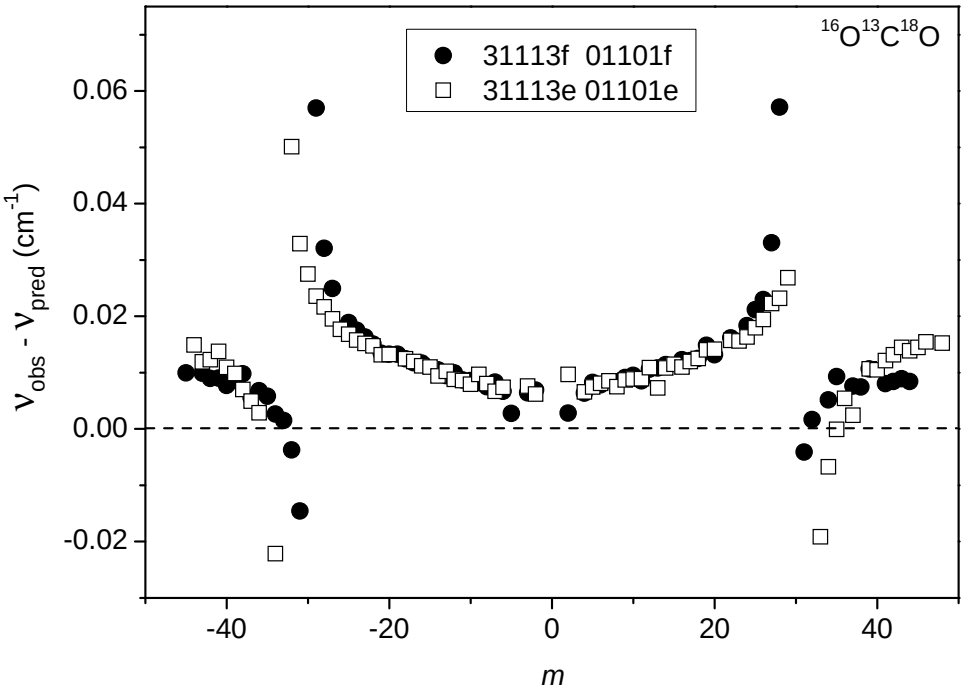

Figure 3.14. Residuals between the measured wavenumbers of the 31113-01101 band of the $^{16}O^{13}C^{18}O$ isotopologue and their values predicted by the effective Hamiltonian model [57]. The observed perturbation is due to the anharmonic interpolyad interaction between 31113 ($P = 10$) and 42202 ($P = 11$) states which is not taken into account by the EH model.

$\langle v_1\ v_2\ \ell_2\ v_3\ J|H^{\text{eff}}|v_1 - 2\ v_2\ \ell_2\ v_3 + 1\ J\rangle$ matrix element of the effective Hamiltonian. The reduced energy plot of the calculated rotational levels of the two interacting states is presented in Fig. 3.15. The energy values used for this plot are unperturbed values calculated using the set of effective Hamiltonian parameters presented in Table 3.7. An energy crossing is predicted for J values around 30 and 33 for the f and e component, respectively, in good qualitative agreement with the observation.

We have re-examined the spectra in the interacting region and improved our previous analysis presented in Ref. [41]: we could unambiguously newly assign twelve extra lines resulting from an intensity transfer from the 31113-01101 band to the 51106-01101 band. The line positions of these extra lines are included in the Supplementary Materials attached to Refs. [48] and [42].

In the case of a dark state interacting with a bright state, the detection of extra lines allows for a quantitative determination of the coupling matrix element, W, and of

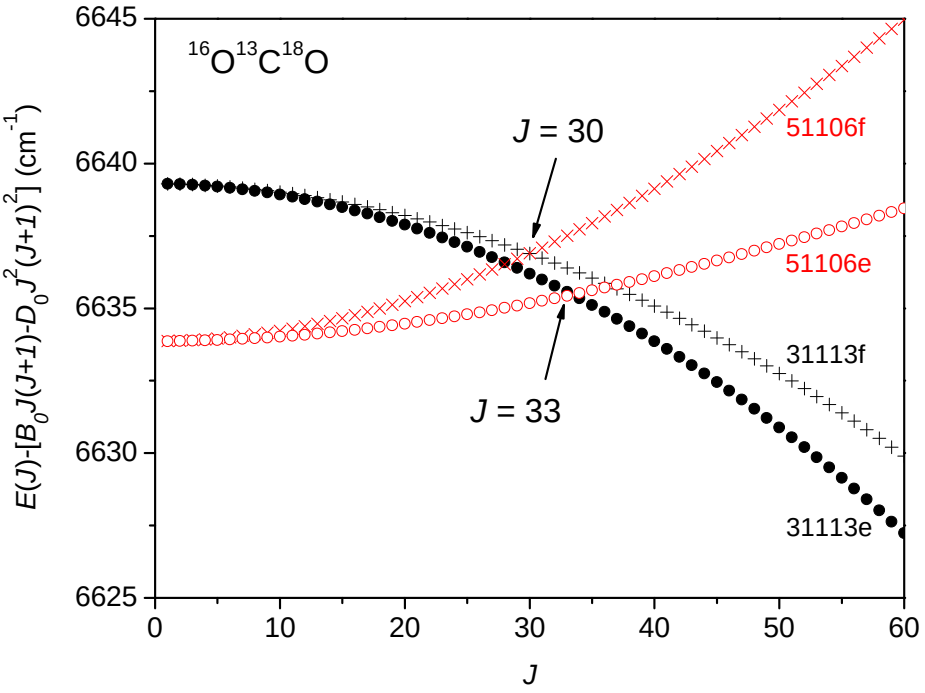

Figure 3.15. Reduced energy plot for the 31113 ($P = 10$) and 51106 ($P = 11$) vibrational states of $^{16}O^{13}C^{18}O$, coupled by an anharmonic interpolyad interaction. The differences between the (unperturbed) energy values calculated with the effective Hamiltonian parameters of Table 3.7 and $B_0J(J+1) - D_0J^2(J+1)^2$ are plotted versus J (B_0 and D_0 are the rotational constants of the ground vibrational state). An energy crossing at $J = 30$ and $J = 33$ is observed for the f and e component, respectively.

the unperturbed energy levels by using the observed line positions and the measured relative intensity of the interacting doublets. The respective procedure is standard and can be found in Ref. [71] for instance. An accurate value of the relative line intensity could be measured for the components of four e doublets and four f doublets listed in Table 3.6, leading to eight independent determinations of W. The excellent agreement obtained between these different values (average value of $W = 0.104$ cm^{-1} and standard deviation of 0.008 cm^{-1}) confirms the anharmonic character of the studied interaction. Note that the obtained unperturbed values of the energy levels of the 51106 dark state, included in Table 3.6, shows a constant shift on the order of 0.43 cm^{-1} compared to the predictions of the effective Hamiltonian model.

The value of the coupling matrix element, W, can also be obtained from a global fit of the observed line positions of the transitions around the energy crossing ($J > 22$) if

Table 3.6. Analysis of the 31113($P = 10$)↔51106($P = 11$) interpolyad interaction.

Interacting doublet	Wavenuber (cm^{-1})		Relative intensity	W (cm^{-1})	Obs. − Calc. (cm^{-1})[a]	
	31113	51106			31113	51106
P(32)e	5969.0805	5968.7538	15.00	0.090	0.0113	0.4176
P(33)e	5968.1357	5968.0947	1.45	0.109	0.0159	0.4109
P(34)e	5967.1524	5967.4724	13.00	0.096	–0.0115	0.4389
R(31)e	6015.9923	6015.9961	1.03	0.112	–0.0066	0.4332
P(28)f	5973.3318	5972.7809	28.13	0.108	–0.0031	0.4394
P(30)f	5971.5588	5971.6705	2.65	0.110	–0.0047	0.4415
R(27)f	6014.5112	6014.2741	6.90	0.106	0.0018	0.4341
R(28)f	6015.0763	6015.2159	3.58	0.102	–0.0189	0.4552
Average value				0.104(8)	–0.002(11)	0.434(14)

[a](Obs.−Calc.) is the difference between the energy value of the unperturbed energy level as obtained from the measured line positions and relative intensity (see Ref. [71]), and the value predicted by the polyad model of effective Hamiltonian.

the unperturbed values of the interacting levels are known (see Ref. [71]). We assumed that the unperturbed energy of the 31113 bright state and of the 51106 dark state are accurately predicted by the polyad model except for a constant shift, δ, for the 51106 state. The parameters W and δ were then fitted simultaneously to the line positions of the e and f sub bands (including extra lines) with J values larger than 22. The obtained values of $W = 0.1119(6)$ cm^{-1} and $\delta = 0.4338(7)$ cm^{-1} are in excellent agreement with the above determination and allow for a reproduction of the 86 lines of the input data set with an RMS value of 3.5×10^{-3} cm^{-1}.

Table 3.7. The effective Hamiltonian parameters for $^{16}O^{13}C^{18}O$.

N	Parameter	Value (cm^{-1})	Order	N	Parameter	Value (cm^{-1})	Order
Diagonal vibrational parameters							
1	ω_1	1314.48192(130)[a]		14	y_{122}	–0.690(92)	10^{-2}
2	ω_2	648.45371(83)		15	y_{123}	7.91(12)	10^{-2}
3	ω_3	2309.76023(91)		16	y_{133}	2.04(10)	10^{-2}
4	x_{11}	–2.75201(28)		17	y_{222}	–0.7052(58)	10^{-2}
5	x_{12}	–4.89244(76)		18	y_{223}	–1.699(19)	10^{-2}
6	x_{13}	–17.8657(23)		19	y_{233}	1.0933(41)	10^{-2}
7	x_{22}	1.48836(17)		20	y_{333}	0.1597(92)	10^{-2}
8	x_{23}	–11.62726(35)		21	$y_{1\ell\ell}{}^*$	1.034(72)	10^{-2}

Table 3.7. (Continued)

N	Parameter	Value (cm^{-1})	Order	N	Parameter	Value (cm^{-1})	Order
9	x_{33}	–11.64105(50)		22	$y_{2\ell\ell}$*	0.6683(72)	10^{-2}
10	$x_{\ell\ell}$*	–0.9397529272		23	$y_{3\ell\ell}$*	2.318(19)	10^{-2}
11	y_{111}**	0.0	10^{-2}	24	z_{1113}	8.1(11)	10^{-4}
12	y_{112}	0.44(14)	10^{-2}	25	z_{1333}	24.9(18)	10^{-4}
13	y_{113}	–8.650(67)	10^{-2}	26	z_{3333}	2.295(12)	10^{-4}
	Diagonal rotational and vibrational-rotational parameters						
27	B_e	0.36947691(13)		36	γ_{33}	0.1351(24)	10^{-5}
28	α_1	1.09543(46)	10^{-3}	37	$\gamma_{\ell\ell}$**	0.0	10^{-5}
29	α_2	–0.66681(16)	10^{-3}	38	ε_{123}	–4.12(23)	10^{-6}
30	α_3	2.81189(17)	10^{-3}	39	ε_{223}	0.116(29)	10^{-6}
31	γ_{11}	–0.1210(91)	10^{-5}	40	D_e	0.116819(13)	10^{-6}
32	γ_{12}**	0.0	10^{-5}	41	β_1**	0.0	10^{-9}
33	γ_{13}	–2.441(89)	10^{-5}	42	β_2	1.9849(37)	10^{-9}
34	γ_{22}	–0.3827(26)	10^{-5}	43	β_3	–0.3002(73)	10^{-9}
35	γ_{23}	0.538(42)	10^{-5}	44	H_e*	0.7504935530	10^{-14}
	Parameters of ℓ-doubling matrix elements						
45	L_e	–0.14187(16)	10^{-3}	48	L_3	–2.76(17)	10^{-6}
46	L_1	2.97(38)	10^{-6}	49	L_{13}	–0.139(22)	10^{-6}
47	L_2**	0.0	10^{-6}	50	L_J	0.1733(36)	10^{-9}
	Parameters of Fermi-interaction matrix elements						
51	F_e	–25.20905(43)		57	F_J	0.108599(18)	10^{-3}
52	F_1	0.23541(48)		58	F_e^L	–0.9176(30)	10^{-5}
53	F_2	0.28864(14)		59	F_e^{IV}	0.01017(20)	
54	F_3	0.11935(23)		60	F_e^{III}	–0.6829(94)	
55	F_{11}	–0.3560(74)	10^{-2}	61	F_e^4	0.2515(37)	
56	F_{13}	1.569(25)	10^{-2}				
	Parameters of Coriolis-interaction matrix elements						
62	C_e	–0.4703(56)	10^{-1}	66	C_J	0.1448(47)	10^{-6}
63	C_1	–0.303(35)	10^{-3}	67	C_{e1}	–0.1206(64)	10^{-2}
64	C_2	0.841(23)	10^{-3}	68	C_{e2}	0.6213(56)	10^{-2}
65	C_3	–0.127(19)	10^{-3}				

[a] Uncertainties in parentheses represent one standard deviation in units of the last quoted digit.

*Fixed to the value given by Chédin [24].

**Fixed to zero.

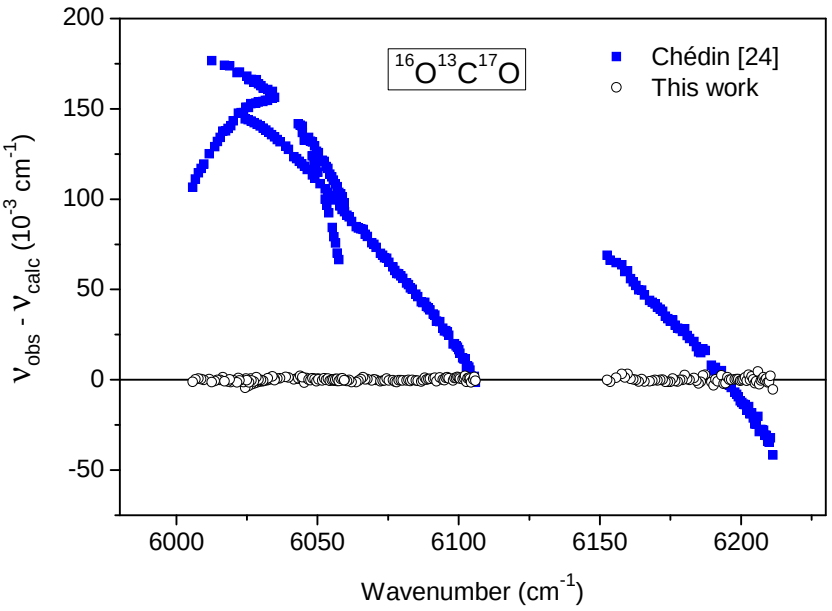

Figure 3.16. Residuals between the observed and calculated line positions for the 30012-00001, 30013-00001 and 31113-01101 bands of $^{16}O^{13}C^{17}O$. The calculations were performed with Chédins' parameters [24] and with the parameters presented in Table 3.9.

3.5.4 $^{16}O^{13}C^{17}O$

A first set of the effective Hamiltonian parameters for this isotopologue was published by Chédin [24] in 1979. His parameters allow for the prediction of the $^{16}O^{13}C^{17}O$ line positions of the highly excited states with accuracy on the level of several tenth of wavenumber [15, 41]. In order to refine this set of effective Hamiltonian parameters, we have gathered the newly assigned transitions and *all* the line positions available from the literature [13, 15, 49, 60, 68, 72]. It resulted in a set of 1151 line positions belonging to eleven bands. The characteristics of these data are presented in Table 3.8. The calibration factors were derived from the term value analysis performed simultaneously for all isotopologues of carbon dioxide (see Ref. [57] for details). Using the collected data, 32 parameters could be refined leading to a weighted standard deviation $\chi = 0.97$ and a global RMS = 0.0013 cm^{-1}. The RMS for each experimental source is presented in Table 3.8 and the parameter values are listed in Table 3.9. It is worth mentioning that many parameters values were constrained to the values obtained by Chédin from the carbon dioxide potential energy surface fitted to the experimental values of

Table 3.8. Spectrum-by-spectrum analysis of the experimental data and statistics of the line positions fit for $^{16}O^{13}C^{17}O$.

Reference	Calibration factor	Precision (10^{-3} cm^{-1})	N_{fit} [a]	RMS (10^{-3} cm^{-1})
This work	1.000000000	2.0	331	1.11
Teffo et al. [49]	1.000000000	0.1	100	0.08
Jolma [60]	1.000000000	0.3[b]	63	0.33
Esplin [72]	0.999999897	1.0[b]	95	1.41
Ding et al. [15]	0.999999983	1.0	461	1.01
Mandin [13]	0.999999381	2.0[c]	42	2.79
Baldacci et al. [68]	0.999999829	3.0	59	3.35

[a] N_{fit} is the number of lines included in the fit.
[b] Our estimated value.
[c] Experimental precision is set to a guessed value.

the G_v, B_v, D_v and H_v spectroscopic constants.Fig. 3.16 illustrates the improvement achieved for the residuals between the observed and calculated line positions for the 30012-00001, 30013-00001 and 31113-01101 bands, compared to the predictions calculated with Chédin's set of parameters [24].

Table 3.9. The effective Hamiltonian parameters for $^{16}O^{13}C^{17}O$.

N	Parameter	Value (cm^{-1})	Order	N	Parameter	Value (cm^{-1})	Order
Diagonal vibrational parameters							
1	ω_1*	1333.322755		13	y_{113}	–29.2(21)	10^{-2}
2	ω_2	651.0747(64)[a]		14	y_{122}	–11.66(38)	10^{-2}
3	ω_3	2318.6771(570)		15	y_{123}	23.6(15)	10^{-2}
4	x_{11}*	–2.909060363		16	y_{133}*	5.89914396	10^{-2}
5	x_{12}*	–4.972003716		17	y_{222}	–2.785(93)	10^{-2}
6	x_{13}*	–18.35226056		18	y_{223}*	–1.936452460	10^{-2}
7	x_{22}*	1.522526926		19	y_{233}*	1.657338070	10^{-2}
8	x_{23}	–11.7956(94)		20	y_{333}	0.753(50)	10^{-2}
9	x_{33}	–11.880(25)		21	$y_{1\ell\ell}$*	5.575493783	10^{-2}
10	$x_{\ell\ell}$*	–0.9482463889		22	$y_{2\ell\ell}$*	0.6303098050	10^{-2}
11	y_{111}	7.9(11)	10^{-2}	23	$y_{3\ell\ell}$*	2.354415718	10^{-2}
12	y_{112}	39.4(15)	10^{-2}				10^{-2}
Diagonal rotational and vibrational-rotational parameters							
24	B_e	0.37998559(56)		32	γ_{23}*	0.9356486770	10^{-5}

Table 3.9. (Continued)

N	Parameter	Value (cm^{-1})	Order	N	Parameter	Value (cm^{-1})	Order
25	α_1	1.17548(70)	10^{-3}	33	$\gamma_{33}{}^*$	0.8001391510	10^{-5}
26	α_2	–0.68489(12)	10^{-3}	34	$\gamma_{\ell\ell}{}^*$	0.5350754176	10^{-5}
27	α_3	2.92556(28)	10^{-3}	35	D_e	0.12198(20)	10^{-6}
28	$\gamma_{11}{}^*$	–0.1546505700	10^{-5}	36	β_1	1.38(26)	10^{-9}
29	$\gamma_{12}{}^*$	1.091753350	10^{-5}	37	β_2	2.463(92)	10^{-9}
30	$\gamma_{13}{}^*$	1.366886410	10^{-5}	38	β_3	0.49(12)	10^{-9}
31	$\gamma_{22}{}^*$	–0.9058067920	10^{-5}	39	$H_e{}^*$	0.8180322330	10^{-14}
		Parameters of ℓ-doubling matrix elements					
40	L_e	–0.146892(79)	10^{-3}	43	L_3	–1.132(59)	10^{-6}
41	L_1	–3.10(13)	10^{-6}	44	L_J	0.267(40)	10^{-9}
42	$L_2{}^*$	–0.4002802140	10^{-6}				
		Parameters of Fermi-interaction matrix elements					
45	F_e	–25.318(12)		50	F_J	0.10399(30)	10^{-3}
46	F_1	0.2426(36)		51	$F_e^{\mathrm{IV}*}$	0.01828874840	
47	F_2	0.2487(23)		52	F_e^{III}	3.88(29)	
48	$F_3{}^*$	0.1456853150		53	F_J^{III}	–0.914(63)	10^{-4}
		Parameters of Coriolis-interaction matrix elements					
54	C_e	–0.4325(27)	10^{-1}	57	$C_2{}^*$	0.4815252030	10^{-3}
55	$C_\ell{}^*$	0.4979475956	10^{-3}	58	$C_3{}^*$	0.1116505590	10^{-3}
56	C_1	2.869(88)	10^{-3}	59	C_J	–0.59(10)	10^{-6}

[a] Uncertainties in parentheses represent one standard deviation in units of the last quoted digit.
* Fixed to the value given by Chédin [24].

Chapter 4

Line intensities

La deuxième partie du travail de la thèse, qui fait l'objet de ce chapitre, décrit les mesures d'intensités absolues effectuées pour les raies de $^{13}C^{16}O_2$ et $^{12}C^{16}O_2$, observées vers 1.6 μm par spectroscopie CW-CRDS. Les intensités de 2039 et 952 raies ont été mesurées pour $^{13}C^{16}O_2$ et $^{12}C^{16}O_2$. Ces données expérimentales ont ensuite été utilisé, combinées à des données publiées dans la littérature ou obtenues à l'Université Libre de Bruxelles par spectroscopie à transformée de Fourier pour $^{13}C^{16}O_2$, pour améliorer les paramètres du moment dipolaire effectif de ces deux isotopologues.

4.1 Introduction

The present Chapter is devoted to the measurements and global modelings of line intensities in the $\Delta P = 9$ series of transitions of $^{12}C^{16}O_2$ and $^{13}C^{16}O_2$ isotopologues. The line intensities have been retrieved from CW-CRDS spectra in the 1.6 μm region in order to increase the experimental data set available for the refinement of the effective dipole moment parameters (see Section 1.3.3). Indeed, because of the high linearity and the large dynamics of the CW-CRDS spectra with respect to the line intensities, this technique is particularly suitable for absolute intensity measurements. The absolute value of the absorption coefficient is obtained straightforwardly from the measured ring down time (see Eq. (2.1) of Chapter 2). The typical sensitivity achieved ($\alpha_{\min} = 3 \times 10^{-10}$ cm^{-1}) allows observation of very weak transitions with intensity

down to 10^{-29} cm/molecule at room temperature. An important advantage of CW-CRDS spectra is that the DFB line width is much smaller than the Doppler broadening [1–5 MHz compared to 0.3 GHz (FWHM)]. The contribution of the apparatus function can therefore be neglected. The CW-CRDS technique allows to measure accurate line intensities down to 10^{-28} cm/molecule which is about two orders of magnitude lower than the FTS detection limit (about 10^{-26} cm/molecule).

$^{13}C^{16}O_2$

Before our work, the line intensities measured by Wang et al. [34] in the 4200–8500 cm^{-1} region together with those recently reported by Toth et al. [50] who performed extensive measurements between 2200 and 6800 cm^{-1} were the only quantitative data available in 1.6 μm region for $^{13}C^{16}O_2$ isotopologue. We have undertaken a collaborative project with ULB (Brussels) in order to improve the previous investigations in the region in particularly that of Wang et al. [34]. The study by Wang et al. [34] by FTS also involved the simultaneous treatment of all the line intensities measured in that work using the effective operators approach. Such a fitting showed that the line intensities measured for strong bands were not reproduced by the theoretical model as well as those obtained for the weaker bands, even if the observed discrepancies were within the experimental accuracy [34]. The affected bands are 30012-00001, 30011-00001 and 00031-00001, observed respectively near 6242, 6364 and 6780 cm^{-1} and belonging to the $\Delta P = 9$ series of transitions. The intensity measurements carried out at ULB [35] in Brussels using high-resolution FTS is an attempt to give insight into this problem. Additionally, they also measured line intensities for the 30013-00001 band of $^{13}C^{16}O_2$.

All the line intensities for $^{13}C^{16}O_2$ measured in our laboratory and in Brussels [35], together with those reported for the weak bands by Wang et al. [34] and the FTS measurements by Toth et al. [50], were then analyzed using the effective operators approach. The present measurements allowed to refine the effective dipole moment parameters for the $\Delta P = 9$ series of transitions.

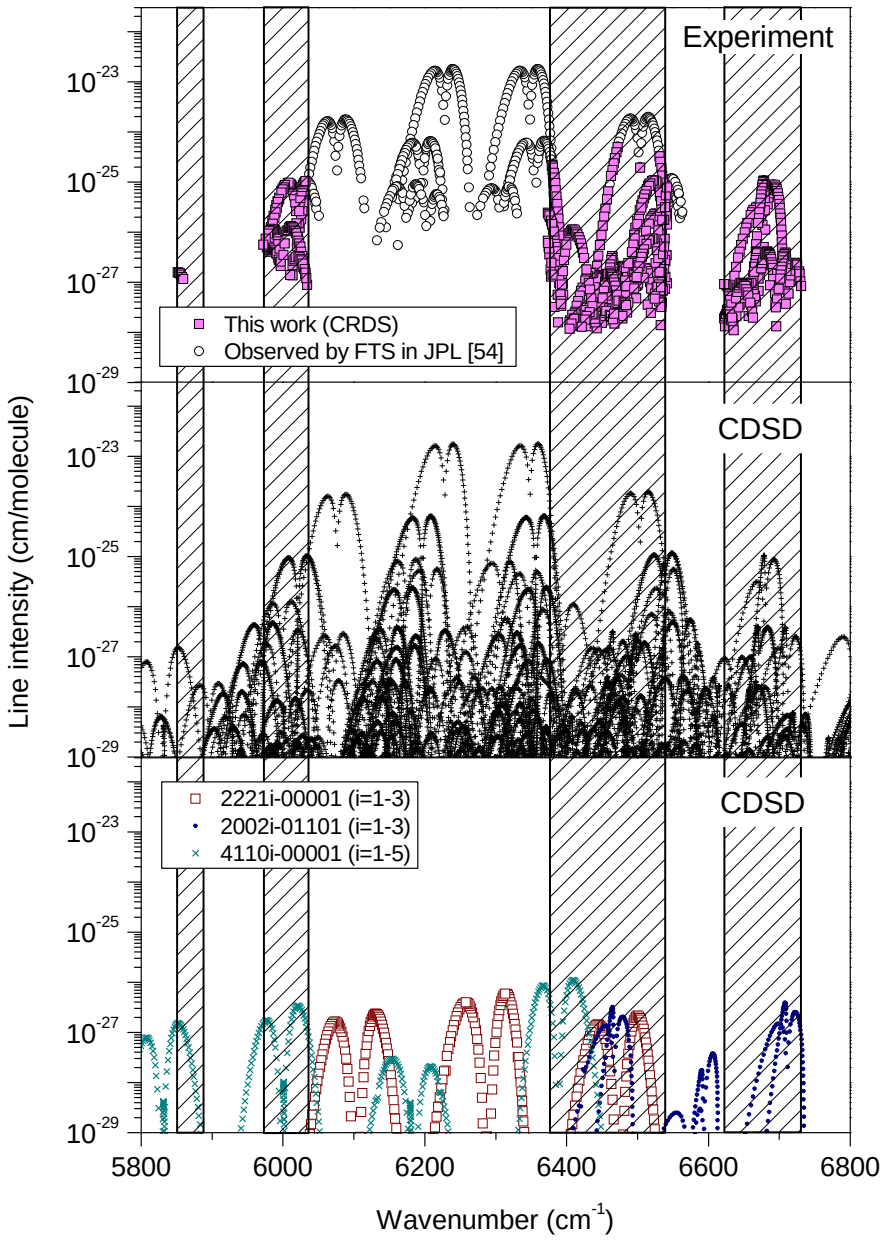

Figure 4.1. Overview of the $^{12}C^{16}O_2$ measured line intensities and those provided by the most recent version of the CDSD database [11], in the 5800–6800 cm^{-1} spectral region. *Top panel*: Transitions whose line strengths were experimentally determined and used as input data for the dipole moment operator fit. The line strengths measured by CW-CRDS are highlighted with squares. *Middle panel*: CDSD database [11]. *Bottom panel*: The weak 4110i–00001 (i = 1–5), 2002i-01101 (i = 1–3) and 2221i-00001 (i = 1–3) bands as provided by the CDSD database. The CW-CRDS recordings were specifically dedicated to the line intensity measurements of these bands. The studied spectral intervals are indicated.

$^{12}C^{16}O_2$

In the 1.6 μm region, the $^{12}C^{16}O_2$ line intensities of the strong cold parallel bands dominating the spectrum have been measured by several authors using different experimental techniques: grating spectrometer [73], Fourier transform spectrometers [54, 74–80] and diode laser absorption spectrometers [80–83]. The comparison of these measured line and band intensities has been detailed in Refs. [54, 79]. The line intensities of the 3111i-01101 (i = 2, 3) and 01131-01101 hot bands have been measured in Ref. [79] and Ref. [77] respectively. In a recent JPL publication [54], accurate line intensity values were reported for the 00031-00001 and 3001i-00001 (i = 1–4) cold bands and for their respective hot bands. The line intensities of two cold perpendicular bands 1112i-00001 (i = 1, 2) were also obtained [54]. However, important experimental information was still missing for the determination of the effective dipole moment parameters of the $\Delta P = 9$ bands [54] which hampered a satisfactory modeling of the CO_2 absorption spectrum near 1.6 μm: no intensity measurements were available for the very weak 4110i-00001 (i = 1–5) and 2002i-01101 (i = 1–3) perpendicular bands and for the 2221i-00001 (i = 1–3) "forbidden" bands. These bands are showed on the bottom panel of Fig. 4.1 together with the four spectral intervals chosen for additional CW-CRDS measurements dedicated to these specific bands: 5851–5881, 5972–6035, 6373–6542 and 6622–6750 cm^{-1}. On the middle panel, the $^{12}C^{16}O_2$ overview spectrum as included in the new version of the CDSD database [11] is presented for the 5800–6800 cm^{-1} region. The transitions measured by FTS in Ref. [54] are displayed in the top panel together with our new CW-CRDS measurements. Note that the line intensities of the bands of interest are lower than 10^{-26} cm/molecule, hence below the FTS detection threshold.

We have gathered our intensity values with measurements available in the literature in order to extend and refine the set of effective dipole moment parameters for the $\Delta P = 9$ series of transitions in $^{12}C^{16}O_2$.

4.2 $^{13}C^{16}O_2$

4.2.1 Experimental details

The sample pressure was measured by high-accuracy MKS Baratron gauge model 122BA. The ^{13}C-enriched sample was purchased from Aldrich Chemical Company. Its stated isotopic composition was 99% ^{13}C, with less than 6% of ^{18}O atoms. The uncertainty on the $^{13}C^{16}O_2$ concentration is directly transferred to the uncertainty on the line intensities. This is why it is crucial to determine accurately the relative concentration of the other CO_2 isotopologues present in the sample. Transitions due to eight CO_2 isotopologues could be identified in the CW-CRDS spectra: $^{13}C^{16}O_2$, $^{16}O^{13}C^{18}O$, $^{12}C^{16}O_2$, $^{16}O^{13}C^{17}O$, $^{16}O^{12}C^{18}O$, $^{13}C^{18}O_2$, $^{17}O^{13}C^{18}O$ and $^{16}O^{12}C^{17}O$ (in decreasing order of concentration). Their concentrations were obtained from the ratio of the measured integrated absorption coefficient and the corresponding line intensity. We used line intensities of $^{12}C^{16}O_2$ available in HITRAN [8], and line intensities predicted using effective dipole moment parameters of $^{12}C^{16}O_2$ [33] and $^{13}C^{16}O_2$ [34] for the other species. The obtained composition of our sample given in Table 3.1 is reprodused in Table 4.1.

Table 4.1. Relative isotopic abundance of ^{13}C-enriched sample purchased from Aldrich Chemical Company and used for CW-CRDS experiments.

Isotopologue	Abundance
$^{13}C^{16}O_2$	0.965
$^{16}O^{13}C^{18}O$	0.022(2)
$^{12}C^{16}O_2$	0.0078(4)
$^{16}O^{13}C^{17}O$	0.0041(4)
$^{16}O^{12}C^{18}O$	0.00019(3)
$^{13}C^{18}O_2$	0.00016(2)
$^{17}O^{13}C^{18}O$	0.000064(6)
$^{16}O^{12}C^{17}O$	0.000038(4)

The numbers between parentheses represent the statistical errors in the units of the last digit quoted.

Apart from $^{13}C^{16}O_2$, we found 2.2% of $^{16}O^{13}C^{18}O$, 0.8% of $^{12}C^{16}O_2$ and 0.4% of $^{16}O^{13}C^{17}O$. Each concentration was determined from several tens of transitions and the

statistical errors (on the order of 10%) are given in Table 4.1. It is worth indicating that differences on the order of 20% were noted between the $^{16}O^{13}C^{18}O$ line intensities extrapolated from the $^{12}C^{16}O_2$ and $^{13}C^{16}O_2$ effective dipole parameters. In the calculation of the $^{16}O^{13}C^{18}O$ concentration, we adopted as $^{16}O^{13}C^{18}O$ line intensities the average of these predicted values. Taking also into account the statistical error, we estimate to 20% the uncertainty on the $^{16}O^{13}C^{18}O$ concentration, which induces an uncertainty on the order of 0.4% on the $^{13}C^{16}O_2$ concentration leading to a value of 96.5(4)% for the $^{13}C^{16}O_2$ species of interest. Note that from the sample composition of Table 4.1, the isotopic abundance of the sample was (in %) 98.7 for ^{13}C, 1.1 for ^{18}O and 0.2 for ^{17}O, in agreement with the stated sample composition (99% of ^{13}C with less than 6% of ^{18}O).

The $^{13}C^{16}O_2$ absolute line intensities were retrieved from spectra recorded with pressure values about 22.7 hPa for the line position analysis [15, 41] and from new recordings performed at lower pressures (13.3, 1.33 and 0.27 hPa) specifically for the intensity measurements. The spectra were recorded at room temperature (296 ± 2K). The sample pressure was measured with relative uncertainty of about 0.5%.

4.2.2 Line intensity retrieval

The integrated absorption coefficient $I = \int \alpha(\nu) d\nu$ (in cm^{-2}) was obtained for each line using an interactive least-squares multi-lines fitting program, which uses the Levenberg-Marquardt algorithm to minimize the deviation between the observed and calculated spectra. Because of the large number of observed transitions (about 10–15 lines/cm^{-1}), lines were frequently blended. For each individual complete laser scan, the fitting program therefore limited automatically the spectral sections of overlapping or nearby transitions that could be treated independently. Because the laser line width is much smaller than the Doppler width, the contribution of the apparatus function can be neglected. The $^{13}C^{16}O_2$ line profile was assumed to be of Voigt type. The position and integrated absorbance of each line, and a baseline (assumed to be a linear or quadratic function of the wavenumber) were provided by the fitting procedure. The Gaussian line widths (0.00551 cm^{-1} (HWHM) at 6000 cm^{-1} for $^{13}C^{16}O_2$) were fixed to values

calculated for the Doppler broadening according to the measured temperature and mass of the considered CO_2 isotopologue. The Lorentzian line widths were calculated as the product of the sample pressure and the self-broadening coefficients provided in the HITRAN database [8]. They were assumed to be independent of the isotopologue and to decrease smoothly with the rotational quantum number J (from about 0.130 cm^{-1} (HWHM) at $J = 0$ to 0.0718 cm^{-1} at $J = 50$). The lines due to water vapor (H_2O and HDO), present as an impurity in the sample, were also fitted. Their Gaussian line widths were fixed to the theoretical values while the Lorentzian component was calculated using the H_2O broadening coefficients due to collisions with CO_2 [84].

Figs. 4.2 and 4.3 illustrate the large dynamics achieved on the measurement of the line intensities and the quality of the spectrum reproduction. Absorption coefficients ranging between 5×10^{-10} and 7×10^{-6} cm^{-1} can be measured in a single CW-CRDS. For a typical sample pressure of 13 hPa (10 Torr), these values correspond to intensities ranging from 2×10^{-29} to 3×10^{-25} cm/molecule. To increase such a dynamics to allow measurements for stronger lines, further recordings were performed with pressures of 1.3 hPa (1.0 Torr) and 0.27 hPa (0.2 Torr). Indeed, for absorption coefficients larger than 7×10^{-6} cm^{-1}, no ring down time could be measured as the light intensity transmitted by the CRDS cavity was too weak. For the strongest lines, the saturated values of the absorption coefficient were excluded from the line profile fitting and only the wings of the lines were considered.

The absolute line intensity or integrated absorption coefficient per pressure unit $\tilde{S}$ (in $cm^{-2} \cdot atm^{-1}$) was deduced from the integrated absorption coefficient I using the equation

$$\tilde{S} = \frac{I}{P}, \tag{4.1}$$

where P is the $^{13}C^{16}O_2$ partial pressure (in atm). Each $\tilde{S}$ value was then converted to the absorption line intensity $S(T_0)$ (in cm/molecule) according to the following expression:

$$S(T_0) = \frac{1}{N_L} \frac{T_0}{273.15} \tilde{S}, \tag{4.2}$$

which represents Eq. (1.81) for $T = T_0 = 296$ K.

The relative concentration of water vapour contaminating the CO_2 sample was re-

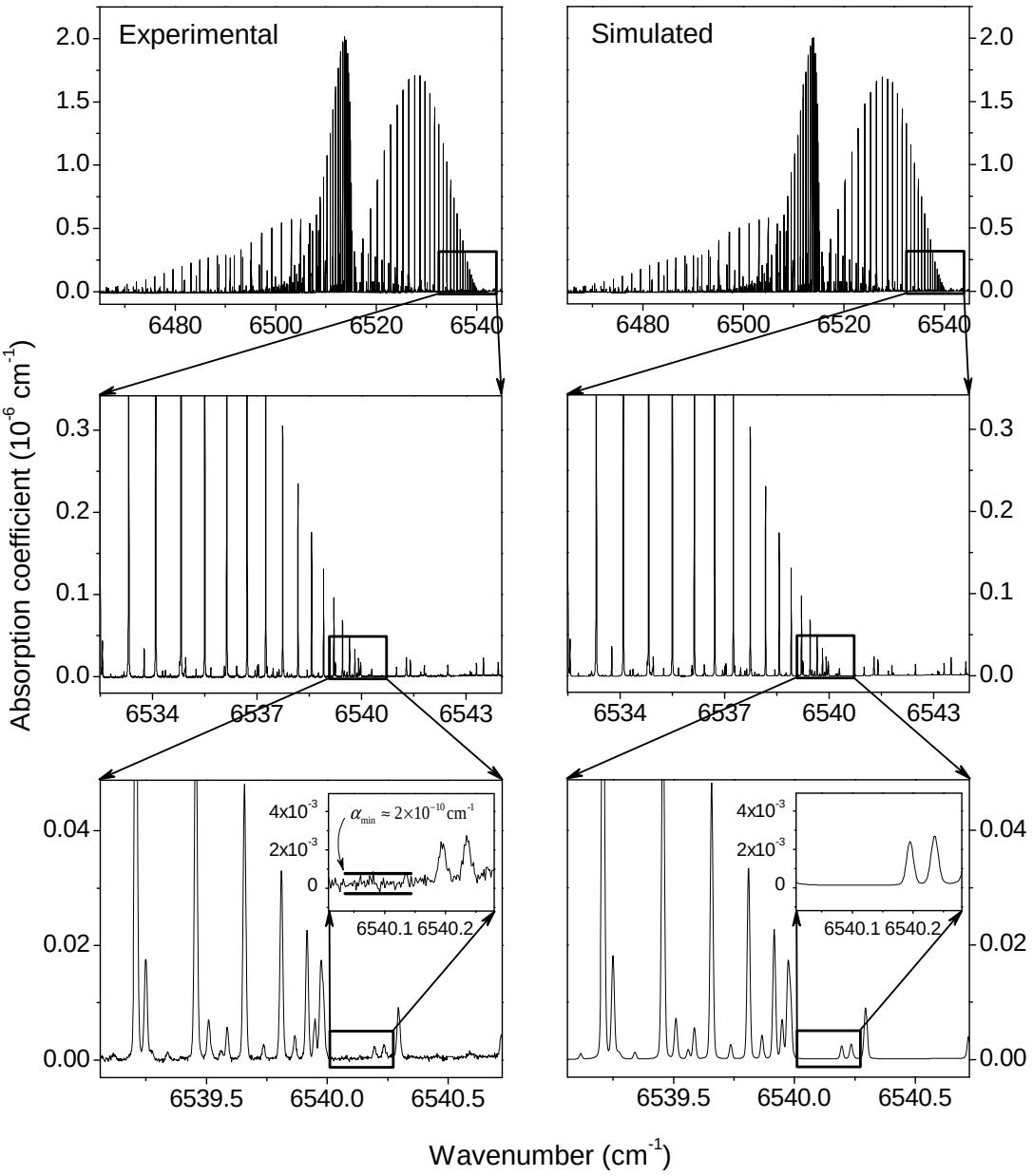

Figure 4.2. Spectra of carbon dioxide ($P = 13.3$ hPa) with 99 % enrichment in ^{13}C in the region of the perpendicular 11121-00001 band centred at 6515.505 cm^{-1}. Several successive enlargements show that line intensities differing by three orders of magnitude can be retrieved from a single CW-CRDS spectrum. The left and right hand panels correspond to the CW-CRDS spectrum and its simulation, respectively. The simulated spectrum was obtained as a sum of Voigt profiles whose parameters were determined with an interactive least squares multi-lines fitting program (see Text)

trieved from the observed H_2O line intensities in different spectral regions. The obtained values were always lower than 2×10^{-3} and the H_2O contribution to the total pressure value was then neglected.

To illustrate the consistency of the line intensities retrieved from spectra recorded at different pressures, we present in Fig. 4.4 the relative differences (in %) between the intensities measured at 13.3 and 1.33 hPa. The mean difference is equal to -1.73% with an root mean square (RMS) deviation of 3.4%.

The line profile fitting was a particularly laborious task. Taking into account the spectra recorded at different pressures (22.7, 13.3, 1.33 and 0.27 hPa) and the transitions due to the different species contributing to the spectra ($^{13}C^{16}O_2$, $^{16}O^{13}C^{18}O$, $^{12}C^{16}O_2$, $^{16}O^{13}C^{17}O$, $^{16}O^{12}C^{18}O$, $^{13}C^{18}O_2$, $^{17}O^{13}C^{18}O$, $^{16}O^{12}C^{17}O$, H_2O, HDO), the total number of fitted transitions reached 13345. As a result, 4934 absorption line intensities ranging between 4.3×10^{-29} and 2.3×10^{-23} cm/molecule were retrieved for $^{13}C^{16}O_2$ (1462, 2104, 1015 and 353 line intensities at 22.7, 13.3, 1.33 and 0.27 hPa, respectively). The fitting error was estimated to be 3% or better for well-isolated lines. The larger errors come mainly from the uncertainty on the baseline determination for the weak lines and from saturation effect for the strongest lines. A total of 1940 absorption line intensities were removed from the list because of insufficient accuracy (very weak, saturated or blended lines). The final set, thus containing 2994 $^{13}C^{16}O_2$ line intensities, was used as input data to the fit of the effective dipole moment parameters (see below). Taking into account fitting errors of the line profile and the uncertainties on the temperature (296 ± 2 K), pressure ($\pm0.5\%$) and concentration ($\pm0.4\%$), we estimated that the accuracy of these 2994 line intensities should be 4% or better for most of the lines and at most 7% for the weakest, strongest or strongly blended lines.

Because the intensity of the same lines has been measured in spectra recorded at different pressures, the input data set corresponds in fact to 2039 transitions. Their (measured) line intensities range between 1.1×10^{-28} and 1.3×10^{-23} cm/molecule. They are indicated by an open circle ($\circ$) in the overview spectrum of Fig. 4.5. In the line list provided as Supplementary material of Ref. [35], the experimental line intensities $S(T_0)$ are given for each pressure. To provide the most complete dataset in the 5851–6580 cm^{-1} region, this list includes *all* the $^{13}C^{16}O_2$ transitions that we assigned by

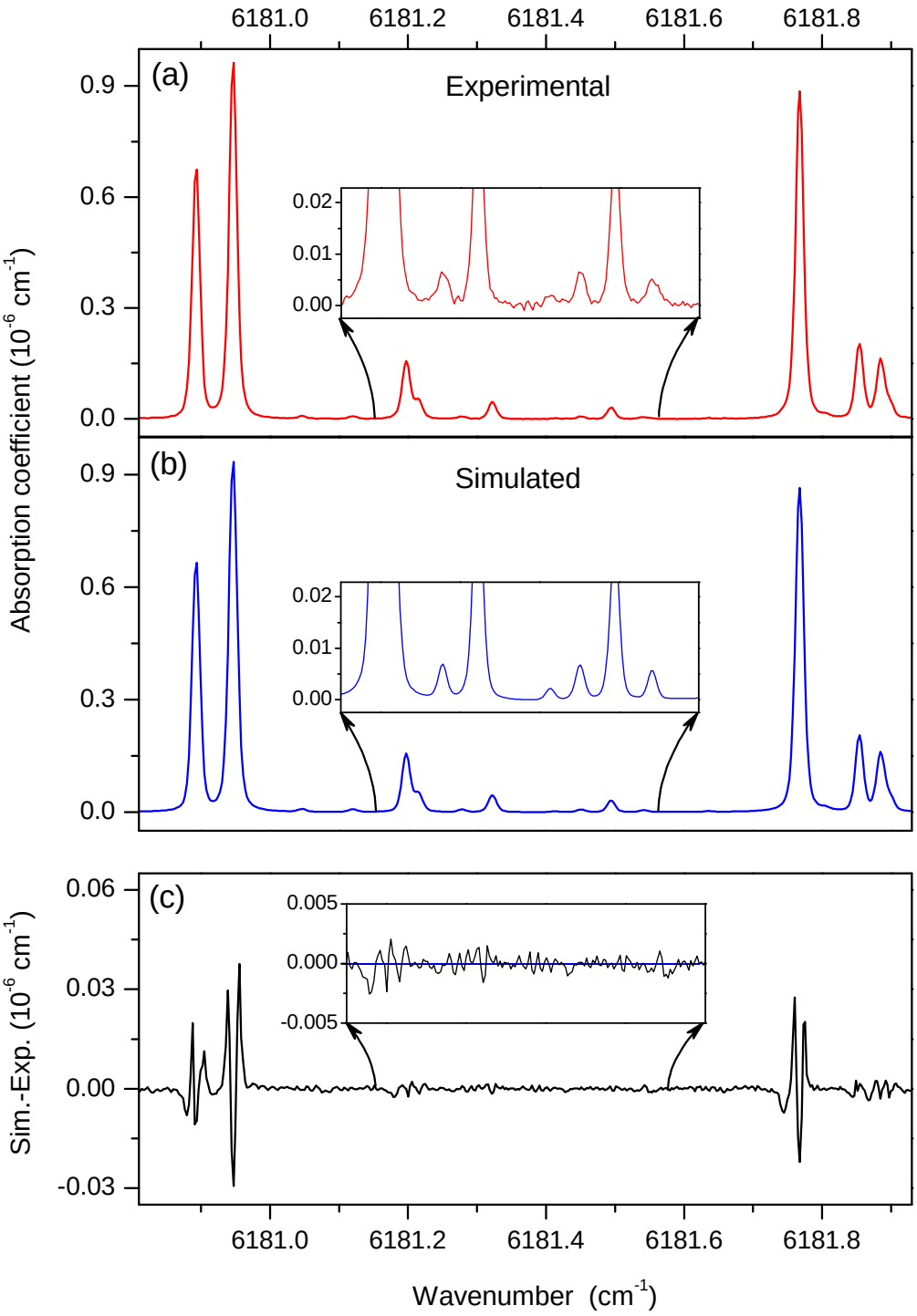

Figure 4.3. Comparison of a CW-CRDS spectrum (99% ^{13}C enrichment, $P = 23.2$ hPa) with its simulation: (a) experimental spectrum, (b) simulated spectrum resulting from the fitting procedure, (c) residuals between the simulated and experimental spectra.

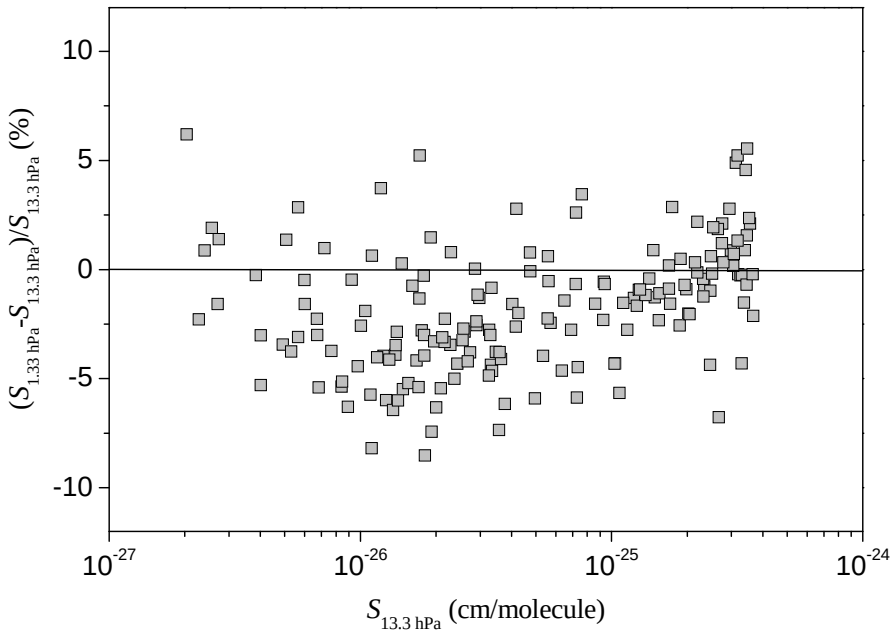

Figure 4.4. Comparison of the $^{13}C^{16}O_2$ absorption line intensities measured by CW-CRDS at pressures of 13.3 and 1.33 hPa. Differences (in %) are plotted versus the absorption line intensities retrieved from the spectra recorded at 13.3 hPa.

CW-CRDS, together with their assignment and intensities calculated by the effective operators model. This list includes 3537 transitions with (calculated) intensities ranging between 1.1×10^{-29} and 2.0×10^{-23} cm/molecule. Note that the number of transitions predicted with an intensity value larger than 2×10^{-28} cm/molecule is about 3958 while 3226 of them were detected, the difference (18%) being mostly due to unrecoverable blended lines.

In our analysis and global line intensity modeling we use also the FTS data obtained in Brussels by T. Deleporte and J. Vander Auwera [35]. A total of 872 line intensities were measured by FTS in the 20013-00001, 20012-00001, 20011-00001, 30013-00001, 30012-00001, 30011-00001 and 00031-00001 bands near 1.6 and 2.0 μm. Their estimated accuracy ranges from 3% to 18% for strong to weak lines. More precisely, 77% of the line intensities have the uncertainties between 3% and 4%, and 6% of the line intensities have the uncertainties larger than 7% (see Ref. [35]).

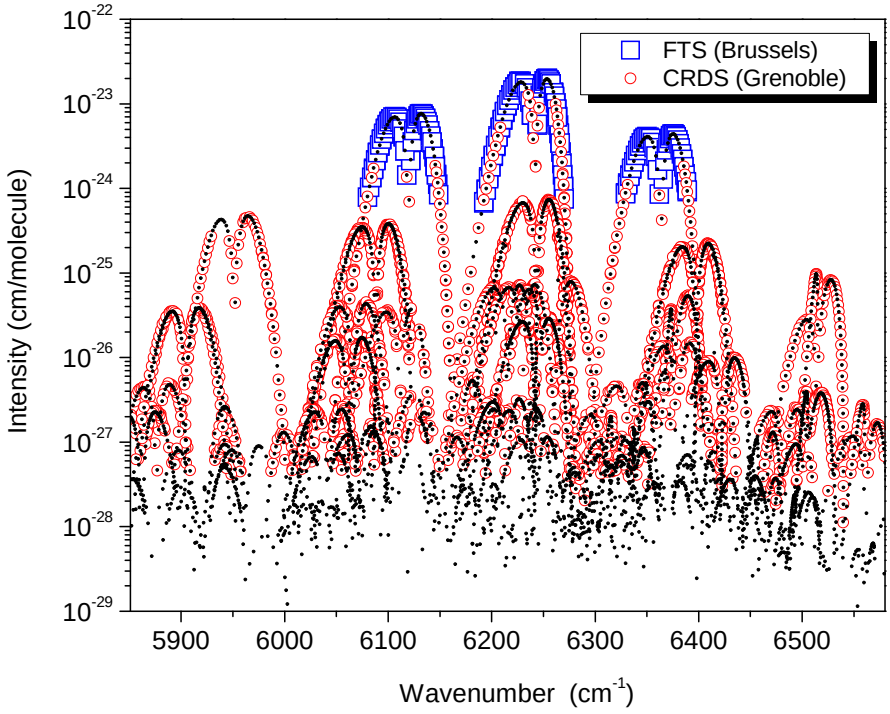

Figure 4.5. Overview of the $^{13}C^{16}O_2$ spectrum in the 5851–6580 cm^{-1} region. Note the logarithmic scale adopted for the line intensities. The calculated line intensities of *all* the 3537 $^{13}C^{16}O_2$ transitions detected by CW-CRDS in the 5851–6580 cm^{-1} region are marked by black points (•). The open circles (○) and open squares (□) represent the intensities measured by CW-CRDS and FTS, respectively, and are included in the fitting of the effective dipole moment parameters.

4.2.3 Data reduction and discussion

The absolute intensity $S_{P'N'J'\varepsilon'\leftarrow PNJ\varepsilon}$ or integrated absorption cross section [expressed in cm/molecule at temperature T in K] is related to the transition moment squared $W_{P'N'J'\varepsilon'\leftarrow PNJ\varepsilon}$ by Eq. (1.82).

Figs. 4.6 and 4.7 show vibrational transition moments squared (measured values of $W_{P'N'J'\varepsilon'\leftarrow PNJ\varepsilon}$ divided by the Hönl-London factor) plotted versus m (m is equal to $-J$ for P-branch lines and $J+1$ for R-branch lines). For the parallel bands presented, the Hönl-London factor, L_J, is equal to $|m|$. Figs. 4.6 and 4.7 show the excellent agreement between the line intensities obtained independently using CW-CRDS in our laboratory and FTS in Brussels. The same is true for the 30012-00001 band. The figures also compare the present results with literature values [12, 34, 50, 85] and HITRAN [8]. In particular, the agreement with the very recent work of Toth et al. [50] is very good

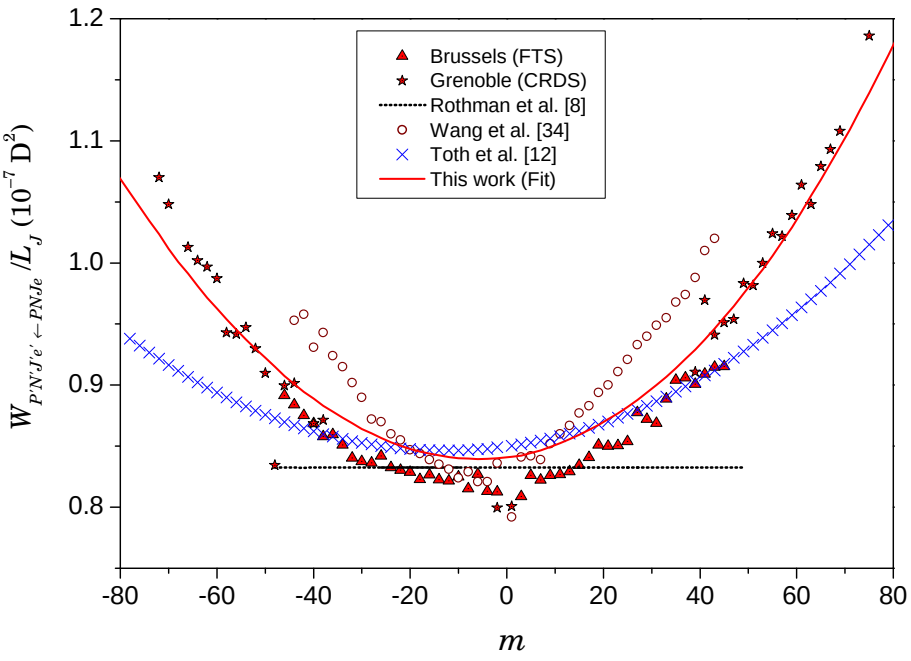

Figure 4.6. Evolution with m of the transition moment squared $W_{P'N'J'\varepsilon' \leftarrow PNJ\varepsilon}$ divided by the corresponding Hönl-London factor factor, for the 30013-00001 band of $^{13}C^{16}O_2$. The weighted average of the values observed for each line using FTS are represented with triangles, and those from CW-CRDS with stars. Literature data come from Rothman et al. [8], Wang et al. [34] and Toth et al. [12, 50]. The solid curve corresponds to the values calculated with the effective dipole moment operator presently determined. Note that the behavior of the calculated values displayed in this figure is governed not only by the displayed experimental data but also by the whole set of experimental values used as input data to the fit of the effective dipole moment parameters.

00031-00001 band (discrepancies $\leqslant 1.2\%$). However, larger discrepancies are observed for the 30013-00001 and 30011-00001 bands (Figs. 4.6 and 4.7): differences of 3.7% and 4.6% (Toth et al. [50] – this work) are observed at $m = 0$, and the Herman-Wallis dependencies do not match in particular for high m values. It is worth underlining that the line intensities in the JPL database [12] are calculated values based on measurements reported in Ref. [50]. In the case of the considered 30013-00001 and 30011-00001 bands, the FTS measurements of Ref. [50] were limited to a maximum J values of 47 and 45 respectively, while the database of Ref. [12] provides line position and intensities up to $|m| = 79$ and 75 respectively. The long-range extrapolation of the line intensities adopted in Ref. [12] is probably responsible for the important deviations observed for high m values. In particular, the steep decrease of the transition moment squared

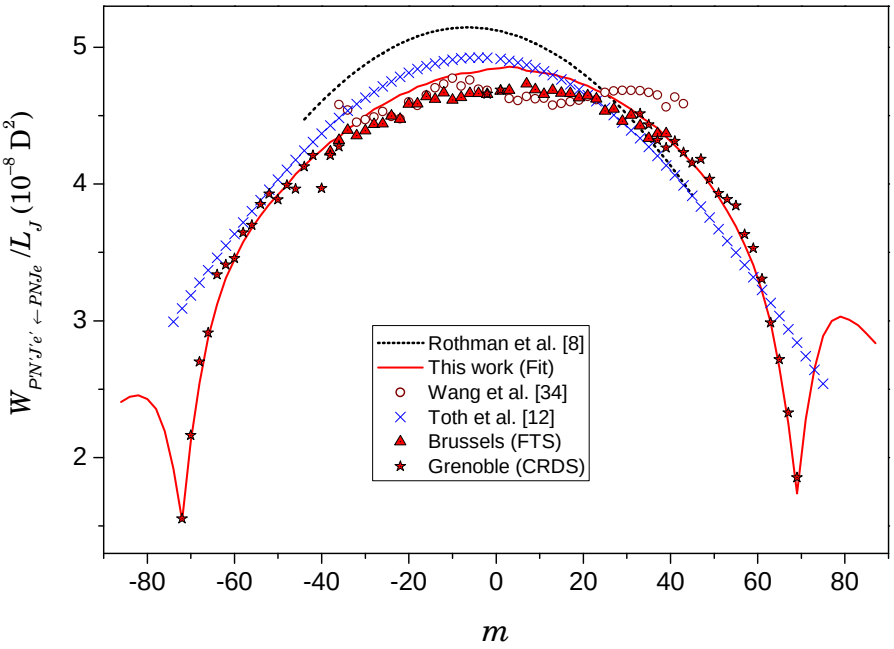

Figure 4.7. Evolution with m of the transition moment squared $W_{P'N'J'\varepsilon' \leftarrow PNJ\varepsilon}$, divided by the corresponding Hönl-London factor, for the 30011-00001 band of $^{13}C^{16}O_2$. The weighted average of the values observed for each line using FTS are represented with triangles, and those from CW-CRDS with stars. Literature data come from Rothman et al. [8], Wang et al. [34] and Toth et al. [12, 50]. The solid curve corresponds to the values calculated with the effective dipole moment operators presently determined. The behavior of the calculated values of the transition moment squared observed near $|m| = 70$ clearly shows the influence of the resonance Coriolis interaction of this band with the 11122-00001 perpendicular band (the energy levels cross at $J = 71$). Note that the behavior of the calculated values displayed in this figure is governed not only by the displayed experimental data but also by the whole set of experimental values used as input data to the fit of the effective dipole moment parameters.

observed near $|m| = 70$ (Fig. 4.7) is due to a resonance Coriolis interaction with the 11122-00001 perpendicular band (energy level crossing at $J = 71$), which cannot be accounted for by a simple extrapolation based on Herman-Wallis coefficients obtained from low m values.

4.2.4 Global modeling

Using the approach described in Section 1.3.3 we have least-squares fitted the line intensities measured by CW-CRDS and FTS together with selected intensity data reported in the literature [34, 50, 85]. The values of the expansion coefficients ${}^{J}C_{PN\varepsilon}^{v_1 v_2 \ell_2 v_3}$

Table 4.2. Experimental data and the results of the global fits.

Reference	Region (cm^{-1})	Abundance	Accuracy (%)	N^a	RMS(%)
Wang et al. [34]	5950–6762	0.985	5–10	334	6.7
Toth et al. [50]	5922–6797	0.985, 0.949, 0.0110574	1–10	252	3.1
Brussels (FTS) [35]	6080–6797	0.98	3–10	439	2.3
Grenoble (CRDS) [35]	5851–6580	0.965	4–7	2891	3.4

[a] N – number of fitted line intensities, RMS – corresponding residuals.

of the eigenfunctions have been obtained from the global fit of the effective Hamiltonian parameters to the observed line positions [14]. The partition functions $Q(T)$ and nuclear statistical weights were taken from Ref. [86].

The aim of the fitting procedure is to minimize the dimensionless weighted standard deviation χ, defined according to the usual formula

$$\chi = \sqrt{\frac{\sum_{i=1}^{N} \left(\frac{S_i^{\mathrm{obs}} - S_i^{\mathrm{calc}}}{\delta_i} \right)^2}{(N-n)}}, \tag{4.3}$$

where S_i^{obs} and S_i^{calc} are, respectively, observed and calculated values of the intensity for the i-th line; $\delta_i = S_i^{\mathrm{obs}} \sigma_i / 100\%$, where σ_i is the measurement error of the i-th line in %, N is the number of fitted line intensities and n is the number of adjusted parameters. To characterize the quality of a fit, we also use the RMS deviation, defined according to the equation

$$\mathrm{RMS} = \sqrt{\frac{\sum_{i=1}^{N} \left(\frac{S_i^{\mathrm{obs}} - S_i^{\mathrm{calc}}}{S_i^{\mathrm{obs}}} \right)^2}{N}} \times 100\%. \tag{4.4}$$

To obtain the set of effective dipole moment parameters for the $\Delta P = 9$ series of transitions, we have fitted both the line intensities measured by CW-CRDS in our laboratory and by FTS in Brussels [35]. The input data also included the line intensities of the hot bands and of the weak 30014-00001 cold band published in Ref. [34], and of five cold bands [3001i-00001 (i = 1–4), 00031-00001] and of the 01131-00001 hot band measured by Toth et al. [50] in JPL (Jet Propulsion Laboratory). The characteristics of the input experimental data and the results of the global fits are presented in Table 4.2.

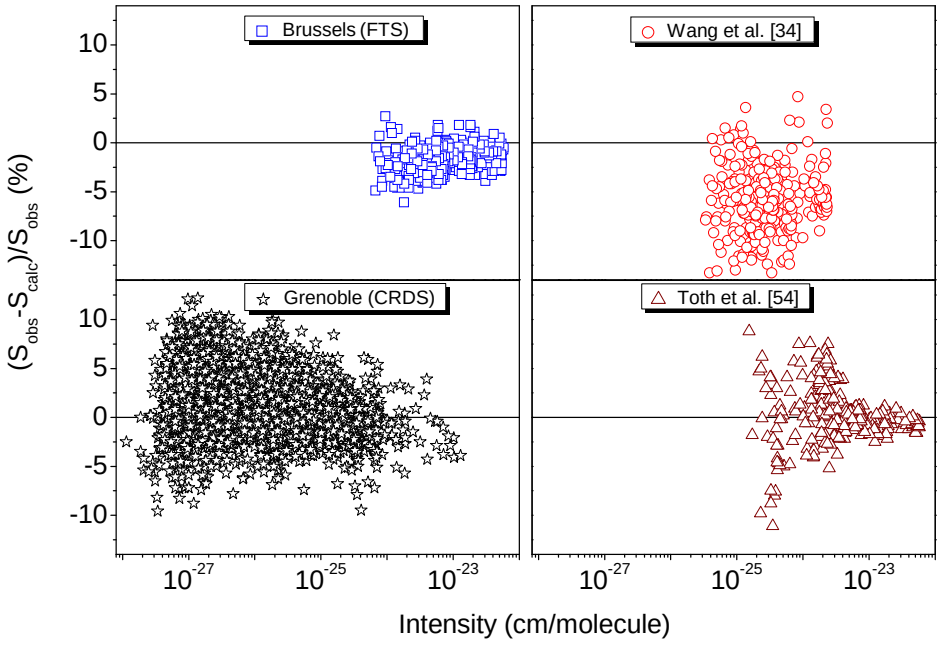

Figure 4.8. Residuals between the observed and calculated line intensities in the 1.6 μm region versus the line intensity values. Note the logarithmic scale adopted for the line intensities

After a preliminary fitting, 103 line intensities of the 2994 lines measured by CW-CRDS (3.4%) were excluded from the fit because they were outliers. Most of them correspond to weak lines. The whole set of input data was then obtained by gathering the CW-CRDS values with the FTS values obtained in Brussels [35] and those of Refs. [34, 50]. The resulting cleaned set of 3916 intensities of 2207 lines was fitted with 16 effective dipole moment parameters. They are presented in Table 4.4. The weighted standard deviation of the fit of the cleaned set of line intensities is $\chi = 0.79$ with a RMS

Table 4.3. Summary of $^{13}C^{16}O_2$ line intensity fits.

ΔP series	Number of lines	Number of bands	J_{max}	S_{min} [a]	S_{max} [a]	χ	RMS (%)	n [b]
9	2201	49	79	1.14×10^{-28}	5.80×10^{-23}	0.79	3.7	16

[a] S_{min} and S_{max} (in cm/molecule) are the minimum and maximum values of line intensity included into the fit.

[b] n is the number of adjusted parameters.

Table 4.4. Effective dipole moment parameters for $\Delta P = 9$ series of transitions in $^{13}C^{16}O_2$.

Parameter[a]	Δv_1	Δv_2	Δv_3	$\Delta \ell_2$	Value	Order
M	0	0	3	0	0.31075(13)	10^{-3}
M	3	0	1	0	–0.243789(76)	10^{-3}
b_J	3	0	1	0	0.277(10)	10^{-3}
M	2	2	1	0	0.17600(42)	10^{-4}
M	1	4	1	0	–0.826(11)	10^{-6}
M	0	6	1	0	0.253(19)	10^{-7}
M	1	1	2	1	0.19296(19)	10^{-4}
b_J	1	1	2	1	6.150(41)	10^{-3}
M	0	3	2	1	–0.7260(58)	10^{-6}
b_J	0	3	2	1	10.99(34)	10^{-3}
M	4	1	0	1	–0.3092(61)	10^{-6}
b_J	4	1	0	1	93.972(74)	10^{-3}
M	3	3	0	1	0.638(93)	10^{-7}
b_J	3	3	0	1	48.4(61)	10^{-3}
M	2	–1	2	1	0.1272(34)	10^{-5}
b_J	2	–1	2	1	32.2(14)	10^{-3}

[a]The parameters M are given in Debye while the b_J parameters are dimensionless. Only relative signs of M parameters within a given series of transitions are determined.

of 3.7%. The results of the global fit are summarized in Tables 4.2 and 4.3. We reached the experimental accuracy without parameters $\kappa_i^{\Delta v}$ $(i = 1, 2, 3)$. Fig. 4.8 presents the variation of the residuals between the observed and calculated line intensities versus the line intensity values. It illustrates the nearly 6 orders of magnitude dynamics of the line intensities covered by the input data and the consistency of the line intensities obtained from different experimental sources, including selected data from Ref. [34]. Nevertheless, the line intensities of the selected bands from Ref. [34] seem to be underestimated by 6% on average, compared to other observations. A fit excluding these data resulted in almost the same set of effective dipole moment parameters, because of the small weights assigned to the majority of the data from Ref. [34], corresponding to a 7–10% experimental uncertainty.

In Figs. 4.6 and 4.7, the calculated transition moments squared divided by the Hönl-London factor are included for the 30013-00001 and 30011-00001 bands respectively, together with the experimental values. The calculations were performed with the

sets of effective dipole moment parameters obtained in the present work. It is worth emphasizing that the effective dipole moment parameters were fitted not only to the line intensities displayed in these figures but also to the line intensities of all the bands belonging to a given series of transitions, in particular hot bands. The evolution with m of the calculated values is therefore governed by the whole set of input experimental data, resulting in the observed discrepancies with the experimental data presented in the figures.

4.3 $^{12}C^{16}O_2$

4.3.1 Experimental results

A total of 15 diode lasers were necessary to cover the four spectral intervals of interest (see Fig. 4.1). The ring down cell was filled with carbon dioxide in natural isotopic abundance (Fluka, stated purity > 99.998%). The pressure, measured by a capacitance gauge, as well as the ringdown cell temperature, were monitored during the spectrum acquisition. The sample pressure was fixed to a value of 13.3 hPa (10.0 Torr) and the room temperature was 296 ± 2 K. The same procedure as described in Section 4.2.2 was adopted for line intensity retrieval.

Taking into account the transitions due to the different CO_2 isotopologues ($^{12}C^{16}O_2$, $^{13}C^{16}O_2$, $^{16}O^{12}C^{18}O$, $^{16}O^{12}C^{17}O$, $^{16}O^{13}C^{18}O$), the lines due H_2O and HDO present as an impurity, the existence of overlapping spectral regions recorded with successive diode lasers, the total number of fitted line profiles was about 4600. After averaging of the line intensities of the same line determined from different spectra, 1572 line intensity values ranging from 1.53×10^{-29} to 4.94×10^{-25} cm/molecule were obtained for $^{12}C^{16}O_2$. Note that the strongest lines ($S > 5 \times 10^{-25}$ cm/molecule) which were saturated on the spectrum were not fitted since the accurate line intensities of these lines were measured in Ref. [54]. We fixed the lower line intensity cutoff to a value of 10^{-28} cm/molecule and removed from the list 214 line intensities below this value because of insufficient accuracy. In addition, 406 intensity values of the lines with unsatisfactory line profile reproduction (blended lines or incorrect baseline) were excluded. The fitting error was estimated to be 3% or better for well-isolated lines. The larger errors were mainly due

Table 4.5. Experimental data and the results of the global fits of the line intensities of transitions in $^{12}C^{16}O_2$.

Reference	Abundance	Accuracy, %	Assumed uncertainty, %	N^a	$\%N^b$	RMS^c
This work [44]	0.9842	2–7	4	928	97.5	3.4
Toth et al. [73]	0.9842	4	4	74	57.2	2.6
Johns et al. [77]	0.9842	2–4		150	94.8	2.2
Henningsen and Simonsen [81]	0.9842	2–12		29	69.0	2.5
Pouchet et al. [82]	0.9842	1.5–3		13	100	1.3
Boudjaadar et al. [79]	1.0	3–5	3, 5^d	269	100	2.0
Régalia-Jarlot et al. [80]	0.9842	1.5–2	2	97	100	1.0
Toth et al. [54]	0.9842, 0.9952	0.5–3	2	808	99.0	2.9

[a] N – number of the fitted line intensities from a given source.
[b] $\%N$ – percentage of the line intensities of a given source included into the fit.
[c] RMS – root mean squares (in %) of the residuals for a given source.
[d] 3% for the cold bands, 5% for the hot bands.

to the uncertainty on the baseline determination which became more important for the weak lines. The final set, thus containing 952 $^{12}C^{16}O_2$ line intensities, was used as input data to the fit of the effective dipole moment parameters (see below). Taking into account the line profile fitting errors and the uncertainties on the temperature (±2 K) and pressure (±0.5%), we estimated that the accuracy of these 952 line intensities should be 4% or better for most of the lines and at most 7% for the weakest and strongly blended lines.

4.3.2 Global modeling

Using the approach described in Section 1.3.3, we have performed the least-squares fitting of the line intensities set obtained by gathering the CW-CRDS results with selected intensity data reported in the literature for the $\Delta P = 9$ series of transitions [54, 73,77,79–82]. The selection has been performed on the basis of the comparative analysis of all published line intensities following the results of Refs. [54,79]. The sources in which the line intensities differ considerably from those confirmed by several authors were not

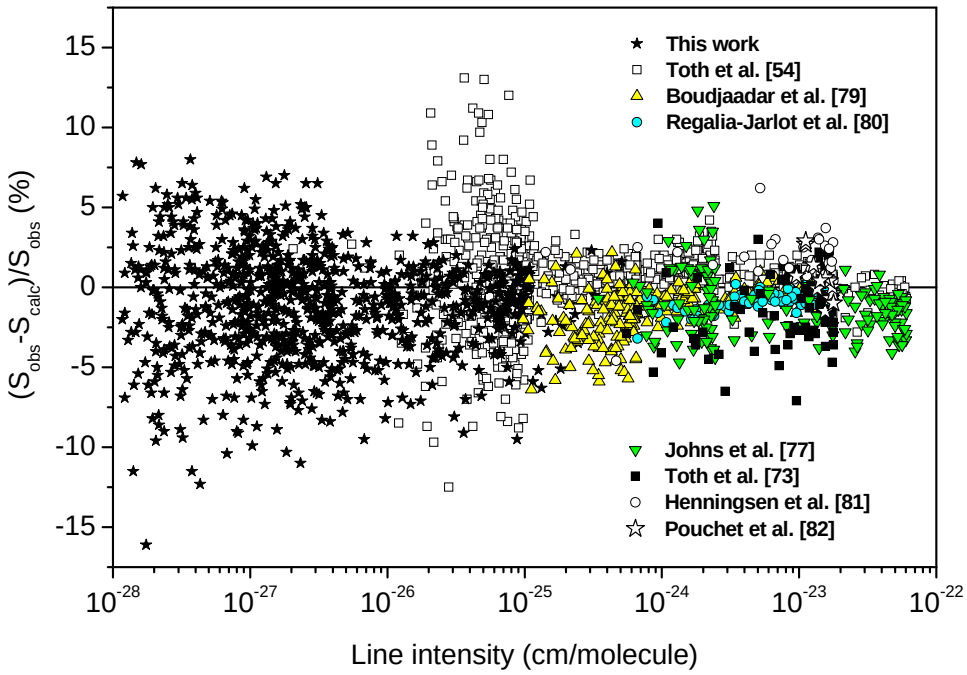

Figure 4.9. Residuals between the observed and calculated line intensities in the 1.6 μm region versus the line intensity values. A different symbol is used for each experimental work.

included in the fit. In general, these discarded data came from rather old publications. Because of the comparative analysis performed in Refs. [54, 79], in several cases, only part of the data presented in a given source were included into the fit. In the fitting process, some evident outliers were excluded from the input file. Table 4.5 presents the sources of the input data and the corresponding percentage of line intensities included in the fit. The values of the expansion coefficients ${}^{J}C_{PN\varepsilon}^{v_1v_2\ell_2v_3}$ of the eigenfunctions have been obtained from the global fit of the effective Hamiltonian parameters to the

Table 4.6. Summary of $^{12}C^{16}O_2$ line intensity fit for the $\Delta P = 9$ transition series.

Number of lines	Number of bands	J_{max}	$S_{min}{}^a$	$S_{max}{}^a$	χ	RMS (%)	n^b
2368	40	84	1.10×10^{-28}	6.12×10^{-23}	1.05	2.9	19

[a] S_{min} and S_{max} (in cm/molecule) are the minimum and maximum values of line intensity included into the fit.

[b] n is the number of adjusted parameters.

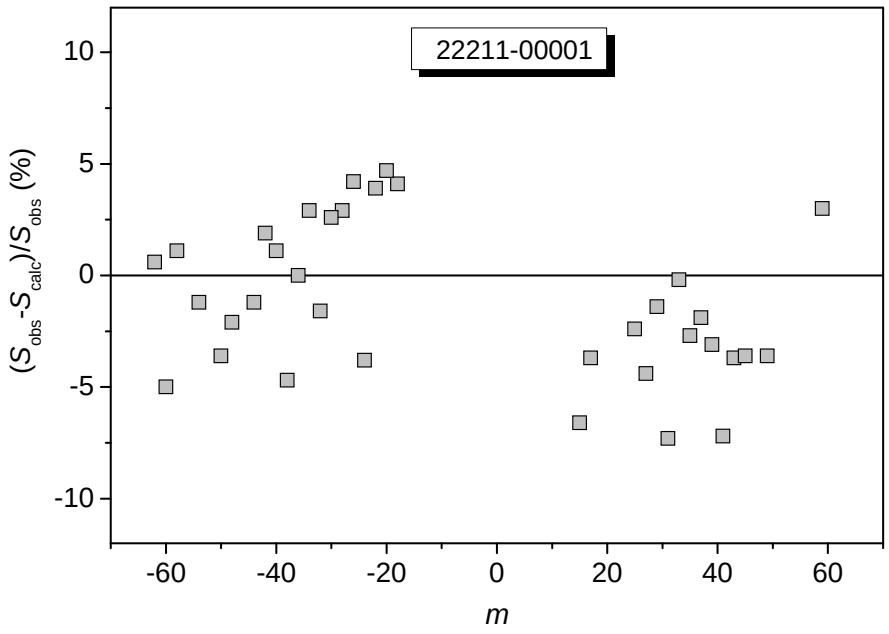

Figure 4.10. Residuals between the observed and calculated line intensities of the 22211-00001 "forbidden" band centered at 6474.532 cm^{-1} versus the rotational quantum number m (where $m = -J$ and $m = J + 1$ for P- and R-branches, respectively). Note that the corresponding line intensities are very small, ranging from 1.5×10^{-28} to 2.2×10^{-27} cm/molecule.

observed line positions. The initial set of effective Hamiltonian parameters taken from Ref. [14] was slightly refined using new observations [43]. The partition functions $Q(T)$ and nuclear statistical weights were taken from Ref. [86].

The fitting results presented in Tables 4.5 and 4.6, show that, in average, our fitted set of effective dipole moment parameters reproduces the line intensities from all involved experimental sources within their uncertainties. The values of the fitted parameters are listed in Table 4.7. Fig. 4.9 presents the variation of the residuals between the observed and calculated line intensities versus the line intensity values. It illustrates the nearly six orders of magnitude dynamics of the line intensities covered by the input data and the consistency of the line intensities obtained from different experimental sources.

As a test of the validity of our model, it is worth emphasizing that no $|\Delta\ell_2| > 1$ effective dipole moment parameters were necessary to describe the line intensities of the $|\Delta\ell_2| > 1$ "forbidden" bands. These "forbidden" bands borrow most of their intensities

Table 4.7. Effective dipole moment parameters for $\Delta P = 9$ series of transitions in $^{12}C^{16}O_2$.

Parameter[a]	Δv_1	Δv_2	Δv_3	$\Delta \ell_2$	Value	Order
M	0	0	3	0	0.31068(34)[b]	10^{-3}
κ_1	0	0	3	0	–20.52(39)	10^{-2}
κ_2	0	0	3	0	2.52(10)	10^{-2}
M	3	0	1	0	–0.26621(13)	10^{-3}
κ_1	3	0	1	0	–0.21(11)	10^{-2}
κ_2	3	0	1	0	–0.318(56)	10^{-2}
b_J	3	0	1	0	0.264(11)	10^{-3}
M	2	2	1	0	0.24145(57)	10^{-4}
M	1	4	1	0	–0.1216(15)	10^{-5}
M	0	6	1	0	0.339(28)	10^{-7}
M	1	1	2	1	0.21783(18)	10^{-4}
b_J	1	1	2	1	3.616(41)	10^{-3}
M	0	3	2	1	–0.9378(62)	10^{-6}
b_J	0	3	2	1	11.58(30)	10^{-3}
M	4	1	0	1	–0.288(32)	10^{-6}
b_J	4	1	0	1	80.6(38)	10^{-3}
M	3	3	0	1	0.57(12)	10^{-7}
b_J	3	3	0	1	99.9(63)	10^{-3}
M	2	–1	2	1	0.1947(58)	10^{-5}

[a]The parameters M are given in Debye while the b_J and κ_i parameters are dimensionless. Only relative signs of M parameters within a given series of transitions are determined.

[b]The numbers in parentheses are one standard deviation in units of the last quoted digit.

from "allowed" bands via ℓ-type and anharmonic + ℓ-type interactions which are taken into account by our effective Hamiltonian model. The $|\Delta \ell_2| > 1$ effective dipole moment parameters give negligible contributions to the intensities therefore no corresponding parameters were included in our fitting. As an example, Fig. 4.10 shows that the line intensities of the very weak 22211-00001 "forbidden" band measured in this thesis, are satisfactorily reproduced with our set of parameters.

Chapter 5

Critical review of the current databases

Ce chapitre est consacré à la dernière partie du travail de la thèse. Elle a consisté en la comparaison des positions et intensités de raies de l'isotopologue principal de CO_2 disponibles dans les bases de données HITRAN, GEISA, HITEMP, et JPL avec les données correspondantes dans les listes de paramètres spectroscopiques de $^{13}C^{16}O_2$ et $^{12}C^{16}O_2$, générées au cours de cette thèse. Ces dernières listes contiennent les positions de raies mesurées par spectroscopie CW-CRDS et les intensités mesurées par CW-CRDS ou calculées par le modèle effectif global et disponibles dans CDSD.

5.1 Introduction

Considering the major importance of carbon dioxide in many fields including combustion and the climate of several planets, the construction of an *accurate* and *complete* spectroscopic database is requested to the spectroscopists community. While laboratory experiments are often the most appropriate to fulfill the accuracy requirement, theoretical modeling is the best way to approach completeness. High-quality experimental data are available mostly for the stronger bands (lines), while parameters of the weaker bands (lines) are generally theoretically predicted (extrapolated). The large amount of new experimental data obtained in this thesis (see Table 5.1) gives us the

opportunity to check the quality of line parameters provided by different databases in the 5851–7045 cm^{-1} spectral region. So our purpose is to discuss the most currently used spectroscopic databases of carbon dioxide: HITRAN [8], GEISA [9], HITEMP [10], and the recent JPL [12] and CDSD [11] databases. The discussion below is limited to line positions and intensities but the variety of atmospheric conditions (pressure, temperature, abundance) existing in every planet confers a crucial importance to the line profile parameters. We will focus our discussion to the principal isotopologue of carbon dioxide. However, for the minor CO_2 isotopologues the discrepancies between observed line parameters and those provided by the HITEMP [10] and JPL [12] databases are also found to be very large because of long range extrapolations and inaccurate theoretical (DND) predictions adopted by these databases. A detailed comparison of our experimental results for three ^{13}C species ($^{13}C^{16}O_2$, $^{16}O^{13}C^{18}O$ and $^{16}O^{13}C^{17}O$) with line positions and intensities provided by the JPL database [12] was published as a Comment [87].

In order to provide the most complete experimental dataset in the 5851–7045 cm^{-1} spectral region we have generated two line lists for the $^{12}CO_2$ and $^{13}CO_2$ isotopologues which are given as Supplementary materials attached to Refs. [43] and [42], respectively. In these line lists, the line positions are experimental values (typical uncertainty in the order of 1×10^{-3} cm^{-1}), while line strengths were calculated at 296 K by using the effective operators parameters derived from the CW-CRDS intensity measurements (see Chapter 4).

5.2 The HITRAN and GEISA databases

Fig. 5.1 includes an overview comparison of our experimental results with the HITRAN database [8] for the principal isotopologue. In its present status, the CO_2 line list provided by the HITRAN database [8] is a mixture of (i) line parameters calculated on the basis of spectroscopic parameters (vibrational term, rotational constants, band strengths, Herman Wallis coefficients, etc.) derived from laboratory data, (ii) some measured values for perturbed bands, and (iii) theoretical predictions from Direct Numerical Diagonalization (DND) [30] and more recently global effective operators

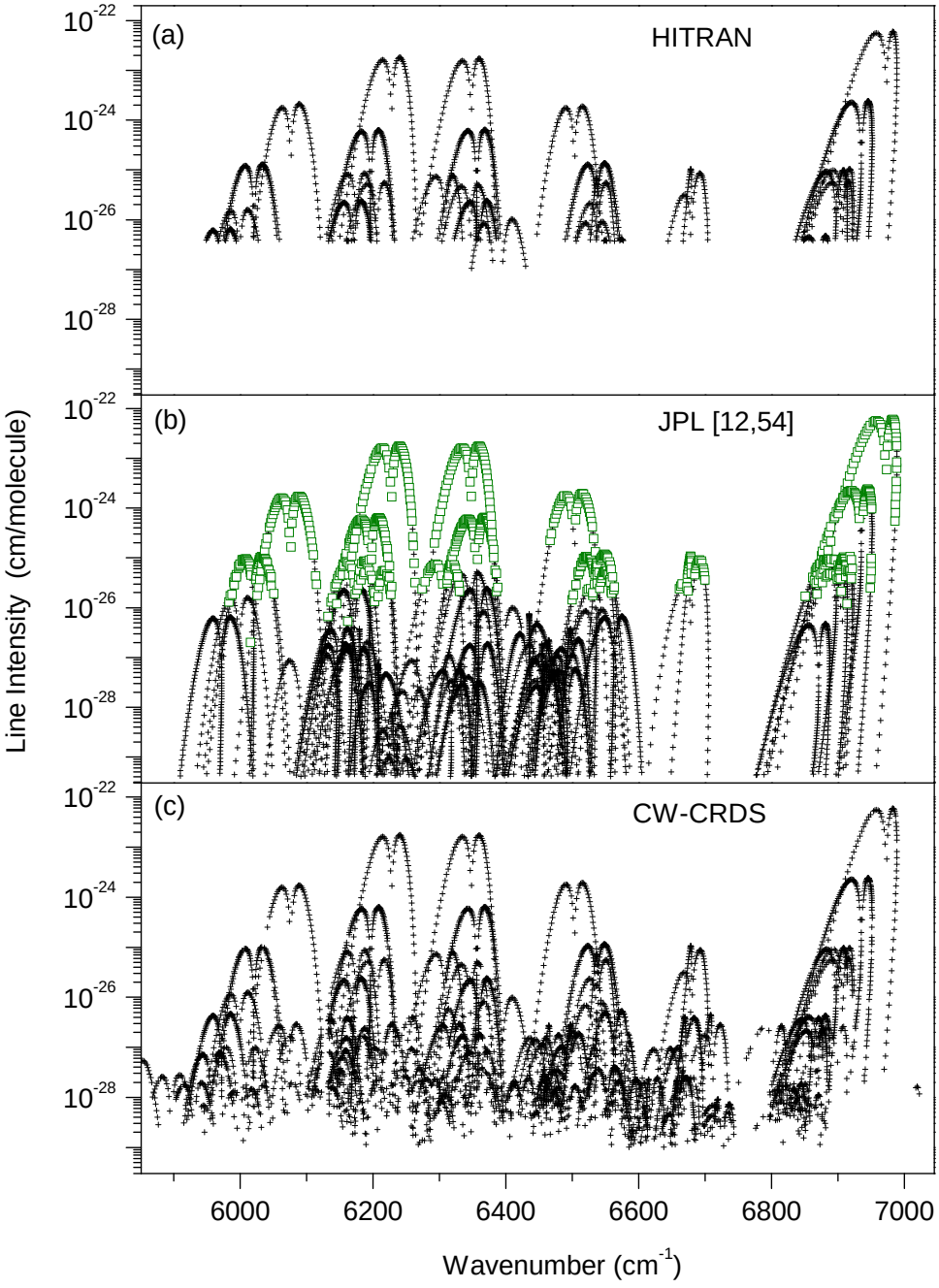

Figure 5.1. Overview of the absorption spectrum of $^{12}C^{16}O_2$ in the 5851–7045 cm^{-1} region. Note the logarithmic scale adopted for the line intensities. (a) HITRAN database [8]. (b) JPL database [12]. The open squares correspond to the transitions observed by Toth et al. [54], other lines are extrapolated or theoretically predicted transitions. (c) CW-CRDS spectrum calculated by using the measured line positions and using the effective dipole moment parameters.

Table 5.1. Comparison of the number of bands and transitions observed by CW-CRDS and in Venus spectra with those provided by different databases for eight isotopologues of carbon dioxide in the 5851–7045 cm^{-1} spectral region.

Molecule	Venus[a] [13]	HITRAN [8]		JPL[b] [12]		CDSD [11]		CRDS	
	bands	bands	lines	bands	lines	bands	lines	bands	lines
$^{12}C^{16}O_2$	40	28	1903	50(18)	6210(816)	247	19961	107	5604
$^{13}C^{16}O_2$	10	8	387	18(8)	1694(259)	99	6424	104	4881
$^{16}O^{12}C^{18}O$	9	7	467	15(3)	2713(179)	53	7080	24	1922
$^{16}O^{12}C^{17}O$	7	3	159	6	1017	9	1511	11	767
$^{16}O^{13}C^{18}O$	2	0	0	4(1)	446(55)	16	1729	28	2466
$^{16}O^{13}C^{17}O$	0	0	0	2	184	9	990	11	992
$^{13}C^{18}O_2$	0	0	0	0	0	0	0	4	170
$^{17}O^{13}C^{18}O$	0	0	0	0	0	0	0	3	130
Total	46	46	2916	95(30)	12264(1309)	433	37695	292	16932

[a]Number of bands observed in Venus spectra [13]. The complete line list is not available.
[b]The number between parenthesis corresponds to the number of line positions measured by FTS, according to the Supplementary materials of Refs. [50, 53, 54, 56]

modelling [8, 25]. The HITRAN intensity cut-off for CO_2 line intensities (in natural abundance) is 3.7×10^{-27} cm/molecule in our region that is about two orders of magnitude above the CW-CRDS detectivity. The comparison presented in Fig. 5.1 for $^{12}C^{16}O_2$ shows that the HITRAN database is complete in the sense that, above the adopted intensity cut-off no bands are missing compared to our observations.

The systematic comparison of the $^{12}C^{16}O_2$ line positions (Fig. 5.2) shows that the $(\nu_{\mathrm{HITRAN}} - \nu_{\mathrm{CRDS}})$ deviations are limited to 0.026 cm^{-1} at maximum, the largest discrepancies being observed for hot bands such as 31114-01101, 31113-01101, 40014-10002, 40012-10001 and 01131-01101. Fig. 5.2 includes a comparison of the line positions with the GEISA database. In the considered region, the HITRAN and GEISA databases mostly coincide. The GEISA database was constructed in the similar way as the HITRAN database but more information has been taken from global effective operators modeling. The same intensity cut-off has been adopted. However, large $(\nu_{\mathrm{GEISA}} - \nu_{\mathrm{CRDS}})$ discrepancies (up to 0.3 cm^{-1}) is noted for a few bands in particular for the 32212e-02201e sub-band (interestingly the associated 32212f-02201f sub-band is found in good agreement with our measurements).

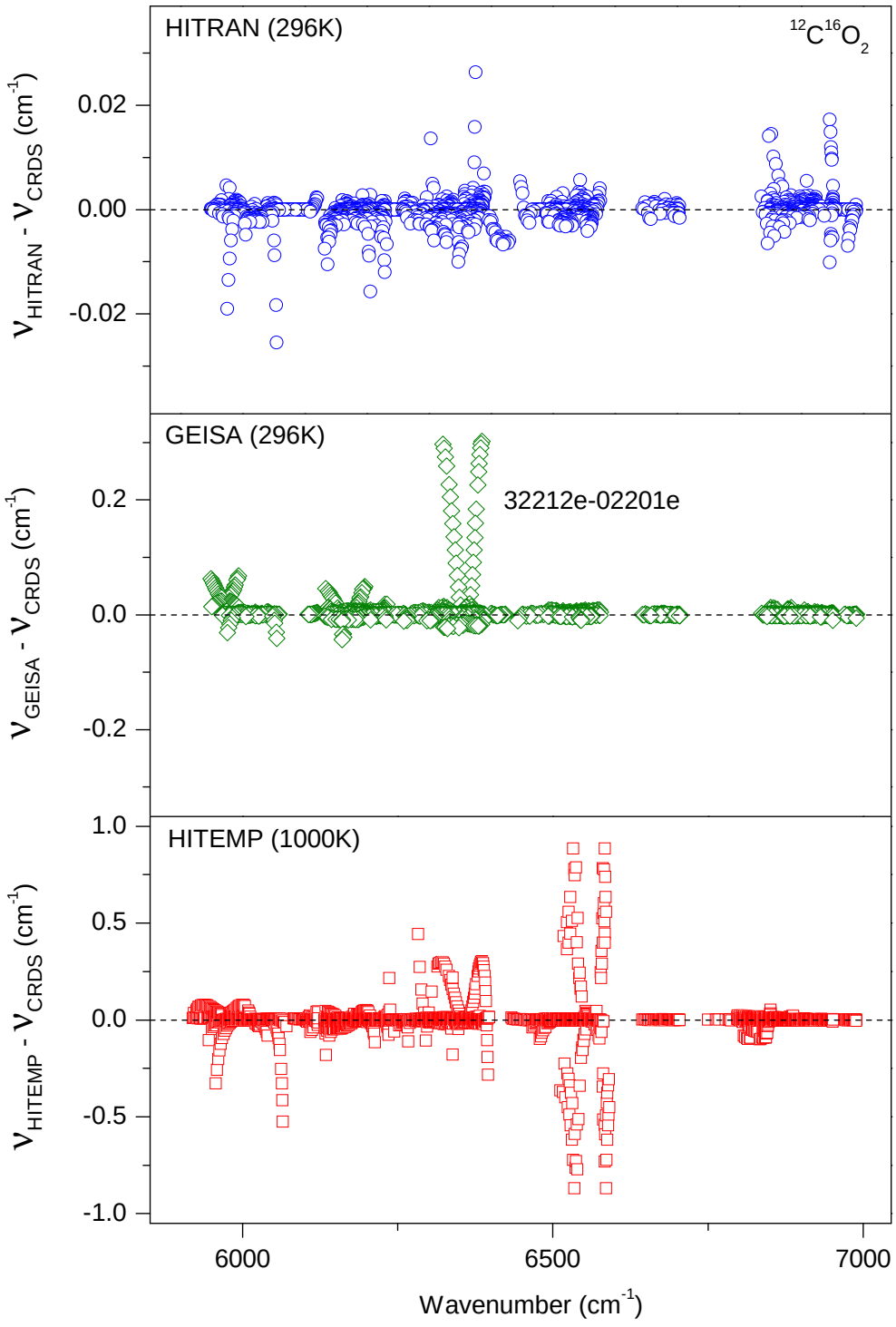

Figure 5.2. Residuals between the $^{12}C^{16}O_2$ measured line positions and those provided by HITRAN, GEISA and HITEMP databases in the 5851–7045 cm^{-1} spectral region, versus the wavenumber. *Top panel*: HITRAN database (296 K) [8]. *Middle panel*: GEISA database (296 K) [9]. *Bottom panel*: HITEMP database (1000 K) [10]. Note that the comparison with the HITEMP database is limited to the lines which are provided with a vibrational assignment in HITEMP (see text).

In the case of principal isotopologue our intensity measurements were limited to the four weak absorption regions (see Section 4.2). In order to check the HITRAN line intensities in the full spectral region of interest we use the intensity values calculated by effective dipole moment model which reproduce *all* the data available in literature and newly obtained experimental line intensities within their experimental uncertainty (see Section 4.3.2). The comparison of our calculated line intensities with those contained in the current version of the HITRAN database [8] shows rather large residuals for some of the hot bands and weak cold bands (see Fig. 5.3). The HITRAN intensities for these bands were calculated using the DND approach [19]. We also note significant residuals even for the strongest bands, 30012-00001 and 30013-00001, in particular for high values of the angular momentum quantum number J. This is due to the fact that the HITRAN line intensities for these two bands are based on measurements [75, 76] with poor accuracies for high J values. Our observations agree with the discussion included in Ref. [54].

5.3 The HITEMP database

Fig. 5.2 includes a comparison for the line positions with the HITEMP database [10] which is the high-temperature ($T_{\rm ref}$ = 1000 K) counterpart of HITRAN. Overall, HITEMP includes 1032269 lines of eight major isotopologues of CO_2. Data of the five less abundant isotopologues ($^{16}O^{12}C^{17}O$, $^{16}O^{13}C^{18}O$, $^{16}O^{13}C^{17}O$, $^{12}C^{18}O_2$, $^{17}O^{12}C^{18}O$) were transferred from HITRAN without any change. The HITEMP data for $^{12}C^{16}O_2$, $^{13}C^{16}O_2$ and $^{16}O^{13}C^{18}O$ are mostly calculated DND data. For these isotopologues, an intensity cut-off of 3×10^{-27} cm/molecule at 1000 K was used. Then all the intensity values were re-scaled to 296 K resulting to the minimal $^{12}C^{16}O_2$ intensity as low as 3.9 10^{-53} cm/molecule. Rotational assignment (branch, J value) is provided for all the lines but only 407308 lines are fully vibrationally assigned. The HITEMP database provides 13970 $^{12}C^{16}O_2$ transitions in our region but the comparison of Fig. 5.2 is limited to the 2816 transitions which are provided with a complete rovibrational assignment. The DND origin of most HITEMP data explains the large ($\nu_{\rm HITEMP} - \nu_{\rm CRDS}$) discrepancies (up to 0.9 cm^{-1}) which are observed for some of the bands which could be compared.

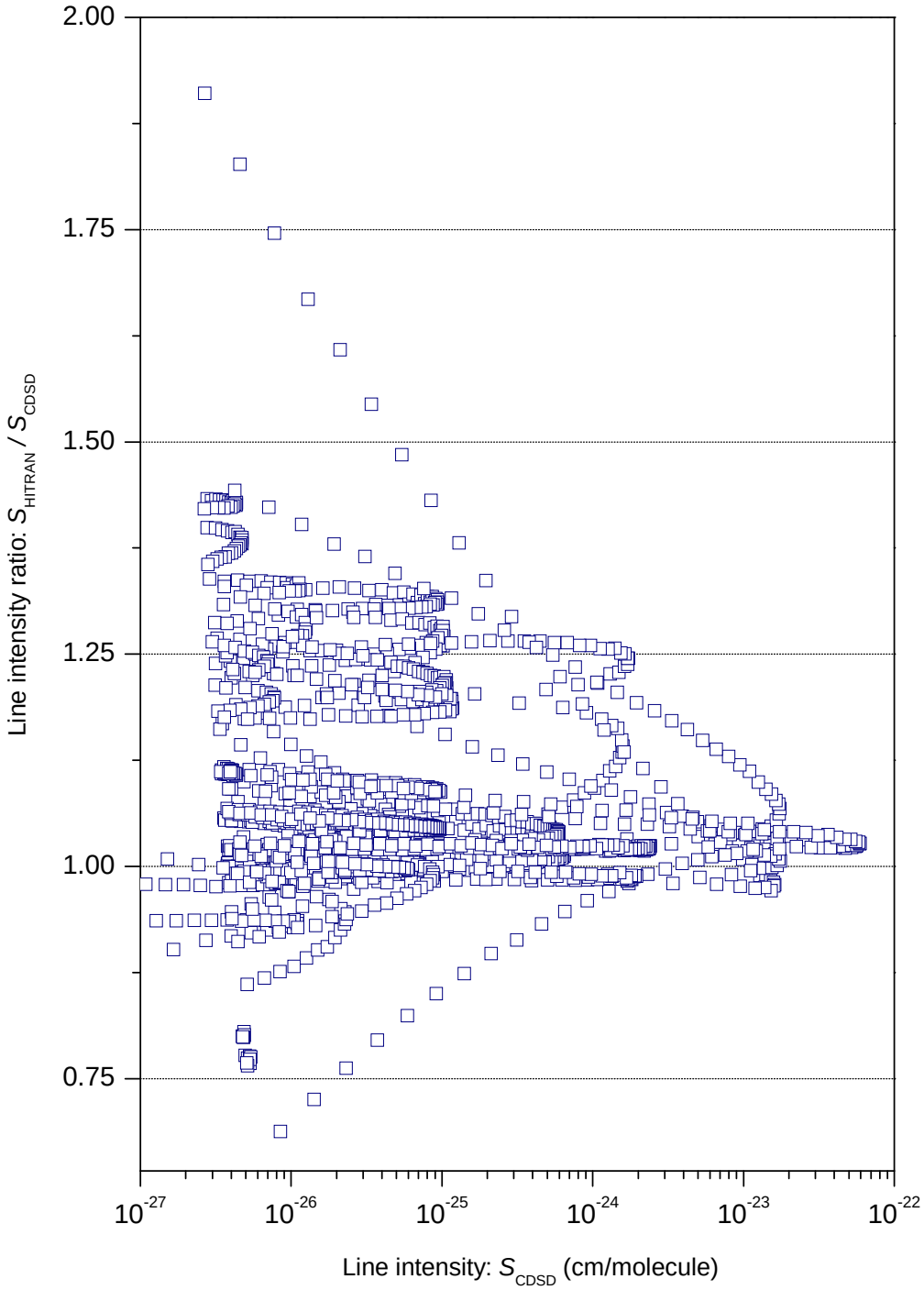

Figure 5.3. Ratio of the $^{12}C^{16}O_2$ line intensities provided in the HITRAN database [8] to the ones given in the CDSD database [11], plotted as a function of the CDSD line intensities. Note the logarithmic scale adopted for the ordinate scale.

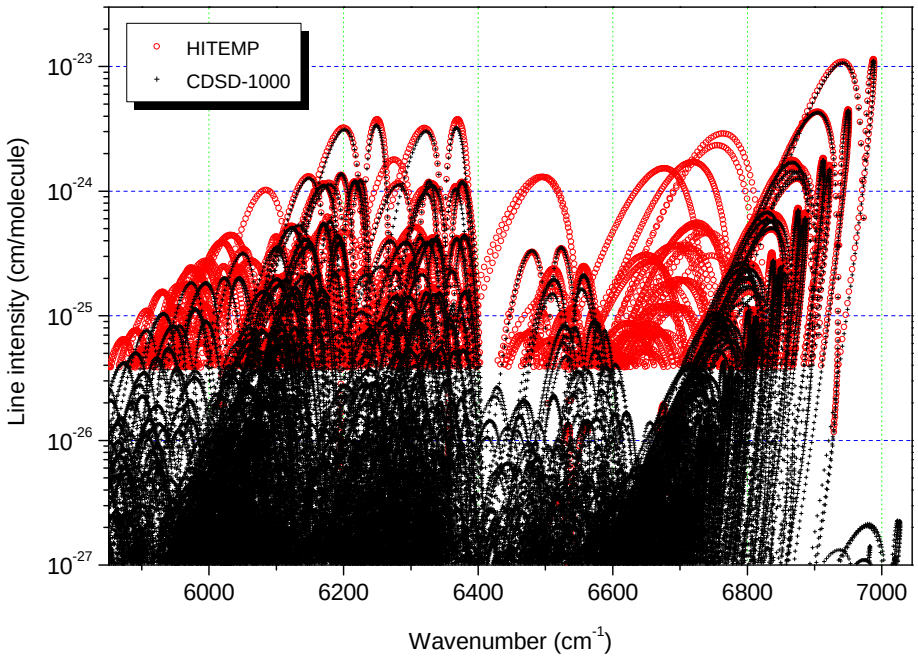

Figure 5.4. Overview of the absorption spectra of $^{12}C^{16}O_2$ in the 5851–7045 cm^{-1} region as provided by HITEMP [10] and CDSD–1000 [11] databases. Note the logarithmic scale adopted for the line intensities.

The line intensities contained in HITEMP database [10] can be compared with our calculated values at temperature of 1000 K as included in CDSD–1000 (high temperature version of CDSD database [11]). Visual comparison of spectra provided by HITEMP [10] and CDSD–1000 [11] databases (see Fig. 5.4) shows that the differences between their line intensities can exceed several orders of magnitude. We believe that these large discrepancies are caused by inaccurate DND predictions which represent the most part of HITEMP data.

5.4 The JPL database

Important experimental results were obtained during the last years at JPL by FTS using natural and isotopically enriched carbon dioxide. They were reported in a series of six publications [50, 53, 54, 56, 88, 89] and include measurements of line strengths and self- and air-broadening and shifting parameters. These results are excellent in terms of accuracy: line positions were reported with accuracy always better than 5×10^{-4} cm^{-1}

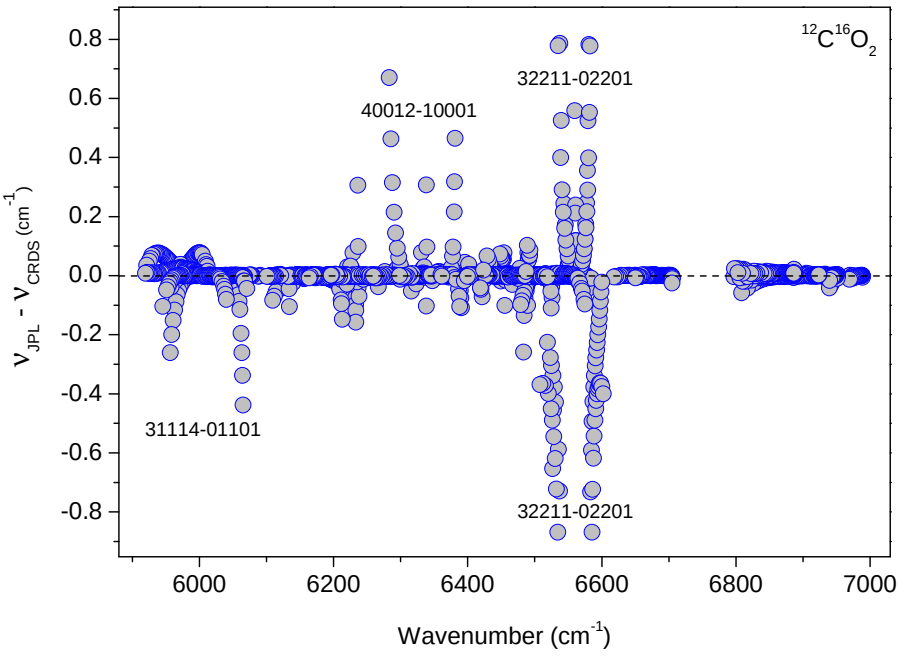

Figure 5.5. Residuals between line positions provided by the JPL database [12] and those measured by CW-CRDS.

(in the fit of the rotational constants, RMS residuals as small as 5×10^{-5} cm^{-1} were achieved for the stronger lines), and the reported line intensities are thought to be accurate to 1% for the major isotopologue [54]. However, only 18 $^{12}C^{16}O_2$ bands were reported in our region (see Fig. 5.1). Indeed, in spite of absorption path lengths up to 409 m, the achieved detectivity threshold in JPL spectra was limited to intensity values on the order of 1×10^{-26} cm/molecule for the main isotopologue, i.e. three orders of magnitude above the CW-CRDS sensitivity.

The recently published JPL database builds upon these considerable experimental efforts. It was constructed for the 4300–7000 cm^{-1} region [12] independently of results previously obtained by CW-CRDS in our laboratory [14, 15, 41]. Overall, the JPL database provides 213 bands of nine CO_2 isotopologues (see the $^{12}C^{16}O_2$ overview spectrum included in Fig. 5.1). Some of the transitions of 153 bands were observed by FTS [54–56], while the line parameters of all the transitions of the 60 remaining bands were obtained by DND or transferred from the present version of HITRAN. The procedure adopted by Toth et al. for the 153 bands observed in their FTS spectra, was

to fit the rovibrational constants (G_v, B_v, D_v and H_v, see Eq. (3.1)), band strengths and Herman Wallis coefficients (see Section 1.3.2) to the accurate experimental line positions and intensities, respectively, and then to include the corresponding computed values in the database. Consequently, very accurate positions and intensities are provided for the transitions where direct measurements were performed. But the line list attached to each of the 153 bands extends far beyond the quantum numbers for which direct FTS measurements were made. In other words, extrapolated values were provided for many weak unobserved lines beyond the FTS detection limit. Toth et al. have chosen to fix to a very low value (4×10^{-30} cm/molecule) the lower intensity cut-off of their database. This value which is far below the FTS detection limit, has led to long range extrapolations to high J values far beyond the quantum numbers for which direct FTS measurements were made (see Fig. 5.1). The very quick increase of the contribution of the distortion terms for high J values is responsible of important deviations between the extrapolated values and our observations (see Fig. 5.5). Another related issue is the inclusion of weak bands unobserved by FTS which were calculated. For instance, in our region, the JPL database provides 50 bands for $^{12}C^{16}O_2$ but only 18 of them were observed by FTS at JPL [54]. The JPL database intensity cut-off is even below our CRDS detection limit (about 1×10^{-29} cm/molecule) which explains that the amount of transitions provided by the JPL database is in fact significantly larger than our set of observations. Nevertheless, the JPL database is far to be complete as many weak bands above the intensity cut-off are missing (see Fig. 5.1). It leads to a paradoxical situation: for $^{12}C^{16}O_2$, the JPL database includes 50 bands and 6210 transitions while we could observe 107 bands but only 5604 transitions.

Fig. 5.6 shows the comparison of our line intensities with those provided in the JPL database [12] and with those measured at JPL [54]. A good agreement is noted with the measured line intensities whereas the residuals between our measurements and the line intensities extrapolated (or theoretically predicted) at JPL can exceed one order of magnitude. The major reason of these disagreements is that simple empirical expansions of the transition moment squared in terms of vibrational moment squared and Herman-Wallis parameters, as used for the transitions beyond JPL observations, cannot be applied in the case of perturbed bands. Moreover, the choice of a low intensity cut-off

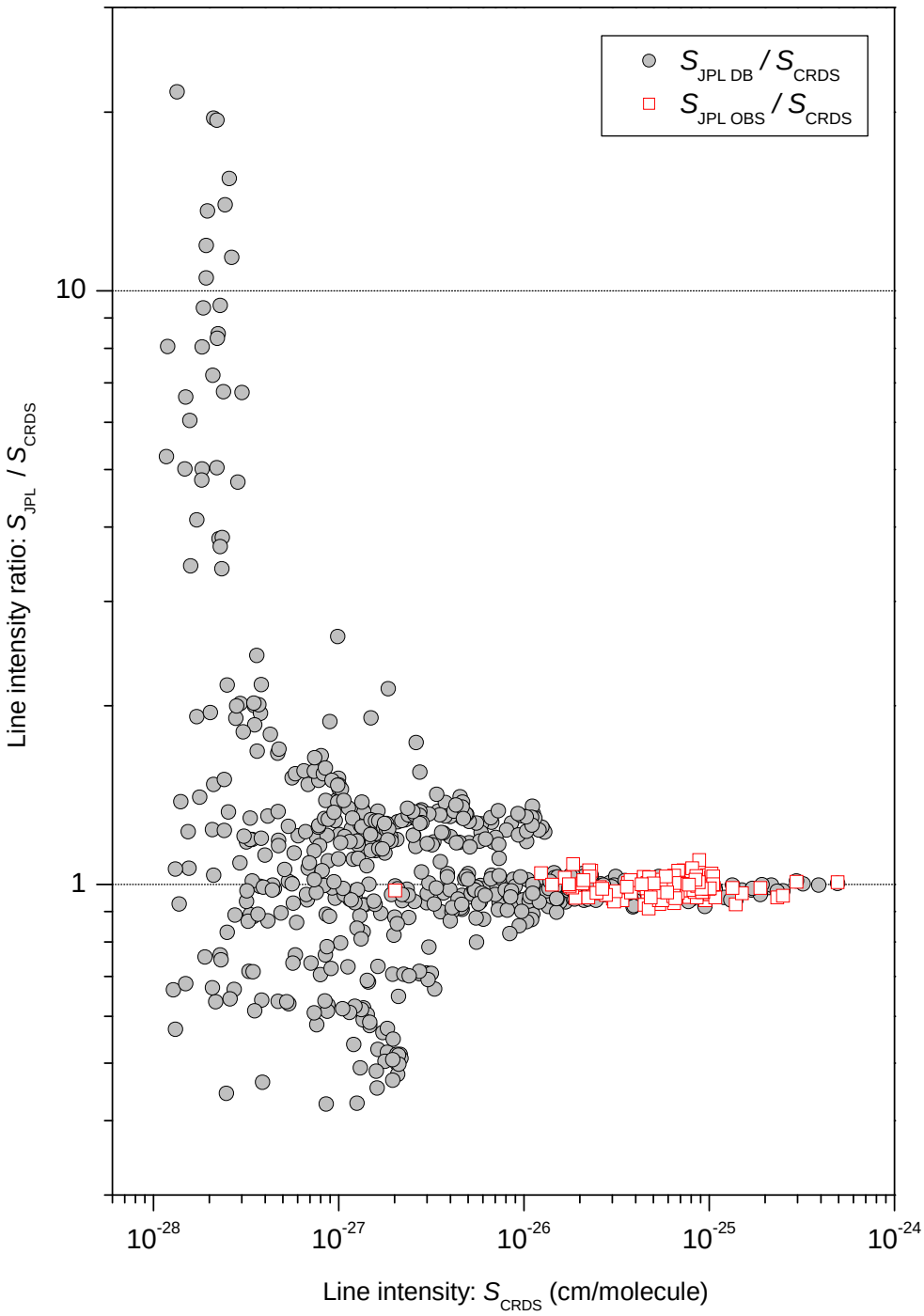

Figure 5.6. Ratio of the $^{12}C^{16}O_2$ line intensities provided in the JPL database [12] to the ones measured by CW-CRDS, plotted as a function of the CW-CRDS intensity values. The JPL database includes measured values [50] and extrapolated (or calculated) values; the corresponding ratios are plotted with open squares and full circles respectively.

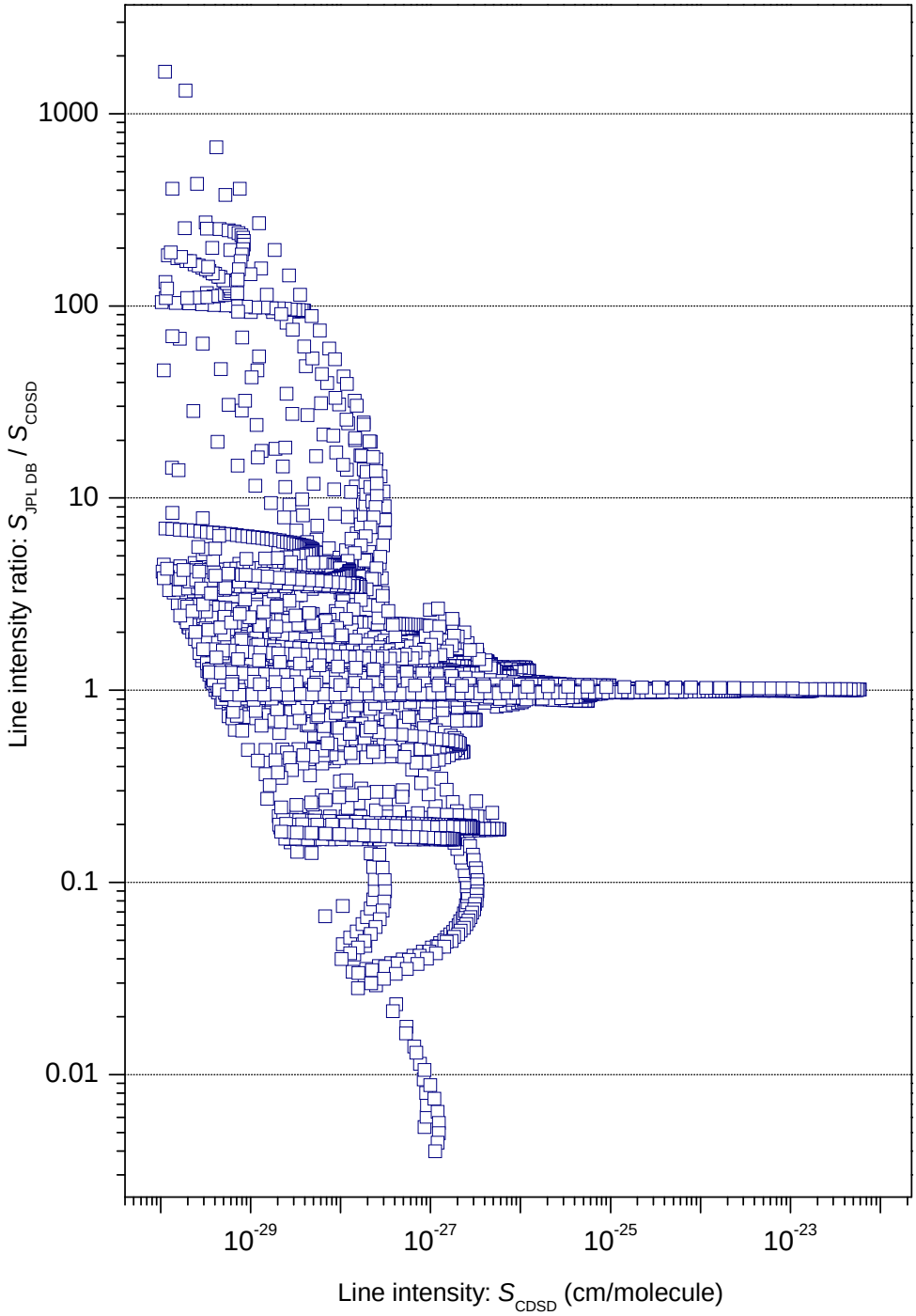

Figure 5.7. Ratio of the $^{12}C^{16}O_2$ line intensities given in the JPL database [12] to the ones provided in the CDSD database [11] (extrapolated or calculated) plotted as a function of the CDSD line intensities. Note the logarithmic scale adopted for the ordinate scale.

(4×10^{-30} cm/molecule) forces long range extrapolations on the angular momentum quantum number J. Such extrapolations are particularly hazardous as occurrences of perturbations are expected to increase with J values. Indeed, Fig. 5.7 shows that the ratios of the CDSD intensities to the (mostly extrapolated) JPL intensities [12] range from 0.004 to 1000, reflecting the poor extrapolation capabilities of the empirical model used in Ref. [12].

Of crucial importance for the potential user of the database is the possibility to know if line parameters were theoretically predicted, extrapolated or supported by laboratory measurements. This information is absent in the present version of the JPL database [12]. This situation leads to provide with apparent equivalent accuracy line parameters at the state of the art level when based on JPL measurements together with hazardous extrapolations or inaccurate theoretical predictions.

The JPL database [12] was presented by its authors as the next HITRAN update. However, the comparison with our CW-CRDS $^{13}C^{16}O_2$ spectrum in the 5851–7045 cm^{-1} region published as a Comment [87], has evidenced the important deviations between the line parameters provided in the database and our previous observations both for line positions (up to 1.7 cm^{-1}) and line intensities (up to a factor 80). After our publication the observed CW-CRDS data and CDSD predictions were chosen for the HITRAN update below the FTS detection limit.

5.5 The CDSD database

The effective operators models used in this thesis for global modeling of lines positions and intensities is a preferable alternative when accurate experimental parameters are not available. These models which use as input data *all* the experimental data available for each isotopologue with their corresponding uncertainty already benefited from the considerable experimental effort performed both at JPL by FTS and in our laboratory by CW-CRDS including the present results. As data reproduction close to the experimental uncertainty is achieved both for line positions and line intensities (see Chapters 3 and 4), the global effective operators models constitute a very powerful approach for the most *accurate* and *complete* CO_2 database. In particular

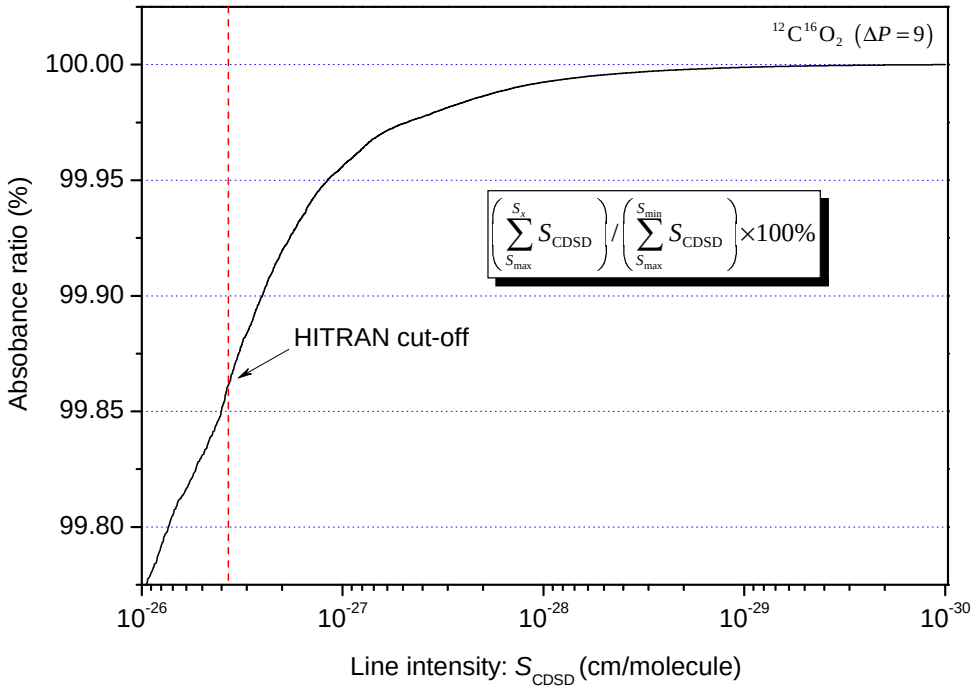

Figure 5.8. The ratios of the integrated absorbances calculated with a given lower intensity cut-off to the overall absorbance of all the $^{12}C^{16}O_2$ transition (cut-off 10^{-30} cm/molecule) belonging to $\Delta P = 9$ series as included in the new version of CDSD database [11], versus the CDSD line intensity.

accidental resonances, intensity transfers and extra lines are accurately accounted for and predicted by these polyad models. The effective operators models have been used to generate the line lists for seven CO_2 isotopologues ($^{12}C^{16}O_2$, $^{13}C^{16}O_2$, $^{16}O^{12}C^{18}O$, $^{16}O^{12}C^{17}O$, $^{16}O^{13}C^{18}O$, $^{16}O^{13}C^{17}O$ and $^{12}C^{18}O_2$) with an intensity cut-off fixed to a value of 10^{-30} cm/molecule. These line lists have been included in the new version of CDSD database [11].

The drawbacks of the effective operators models and, consequently, CDSD database [11] are the following: (i) The high precision experimental line positions measured at JPL cannot be reproduced within their experimental accuracy. Moreover, our CW-CRDS line positions are reproduced with RMS value of about 2×10^{-2} cm^{-1} while we estimate our accuracy to be about 1×10^{-2} cm^{-1} (see Section 3.3.2). (ii) A very minor limitation of the polyad models is that four occurrences of interpolyad resonance interaction were evidenced in this thesis for the first time in the case of carbon dioxide.

Table 5.2. Summary of advantages and drawbacks of different databases.

	Advantages	**Drawbacks**
HITRAN, GEISA	• Complete above 4×10^{-27} cm/molecule	• Not sensitive • Deviations < 0.025 cm^{-1} (< 0.25 cm^{-1} for GEISA)
JPL	• Very accurate observations for the strongest bands • Pressure shifts and self and air broadening coefficients	• Incomplete • Too long range extrapolation • Some very large deviations • Traceability
HITEMP		• Incomplete • Very large deviations
CDSD	• Complete for $^{12}C^{16}O_2$, $^{13}C^{16}O_2$, $^{12}C^{18}O_2$	• Interpolyad coupling are not included • Cannot reproduce JPL accuracy
	• Excellent predictive abilities	• A factor of 2 worse than the CRDS accuracy for line centers of the weak bands

These interactions are not yet taken into account in the global model. Although these resonance interactions are very seldom in the case of CO_2, a very few deviations of the predicted line positions and line intensities values from their real values cannot be ruled out. (iii) The parameters of both effective Hamiltonian and effective dipole moment models of five minor isotopologues still suffer of a lack of experimental data in various spectral regions. The full sets of effective dipole moment parameters for $\Delta P = 9$ series of transitions are available only for $^{12}C^{16}O_2$ and $^{13}C^{16}O_2$ isotopologues. We have found that the sets of effective dipole moment parameters of different isotopologues for any series of transitions do not differ considerably each from other. Because of this in the case of the $\Delta P = 9$ series of transitions we used the sets of the effective dipole moment parameters of the $^{12}C^{16}O_2$ and $^{13}C^{16}O_2$ isotopologues to calculate line intensities of other five isotopologues. We estimate that it can introduce an error of 20% in their calculated line intensities. The bands belonging to the $\Delta P = 8$ and 10 series of transitions which could be observed for asymmetric species are not yet included in CDSD

database [11] because the respective effective dipole moment parameters are not yet available.

It is instructive to estimate the impact of the weak lines not included in the HITRAN [8] and GEISA [9] databases in the overall absorbance. For this purpose we have calculated the ratios of integrated absorbances with variable lower intensity cut-off to the overall absorbance of all the $^{12}C^{16}O_2$ transition (cut-off 10^{-30} cm/molecule) belonging to $\Delta P = 9$ series as included in the new version of CDSD database [11] (see Fig. 5.8). Fig. 5.8 illustrates that all the lines lying below the HITRAN intensity cut-off (3.7×10^{-27} cm/molecule) represents only 0.24% of the total absorbance of all the $\Delta P = 9$ transitions. Obviously, in the regions of weak absortion the impact of these missed weak lines will be much more significant.

Conclusion

Cette thèse présente une analyse du spectre du dioxyde de carbone obtenu par la technique Cavity Ring Down Spectroscopy dans la région allant de 1.4 à 1.7 μm. Au total, environ 8000 raies provenant de huit isotopologues ont été mesurées avec la sensibilité extrêmement élevée que permet la technique CRDS, et les constantes spectroscopiques de 238 bandes ont ainsi été déterminées. Ceci a permis d'améliorer significativement les paramètres des Hamiltoniens effectifs de six de ces isotopologues. Quatre cas de résonance inter-polyades ont par ailleurs été observés pour la première fois. Enfin un travail sur les intensités des bandes de $^{13}C^{16}O_2$ et $^{12}C^{16}O_2$ a été effectué. En combinant les intensités mesurées sur près de 3000 raies faibles avec d'autres données dans la littérature, les paramètres du moment dipolaire effectif ont été nettement améliorés. Tout ce travail a produit des modèles d'opérateurs effectifs qui ont été utilisés pour générer des listes de raies de CO_2 qui ont été incluses dans la nouvelle version de la base de données CDSD. Les raies faibles mesurées par CRDS et celles calculées pour la base CDSD ont été incluses dans la nouvelle version de la base de données HITRAN.

The work presented in this thesis was focused on the the investigations of the high resolution infrared spectra of CO_2 molecule near 1.6 μm: experimental measurements and theoretical modeling of line positions and strengths. This work aimed to increase the experimental dataset available for the global modeling of carbon dioxide spectra by the effective operators approach in order to provide the most *accurate* and *complete* line list for the new version of CDSD database [11]. The presented results were published in seven contributions [35, 41–44, 48, 87]. The CW-CRDS technique allows also measurements of other line parameters such as line width, line shift and exponents of

temperature dependences. However, this measurements were out of scope of the present research.

The CW-CRDS spectra of natural and ^{13}C-enriched carbon dioxide in the 5851–6130 and 6750–7045 cm^{-1} regions were recorded and analysed, the spectra in the previously investigated 6130–6750 cm^{-1} region [14, 15] were re-examined in order to reduce the fraction of unassigned lines. Only about 5% of lines we have left unassigned and we believe that most part of these remaining unidentified transitions is due to impurities. The newly observed results represent a significant extension of the available data. About 8000 transitions belonging to eight CO_2 isotopologues ($^{12}C^{16}O_2$, $^{13}C^{16}O_2$, $^{16}O^{12}C^{18}O$, $^{16}O^{12}C^{17}O$, $^{16}O^{13}C^{18}O$, $^{16}O^{13}C^{17}O$, $^{13}C^{18}O_2$, $^{17}O^{13}C^{18}O$) were newly observed increasing the total number of CO_2 line positions measured by CW-CRDS in the 5851–7045 cm^{-1} region to the value of 16932 while only 2916 lines are listed in the current version of HITRAN database [8]. We have retrieved rovibrational parameters for a total of 238 bands belonging to eight CO_2 isotopologues (see Appendix) which correspond to a total of 213 vibrational upper states as several upper states are accessed through different bands. A number of resonance intersections perturbing upper states were observed and identified. The newly observed line positions were added to the input datasets in order to refine the effective Hamiltonian parameters for six CO_2 isotopologues. The fitted sets of effective Hamiltonian parameters reproduces the line positions from all involved experimental sources close to their experimental uncertainties.

Because of the high linearity and the large dynamics of the CW-CRDS spectra the accurate line intensities down to 10^{-28} cm/molecule could be measured. The line strengths of 2039 transitions were obtained for $^{13}C^{16}O_2$ isotopologue in the 5851–6580 cm^{-1} region. Thirty percents of these measured intensities belong to perpendicular and "forbidden" bands. In the case of the principal isotopologue we have measured 952 line intensities in four spectral intervals of weak absorption: 5851–5881, 5972–6035, 6373–6542 and 6622–6750 cm^{-1}. The fraction of the measured intensities belonging to perpendicular and "forbidden" bands was 60% in these specific spectral regions. Using the effective dipole moment model, we have performed the least-squares fittings of the line intensity sets obtained by gathering the CW-CRDS results with the selected intensity data reported in the literature for the $\Delta P = 9$ series of transitions. The fitted sets

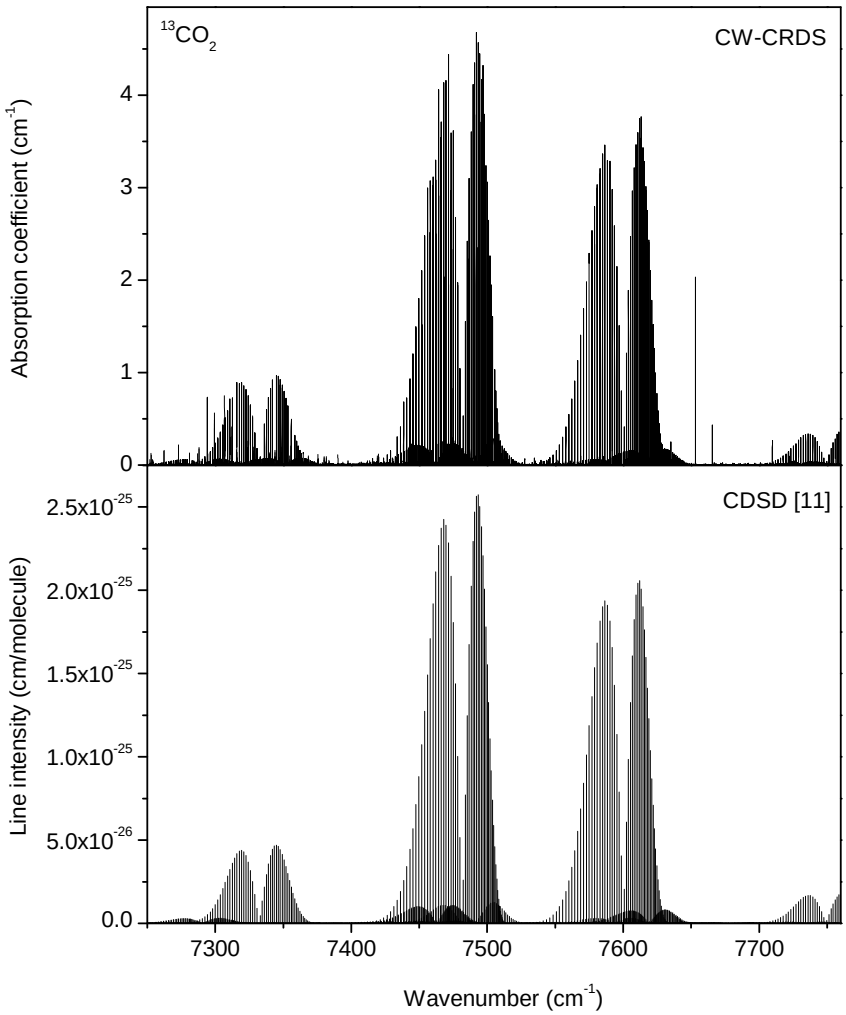

Figure 5.9. The spectra of ^{13}C-enriched carbon dioxide in the 7250–7760 cm^{-1} region. *Top panel*: The experimental spectra recorded by CW-CRDS. *Lower panel*: The stick spectrum provided by CDSD database [11].

of effective dipole moment parameters reproduces the line intensities from all involved experimental sources within their uncertainties.

Our measurements had a great impact on the global modeling of high resolution spectra of carbon dioxide. They allowed to refine and extend the sets of effective dipole moment and effective Hamiltonian parameters. A data reproduction close to the experimental uncertainty is achieved both for the line positions and intensities. In particular accidental resonances, intensity transfers and extra lines are accurately accounted for and predicted by these polyad models of effective Hamiltonian and effective dipole mo-

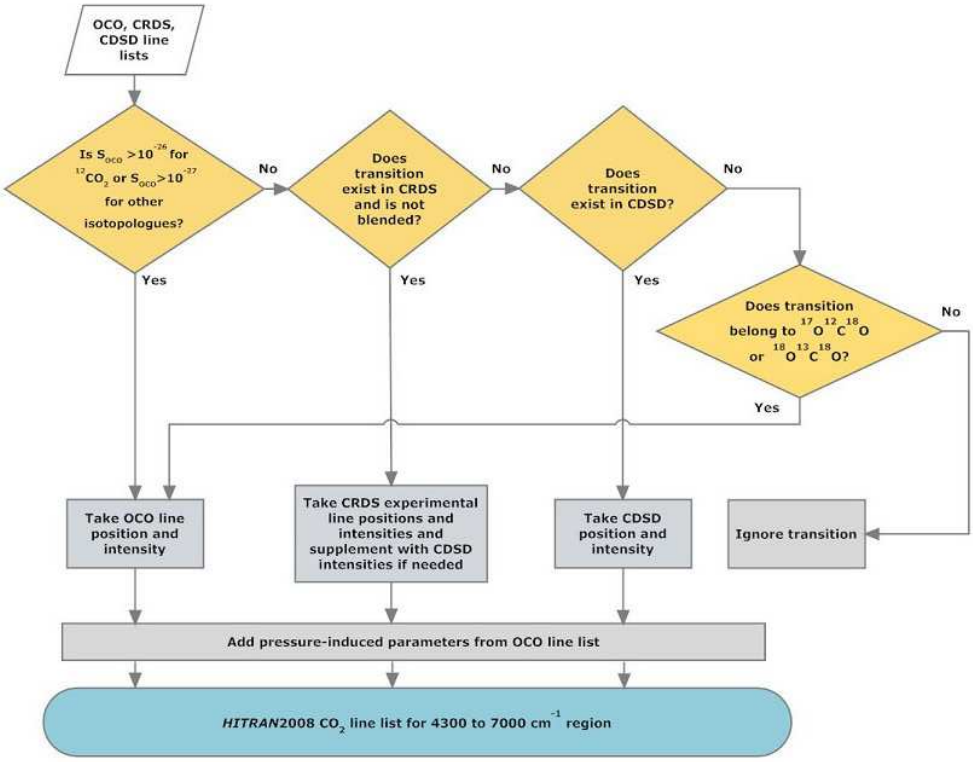

Figure 5.10. Scheme of the construction of a new version of the HITRAN database for carbon dioxide. OCO is the JPL database [12].

ment operator. Four occurrences of interpolyad resonance interaction were evidenced in this work for the first time in the case of carbon dioxide. It constitutes minor limitation of the polyad models of effective Hamiltonian and effective dipole moment operator. All these interpolyad resonance interactions affecting the bands of non-symmetric CO_2 isotopologues are of anharmonic type: $^{16}O^{12}C^{18}O$: 1 occurrence [43], $^{16}O^{13}C^{18}O$: 2 occurrences [42, 48], $^{16}O^{13}C^{17}O$: 1 occurrence [48]. These interactions are not yet taken into account in the global modeling. The interpolyad resonance interactions are very seldom in the case of carbon dioxide, so only few deviations of the predicted line positions and line intensities values from their real values cannot be ruled out.

The effective operators models have been used to generate the line lists for seven CO_2 isotopologues ($^{12}C^{16}O_2$, $^{13}C^{16}O_2$, $^{16}O^{12}C^{18}O$, $^{16}O^{12}C^{17}O$, $^{16}O^{13}C^{18}O$, $^{16}O^{13}C^{17}O$ and $^{12}C^{18}O_2$) which were included in the new version of CDSD database [11].

The present work has also a great impact on the further experimental study of carbon

dioxide spectra. The new CW-CRDS setup which covers the 7000–7760 cm^{-1} region has been developed by S. Kassi in our laboratory and the spectra of natural and ^{13}C-enriched carbon dioxide are already recorded in the 1.3 μm region which corresponds to the $\Delta P = 11$ series of transitions. To our knowledge, the experimental data available for carbon dioxide in this region are limited but the CDSD database [11] improved due to our researches contains the predicted spectra corresponding to this series of transitions. The rough comparison of newly recorded CW-CRDS spectra of ^{13}C-enriched carbon dioxide with those provided by CDSD database [11] shows an overall good agreement between the observed and predicted spectra corresponding to this series of transitions (see Fig. 5.9). The same iterative process will be used in the future analysis of the 7000–7760 cm^{-1} region: the predictions of the CDSD database will help for the rovibrational assignment of the spectra and our CRDS observations will allow to feed the input data of the EH models and to improve their parameters.

Probably the most important recognition of this work is that the line lists provided by CDSD database [11] and our experimental data have just been adopted for the 2008 version of HITRAN database together with JPL data [12]. The new version of HITRAN database is constructed according to the scheme presented in Fig. 5.10.

References

[1] D. Crisp, R.M. Atlas, F.M. Breon, L.R. Brown, J.P. Burrows, P. Ciais, B.J. Connor, et al. *Adv. Space Res.* **34**, 700–709 (2004).

[2] Greenhouse gases Observing SATellite, http://gosat.nies.go.jp/.

[3] D.V. Titov, H. Svedhem, D. McCoy, J.-P. Lebreton, S. Barabash, J.-L. Bertaux, et al. *Cosmic. Res.* **44**, 334–348 (2006).

[4] D. Nevejans, E. Neefs, E. Van Ransbeeck, S. Berkenbosch, R. Clairquin, L. De Vos et al. *Appl. Opt.* **45**, 5191–5206 (2006).

[5] J.E. Graf, R.W. Zurek, J.K. Erikson, B. Jai, M.D. Johnston, R. De Paula. *Acta Astron.* **61**, 44–51 (2007).

[6] J. Bailey, A. Simpson, D. Crisp. *Publ. Astron. Soc. Pacific.* **119**, 228–236 (2007).

[7] V.A. Krasnopolsky. *Icarus* **185**, 153–170 (2006).

[8] L.S. Rothman, D. Jacquemart, A. Barbe, D. Chris Benner, M. Birk, L.R. Brown, M.R. Carleer, C. Chackerian Jr., K. Chance, V. Dana, V.M. Devi, J.-M. Flaud, R.R. Gamache, A. Goldman, J.-M. Hartmann, K.W. Jucks, A.G. Maki, J.-Y. Mandin, S.T. Massie, J. Orphal, A. Perrin, C.P. Rinsland, M.A.H. Smith, J. Tennyson, R.N. Tolchenov, R.A. Toth, J. Vander Auwera, P. Varanasi, G. Wagner. *J. Quant. Spectrosc. Radiat. Transfer.* **96**, 139–204 (2005).

[9] N. Jacquinet-Husson, N.A. Scott, A. Chédin, L. Crépeau, R. Armante, V. Capelle, J. Orphal, A. Coustenis, C. Boonne, N. Poulet-Crovisier, A. Barbe, M. Birk, L.R. Brown, C. Camy-Peyret, C. Claveau, K. Chance, N. Christidis, C. Clerbaux, P.F. Coheur, V. Dana, et al. *J. Quant. Spectrosc. Radiat. Transfer.* **109**, 1043–1059 (2008).

[10] L.S. Rothman, R.B. Wattson, R.R. Gamache, J. Schroeder, A. McCann. *Proc SPIE* **2471**, 105–111 (1995).

[11] S.A. Tashkun, V.I. Perevalov, ftp://ftp.iao.ru/pub/CDSD-2008.

[12] R.A. Toth, L.R. Brown, C.E. Miller, V. Malathy Devi, D.Chris. Benner. *J. Quant. Spectrosc. Radiat. Transfer.* **109**, 906–921 (2008).

[13] J.-Y. Mandin. *J. Mol. Spectrosc.* **67**, 304–321 (1977).

[14] Z. Majcherova, P. Macko, D. Romanini, V.I. Perevalov, S.A. Tashkun, J.-L. Teffo, A. Campargue. *J. Mol. Spectrosc.* **230**, 1–21 (2005).

[15] Y. Ding, P. Macko, D. Romanini, V.I. Perevalov, S.A. Tashkun, J.-L. Teffo, S.-M. Hu, A. Campargue. *J. Mol. Spectrosc.* **226**, 146–160 (2004).

[16] I. Suzuki. *Bull. Chem. Soc. Japan.* **48**, 3565 (1975).

[17] R.J. Whitehead, N.C. Handy. *J. Mol. Spectrosc.* **55**, 356–373 (1975).

[18] R.B. Wattson, L.S. Rothman. *J. Mol. Spectrosc.* **119**, 83–100 (1986).

[19] R.B. Wattson, L.S. Rothman. *J. Quant. Spectrosc. Radiat. Transfer.* **48**, 763–780 (1992).

[20] J.-L. Teffo . *Molec. Phys.* **78**, 1493–1512 (1993).

[21] J.-L. Teffo; J.F. Ogilvie. *Molec. Phys.* **80**, 1507–1524 (1993).

[22] M.R. Aliev and D. Papousek. *Molecular vibrational-rotational spectra.* Elsevier, (1982).

[23] J.K.J. Watson. *Mol. Phys.* **19**, 465–487 (1970).

[24] A. Chédin. *J. Mol. Spectrosc.* **76**, 430–491 (1979).

[25] J.-L. Teffo, O.N. Sulakshina, V.I. Perevalov. *J. Mol. Spectrosc.* **156**, 48–64 (1992).

[26] S.A. Tashkun, V.I. Perevalov, J.-L. Teffo, L.S. Rothman, V.G. Tyuterev. *J. Quant. Spectrosc. Radiat. Transfer.* **60**, 785–801 (1998).

[27] S.A. Tashkun, V.I. Perevalov, J.-L. Teffo, M. Lecoutre, T.R. Huet, A. Campargue, D. Bailly, M.P. Esplin. *J. Mol. Spectrosc.* **200**, 162–176 (2000).

[28] V.I. Perevalov, O.N. Sulakshina, J.-L. Teffo. *J. Mol. Spectrosc.* **155**, 433–435 (1992).

[29] S.A. Tashkun and Vl.G. Tyuterev, "Proceedings of the 11^{th} Symposium and School on High-Resolution Molecular Spectroscopy" (A.I. Nadezhdinskii, Yu.N. Ponomarev and L.N. Sinitsa, Eds.). *SPIE* **2205**, 188–191 (1993).

[30] L. S. Rothman, R. L. Hawkins, R. B. Wattson, R. R. Gamache. *J. Quant. Spectrosc. Radiat. Transfer.* **48**, 537–566 (1992).

[31] V.I. Perevalov, E.I. Lobodenko, O.M. Lyulin, J.-L. Teffo. *J. Mol. Spectrosc.* **171**, 435–452 (1995).

[32] J.-L. Teffo, O.M. Lyulin, V.I. Perevalov, E.I. Lobodenko. *J. Mol. Spectrosc.* **1**, 28–41 (1998).

[33] S.A. Tashkun, V.I. Perevalov, J-L. Teffo, VI.G. Tyuterev. *J. Quant. Spectrosc. Radiat. Transfer.* **62**, 571–598 (1999).

[34] L. Wang, V.I. Perevalov, S.A. Tashkun, Y. Ding, S.-M. Hu. *J. Mol. Spectrosc.* **234**, 84–92 (2005).

[35] B.V. Perevalov, T. Deleporte, A.W. Liu, S. Kassi, A. Campargue, J. Vander Auwera, S.A. Tashkun, V.I. Perevalov. *J. Quant. Spectrosc. Radiat. Transfer.* **109**, 2009–2026 (2008).

[36] D. Romanini and K.K. Lehmann. *J. Chem. Phys.* **99**, 6287–6301 (1993).

[37] G. Meijer, M.G.H. Boogaarts, R.T. Jongma, D.H. Parker, A.M. Wodtke. *Chem. Phys. Lett.* **217**, 112–116 (1994).

[38] D. Romanini, A.A. Kachanov, N. Sadeghi, F. Stoeckel. *Chem. Phys. Lett.* **264**, 316–322 (1997).

[39] D. Romanini, A.A. Kachanov, F. Stoeckel. *Chem. Phys. Lett.* **270**, 538–545 (1997).

[40] J. Morville, D. Romanini, A.A. Kachanov, M. Chenevier. *Appl. Phys.* **B 78**, 465–476 (2004).

[41] B.V. Perevalov, S. Kassi, D. Romanini, V.I. Perevalov, S.A. Tashkun, A. Campargue. *J. Mol. Spectrosc.* **238**, 241–255 (2006).

[42] B.V. Perevalov, V.I. Perevalov, A. Campargue. *J. Quant. Spectrosc. Radiat. Transfer.* **109**, 2437–2462 (2008).

[43] B.V. Perevalov, S. Kassi, V.I. Perevalov, S.A. Tashkun, and A. Campargue. *J. Mol. Spectrosc.* **252** (2008).

[44] B.V. Perevalov, A. Campargue, B. Gao, S. Kassi, S.A. Tashkun and V.I. Perevalov. *J. Mol. Spectrosc.* **252**, 190–197 (2008).

[45] S. Kassi, D. Romanini, A. Campargue, B. Bussery-Honvault. *Chem. Phys. Lett.* **409**, 281–287 (2005).

[46] L. Daumont, L. Régalia-Jarlot, Vl.G. Tyuterev, M. Carleer, A.C. Vandaele, S. Mikhailenko and S. Fally. *J. Quant. Spectrosc. Radiat. Transfer.* **105**, 326–355 (2007).

[47] A. Chédin, J.-L. Teffo. *J. Mol. Spectrosc.* **107**, 333–342 (1984).

[48] B.V. Perevalov, S. Kassi, D. Romanini, V.I. Perevalov, S.A. Tashkun, A. Campargue. *J. Mol. Spectrosc.* **241**, 90–100 (2007).

[49] J.-L. Teffo, C. Claveau, A. Valentin. *J. Quant. Spectrosc. Radiat. Transfer.* **59**, 151–164 (1998).

[50] R.A. Toth, C.E. Miller, L.R. Brown, V. Malathy Devi, D.Chris. Benner. *J. Mol. Spectrosc.* **251**, 64–89 (2008).

[51] S.A. Tashkun, V.I. Perevalov, and J.-L. Teffo. *J. Mol. Spectrosc.* **210**, 137–145 (2001).

[52] L. Wang, V.I. Perevalov, S.A. Tashkun, K.-F. Song, S.-M. Hu. *J. Mol. Spectrosc.* **247**, 64–75 (2008).

[53] R.A. Toth, C.E. Miller, L.R. Brown, V. Malathy Devi, D.Chris. Benner. *J. Mol. Spectrosc.* **243**, 43–61 (2007).

[54] R.A. Toth, C.E. Miller, L.R. Brown, V. Malathy Devi, D.Chris. Benner. *J. Mol. Spectrosc.* **239**, 221–242 (2006).

[55] C.E. Miller, L.R. Brown. *J. Mol. Spectrosc.* **228**, 329–354 (2004).

[56] C.E. Miller, M.A. Montgomery, R.M. Onorato, C. Johnstone, T.P. McNicholas, B. Kovaric, L.R. Brown. *J. Mol. Spectrosc.* **228**, 355–374 (2004).

[57] Y. Ding, V.I. Perevalov, S.A. Tashkun, J.-L. Teffo, A.-W. Liu, S.-M. Hu. *J. Mol. Spectrosc.* **222**, 276–283 (2003).

[58] L.C. Bradley, K.L. Soohoo, C. Freed. *IEEE J. Quantum Electron.* **22**, 234–267 (1986).

[59] R.A. Toth. *Appl. Opt.* **24**, 261–274 (1985).

[60] K. Jolma. *J. Mol. Spectrosc.* **111**, 211–218 (1985).

[61] V. Malathy Devi, C.P. Rinsland, D.C. Benner. *Appl. Opt.* **23**, 4067–4075 (1984).

[62] C.P. Rinsland, D.C. Benner, V. Malathy Devi. *Appl. Opt.* **24**, 1644–1650 (1985).

[63] D. Bailly, C. Rossetti. *J. Mol. Spectrosc.* **119**, 388–397 (1986).

[64] M.P. Esplin, M.L. Hoke, in: High Resolution Fourier Transform Spectroscopy Technical Digest, Optical Society of America, Washington, DC. , 78–80 (1992).

[65] M.P. Esplin, R.J. Huppi, G.A. Vanasse. *Appl. Opt.* **21**, 1681–1685 (1982).

[66] M.P. Esplin, L.S. Rothman. *J. Mol. Spectrosc.* **100**, 193–204 (1983).

[67] M.P. Esplin, L.S. Rothman. *J. Mol. Spectrosc.* **116**, 351–363 (1986).

[68] A. Baldacci, L. Linden, V. Malathy Devi, K. Narahari Rao, B. Fridovich. *J. Mol. Spectrosc.* **72**, 135–142 (1978).

[69] A. Baldacci, C.P. Rinsland, M.A.H. Smith, K.N. Rao. *J. Mol. Spectrosc.* **94**, 351–362 (1982).

[70] Y. Ding, A. Campargue, E. Bertseva, S.A. Tashkun, V.I. Perevalov. *J. Mol. Spectrosc.* **231**, 117–123 (2005).

[71] M. Herman, J. Liévin, J. Vander Auwera, A. Campargue. *Adv. Chem. Phys.* **108**, 1–431 (1999).

[72] M.P. Esplin, AFGL-TR-0046. (1986).

[73] R.A. Toth, R.H. Hunt, E.K. Plyler. *J. Mol. Spectrosc.* **38**, 107–117 (1971).

[74] C.B. Suárez, F.P.J. Valero. *J. Quant. Spectrosc. Radiat. Transfer.* **19**, 569–578 (1977).

[75] F.P.J. Valero, C.B. Suárez. *J. Quant. Spectrosc. Radiat. Transfer.* **19**, 579–590 (1977).

[76] C.B. Suárez, F.P.J. Valero. *J. Mol. Spectrosc.* **71**, 46–63 (1978).

[77] J.W.C. Johns, Z. Lu, F. Thibault, R. Le Doucen, Ph. Arcas, Ch. Boulet. *J. Mol. Spectrosc.* **159**, 259–264 (1993).

[78] M. Fukabori, T.A. Aoki, T.E. Aoki, H. Ishida, T. Watanabe. *Adv. Space Res.* **25**, 985–988 (2000).

[79] D. Boudjaadar, J.Y. Mandin, V. Dana, N. Picqé, G. Guelachvili. *J. Mol. Spectrosc.* **236**, 158–167 (2006).

[80] L. Régalia-Jarlot, V. Zéninari, B. Parvitte, A. Grossel, X. Thomas, P. Von der Heyden, G. Durry. *J. Quant. Spectrosc. Radiat. Transfer.* **101**, 325–338 (2006).

[81] J. Henningsen, H. Simonsen. *J. Mol. Spectrosc.* **203**, 16–27 (2000).

[82] I. Pouchet, V. Zéninari, B. Parvitte, G. Durry. *J. Quant. Spectrosc. Radiat. Transfer.* **83**, 619–628 (2004).

[83] T. Hikida, K.M.T. Yamada, M. Fukabori, T. Aoki. *J. Mol. Spectrosc.* **232**, 202–212 (2005).

[84] N.N. Lavrentieva, private communication. .

[85] T. Le Barbu, V. Zéninari, B. Parvitte, D. Courtois, G. Durry. *J. Quant. Spectrosc. Radiat. Transfer.* **98**, 264–276 (2006).

[86] J. Fischer, R.R. Gamache, A. Goldman. *J. Quant. Spectrosc. Radiat. Transfer.* **82**, 401–412 (2003).

[87] A. Campargue, B.V. Perevalov. *J. Quant. Spectrosc. Radiat. Transfer.* **109**, 2261–2271 (2008).

[88] R.A. Toth, L.R. Brown, C.E. Miller, V. Malathy Devi, D. Chris Benner. *J. Mol. Spectrosc.* **239**, 243–271 (2006).

[89] R.A. Toth, C.E. Miller, V. Malathy Devi, D.C. Benner, L.R. Brown,. *J. Mol. Spectrosc.* **246**, 133–157 (2007).

Appendix

Tables of fitted spectroscopic band parameter values for the eight isotopologues of carbon dioxide: $^{12}C^{16}O_2$, $^{13}C^{16}O_2$, $^{16}O^{12}C^{18}O$, $^{16}O^{12}C^{17}O$, $^{16}O^{13}C^{18}O$, $^{16}O^{13}C^{17}O$, $^{13}C^{18}O_2$ and $^{17}O^{13}C^{18}O$. The listed bands are ordered according to the band centers.

Table 5.3. Spectroscopic constants of the $^{12}C^{16}O_2$ bands identified in the CW-CRDS spectrum recorded in the 5851–7045 cm^{-1} region.

$^{12}C^{16}O_2$	ΔG_v	G_v	B_v	$D_v \times 10^7$	$H_v \times 10^{12}$	RMS $\times 10^3$	N_{fit}/N_{obs}	J_{MAX} $P/\ Q/R$	*Note*
41104e 00001e	5830.8015(13)	5830.8015(13)	0.3900199(13)	1.6955(29)	–	0.81	16/17	/ /61	
40015e 10001e	5895.79100(45)	7283.97509(45)	0.3895861(15)	2.4953(88)	–	1.33	33/33	33/ /43	
33314e 03301e	5928.97752(43)	7932.22367(43)	0.3906358(17)	1.659(13)	–	0.67	16/20	30/ /36	
33314f 03301f	5928.98047(67)	7932.22662(67)	0.3906265(18)	1.5934(92)	–	1.09	19/24	29/ /43	
50016e 20003e	5931.8641(27)	8480.2311(27)	0.390398(11)	3.335(95)	–	1.23	7/8	/ /31	
41115e 11102e	5956.63037(38)	7889.10050(38)	0.38882144(94)	1.7782(43)	–	1.18	38/41	44/ /50	
41115f 11102f	5956.63150(35)	7889.10163(35)	0.39091097(88)	2.1598(40)	–	1.06	38/40	49/ /53	
32214e 02201e	5972.51515(24)	7307.64655(24)	0.38995490(85)	1.1096(70)	−2.79(15)	0.68	47/51	57/ /57	
32214e 02201f	–	–	–	–	–	–	/4	/13/	
32214f 02201e	–	–	–	–	–	–	/6	/18/	
32214f 02201f	5972.51550(20)	7307.64689(20)	0.38995319(35)	1.8296(11)	–	0.69	47/50	58/ /60	
40015e 10002e	5998.56821(28)	7283.97632(28)	0.38958878(87)	2.5701(63)	3.25(12)	0.88	54/56	61/ /59	
41103e 00001e	6000.53220(36)	6000.53220(36)	0.38917136(55)	1.3490(16)	–	1.20	47/49	63/ /63	
41114e 11101e	6005.0145(20)	8081.8704(20)	0.3871315(43)	1.796(21)	–	1.06	9/10	34/ /42	
41114f 11101f	6005.0268(12)	8081.8827(12)	0.3888637(43)	1.796(30)	–	1.55	17/18	25/ /37	
31114e 01101e	6020.79591(25)	6688.17574(25)	0.38854089(79)	1.7727(58)	3.40(11)	0.79	51/62	68/ /72	Coriolis resonance interaction with 42203e (energy levels crossing at $J = 84$). Perturbed lines ($J > 60$) excluded from the fit.
31114e 01101f	6020.79703(66)	6688.17686(66)	0.3885408(37)	1.744(40)	–	0.90	11/11	/30/	
31114f 01101e	–	–	–	–	–	–	/4	/25/	
31114f 01101f	6020.79593(20)	6688.17576(20)	0.39025786(44)	1.9372(23)	0.613(31)	0.68	55/63	71/ /73	
50003e 01101e	6057.8872(11)	6725.2670(11)	0.3889818(20)	0.7485(76)	–	1.77	20/23	52/ /44	
40014e 10001e	6072.33628(27)	7460.52038(27)	0.38734844(64)	1.9718(27)	–	0.95	44/45	53/ /51	
30014e 00001e	6075.97973(12)	6075.97973(12)	0.38890524(24)	2.1209(10)	1.400(12)	0.46	67/67	79/ /69	
22213e 00001e	6103.68331(91)	6103.68331(91)	0.3894200(19)	1.2814(92)	−1.67(13)	1.41	35/36	67/ /69	
42214e 12202e	6126.75498(98)	8711.77711(98)	0.3889084(59)	1.494(71)	–	0.77	9/9	15/ /27	
42214f 12202f	6126.7564(11)	8711.7786(11)	0.3888974(30)	1.749(15)	–	1.24	13/13	14/ /42	

Table 5.3. (Continued)

$^{12}C^{16}O_2$	ΔG_v	G_v	B_v	$D_v \times 10^7$	$H_v \times 10^{12}$	RMS $\times 10^3$	N_{fit}/N_{obs}	J_{MAX} $P/\ Q/R$	*Note*
50015e 20003e	6128.34336(77)	8676.71043(77)	0.3881140(37)	2.269(32)	–	0.84	11/11	33/ /31	
30023e 00011e	6139.26763(68)	8488.41031(68)	0.3838268(16)	1.6870(68)	–	1.41	17/17	40/ /50	
33313e 03301e	6146.71213(37)	8149.95828(37)	0.3894594(12)	1.4857(66)	–	0.87	22/22	42/ /44	
33313e 03301f	–	–	–	–	–	–	/4	/10/	
33313f 03301e	–	–	–	–	–	–	/5	/15/	
33313f 03301f	6146.71241(54)	8149.95856(54)	0.3894581(19)	1.481(12)	–	1.15	22/23	41/ /39	
42213f 12201f	–	–	–	–	–	–	/4	/ /30	
41114e 11102e	6149.41251(30)	8081.88264(30)	0.38709656(62)	1.5964(24)	–	0.97	37/37	44/ /54	
41114f 11102f	6149.41369(45)	8081.88382(45)	0.38885717(86)	1.7576(30)	–	1.47	38/40	51/ /59	
50014e 20002e	6160.32933(60)	8831.47248(60)	0.3851409(24)	0.929(17)	–	1.34	19/22	25/ /49	Coriolis resonance interaction with 61103e. Perturbed lines ($J > 39$) excluded from the fit.
50013e 20001e	6168.0797(12)	8965.2156(12)	0.3858977(74)	0.687(79)	–	1.36	11/12	21/ /29	
32213e 02201e	6170.10960(30)	7505.24100(30)	0.38860862(61)	1.4500(22)	–	0.92	40/41	53/ /53	
32213e 02201f	6170.10961(54)	7505.24101(54)	0.3886009(31)	1.403(29)	–	0.88	13/14	/33/	
32213f 02201e	6170.10949(64)	7505.24089(64)	0.3885979(37)	1.488(35)	–	1.02	12/13	/32/	
32213f 02201f	6170.11075(28)	7505.24215(28)	0.38860130(50)	1.5485(15)	–	0.90	40/47	62/ /60	
41113e 11101e	6173.77025(66)	8250.62614(66)	0.3862468(19)	1.3326(94)	–	1.69	24/26	42/ /46	
41113e 11101f	–	–	–	–	–	–	/3	/12/	
41113f 11101e	–	–	–	–	–	–	/2	/ 5/	
41113f 11101f	6173.77073(41)	8250.62663(41)	0.38782469(98)	1.3394(43)	–	1.20	32/37	43/ /57	
40014e 10002e	6175.11279(26)	7460.52090(26)	0.38735332(65)	2.0265(36)	1.423(52)	0.94	54/55	65/ /71	
41102e 00001e	6179.0391(11)	6179.0391(11)	0.3895909(22)	1.0430(68)	–	1.71	15/29	55/ /63	Coriolis + ℓ-type ($\Delta\ell_2 = \pm 3$) resonance interaction with 14412e (energy levels crossing at $J = 56$). Perturbed lines ($J > 35$) excluded from the fit.
14412e 00001e	–	–	–	–	–	–	/1	55/ /	Extra line of 41102-00001 band.
31113e 01101e	6196.17497(26)	6863.55480(26)	0.38692823(56)	1.4092(26)	−0.547(33)	0.94	63/67	62/ /78	
31113e 01101f	6196.17767(70)	6863.55750(70)	0.3869189(30)	1.362(24)	–	1.32	16/17	/36/	
31113f 01101e	6196.17580(61)	6863.55563(61)	0.3883370(15)	1.5214(55)	–	1.30	17/17	/53/	
31113f 01101f	6196.17547(23)	6863.55530(23)	0.38833865(49)	1.5214(23)	−0.330(28)	0.80	57/63	73/ /77	

Table 5.3. (Continued)

$^{12}C^{16}O_2$	ΔG_v	G_v	B_v	$D_v \times 10^7$	$H_v \times 10^{12}$	RMS $\times 10^3$	N_{fit}/N_{obs}	J_{MAX} $P/\ Q/R$		*Note*
40013e 10001e	6205.50639(33)	7593.69048(33)	0.38557688(64)	1.1133(24)	–	1.14	46/56	65/	/69	Coriolis + ℓ-type ($\Delta\ell_2 = \pm 3$) resonance interaction with 43302e (energy levels crossing at $J = 67$). Perturbed lines ($J > 55$) excluded from the fit.
42202e 01101e	6207.71007(54)	6875.08989(54)	0.39123434(86)	2.0768(26)	–	1.37	32/36	58/	/58	
42202f 01101f	6207.71207(64)	6875.09190(64)	0.39122360(94)	1.2174(27)	–	1.46	35/40	59/	/67	
30013e 00001e	6227.91590(20)	6227.91590(20)	0.38671425(34)	1.7353(13)	1.328(13)	0.83	81/83	85/	/89	
51102e 10001e	6228.4501(14)	7616.6342(14)	0.3895976(31)	1.069(14)	–	2.55	20/20	39/	/49	
43302e 02201e	–	–	–	–	–	–	/3	/	/41	
43302f 02201f	–	–	–	–	–	–	/1	/	/36	
50002e 01101e	6236.54910(86)	6903.92892(86)	0.3904850(13)	0.2826(36)	–	2.00	34/35	60/	/58	
30022e 00011e	6257.98995(69)	8607.13263(69)	0.3832395(22)	0.690(11)	–	1.56	22/26	30/	/50	Anharmonic resonance interaction with 60001 (energy levels crossing at $J = 50$). Perturbed lines ($J > 44$) excluded from the fit.
23312e 01101e	–	–	–	–	–	–	/7	/	/54	
23312f 01101f	–	–	–	–	–	–	/3	/	/45	
50014e 20003e	6283.10810(56)	8831.47517(56)	0.3851201(29)	0.670(28)	–	1.23	19/26	29/	/33	
22212e 00001e	6288.49339(74)	6288.49339(74)	0.38847947(86)	1.4667(16)	–	2.07	38/50	73/	/73	Coriolis + ℓ-type ($\Delta\ell_2 = \pm 3$) resonance interaction with 25501e (energy levels crossing at $J = 65$). Perturbed lines ($51 < J < 67$) excluded from the fit.
25501e 00001e	–	–	–	–	–	–	/2	65/	/65	Extra lines of 22212e-00001e band.
50013e 20002e	6294.07488(68)	8965.21803(68)	0.3858968(21)	0.709(11)	–	1.53	24/26	37/	/45	
32212e 10001e	–	–	–	–	–	–	/5	43/	/45	
40013e 10002e	6308.28369(33)	7593.69180(33)	0.38557430(62)	1.1063(22)	–	1.17	51/57	59/	/69	Coriolis + ℓ-type ($\Delta\ell_2 = \pm 3$) resonance interaction with 43302e (energy levels crossing at $J = 67$). Perturbed lines ($J > 57$) excluded from the fit.
41113e 11102e	6318.15901(66)	8250.62914(66)	0.3862356(11)	1.2638(37)	–	1.51	31/37	52/	/56	

Table 5.3. (Continued)

$^{12}C^{16}O_2$	ΔG_v	G_v	B_v	$D_v \times 10^7$	$H_v \times 10^{12}$	RMS $\times 10^3$	N_{fit}/N_{obs}	J_{MAX} $P/\,Q/R$	*Note*
41113f 11102e	–	–	–	–	–	–	/2	/ 9/	
41113f 11102f	6318.15855(61)	8250.62868(61)	0.3878183(14)	1.2884(56)	–	1.88	37/41	55/ /51	
42213e 12202e	6322.4405(32)	8907.4626(32)	0.3880664(74)	1.567(38)	–	2.19	10/11	33/ /41	
42213f 12202f	6322.4465(21)	8907.4686(21)	0.3880616(65)	1.393(37)	–	2.17	10/10	40/ /24	
51102e 10002e	6331.2176(30)	7616.6258(30)	0.3896190(80)	1.175(41)	–	2.51	12/13	39/ /41	
50012e 20001e	–	–	–	–	–	–	/6	29/ /11	
40012e 10001e	6346.26322(55)	7734.44731(55)	0.3869641(18)	0.955(10)	–	1.62	33/54	67/ /61	Coriolis resonance interaction with 21123e (energy levels crossing at $J = 65$). Perturbed lines ($J > 43$) excluded from the fit.
33301e 00001e	6346.70932(93)	6346.70932(93)	0.3921421(17)	1.5499(62)	–	1.54	22/25	45/ /53	
30012e 00001e	6347.85080(19)	6347.85080(19)	0.38645569(31)	0.9865(12)	0.643(11)	0.76	82/82	83/ /85	
41112e 11101e	6348.14248(41)	8424.99837(41)	0.3868207(11)	1.0003(47)	–	1.29	33/41	50/ /50	
41112f 11101f	6348.14164(52)	8424.99753(52)	0.3885225(11)	0.9697(39)	–	1.45	29/30	39/ /55	
21123e 10001e	–	–	–	–	–	–	/28	65/ /65	Coriolis resonance interaction with 40012 (energy levels crossing at $J = 65$). Not fitted.
31112e 01101e	6356.29456(31)	7023.67439(31)	0.38674887(59)	1.1941(26)	0.359(31)	1.13	68/73	74/ /78	
31112e 01101f	6356.29425(52)	7023.67408(52)	0.3867506(22)	1.200(15)	–	0.91	14/14	/38/	
31112f 01101e	6356.29612(69)	7023.67594(69)	0.3881169(26)	1.148(15)	–	1.20	12/14	/41/	
31112f 01101f	6356.29529(23)	7023.67511(23)	0.38811522(27)	1.13766(58)	–	0.91	54/69	69/ /75	
32212e 02201e	6359.27319(35)	7694.40459(35)	0.38828717(96)	1.4669(57)	−1.241(89)	1.02	47/55	63/ /67	
32212e 02201f	6359.27020(63)	7694.40160(63)	0.3882832(29)	1.440(23)	–	0.98	11/11	/35/	
32212f 02201e	6359.26956(67)	7694.40096(67)	0.3882980(58)	1.360(70)	–	0.91	8/9	/28/	
32212f 02201f	6359.27329(37)	7694.40469(37)	0.38828545(57)	1.2130(15)	–	1.29	45/54	62/ /64	
33312e 03301e	–	–	–	–	–	–	/25	48/ /50	Coriolis resonance interaction with 22223e. Not fitted.
33312e 03301f	–	–	–	–	–	–	/1	/ 4/	
33312f 03301e	–	–	–	–	–	–	/3	/ 7/	

Table 5.3. (Continued)

$^{12}C^{16}O_2$	ΔG_v	G_v	B_v	$D_v \times 10^7$	$H_v \times 10^{12}$	RMS $\times 10^3$	N_{fit}/N_{obs}	J_{MAX} $P/\ Q/R$	*Note*
33312f 03301f	6359.6020(16)	8362.8482(16)	0.3894277(66)	2.323(56)	–	2.49	20/27	39/ /45	Coriolis resonance interaction with 22223f. Perturbed lines ($J > 33$) excluded from the fit.
41101e 00001e	6388.07982(36)	6388.07982(36)	0.39030544(88)	1.0398(48)	2.292(71)	1.16	59/61	69/ /67	
30021e 00011e	–	–	–	–	–	–	/3	26/ /20	
21123f 02201e	–	–	–	–	–	–	/5	/16/	
21123f 02201f	–	–	–	–	–	–	/1	/ 2/	
42201e 01101e	6434.75778(93)	7102.13761(93)	0.3917100(21)	2.8740(93)	–	1.60	31/35	52/ /50	
42201f 01101f	6434.76066(93)	7102.14049(93)	0.3917023(20)	1.0241(87)	–	1.58	28/28	45/ /47	
40012e 10002e	6449.03931(46)	7734.44742(46)	0.3869647(15)	0.9592(91)	–	1.54	40/47	49/ /47	Coriolis resonance interaction with 21123e (energy levels crossing at $J = 65$). Perturbed lines ($J > 43$) excluded from the fit.
50001e 01101e	6454.36198(72)	7121.74181(72)	0.3913859(24)	−0.546(16)	–	1.22	27/34	48/ /42	Anharmonic resonance interaction with 20023 (energy levels crossing at $J = 43$). Perturbed lines ($J > 38$) excluded from the fit.
21123e 10002e	6458.28935(51)	7743.69746(51)	0.3853050(21)	1.408(16)	–	1.05	21/26	23/ /51	Coriolis resonance interaction with 40012 (energy levels crossing at $J = 65$). Perturbed lines ($J > 37$) excluded from the fit.
21123f 10002e	6458.28810(63)	7743.69622(63)	0.3865256(24)	1.769(16)	–	1.02	15/17	/38/	
13322e 02201e	6461.9666(10)	7797.0980(10)	0.3867671(53)	1.447(58)	–	1.10	12/13	25/ /29	
13322e 02201f	6461.96254(90)	7797.09394(90)	0.3867731(49)	1.430(42)	–	0.97	9/12	/33/	
13322f 02201e	6461.96347(58)	7797.09487(58)	0.3867743(20)	1.465(12)	–	0.84	11/14	/40/	
13322f 02201f	6461.9627(14)	7797.0941(14)	0.3867774(53)	1.502(38)	–	1.41	9/13	22/ /36	
20023e 01101e	6466.43919(56)	7133.81901(56)	0.3852935(12)	1.8208(35)	–	1.59	30/46	40/ /58	Anharmonic resonance interaction with 50001 (energy levels crossing at $J = 43$). Perturbed lines ($33 > J > 54$) excluded from the fit.
20023e 01101f	6466.44143(52)	7133.82126(52)	0.3852917(14)	1.8326(46)	–	1.13	16/26	/54/	
22211e 00001e	6474.53179(44)	6474.53179(44)	0.38864430(53)	1.5030(12)	–	1.06	44/51	63/ /67	
41112e 11102e	6492.53000(81)	8425.00013(81)	0.3868171(36)	0.950(29)	–	1.48	20/22	34/ /34	

Table 5.3. (Continued)

$^{12}C^{16}O_2$	ΔG_v	G_v	B_v	$D_v \times 10^7$	$H_v \times 10^{12}$	RMS $\times 10^3$	N_{fit}/N_{obs}	J_{MAX} $P/\ Q/R$	*Note*
41112f 11102f	6492.53075(53)	8425.00088(53)	0.3885165(20)	0.919(13)	–	1.10	18/20	27/ /41	
12222e 01101e	6498.65510(37)	7166.03493(37)	0.3860367(13)	1.1425(82)	–	1.32	32/42	44/ /56	Coriolis resonance interaction with
12222e 01101f	6498.65303(41)	7166.03286(41)	0.3860425(14)	1.1775(92)	–	0.83	18/24	/54/	23311 (energy levels crossing at
12222f 01101e	6498.65305(38)	7166.03288(38)	0.3860397(13)	1.3048(85)	–	0.66	17/22	/49/	$J = 58$). Perturbed lines ($J > 40$)
12222f 01101f	6498.65437(51)	7166.03419(51)	0.3860403(18)	1.320(12)	–	1.27	33/42	47/ /57	excluded from the fit.
30011e 00001e	6503.08116(25)	6503.08116(25)	0.38797022(25)	0.70340(43)	–	1.17	75/81	79/ /81	
32211e 10001e	–	–	–	–	–	–	/3	27/ /	
21122e 10001e	–	–	–	–	–	–	/7	33/ /	
21122f 10001e	–	–	–	–	–	–	/7	/30/	
40011e 10001e	6532.64896(35)	7920.83305(35)	0.3885486(10)	0.5314(74)	1.52(14)	0.97	48/54	61/ /61	
31111e 01101e	6536.44614(30)	7203.82597(30)	0.38759574(64)	1.0131(32)	0.818(41)	1.07	65/69	70/ /74	
31111e 01101f	6536.44408(74)	7203.82391(74)	0.3875937(37)	0.962(32)	–	1.11	11/11	/34/	
31111f 01101e	6536.44456(57)	7203.82439(57)	0.3891540(24)	0.920(18)	–	0.70	10/12	/35/	
31111f 01101f	6536.44590(36)	7203.82573(36)	0.38915679(85)	0.9627(46)	0.331(66)	1.28	64/67	67/ /75	
11122e 00001e	6537.95976(23)	6537.95976(23)	0.38482012(56)	1.4971(30)	0.423(40)	0.81	52/57	55/ /73	
11122f 00001e	6537.95834(30)	6537.95834(30)	0.38572573(40)	1.56177(91)	–	0.85	29/29	/68/	
41111e 11101e	6551.80854(56)	8628.66444(56)	0.3882420(16)	0.7179(86)	–	1.32	27/32	36/ /44	
41111f 11101f	6551.80682(53)	8628.66271(53)	0.3897813(14)	0.7705(61)	–	1.68	36/39	33/ /49	
32211e 02201e	6562.4302(15)	7897.5616(15)	0.388835(16)	9.30(35)	–	2.57	19/49	47/ /61	Coriolis resonance interaction with
32211e 02201f	6562.43375(50)	7897.56515(50)	0.3888038(68)	8.66(14)	–	0.48	7/8	/21/	21122 (energy levels crossing: e at
32211f 02201e	6562.43223(91)	7897.56363(91)	0.388806(11)	5.66(21)	–	0.99	7/8	/28/	$J = 28$ and f at $J = 32$). Perturbed
32211f 02201f	6562.43114(87)	7897.56254(87)	0.3887902(88)	5.45(17)	–	1.47	19/53	58/ /64	lines with $J > 21$ (e states) and $J > 22$ (f states) excluded from the fit.
21122e 02201e	–	–	–	–	–	–	/32	39/ /53	Coriolis resonance interaction with
21122f 02201f	–	–	–	–	–	–	/28	44/ /52	32211 (energy levels crossing: e at $J = 28$ and f at $J = 32$). Not fitted.
33311e 03301e	–	–	–	–	–	–	/29	34/ /40	Coriolis + ℓ-type ($\Delta\ell_2 = \pm 3$) resonance interaction with 60001e (energy levels crossing at $J = 31$). Not fitted.
33311e 03301f	–	–	–	–	–	–	/2	/ 6/	
33311f 03301e	–	–	–	–	–	–	/2	/ 5/	

Table 5.3. (Continued)

$^{12}C^{16}O_2$	ΔG_v	G_v	B_v	$D_v \times 10^7$	$H_v \times 10^{12}$	RMS $\times 10^3$	N_{fit}/N_{obs}	J_{MAX} $P/\ Q/R$	*Note*
33311f 03301f	6583.40050(36)	8586.64665(36)	0.3899430(11)	0.6158(64)	–	0.85	27/33	37/ /43	
60001e 03301e	–	–	–	–	–	–	/4	30/ /34	Extra lines of 33311e-03301e band.
20022e 01101e	6592.38749(47)	7259.76732(47)	0.38350726(82)	1.3532(29)	–	0.98	25/31	42/ /54	
20022e 01101f	6592.38892(54)	7259.76874(54)	0.3835076(46)	1.381(76)	–	0.64	11/11	/24/	
21122e 10002e	–	–	–	–	–	–	/35	23/ /53	Coriolis resonance interaction with 32211 (energy levels crossing: e at $J = 28$ and f at $J = 32$). Not fitted.
21122f 10002e	–	–	–	–	–	–	/20	/48/	
32211e 10002e	–	–	–	–	–	–	/9	/ /35	
32211f 10002e	–	–	–	–	–	–	/5	/36/	
40011e 10002e	6635.42215(33)	7920.83026(33)	0.3885577(14)	0.610(13)	3.20(30)	0.99	41/46	49/ /55	
13321e 02201e	6659.23103(55)	7994.36243(55)	0.3862742(14)	1.3104(66)	–	1.24	24/27	25/ /47	
13321e 02201f	6659.23139(76)	7994.36279(76)	0.3862770(25)	1.328(15)	–	1.30	16/18	/41/	
13321f 02201e	6659.23512(69)	7994.36652(69)	0.3862682(15)	1.2820(65)	–	0.85	14/17	/46/	
13321f 02201f	6659.23259(61)	7994.36398(61)	0.3862674(14)	1.2726(53)	–	1.38	26/31	24/ /52	
21121e 10001e	6667.83880(64)	8056.02289(64)	0.3844049(16)	1.1009(71)	–	1.36	23/27	35/ /47	
21121f 10001e	6667.83819(45)	8056.02228(45)	0.3855167(12)	1.0499(63)	–	0.53	14/16	/42/	
12221e 01101e	6670.77918(35)	7338.15901(35)	0.38549942(49)	1.3561(12)	–	1.14	40/43	44/ /66	
12221e 01101f	6670.77842(43)	7338.15824(43)	0.38549901(68)	1.3521(18)	–	1.06	25/27	/62/	
12221f 01101e	6670.77937(45)	7338.15920(45)	0.38549532(72)	1.2412(20)	–	1.13	26/27	/61/	
12221f 01101f	6670.77992(24)	7338.15975(24)	0.38549492(36)	1.24057(98)	–	0.79	45/49	45/ /63	
11121e 00001e	6679.70601(25)	6679.70601(25)	0.38431321(30)	1.21952(69)	–	1.10	61/61	55/ /75	
11121f 00001e	6679.70453(34)	6679.70453(34)	0.38513456(37)	1.18865(69)	–	1.04	34/35	/76/	
41111e 11102e	–	–	–	–	–	–	/4	14/ /16	
41111f 11102f	–	–	–	–	–	–	/2	19/ /	
20021e 01101e	6710.32562(35)	7377.70545(35)	0.38437819(72)	0.9423(26)	–	1.16	39/46	48/ /64	
20021e 01101f	6710.32620(30)	7377.70603(30)	0.38437609(47)	0.9378(14)	–	0.74	25/26	/62/	
21121e 02201e	6720.8919(14)	8056.0233(14)	0.3843963(82)	0.953(92)	–	1.57	9/9	27/ /29	
21121e 02201f	6720.8942(21)	8056.0256(21)	0.3843939(67)	1.026(44)	–	1.67	7/7	/37/	
21121f 02201e	6720.89281(76)	8056.02421(76)	0.3855153(24)	1.028(15)	–	1.01	12/12	/40/	

Table 5.3. (Continued)

$^{12}C^{16}O_2$	ΔG_v	G_v	B_v	$D_v \times 10^7$	$H_v \times 10^{12}$	RMS $\times 10^3$	N_{fit}/N_{obs}	J_{MAX} $P/\ Q/R$	*Note*
21121f 02201f	6720.8936(13)	8056.0250(13)	0.3855136(63)	0.989(56)	–	1.47	12/13	22/ /32	
11132e 11101e	6726.40634(36)	8803.26224(36)	0.3818569(16)	1.475(11)	–	0.77	17/22	38/ /38	
11132f 11101f	6726.40816(57)	8803.26405(57)	0.3827380(26)	1.465(19)	–	0.68	14/19	25/ /35	
10032e 10001e	6804.36592(34)	8192.55001(34)	0.38155867(73)	1.5705(27)	–	1.00	30/34	53/ /55	
04431e 04401e	6823.17679(71)	9494.89138(71)	0.3841735(22)	1.387(12)	–	0.95	12/15	39/ /43	
04431e 04401f	–	–	–	–	–	–	/3	/ 9/	
04431f 04401e	–	–	–	–	–	–	/2	/ 6/	
04431f 04401f	6823.17868(79)	9494.89327(79)	0.3841687(25)	1.370(14)	–	0.96	12/12	40/ /30	
12231e 12201e	6829.1945(19)	9589.9193(19)	0.3824583(66)	1.272(43)	–	1.36	7/8	21/ /37	
12231f 12201f	6829.1963(11)	9589.9210(11)	0.3824426(67)	0.979(79)	–	0.99	8/9	16/ /28	
12232e 12202e	6834.15963(63)	9419.18176(63)	0.3830799(23)	1.330(14)	–	1.27	18/20	27/ /41	
12232f 12202f	6834.16013(54)	9419.18226(54)	0.3830745(17)	1.4348(88)	–	1.01	15/21	32/ /44	
20031e 20001e	6834.20306(81)	9631.33897(81)	0.3812434(35)	0.917(27)	–	0.38	5/6	/ /33	
20033e 20003e	6840.61505(46)	9388.98212(46)	0.3823755(16)	1.780(10)	–	0.99	20/27	37/ /41	
20032e 20002e	6845.8125(22)	9516.9556(22)	0.3804986(89)	1.411(79)	–	1.28	8/9	31/ /25	
03331e 03301e	6860.43362(28)	8863.67977(28)	0.38337219(46)	1.3702(12)	–	0.95	39/41	56/ /64	
03331e 03301f	6860.43350(68)	8863.67965(68)	0.3833711(31)	1.374(24)	–	1.03	11/12	/36/	
03331f 03301e	–	–	–	–	–	–	/7	/21/	
03331f 03301f	6860.43341(32)	8863.67956(32)	0.38337344(81)	1.3763(39)	–	0.84	34/36	47/ /41	
01141e 01111e	6860.43862(88)	9864.45092(88)	0.3784645(35)	1.333(28)	–	1.14	15/18	29/ /35	
01141f 01111f	6860.44091(55)	9864.45321(55)	0.3790106(24)	1.329(18)	–	0.80	11/12	28/ /36	
11131e 11101e	6867.27682(18)	8944.13271(18)	0.38125948(36)	1.2103(12)	–	0.63	39/44	54/ /58	
11131e 11101f	–	–	–	–	–	–	/2	/ 6/	
11131f 11101e	–	–	–	–	–	–	/1	/ 1/	
11131f 11101f	6867.27659(30)	8944.13249(30)	0.38203411(59)	1.1840(21)	–	1.02	42/45	53/ /57	
11132e 11102e	6870.79185(35)	8803.26198(35)	0.38185214(78)	1.4376(28)	–	1.07	33/39	56/ /52	
11132e 11102f	–	–	–	–	–	–	/1	/ 2/	
11132f 11102e	–	–	–	–	–	–	/13	/13/	
11132f 11102f	6870.79231(25)	8803.26244(25)	0.38274444(54)	1.5194(20)	–	0.84	40/42	53/ /55	
02231e 02201e	6897.75247(26)	8232.88387(26)	0.38258220(40)	1.3557(10)	–	0.94	42/44	67/ /39	
02231e 02201f	6897.75227(49)	8232.88367(49)	0.3825816(23)	1.352(11)	–	0.73	11/13	/45/	

Table 5.3. (Continued)

$^{12}C^{16}O_2$	ΔG_v	G_v	B_v	$D_v \times 10^7$	$H_v \times 10^{12}$	RMS $\times 10^3$	N_{fit}/N_{obs}	J_{MAX} $P/Q/R$	*Note*
02231f 02201e	6897.75261(25)	8232.88401(25)	0.38258065(97)	1.3724(57)	–	0.49	14/14	/42/	
02231f 02201f	6897.75297(27)	8232.88437(27)	0.38257885(37)	1.36116(85)	–	1.00	50/50	70/ /40	
00041e 00011e	6897.79041(40)	9246.93309(40)	0.37792425(68)	1.3236(21)	–	1.12	31/33	60/ /50	
10031e 10001e	6905.76741(30)	8293.95150(30)	0.38080370(42)	1.12015(99)	–	1.20	52/54	69/ /41	
10032e 10002e	6907.14196(23)	8192.55007(23)	0.38155938(36)	1.5697(10)	–	0.85	46/47	65/ /43	
01131e 01101e	6935.13420(16)	7602.51403(16)	0.38150363(15)	1.33577(26)	–	0.69	71/74	82/ /78	
01131e 01101f	6935.13343(30)	7602.51325(30)	0.3815015(15)	1.304(12)	–	0.53	11/13	/36/	
01131f 01101e	6935.13316(32)	7602.51299(32)	0.38206887(91)	1.3403(51)	–	0.56	14/17	/43/	
01131f 01101f	6935.13388(16)	7602.51371(16)	0.38206928(17)	1.35037(29)	–	0.72	63/70	81/ /77	
00031e 00001e	6972.577396(77)	6972.577396(77)	0.380992705(59)	1.321913(81)	–	0.37	84/86	91/ /87	
10031e 10002e	–	–	–	–	–	–	/4	/ /27	

Notes: Spectroscopic constants of the lower states were taken from Refs. [30, 55]; *RMS*, root mean squares of the fit of the rovibrational parameters; N_{fit}, number of line positions included in the fit of the spectroscopic parameters; N_{obs}, number of the observed line positions; J_{MAX}, maximum value of the rotational quantum number of the assigned transitions.

Table 5.4. Spectroscopic constants of the $^{13}C^{16}O_2$ bands identified in the CW-CRDS spectrum recorded in the 5851–7045 cm^{-1} region.

$^{13}C^{16}O_2$	ΔG_v	G_v	B_v	$D_v \times 10^7$	$H_v \times 10^{12}$	RMS $\times 10^3$	N_{fit}/N_{obs}	J_{MAX} $P/Q/R$	$Note$
41115e 11102e	5840.8690(12)	7737.4066(12)	0.3893224(26)	2.019(11)	–	0.70	9/9	/ /44	
41115f 11102f	5840.8693(15)	7737.4069(15)	0.3918802(53)	2.255(40)	–	0.62	8/9	/ /33	
32214e 02201e	5861.97233(25)	7159.23730(25)	0.39065528(83)	0.9521(44)	–	0.70	25/26	11/ /45	
32214f 02201e	–	–	–	–	–	–	/1	/ 2/	
32214f 02201f	5861.97222(25)	7159.23718(25)	0.39065281(83)	1.7478(39)	–	0.70	24/24	12/ /48	
40015e 10002e	5876.33240(21)	7142.16023(21)	0.39010205(92)	3.7666(90)	13.17(23)	0.64	40/41	29/ /53	
51104e 10002e	5884.5587(15)	7150.3865(15)	0.3892958(27)	1.116(10)	–	1.28	14/16	33/ /49	
41114e 11101e	–	–	–	–	–	–	/2	/ /28	
41114f 11101f	–	–	–	–	–	–	/2	/ /17	
31114e 01101e	5904.44409(15)	6552.92245(15)	0.38907350(42)	1.7863(28)	0.748(48)	0.50	59/60	56/ /64	
31114e 01101f	5904.44399(40)	6552.92235(40)	0.3890778(39)	1.817(60)	–	0.41	8/9	/24/	
31114f 01101e	–	–	–	–	–	–	/1	/ 1/	
31114f 01101f	5904.44391(17)	6552.92227(17)	0.39095931(47)	2.0342(30)	0.456(50)	0.58	59/62	63/ /65	
42203e 01101e	5920.60535(81)	6569.08371(81)	0.3908007(16)	1.4126(68)	–	1.19	23/26	48/ /46	
42203f 01101f	5920.60995(62)	6569.08831(62)	0.3907866(11)	1.4701(36)	–	0.88	21/24	43/ /53	
41103e 00001e	5922.73135(36)	5922.73135(36)	0.38901693(62)	1.5030(21)	–	0.95	39/41	51/ /57	
41103f 00001e	–	–	–	–	–	–	/4	/20/	
30014e 00001e	5951.60082(15)	5951.60082(15)	0.38964250(34)	2.3651(17)	2.903(23)	0.57	72/74	73/ /77	
40014e 10001e	5962.14225(34)	7332.20441(34)	0.3885216(13)	2.171(10)	3.49(21)	1.00	35/39	47/ /59	
22213e 00001e	5970.94184(79)	5970.94184(79)	0.3899060(16)	0.9866(84)	−2.64(13)	1.00	41/43	65/ /59	
50003e 01101e	–	–	–	–	–	–	/9	48/ /36	
42214e 12202e	–	–	–	–	–	–	/6	27/ /11	
42214f 12202f	–	–	–	–	–	–	/5	24/ /32	
50015e 20003e	6022.14924(67)	8529.67878(67)	0.3885701(34)	3.152(28)	–	1.26	17/19	31/ /35	
30023e 00011e	6033.67700(93)	8317.16416(93)	0.3848355(31)	1.745(21)	–	1.15	10/10	28/ /38	
33313e 03301e	6039.50886(43)	7985.85884(43)	0.3899370(19)	1.432(15)	–	0.69	17/19	34/ /34	
33313f 03301f	6039.50973(77)	7985.85971(77)	0.3899355(22)	1.423(13)	–	1.15	21/22	35/ /41	
41114e 11102e	6042.57150(32)	7939.10909(32)	0.38783064(80)	1.7496(37)	–	0.95	36/37	46/ /48	

Table 5.4. (Continued)

$^{13}C^{16}O_2$	ΔG_v	G_v	B_v	$D_v \times 10^7$	$H_v \times 10^{12}$	RMS $\times 10^3$	N_{fit}/N_{obs}	J_{MAX} $P/Q/R$	*Note*
41114f 11102f	6042.57082(34)	7939.10840(34)	0.38973107(80)	1.9492(36)	–	0.94	35/37	49/ /45	
51103e 10002e	6050.8093(17)	7316.6371(17)	0.3879289(38)	1.330(19)	–	0.67	12/12	33/ /39	
50014e 20002e	6058.34523(88)	8703.41309(88)	0.3859184(50)	1.326(48)	–	0.92	11/12	31/ /27	
32213e 02201e	6062.42859(21)	7359.69356(21)	0.38894580(76)	1.1691(61)	−1.87(13)	0.63	49/51	55/ /57	
32213e 02201f	–	–	–	–	–	–	/7	/21/	
32213f 02201e	–	–	–	–	–	–	/8	/16/	
32213f 02201f	6062.42928(25)	7359.69425(25)	0.38894250(44)	1.5898(14)	–	0.89	49/49	56/ /58	
40014e 10002e	6066.37723(21)	7332.20506(21)	0.38851782(68)	2.1327(49)	2.598(93)	0.69	54/55	59/ /61	
41113e 11101e	6074.28855(29)	8111.38212(29)	0.38625031(83)	1.4560(42)	–	0.79	32/33	46/ /42	
41113f 11101f	6074.28793(27)	8111.38150(27)	0.38793378(96)	1.5611(56)	–	0.72	24/25	35/ /43	
41102e 00001e	–	–	–	–	–	–	/5	35/ /	
50013e 20001e	–	–	–	–	–	–	/4	21/ /23	
31113e 01101e	6088.21440(19)	6736.69276(19)	0.38736114(23)	1.53525(52)	–	0.77	60/62	72/ /58	
31113e 01101f	6088.21522(42)	6736.69358(42)	0.3873527(23)	1.428(21)	–	0.63	12/12	/32/	
31113f 01101e	6088.21433(61)	6736.69269(61)	0.3889041(27)	1.640(21)	–	0.81	11/11	/35/	
31113f 01101f	6088.21416(19)	6736.69252(19)	0.38890844(40)	1.6835(19)	0.316(24)	0.69	59/61	69/ /77	
42202e 01101e	6106.04258(62)	6754.52094(62)	0.3904303(10)	1.7700(30)	–	1.40	30/31	52/ /58	
42202f 01101f	6106.04372(55)	6754.52208(55)	0.39041887(81)	1.2457(24)	–	1.03	26/27	51/ /59	
40013e 10001e	6111.51137(55)	7481.57353(55)	0.3853042(47)	−0.908(66)	–	1.27	21/47	61/ /59	Coriolis resonance interaction with 51102e. Perturbed lines ($J > 27$) excluded from the fit.
51102e 10001e	–	–	–	–	–	–	/28	49/ /57	Coriolis resonance interaction with 40013. Not fitted.
30013e 00001e	6119.61975(13)	6119.61975(13)	0.38759252(22)	1.81132(83)	1.0911(83)	0.53	80/82	85/ /89	
50002e 01101e	6145.89228(54)	6794.37064(54)	0.38915643(96)	0.4316(34)	–	0.99	24/25	40/ /54	
22212e 00001e	6155.41766(50)	6155.41766(50)	0.38851392(89)	1.2699(43)	−1.009(58)	0.72	42/44	67/ /69	
30022e 00011e	–	–	–	–	–	–	/14	24/ /50	Coriolis resonance interaction with 41111e (energy levels crossing at $J = 20$). Not fitted.

Table 5.4. (Continued)

$^{13}C^{16}O_2$	ΔG_v	G_v	B_v	$D_v \times 10^7$	$H_v \times 10^{12}$	RMS $\times 10^3$	N_{fit}/N_{obs}	J_{MAX} $P/\ Q/R$	*Note*
41111e 00011e	–	–	–	–	–	–	/9	24/ /32	Extra lines of 30022-00011 band.
50013e 20002e	6190.50016(69)	8835.56802(69)	0.3849194(48)	1.251(67)	–	1.04	14/15	23/ /27	
50014e 20003e	6195.88448(65)	8703.41402(65)	0.3859244(43)	1.386(56)	–	0.69	9/11	27/ /23	
42213e 12202e	–	–	–	–	–	–	/6	19/ /30	
42213f 12202f	–	–	–	–	–	–	/4	30/ /20	
41113e 11102e	6214.84453(33)	8111.38212(33)	0.38625028(70)	1.4534(29)	–	0.86	34/38	52/ /50	
41113f 11102e	–	–	–	–	–	–	/1	/11/	
41113f 11102f	6214.84495(36)	8111.38253(36)	0.38792830(73)	1.5257(28)	–	1.20	42/43	51/ /55	
40013e 10002e	6215.74663(50)	7481.57446(50)	0.3853173(38)	−0.689(52)	–	1.20	22/56	59/ /63	Coriolis resonance interaction with 51102e. Perturbed lines ($J > 27$) excluded from the fit.
51102e 10002e	–	–	–	–	–	–	/30	47/ /51	Coriolis resonance interaction with 40013. Not fitted.
50012e 20001e	–	–	–	–	–	–	/5	23/ /13	
40012e 10001e	6230.05959(25)	7600.12175(25)	0.38587759(78)	0.8324(51)	0.818(91)	0.81	50/61	63/ /61	
41112e 11101e	6230.51643(33)	8267.61001(33)	0.38606000(74)	1.0436(30)	–	0.83	25/33	48/ /52	
41112e 11101f	–	–	–	–	–	–	/1	/ 2/	
41112f 11101e	–	–	–	–	–	–	/1	/ 1/	
41112f 11101f	6230.51574(36)	8267.60932(36)	0.38764851(78)	1.0124(30)	–	1.09	30/36	55/ /45	
42212e 12201e	–	–	–	–	–	–	/2	21/ /15	
42212f 12201f	–	–	–	–	–	–	/6	24/ /8	
33312e 03301e	6241.62580(60)	8187.97578(60)	0.3890889(17)	1.3132(81)	–	1.26	20/25	44/ /46	
33312e 03301f	–	–	–	–	–	–	/2	/14/	
33312f 03301e	–	–	–	–	–	–	/2	/ 9/	
33312f 03301f	6241.62770(44)	8187.97768(44)	0.3890747(12)	1.1455(58)	–	1.06	22/26	33/ /47	

Table 5.4. (Continued)

$^{13}C^{16}O_2$	ΔG_v	G_v	B_v	$D_v \times 10^7$	$H_v \times 10^{12}$	RMS $\times 10^3$	N_{fit}/N_{obs}	J_{MAX} $P/\ Q/R$	*Note*
30012e 00001e	6241.96834(15)	6241.96834(15)	0.38585826(21)	1.10492(53)	–	0.62	66/83	77/ /79	Anharmonic + ℓ-type ($\Delta\ell_2 = \pm 4$) resonance interaction with 14411e (energy levels crossing at $J = 39$). Coriolis + ℓ-type ($\Delta\ell_2 = \pm 3$) resonance interaction with 33301e (energy levels crossing at $J = 79$). Perturbed lines ($J > 69$) excluded from the fit.
14411e 00001e	–	–	–	–	–	–	/8	39/ /45	Extra lines of 30012-00001 band.
33301e 00001e	–	–	–	–	–	–	/1	/ /79	Extra line of 30012-00001 band.
32212e 02201e	6243.25747(44)	7540.52243(44)	0.3879631(12)	1.3248(76)	−2.60(13)	1.13	36/44	51/ /65	
32212e 02201f	–	–	–	–	–	–	/7	/33/	
32212f 02201e	–	–	–	–	–	–	/5	/26/	
32212f 02201f	6243.25755(34)	7540.52251(34)	0.38796326(47)	1.2764(13)	–	1.09	45/54	58/ /64	
31112e 01101e	6243.57196(17)	6892.05032(17)	0.38640897(35)	1.2825(17)	0.480(21)	0.60	61/65	68/ /76	Coriolis + ℓ-type ($\Delta\ell_2 = \pm 3$) resonance interaction with 34401 (energy levels crossing: e at $J = 32$, f at $J = 37$). Anharmonic + ℓ-type ($\Delta\ell_2 = \pm 4$) resonance interaction with 15511 (energy levels crossing: e at $J = 50$, f at $J = 61$).
31112e 01101f	6243.57183(59)	6892.05019(59)	0.3864081(20)	1.267(12)	–	0.99	15/17	/40/	
31112f 01101e	–	–	–	–	–	–	/10	/31/	
31112f 01101f	6243.57195(28)	6892.05031(28)	0.38773582(55)	1.2877(26)	0.597(32)	0.91	56/65	67/ /77	
34401e 01101e	–	–	–	–	–	–	/6	34/ /36	
34401e 01101f	–	–	–	–	–	–	/1	/32/	Extra lines of 31112-01101 band.
34401f 01101f	–	–	–	–	–	–	/5	39/ /39	
15511e 01101e	–	–	–	–	–	–	/1	/ /50	Extra lines of 31112-01101 band.
15511f 01101f	–	–	–	–	–	–	/1	/ /61	
41101e 00001e	6257.01757(44)	6257.01757(44)	0.3893811(10)	1.1960(52)	2.532(75)	1.10	50/56	67/ /73	
30021e 00011e	–	–	–	–	–	–	/11	12/ /28	
21123e 10002e	6297.47597(51)	7563.30380(51)	0.3858176(36)	1.480(41)	–	0.68	10/13	23/ /27	
21123f 10002e	6297.47286(91)	7563.30069(91)	0.3872815(33)	1.714(22)	–	1.18	11/13	/38/	
42201e 01101e	6302.81141(55)	6951.28977(55)	0.39063643(25)	2.4592(38)	–	0.99	29/31	50/ /54	Anharmonic + ℓ-type ($\Delta\ell_2 = \pm 2$) resonance interaction with 20023e (energy levels crossing at $J = 54$). Perturbed lines ($J > 50$) excluded from the fit.

Table 5.4. (Continued)

$^{13}C^{16}O_2$	ΔG_v	G_v	B_v	$D_v \times 10^7$	$H_v \times 10^{12}$	RMS $\times 10^3$	N_{fit}/N_{obs}	J_{MAX} $P/\,Q/R$	*Note*
42201f 01101f	6302.81333(56)	6951.29170(56)	0.39062725(90)	1.0857(26)	–	1.20	31/32	53/ /59	
51101e 10001e	–	–	–	–	–	–	/9	33/ /29	
13322e 02201e	–	–	–	–	–	–	/4	19/ /25	
13322e 02201f	–	–	–	–	–	–	/5	/21/	
13322f 02201e	–	–	–	–	–	–	/4	/22/	
13322f 02201f	–	–	–	–	–	–	/1	22/ /	
20023e 01101e	6316.66769(44)	6965.14605(44)	0.3860302(13)	1.8496(67)	–	1.22	28/33	46/ /42	
20023e 01101f	6316.66545(57)	6965.14381(57)	0.3860347(13)	1.8584(58)	–	1.13	21/23	/21/	
22211e 00001e	6326.03597(52)	6326.03597(52)	0.38812056(65)	1.3708(16)	–	1.14	40/41	61/ /63	
50001e 01101e	6326.15966(65)	6974.63802(65)	0.3902233(13)	−0.1149(45)	–	1.22	27/30	52/ /48	
40012e 10002e	6334.29267(33)	7600.12050(33)	0.38587984(79)	0.8214(31)	–	1.19	40/46	53/ /49	
23311e 01101e	–	–	–	–	–	–	/8	24/ /30	Coriolis resonance interaction with 12222 (energy levels crossings at $J = 20$). Not fitted.
23311e 01101f	–	–	–	–	–	–	/5	/28/	
23311f 01101e	–	–	–	–	–	–	/5	/31/	
23311f 01101f	–	–	–	–	–	–	/11	21/ /25	
12222e 01101e	–	–	–	–	–	–	/27	44/ /38	Coriolis resonance interaction with 23311 (energy levels crossings at $J = 20$). Not fitted.
12222e 01101f	–	–	–	–	–	–	/18	/46/	
12222f 01101e	–	–	–	–	–	–	/14	/51/	
12222f 01101f	–	–	–	–	–	–	/28	45/ /39	
30011e 00001e	6363.62105(14)	6363.62105(14)	0.38702786(38)	0.8700(18)	–	0.50	48/79	75/ /83	Coriolis resonance interaction with 11122e (energy levels crossings at $J = 71$). Perturbed lines ($J > 47$) excluded from the fit.
41112e 11102e	6371.07143(70)	8267.60902(70)	0.3860601(32)	1.039(25)	–	1.14	13/15	36/ /32	
41112f 11102f	6371.06943(55)	8267.60702(55)	0.3876551(14)	1.0818(68)	–	1.11	19/22	39/ /47	
11122e 00001e	6374.50349(33)	6374.50349(33)	0.38528587(87)	1.3646(41)	–	1.08	41/64	69/ /75	Coriolis resonance interaction with 30011 (energy levels crossings at $J = 71$). Perturbed lines ($J > 47$) excluded from the fit.
11122f 00001e	6374.50405(37)	6374.50405(37)	0.38626687(52)	1.5464(14)	–	1.03	28/28	/66/	
40011e 10001e	6379.02032(37)	7749.08248(37)	0.38756008(71)	0.5722(24)	–	1.36	47/53	55/ /57	

Table 5.4. (Continued)

$^{13}C^{16}O_2$	ΔG_v	G_v	B_v	$D_v \times 10^7$	$H_v \times 10^{12}$	RMS $\times 10^3$	N_{fit}/N_{obs}	J_{MAX} $P/\ Q/R$	*Note*
04421e 01101e	6397.3031(17)	7045.7814(17)	0.3872557(36)	1.364(16)	–	1.38	18/19	38/ /44	
31111e 01101e	6397.55051(32)	7046.02887(32)	0.38683966(44)	0.9682(11)	–	1.30	59/59	62/ /68	
31111e 01101f	–	–	–	–	–	–	/13	/30/	
31111f 01101e	–	–	–	–	–	–	/10	/23/	
31111f 01101f	6397.54992(27)	7046.02828(27)	0.38823990(34)	0.90797(76)	–	1.15	65/66	65/ /71	
41111e 11101e	–	–	–	–	–	–	/27	30/ /42	Coriolis resonance interaction with 30022e (energy levels crossing at $J = 20$). Perturbed lines ($J > 18$) excluded from the fit.
41111f 11101f	6402.09522(58)	8439.18879(58)	0.3887143(19)	0.747(11)	–	1.14	22/26	31/ /41	
30022e 11101e	–	–	–	–	–	–	/6	/ /26	Extra lines of 41111-11101 band.
32211e 02201e	6422.85527(77)	7720.12023(77)	0.3880842(62)	3.528(95)	–	1.54	23/45	49/ /61	Coriolis resonance interaction with 21122 (energy levels crossing: e at $J = 41$, f at $J = 48$). Perturbed lines with $J > 25$ (e states) and $J > 28$ (f states) excluded from the fit.
32211e 02201f	6422.85758(74)	7720.12254(74)	0.3880793(72)	3.40(13)	–	0.93	10/10	/23/	
32211f 02201e	6422.85914(49)	7720.12410(49)	0.3880548(53)	1.80(11)	–	0.67	11/11	/22/	
32211f 02201f	6422.85618(65)	7720.12115(65)	0.3880698(44)	2.129(54)	–	1.39	25/46	50/ /54	
21122e 02201e	–	–	–	–	–	–	/19	43/ /45	Coriolis resonance interaction with 32211 (energy levels crossings: e at $J = 41$, f at $J = 48$). Not fitted.
21122f 02201f	–	–	–	–	–	–	/17	40/ /52	
33311e 03301e	6442.8350(17)	8389.1850(17)	0.3903674(63)	2.384(45)	–	3.73	27/31	32/ /38	
33311e 03301f	–	–	–	–	–	–	/4	/10/	
33311f 03301e	–	–	–	–	–	–	/4	/ 9/	
33311f 03301f	6442.84294(33)	8389.19292(33)	0.3902916(11)	0.8695(62)	–	0.79	25/30	31/ /43	
32211e 10002e	–	–	–	–	–	–	/5	/ /39	Extra lines of 21122-10002 band.
20022e 01101e	6457.92346(41)	7106.40183(41)	0.38399819(88)	1.4917(32)	–	1.10	28/32	22/ /56	
20022e 01101f	6457.92351(38)	7106.40187(38)	0.3839988(16)	1.5049(93)	–	0.76	14/19	/42/	
21122e 10002e	–	–	–	–	–	–	/19	4/ /39	Coriolis resonance interaction with 32211. (energy levels crossings: e at $J = 41$, f at $J = 48$). Not fitted.
21122f 10002e	–	–	–	–	–	–	/14	/42/	
40011e 10002e	6483.25566(39)	7749.08349(39)	0.38756181(94)	0.5847(39)	–	1.38	40/46	45/ /55	
13321e 02201e	6494.29263(30)	7791.55759(30)	0.3861614(11)	1.2582(61)	–	0.72	21/22	17/ /43	
13321e 02201f	6494.28985(61)	7791.55481(61)	0.3861750(21)	1.365(14)	–	1.03	16/18	/41/	

Table 5.4. (Continued)

$^{13}C^{16}O_2$	ΔG_v	G_v	B_v	$D_v \times 10^7$	$H_v \times 10^{12}$	RMS $\times 10^3$	N_{fit}/N_{obs}	J_{MAX} $P/\,Q/R$	$Note$
13321f 02201e	6494.2902(11)	7791.5552(11)	0.3861671(25)	1.280(13)	–	0.90	12/12	/42/	
13321f 02201f	6494.29236(34)	7791.55733(34)	0.3861613(11)	1.2569(59)	–	0.70	19/19	18/ /44	
21121e 10001e	6497.76842(40)	7867.83058(40)	0.3839760(12)	1.1009(62)	–	0.96	25/25	25/ /45	
21121f 10001e	6497.76808(49)	7867.83024(49)	0.3849656(20)	1.053(15)	–	0.84	16/16	/36/	
12221e 01101e	6505.77628(33)	7154.25464(33)	0.38538040(59)	1.2810(18)	–	1.15	43/46	38/ /60	
12221e 01101f	6505.77716(36)	7154.25552(36)	0.38537922(66)	1.2764(22)	–	0.87	24/26	/56/	
12221f 01101e	6505.77779(47)	7154.25615(47)	0.38537614(79)	1.2526(25)	–	0.99	24/26	/57/	
12221f 01101f	6505.77688(28)	7154.25524(28)	0.38537567(50)	1.2477(16)	–	0.94	42/43	39/ /59	
11121e 00001e	6515.12091(22)	6515.12091(22)	0.38420058(25)	1.23502(50)	–	0.95	64/64	51/ /75	
11121f 00001e	6515.12041(30)	6515.12041(30)	0.38496562(35)	1.21274(74)	–	0.88	33/33	/72/	
41111e 11102e	–	–	–	–	–	–	/3	22/ /18	
41111f 11102f	–	–	–	–	–	–	/10	23/ /27	
20021e 01101e	6560.70028(22)	7209.17864(22)	0.38369699(79)	1.0023(62)	1.25(12)	0.73	48/49	44/ /60	
20021e 01101f	6560.70073(33)	7209.17909(33)	0.38369269(65)	0.9561(24)	–	0.82	26/27	/54/	
21121e 10002e	–	–	–	–	–	–	/1	/ /13	
21121f 10002e	–	–	–	–	–	–	/4	/20/	
10032e 10001e	6611.11875(26)	7981.18091(26)	0.38227747(70)	1.5572(32)	–	0.92	43/45	49/ /51	
04431e 04401e	6640.15275(55)	9235.91175(55)	0.3844091(23)	1.427(19)	–	1.01	19/21	35/ /35	
04431e 04401f	–	–	–	–	–	–	/1	/11/	
04431f 04401e	–	–	–	–	–	–	/2	/14/	
04431f 04401f	6640.15337(69)	9235.91237(69)	0.3844068(26)	1.397(21)	–	1.09	16/16	36/ /32	
12231e 12201e	6646.29748(65)	9346.56192(65)	0.3824778(22)	1.389(15)	–	0.87	14/15	31/ /37	
12231f 12201f	–	–	–	–	–	–	/5	30/ /18	
12232e 12202e	6647.81074(92)	9179.48888(92)	0.3836181(34)	0.845(24)	–	1.34	15/16	37/ /33	
12232f 12202f	6647.81035(65)	9179.48849(65)	0.3836201(22)	1.198(13)	–	1.22	17/19	40/ /40	
20033e 20003e	6651.34901(62)	9158.87855(62)	0.3831914(26)	1.657(21)	–	1.34	19/21	37/ /35	
20031e 20001e	–	–	–	–	–	–	/4	11/ /21	
20032e 20002e	–	–	–	–	–	–	/3	31/ /	
21121e 02201e	–	–	–	–	–	–	/9	19/ /31	
21121e 02201f	–	–	–	–	–	–	/9	/29/	

Table 5.4. (Continued)

$^{13}C^{16}O_2$	ΔG_v	G_v	B_v	$D_v \times 10^7$	$H_v \times 10^{12}$	RMS $\times 10^3$	N_{fit}/N_{obs}	J_{MAX} $P/\,Q/R$	*Note*
21121f 02201e	–	–	–	–	–	–	/3	/16/	
01141e 01111e	–	–	–	–	–	–	/3	27/ /7	
01141f 01111f	–	–	–	–	–	–	/3	/ /28	
03331e 03301e	6675.08206(48)	8621.43204(48)	0.38362980(83)	1.3554(26)	–	1.36	39/44	58/ /52	
03331e 03301f	–	–	–	–	–	–	/2	/ 8/	
03331f 03301e	–	–	–	–	–	–	/2	/ 7/	
03331f 03301f	6675.08271(47)	8621.43269(47)	0.38362942(89)	1.3526(31)	–	1.33	41/44	55/ /49	
11132e 11102e	6681.84826(38)	8578.38584(38)	0.38242846(76)	1.4233(26)	–	1.34	43/48	58/ /50	
11132f 11102f	6681.84814(53)	8578.38573(53)	0.38339066(97)	1.5220(30)	–	1.57	33/39	59/ /47	
11131e 11101e	6682.29768(42)	8719.39125(42)	0.38127288(95)	1.2301(35)	–	1.19	29/29	54/ /44	
11131f 11101f	6682.29741(51)	8719.39099(51)	0.3819947(11)	1.2210(43)	–	1.17	24/27	51/ /35	
00041e 00011e	6710.02045(52)	8993.50761(52)	0.3783923(16)	1.3140(91)	–	0.92	20/20	42/ /40	
02231e 02201e	6710.06918(27)	8007.33414(27)	0.38286777(39)	1.2938(10)	–	1.06	55/60	71/ /59	
02231e 02201f	6710.07016(54)	8007.33512(54)	0.3828704(37)	1.366(42)	–	0.68	9/10	/29/	
02231f 02201e	6710.07022(33)	8007.33518(33)	0.3828634(19)	1.357(16)	–	0.39	6/7	/34/	
02231f 02201f	6710.07068(25)	8007.33565(25)	0.38286396(36)	1.35624(91)	–	0.94	54/55	66/ /62	
10032e 10002e	6715.35214(30)	7981.17996(30)	0.38227676(46)	1.5502(12)	–	1.01	47/55	71/ /63	
10031e 10001e	6718.95872(29)	8089.02089(29)	0.38073662(44)	1.1828(12)	–	1.11	52/52	65/ /55	
01131e 01101e	6745.11228(19)	7393.59064(19)	0.38181911(18)	1.33322(31)	–	0.87	67/73	82/ /80	
01131e 01101f	6745.11163(63)	7393.58999(63)	0.3818214(22)	1.342(13)	–	1.14	12/12	/42/	
01131f 01101e	6745.11165(38)	7393.59001(38)	0.3823965(14)	1.3409(75)	–	0.77	13/13	/43/	
01131f 01101f	6745.11222(17)	7393.59058(17)	0.38239711(21)	1.34870(42)	–	0.74	62/65	75/ /69	
00031e 00001e	6780.21108(11)	6780.21108(11)	0.381350775(88)	1.32026(12)	–	0.57	85/88	89/ /91	
10031e 10002e	6823.19145(62)	8089.01928(62)	0.3807443(37)	1.212(39)	–	1.12	18/20	21/ /31	

Notes: Spectroscopic constants of the lower states were taken from Refs. [30, 56]; *RMS*, root mean squares of the fit of the rovibrational parameters; N_{fit}, number of line positions included in the fit of the spectroscopic parameters; N_{obs}, number of the observed line positions; J_{MAX}, maximum value of the rotational quantum number of the assigned transitions.

Table 5.5. Spectroscopic constants of the $^{16}O^{12}C^{18}O$ bands identified in the CW-CRDS spectrum recorded in the 5851–7045 cm^{-1} region.

$^{16}O^{12}C^{18}O$	ΔG_v	G_v	B_v	$D_v \times 10^7$	$H_v \times 10^{12}$	RMS $\times 10^3$	N_{fit}/N_{obs}	J_{MAX} $P/$	Q/R	*Note*
10022e 00001e	5858.025440(94)	5858.025440(94)	0.36250082(16)	1.37591(50)	–	0.45	68/69	7/	/63	
50003e 01101e	–	–	–	–	–	–	/10	34/	/35	
31114e 01101e	5935.33429(77)	6597.70764(77)	0.3663333(55)	−1.729(81)	–	1.47	35/56	31/	/38	Coriolis resonance interaction with 50003 (energy levels crossing at $J = 33$). Perturbed lines ($J > 25$) excluded from the fit.
31114f 01101f	5935.33046(27)	6597.70381(27)	0.36758699(90)	1.7177(57)	–	0.83	49/56	35/	/42	
11121e 01101e	5956.18363(49)	6618.55698(49)	0.3628785(16)	1.072(10)	–	1.20	39/49	42/	/30	
11121f 01101f	5956.18323(45)	6618.55658(45)	0.3636723(14)	1.0581(89)	–	1.11	44/54	40/	/38	
10021e 00001e	5959.95482(13)	5959.95482(13)	0.36262847(23)	0.99780(75)	–	0.71	103/105	57/	/60	
30014e 00001e	5993.58310(19)	5993.58310(19)	0.36635569(60)	1.8119(43)	0.875(81)	0.91	105/110	60/	/62	
32213e 02201e	–	–	–	–	–	–	/6	32/	/	
32213f 02201f	–	–	–	–	–	–	/8	36/	/	
40014e 10002e	6079.34942(41)	7338.77462(41)	0.36472560(83)	1.6405(32)	–	1.01	30/34	39/	/53	
31113e 01101e	6100.30074(31)	6762.67409(31)	0.36498475(75)	1.1927(31)	–	1.18	54/64	53/	/36	
31113e 01101f	–	–	–	–	–	–	/1	/ 2/		
31113f 01101f	6100.30106(34)	6762.67441(34)	0.36619964(81)	1.2561(35)	–	1.24	52/64	51/	/35	
30013e 00001e	6127.78234(29)	6127.78234(29)	0.36451610(70)	1.3892(41)	1.302(64)	1.08	105/111	66/	/70	
40013e 10002e	6205.67141(71)	7465.09661(71)	0.3643189(22)	0.894(13)	–	1.16	17/23	38/	/41	
30012e 00001e	6254.59158(22)	6254.59158(22)	0.36528224(30)	0.82519(76)	–	1.18	105/117	63/	/70	
40012e 10001e	6259.71042(54)	7625.55385(54)	0.3658903(20)	0.606(13)	–	1.33	27/31	23/	/40	
31112e 01101e	6265.20559(43)	6927.57894(43)	0.3653234(22)	0.957(19)	–	1.30	37/54	43/	/50	Interpolyad anharmonic resonance interaction with 51105 (energy levels crossing: e at $J = 39$ and f at $J = 35$). Perturbed lines with $J > 34$ (e states) and $J > 30$ (f states) excluded from the fit.
31112f 01101f	6265.20326(64)	6927.57661(64)	0.3666415(18)	1.0593(70)	–	2.08	39/63	44/	/52	
32212e 02201e	6269.71379(82)	7594.85479(82)	0.3667016(45)	1.519(42)	–	1.16	13/18	20/	/32	
32212f 02201f	6269.71734(82)	7594.85834(82)	0.3666613(59)	0.690(79)	–	1.24	16/19	27/	/32	

Table 5.5. (Continued)

$^{16}O^{12}C^{18}O$	ΔG_v	G_v	B_v	$D_v \times 10^7$	$H_v \times 10^{12}$	RMS $\times 10^3$	N_{fit}/N_{obs}	J_{MAX} $P/\ Q/R$	*Note*
30011e 00001e	6429.17251(24)	6429.17251(24)	0.36663060(48)	0.6015(17)	–	1.27	92/97	48/ /57	
31111e 01101e	6460.27379(55)	7122.64714(55)	0.3662138(19)	0.865(12)	–	1.44	38/44	29/ /40	
31111f 01101f	6460.27283(64)	7122.64618(64)	0.3677439(39)	0.908(44)	–	1.38	29/37	30/ /35	
11122e 00001e	6475.81140(54)	6475.81140(54)	0.3629133(16)	1.3067(87)	–	1.41	31/36	16/ /44	
11122f 00001e	6475.80726(60)	6475.80726(60)	0.3636909(18)	1.3896(98)	–	1.37	29/32	/43/	
11121e 00001e	6618.55778(28)	6618.55778(28)	0.36287599(76)	1.0696(35)	–	1.14	56/69	29/ /50	
11121f 00001e	6618.55655(25)	6618.55655(25)	0.36367488(73)	1.0736(40)	–	0.75	35/36	/45/	
02231e 02201e	6848.17322(32)	8173.31422(32)	0.3609959(12)	1.2064(81)	–	1.03	46/46	37/ /39	All the e and f components are not
02231e 02201f	–	–	–	–	–	–	/1	/ 2/	resolved. Small differences between line
02231f 02201e	–	–	–	–	–	–	/1	/ 2/	parameters of sub-bands induced by
02231f 02201f	6848.17322(34)	8173.31422(34)	0.3609958(12)	1.1836(86)	–	1.09	46/46	37/ /39	lower state line parameters.
10031e 10001e	6854.51376(63)	8220.35719(63)	0.3596843(33)	1.035(34)	–	1.10	22/27	30/ /31	
10032e 10002e	6860.67602(47)	8120.10122(47)	0.3597046(21)	1.381(19)	–	1.18	32/37	32/ /34	
01131e 01101e	6885.15507(34)	7547.52842(34)	0.35999177(53)	1.1857(16)	–	0.94	49/81	58/ /55	The e and f components are blended
01131e 01101f	–	–	–	–	–	–	/6	/14/	up to $J = 6$ for P-branch and up to
01131f 01101e	–	–	–	–	–	–	/5	/ 9/	$J = 32$ for R-branch. The unresolved
01131f 01101f	6885.15366(27)	7547.52701(27)	0.36050509(40)	1.2056(12)	–	0.74	50/82	59/ /41	lines excluded from the fit.
00031e 00001e	6922.19588(13)	6922.19588(13)	0.35949861(18)	1.18035(42)	–	0.78	115/117	70/ /66	

Notes: Spectroscopic constants of the lower states were taken from Refs. [13, 53]; *RMS*, root mean squares of the fit of the rovibrational parameters; N_{fit}, number of line positions included in the fit of the spectroscopic parameters; N_{obs}, number of the observed line positions; J_{MAX}, maximum value of the rotational quantum number of the assigned transitions.

Table 5.6. Spectroscopic constants of the $^{16}O^{12}C^{17}O$ bands identified in the CW-CRDS spectrum recorded in the 5851–7045 cm^{-1} region.

$^{16}O^{12}C^{17}O$	ΔG_v	G_v	B_v	$D_v \times 10^7$	RMS $\times 10^3$	N_{fit}/N_{obs}	J_{MAX} $P/Q/R$	*Note*
10022e 00001e	5885.32111(29)	5885.32111(29)	0.3729238(10)	1.4667(65)	0.99	51/60	27/ /45	
10021e 00001e	5986.12970(32)	5986.12970(32)	0.3727140(14)	1.040(11)	0.96	42/42	35/ /37	
30014e 00001e	6033.47685(30)	6033.47685(30)	0.37703971(84)	1.9216(43)	1.25	56/65	50/ /48	
31113e 01101e	6146.16701(46)	6810.89615(46)	0.3753434(19)	1.238(13)	1.06	28/30	16/ /38	
31113f 01101f	6146.16646(36)	6810.89560(36)	0.3766497(14)	1.3307(99)	0.82	26/32	36/ /39	
30013e 00001e	6175.95248(25)	6175.95248(25)	0.37497849(43)	1.4948(13)	1.23	77/90	46/ /62	
30012e 00001e	6298.11453(24)	6298.11453(24)	0.37531119(51)	0.8863(20)	1.14	80/87	53/ /55	
31112e 01101e	6308.00223(35)	6972.73137(35)	0.3754542(16)	1.043(15)	0.96	35/44	32/ /35	
31112f 01101f	6308.00252(42)	6972.73166(42)	0.3767911(22)	1.023(17)	1.26	29/36	38/ /18	
30011e 00001e	6463.48139(28)	6463.48139(28)	0.37675125(88)	0.6673(49)	1.19	67/81	44/ /46	
02231e 02201e	–	–	–	–	–	/8	17/ /14	All the e and f components are not resolved.
02231f 02201f	–	–	–	–	–	/8	17/ /14	
01131e 01101e	6908.36502(58)	7573.09416(58)	0.3701674(14)	1.2268(69)	0.84	18/44	44/ /41	The e and f components are blended up to $J = 7$ for P-branch and all the lines of R-branch are not resolved. The unresolved lines excluded from the fit.
01131f 01101f	6908.36407(80)	7573.09321(80)	0.3707076(19)	1.2591(88)	1.06	22/45	44/ /32	
00031e 00001e	6945.59701(17)	6945.59701(17)	0.36967109(30)	1.25099(97)	0.87	90/95	60/ /59	

Notes: Spectroscopic constants of the lower states were taken from Ref. [30]; *RMS*, root mean squares of the fit of the rovibrational parameters; N_{fit}, number of line positions included in the fit of the spectroscopic parameters; N_{obs}, number of the observed line positions; J_{MAX}, maximum value of the rotational quantum number of the assigned transitions.

Table 5.7. Spectroscopic constants of the $^{16}O^{13}C^{18}O$ bands identified in the CW-CRDS spectrum recorded in the 5851–7045 cm^{-1} region.

$^{16}O^{13}C^{18}O$	ΔG_v	G_v	B_v	$D_v \times 10^7$	$H_v \times 10^{12}$	RMS $\times 10^3$	N_{fit}/N_{obs}	J_{MAX} $P/\ Q/R$	Note
31114e 01101e	–	–	–	–	–	–	/2	/ /43	
31114f 01101f	–	–	–	–	–	–	/9	/ /49	
30014e 00001e	5876.59482(12)	5876.59482(12)	0.36716801(35)	1.9213(23)	1.394(38)	0.57	90/91	31/ /67	
32213e 02201e	5971.05620(35)	7258.02908(35)	0.3667569(13)	1.1530(91)	–	1.05	46/54	30/ /42	The e and f components are blended up to $J = 24$.
32213f 02201e	–	–	–	–	–	–	/2	/ 6/	
32213f 02201f	5971.05632(44)	7258.02919(44)	0.3667636(14)	1.4026(76)	–	1.55	50/53	30/ /45	
40014e 10002e	5975.83766(27)	7220.73744(27)	0.3658266(16)	1.717(18)	–	0.72	44/59	29/ /45	Interpolyad anharmonic resonance interaction with 60007 (energy levels crossing at $J = 38$).
31113e 01101e	5995.98294(35)	6639.30168(35)	0.3651508(17)	0.822(14)	−7.09(30)	1.18	65/95	55/ /58	Interpolyad anharmonic resonance interaction with 51106 (energy levels crossing: e at $J = 33$, f at $J = 30$). Perturbed lines (e: $22 < J < 38$, f: $21 < J < 37$) excluded from the fit.
31113e 01101f	–	–	–	–	–	–	/8	/13/	
31113f 01101e	–	–	–	–	–	–	/5	/12/	
31113f 01101f	5995.98348(33)	6639.30222(33)	0.3664766(15)	0.966(12)	−5.61(25)	1.09	64/92	57/ /54	
42202e 01101e	6000.1260(19)	6643.4447(19)	0.3689873(62)	1.923(45)	–	0.94	14/14	33/ /29	
42202f 01101f	6000.1146(17)	6643.4334(17)	0.3690257(49)	1.463(31)	–	1.38	18/22	39/ /29	
40013e 10001e	6009.40981(57)	7351.68697(57)	0.3637792(18)	0.735(10)	–	2.15	61/62	44/ /43	Coriolis resonance interaction with 51102e. Perturbed lines are fitted.
30013e 00001e	6026.62396(11)	6026.62396(11)	0.36517652(26)	1.5694(15)	0.854(22)	0.56	128/131	70/ /67	
40013e 10002e	6106.78745(69)	7351.6872(69)	0.3637807(24)	0.752(13)	–	2.19	34/36	43/ /23	Coriolis resonance interaction with 51102e. Perturbed lines are fitted.
40012e 10001e	6136.34701(35)	7478.62416(35)	0.3648661(22)	0.788(30)	11.23(20)	0.83	41/42	37/ /42	
30012e 00001e	6140.12308(12)	6140.12308(12)	0.36453164(27)	0.8748(11)	–	0.64	102/138	70/ /78	Coriolis + ℓ-type ($\Delta\ell_2 = \pm 3$) resonance interaction with 33301e (energy levels crossing at $J = 58$). Perturbed lines ($J > 52$) excluded from the fit.
31112e 01101e	6146.94919(17)	6790.26793(17)	0.36488734(30)	1.0661(10)	–	0.83	78/82	57/ /61	
31112f 01101f	6146.94914(18)	6790.26789(18)	0.36613168(35)	1.0379(12)	–	0.84	76/82	57/ /56	
32212e 02201e	6149.25533(47)	7436.22820(47)	0.3663215(26)	1.389(25)	–	1.13	26/29	21/ /33	The e and f components are blended up to $J = 24$.
32212f 02201f	6149.25616(45)	7436.22903(45)	0.3663068(17)	1.0834(84)	–	1.22	24/28	21/ /46	
41101e 00001e	6164.57912(78)	6164.57912(78)	0.3680600(21)	0.873(12)	–	0.90	22/23	39/ /40	
30011e 00001e	6279.48793(17)	6279.48793(17)	0.36591684(50)	0.6992(35)	0.810(62)	0.78	102/103	62/ /63	

Table 5.7. (Continued)

$^{16}O^{13}C^{18}O$	ΔG_v	G_v	B_v	$D_v \times 10^7$	$H_v \times 10^{12}$	RMS $\times 10^3$	N_{fit}/N_{obs}	J_{MAX} $P/\ Q/R$	*Note*
40011e 10001e	–	–	–	–	–	–	/11	26/ /20	
31111e 01101e	6311.98861(28)	6955.30735(28)	0.36557602(62)	0.8824(25)	–	1.28	81/85	48/ /53	
31111f 01101f	6311.98767(32)	6955.30642(32)	0.36698781(80)	0.8395(37)	–	1.40	72/76	50/ /48	
11122e 00001e	6314.55689(38)	6314.55689(38)	0.3633372(11)	1.3119(49)	–	1.36	39/42	26/ /50	
11122f 00001e	6314.55488(41)	6314.55488(41)	0.36419968(98)	1.3990(43)	–	1.08	31/34	/50/	
11121e 00001e	6449.11837(27)	6449.11837(27)	0.36273493(61)	1.0987(23)	–	1.11	69/76	28/ /53	
11121f 00001e	6449.11885(26)	6449.11885(26)	0.36347375(61)	1.0627(27)	–	0.81	43/44	/50/	
03331e 03301e*) 03331f 03301f	6624.42752(63)	–	0.3619342(34)	1.193(35)	–	1.24	33/36	30/ /30	All the e and f components are blended leading to a single set of parameters for both components.
11132e 11102e	6633.17982(87)	8502.41884(87)	0.3606574(36)	1.370(28)	–	0.93	13/15	34/ /34	
11132f 11102f	–	–	–	–	–	–	/11	32/ /34	
02231e 02201e 02231f 02201f	6659.01424(39)	7945.98712(39)	0.36124741(93)	1.1916(42)	–	1.52	69/78	53/ /43	All the e and f components are blended leading to a single set of parameters for both components.
02231e 02201f 02231f 02201e	–	–	–	–	–	–	/5	/14/	
10032e 10002e	6666.66806(33)	7911.56784(33)	0.36043380(73)	1.3941(28)	–	1.46	66/71	55/ /38	
10031e 10001e	6666.97474(47)	8009.25189(47)	0.3595268(12)	1.0173(52)	–	1.41	42/47	49/ /38	
01131e 01101e	6693.65622(41)	7336.97496(41)	0.36027252(50)	1.1928(12)	–	1.39	68/99	66/ /62	The e and f components are blended up to $J = 4$ for P-branch and up to $J = 32$ for R-branch. The unresolved lines excluded from the fit.
01131e 01101f	–	–	–	–	–	–	/4	/11/	
01131f 01101e	–	–	–	–	–	–	/6	/ 9/	
01131f 01101f	6693.65563(34)	7336.97437(34)	0.36079557(39)	1.20280(91)	–	1.11	66/99	67/ /57	
00031e 00001e	6728.35494(13)	6728.35494(13)	0.35981636(15)	1.17607(30)	–	0.81	129/133	77/ /72	
20023e 00001e	6893.66279(55)	6893.66279(55)	0.3638500(17)	1.567(10)	–	1.67	38/42	45/ /39	
20022e 00001e	7017.89243(41)	7017.89243(41)	0.3621140(13)	1.2530(72)	–	1.28	45/51	49/ /34	

Notes: Spectroscopic constants of the lower states were taken from Ref. [30]; *RMS*, root mean squares of the fit of the rovibrational parameters; N_{fit}, number of line positions included in the fit of the spectroscopic parameters; N_{obs}, number of the observed line positions; J_{MAX}, maximum value of the rotational quantum number of the assigned transitions.

*) Spectroscopic constants for the lower state ($B_v = 0.370105(14)$, $D_v = 1.22(12) \times 10^{-7}$) were fitted using the method of combination differences.

Table 5.8. Spectroscopic constants of the $^{16}O^{13}C^{17}O$ bands identified in the CW-CRDS spectrum recorded in the 5851–7045 cm^{-1} region.

$^{16}O^{13}C^{17}O$	ΔG_v	G_v	B_v	$D_v \times 10^7$	$H_v \times 10^{12}$	RMS $\times 10^3$	N_{fit}/N_{obs}	J_{MAX} $P/\,Q/R$	*Note*
30014e 00001e	5912.72743(16)	5912.72743(16)	0.37780408(47)	2.0523(25)	–	0.73	75/80	46/ /50	
31113e 01101e	6040.24946(46)	6685.99346(46)	0.3756466(14)	1.2701(78)	–	1.50	49/60	43/ /43	Interpolyad anharmonic resonance
31113f 01101f	6040.24854(37)	6685.99254(37)	0.3771285(12)	1.5041(72)	–	1.02	38/49	43/ /39	interaction with 51106 (energy levels crossing: e at $J = 38$, f at $J = 31$).
30013e 00001e	6071.57307(16)	6071.57307(16)	0.37578586(54)	1.6811(40)	0.996(77)	0.75	100/101	60/ /60	
30012e 00001e	6188.05258(20)	6188.05258(20)	0.37458944(37)	0.9661(12)	–	1.08	103/106	57/ /59	
31112e 01101e	6192.54276(59)	6838.28676(59)	0.3750286(14)	1.1045(58)	–	2.06	52/63	47/ /50	
31112f 01101f	6192.54279(31)	6838.28679(31)	0.37634972(89)	1.1026(49)	–	1.05	52/59	43/ /45	
30011e 00001e	6318.43390(26)	6318.43390(26)	0.37592801(50)	0.7007(17)	–	1.36	96/100	58/ /56	
31111e 01101e	6351.76882(48)	6997.51282(48)	0.3756286(34)	1.058(47)	–	0.81	15/20	27/ /22	
31111f 01101f	6351.76617(61)	6997.51017(61)	0.3770712(20)	0.831(12)	–	1.25	26/27	41/ /33	
11121e 00001e	6479.81785(34)	6479.81785(34)	0.3728866(13)	1.1358(82)	–	1.08	37/41	18/ /42	
11121f 00001e	6479.81723(21)	6479.81723(21)	0.37364131(83)	1.1341(60)	–	0.58	33/34	/38/	
02231e 02201e 02231f 02201f	6682.6878(11)	7974.5148(11)	0.3714961(33)	1.274(20)	–	1.22	14/14	39/ /	All the e and f components are blended leading to a single set of parameters for both components.
01131e 01101e	6717.52035(59)	7363.26435(59)	0.3704376(11)	1.2094(38)	–	1.26	30/54	54/ /43	The e and f components are blended
01131f 01101f	6717.52407(66)	7363.26807(66)	0.3710210(10)	1.2029(36)	–	1.48	34/58	56/ /41	up to $J = 6$ for P-branch and up to $J = 29$ for R-branch. The unresolved lines excluded from the fit.
00031e 00001e	6752.41230(20)	6752.41230(20)	0.37000423(26)	1.23138(61)	–	1.06	104/110	66/ /70	

Notes: Spectroscopic constants of the lower states were taken from Ref. [30]; *RMS*, root mean squares of the fit of the rovibrational parameters; N_{fit}, number of line positions included in the fit of the spectroscopic parameters; N_{obs}, number of the observed line positions; J_{MAX}, maximum value of the rotational quantum number of the assigned transitions.

Table 5.9. Spectroscopic constants of the $^{13}C^{18}O_2$ bands identified in the CW-CRDS spectrum recorded in the 5851–7045 cm^{-1} region.

$^{13}C^{18}O_2$	ΔG_v	G_v	B_v	$D_v \times 10^7$	RMS $\times 10^3$	N_{fit}/N_{obs}	J_{MAX} P/R
30013e 00001e	5927.25629(23)	5927.25629(23)	0.34359260(49)	1.2394(19)	0.82	47/47	53/53
30012e 00001e	6043.49559(43)	6043.49559(43)	0.3440003(12)	0.7397(56)	1.10	27/27	43/47
01131e 01101e	6638.97470(60)	7277.44030(60)	0.3393925(15)	1.0345(75)	1.32	25/28	45/34
01131f 01101f	6638.97496(63)	7277.44056(63)	0.3398844(19)	1.026(11)	1.54	26/27	43/35
00031e 00001e	6673.29972(34)	6673.29972(34)	0.33896216(60)	1.0430(20)	1.16	41/41	59/45

Notes: Spectroscopic constants of the lower states were taken from Ref. [50]; *RMS*, root mean squares of the fit of the rovibrational parameters; N_{fit}, number of line positions included in the fit of the spectroscopic parameters; N_{obs}, number of the observed line positions; J_{MAX}, maximum value of the rotational quantum number of the assigned transitions.

Table 5.10. Spectroscopic constants of the $^{17}O^{13}C^{18}O$ bands identified in the CW-CRDS spectrum recorded in the 5851–7045 cm^{-1} region.

$^{17}O^{13}C^{18}O$	ΔG_v	G_v	B_v	$D_v \times 10^7$	RMS $\times 10^3$	N_{fit}/N_{obs}	J_{MAX} P/R
30013e 00001e	5975.17655(26)	5975.17655(26)	0.35379342(91)	1.4161(61)	0.87	54/54	34/40
30012e 00001e	6088.67260(42)	6088.67260(42)	0.3537195(21)	0.750(18)	1.09	31/31	34/34
00031e 00001e	6698.86028(48)	6698.86028(48)	0.3488406(10)	1.1110(43)	1.37	42/45	50/43

Notes: Spectroscopic constants of the lower states were taken from Ref. [49]; *RMS*, root mean squares of the fit of the rovibrational parameters; N_{fit}, number of line positions included in the fit of the spectroscopic parameters; N_{obs}, number of the observed line positions; J_{MAX}, maximum value of the rotational quantum number of the assigned transitions.